CHARACTERISATION OF HIGH-BURNUP LWR FUEL RODS THROUGH GAMMA TOMOGRAPHY

THÈSE N^O 3762 (2007)

PRÉSENTÉE LE 5 AVRIL 2007
À LA FACULTÉ DES SCIENCES DE BASE
Institut de physique de l'énergie et des particules
SECTION DE PHYSIQUE

ÉCOLE POLYTECHNIQUE FÉDÉRALE DE LAUSANNE

POUR L'OBTENTION DU GRADE DE DOCTEUR ÈS SCIENCES

PAR

Stefano CARUSO

laurea in ingegneria nucleare, Università degli studi di Roma, Italie
et de nationalité italienne

acceptée sur proposition du jury:

Prof. R. Schaller, président du jury
Prof. R. Chawla, directeur de thèse
Prof. H.-D. Berger, rapporteur
Prof. K. Peddicord, rapporteur
Prof. O. Schneider, rapporteur

EPFL
ÉCOLE POLYTECHNIQUE
FÉDÉRALE DE LAUSANNE

Lausanne, EPFL
2007

This research work is dedicated to

my parents, Giovanni and Luisa
my wife, Francesca
and my son, Gabriele

Abstract

Current fuel management strategies for light water reactors (LWRs), in countries with high back-end costs, progressively extend the discharge burnup at the expense of increasing the ^{235}U enrichment of the fresh UO_2 fuel loaded. In this perspective, standard non-destructive assay (NDA) techniques, which are very attractive because they are fast, cheap, and preserve the fuel integrity, in contrast to destructive approaches, require further validation when burnup values become higher than 50 GWd/t.

This doctoral work has been devoted to the development and optimisation of non-destructive assay (NDA) techniques based on gamma-ray emissions from irradiated fuel. It represents an important extension of the unique, high-burnup related database, generated in the framework of the LWR-PROTEUS Phase II experiments.

A novel tomographic measurement station has been designed and developed for the investigation of irradiated fuel rod segments. A unique feature of the station is that it allows both gamma-ray transmission and emission computerised tomography to be performed on single fuel rods. Four burnt UO_2 fuel rod segments of 400 mm length have been investigated, two with very high (52 GWd/t and 71 GWd/t) and two with ultra-high (91 GWd/t and 126 GWd/t) burnup. Several research areas have been addressed, as described below.

The application of transmission tomography to spent fuel rods has been a major task, because of difficulties of implementation and the uniqueness of the experiments. The main achievements, in this context, have been the determination of fuel rod average material density (a linear relationship between density and burnup was established), fuel rod linear attenuation coefficient distribution (for use in emission tomography), and fuel rod material density distribution.

The non-destructive technique of emission computerised tomography (CT) has been applied to the very high and ultra-high burnup fuel rod samples for determining their within-rod distributions of caesium and europium fission-product radionuclides. As indicated above, results provided by the transmission tomography measurements were employed in the emission tomography reconstruction phase, together with a calculated global efficiency matrix and input sinograms derived from the processing of measured projections. Different tomographic algorithms were tested and "tuned", on the basis of known test distributions, before being applied to the actual fuel rod measurements. Amongst the various possibilities, the Paraboloidal Surrogates Coordinate Ascent (PSCA) penalised likelihood method has been chosen for presentation of the final results, because it ensures high precision, especially in resolving the most difficult peripheral regions of the rods. The results of the emission tomography have indicated large central depressions in the caesium distributions, but of varying extent from sample to sample. Particularly interesting is the case of the 126 GWd/t sample, showing a

very deep central depression (a factor of ~2.5 for ^{137}Cs, a factor of ~3 for ^{134}Cs). Differences in the relative activity distributions of ^{137}Cs and ^{134}Cs have, in fact, been observed for all the samples. The depression of ^{134}Cs is more marked than that of ^{137}Cs, probably due to the different origins of the two isotopes. In contrast, the europium shows an almost flat distribution. In order to support the tomographically measured caesium distributions, the results of destructive chemical techniques applied on samples from the same fuel rod (126 GWd/t sample) were examined and found to show reasonably good agreement with the tomography, thus confirming the depressed distributions at the centre of the rod.

In addition to the tomographic reconstructions, the present research has also investigated the possibility to use single isotope activities, and/or isotopic concentration ratios from ^{134}Cs, ^{137}Cs, and ^{154}Eu, as burnup indicators at very high and ultra-high burnups. The corresponding non-destructive measurements, performed using three different approaches, have been compared with chemical assays, as well as with reactor physics calculations (CASMO). Whereas the chemical results confirm the current gamma-spectroscopic measurements within uncertainties, the agreement between measurements and calculations is not satisfactory. It has been shown that certain indicators, well established for application at low and medium burnups, suffer a serious loss of reliability at high burnup. Nevertheless, the possibility of successfully employing other burnup monitors has been clearly highlighted.

Considering that the overall effort required for the destructive chemical analysis of fuel samples is much greater, the current investigations have clearly demonstrated that non-destructive gamma spectrometry, in conjunction with corresponding transmission and emission tomography measurements, can indeed be considered a valid approach for characterising fuel burnup in the high/ultra-high range.

Version Abrégée

Dans les pays où l'industrie nucléaire prend à sa charge les couts élevés de retraitement ou de stockage du combustible usé des réacteurs à eau légère (Light Water Reactor), la stratégie de gestion du combustible s'oriente vers une augmentation du taux de combustion en fin de cycle rendu possible par l'augmentation de l'enrichissement en ^{235}U du combustible frais. Dans cette optique, les techniques non-destructives de caractérisation du combustible (« Non-Destructive Assay », NDA), qui sont très attractives car rapides, à faible coût et préservant l'intégrité du combustible, nécessitent d'être qualifiées pour des taux de combustions supérieurs à 50 GWd/t.

Ce travail de thèse se focalise sur le développement et l'optimisation des techniques non-destructives de caractérisation de combustible basées sur l'émission photonique du combustible irradié. Il représente une extension conséquente de la base de données sur les combustibles à hauts taux de combustion créée dans le cadre des expériences de la Phase II du programme LWR-PROTEUS.

Un poste de mesure par tomographie a été conçu et développé pour caractériser des segments de combustible irradiés. Il a l'avantage de réaliser simultanément des tomographies par transmission et émission de photons du même segment de combustible. Quatre segments de combustibles d'UO_2 brûlés ayant chacun une longueur de 400 mm ont été étudiés. Alors que deux segments se caractérisent par des taux de combustion déjà très hauts (52 GWd/t et 71 GWd/t), les deux autres possèdent des taux de combustion extrêmement élevés (91 GWd/t et 126 GWd/t).

L'application de la tomographie par transmission aux barres de combustible irradiées a été une composante majeure de ce travail de thèse en raison des difficultés de mise en œuvre de ces expériences et de son caractère novateur. Les principaux résultats obtenus dans ce contexte sont : la densité moyenne du combustible (une relation linéaire entre la densité et le taux de combustion a été établie), la distribution de coefficient d'atténuation linéaire dans le combustible (utilisé pour la tomographie par émission), et la distribution de densité dans le combustible.

La tomographie par émission assistée par ordinateur (« Computerised Tomography ») a été utilisée afin de déterminer la distribution au sein des segments de combustibles à haut et très haut taux de combustion des isotopes du césium et de l'europium qui sont produits par fissions et émettent des photons. Dans la phase de reconstruction de la tomographie par émission nous avons utilisé la distribution de coefficient d'atténuation linéaire obtenue lors de la tomographie par transmission, une matrice globale d'efficacité calculée à partir de la géométrie de mesure par un code de transport photonique, et des sinogrammes provenant des projections des mesures. Différents algorithmes tomographiques ont été testés et ajustés, sur la base de distributions test connues, avant d'être appliqués aux mesures. Parmi ceux-ci, un algorithme spécifique (« Paraboloidal Surrogates Coordinate Ascent », PSCA) a été utilisé pour présenter les résultats finaux, car il est très précis et permet notamment de résoudre les difficultés rencontrées à la périphérie des pastilles de combustible.

La tomographie par émission a montré une large dépression de la distribution de césium au centre de la pastille combustible. Cette dépression varie d'un segment combustible à l'autre. L'échantillon ayant un taux de combustion de 126 GWd/t est particulièrement intéressant car la dépression centrale est très marquée (un facteur ~2.5 pour le ^{137}C et ~3 pour le ^{134}C entre la périphérie et le centre). Les distributions relatives du ^{137}Cs et du ^{134}Cs sont différentes pour chaque échantillon. La dépression du ^{134}Cs est plus marquée que celle du ^{137}Cs, probablement en raison des différents mécanismes de production des deux isotopes. Au contraire, la distribution de l'europium est plate. Pour confirmer la forme de la distribution de césium obtenue par tomographie, les résultats obtenus pour l'échantillon au taux de combustion de 126 GWd/t ont été comparés à des mesures effectuées par des techniques destructives d'analyses chimiques sur une autre portion du barreau de 126 GWd/t. Ces analyses ont confirmé la dépression de la distribution de césium au centre du combustible.

En plus de reconstructions tomographiques, cette thèse a eu pour but de tester la possibilité d'utiliser les activités des isotopes ^{134}Cs, ^{137}Cs, et ^{154}Eu ainsi que leurs rapports comme indicateurs du taux de combustion d'échantillons à haut et très haut taux de combustion. Les résultats obtenus par de telles méthodes non-destructives, utilisant trois approches différentes, ont été comparés avec ceux issus d'analyses chimiques et avec les prédictions résultant du code de physique des réacteurs CASMO. Les résultats des analyses chimiques confirment, aux incertitudes près, ceux obtenus par les méthodes non destructives. Ce n'est pas le cas des prédictions de calcul. Nous avons également montré que certains indicateurs de taux de combustion, utilisés couramment pour de faibles et moyens taux de combustion, perdent beaucoup de leur fiabilité pour de hauts taux de combustion. Cependant la possibilité d'utiliser d'autres indicateurs pour les échantillons à haut et très haut taux de combustion a été clairement démontrée.

Considérant les efforts importants nécessités par les méthodes destructives d'analyse chimique du combustible, ce travail de thèse a clairement démontré que la spectrométrie gamma non-destructive, utilisée en conjonction avec des mesures de tomographie par transmission et émission, peut tout à fait être considérée comme une approche valide pour caractériser les combustibles à haut et très haut taux de combustion.

Mots-clés: analyse non destructive, combustible irradié, réacteurs à eau légère, taux de combustion élevé, spectrométrie gamma, tomographie par transmission, tomographie par émission, densité du combustible, indicateurs du taux de combustion.

Contents

1. Introduction

The worldwide demand for electricity is growing continuously. In 2003, nuclear power accounted for 16% of global electricity generation with 439 nuclear power plants in operation around the world. Since the late 1980s, nuclear electricity generation has grown about 2.5% per year, at the same rate of overall global electricity generation but well below the rate of expansion observed in the 1970s and early 1980s [iae].

The future of nuclear power depends not only on resolving issues of economics, safety and security, waste management and proliferation resistance, but also on the development of innovative technologies. The management and disposal of spent fuel continues to be a critical issue in terms of public acceptance and specially for any planning of nuclear energy expansion in the future. In this frame, efforts towards understanding the evolution of nuclear fuel during its life in the reactor are really crucial. The improvement of fuel efficiency, together with the achievement of a high level of safety, is a prime target for research, and there is thus a need for detailed information about fuel performance in different reactors.

In particular, it is extremely important to have an accurate knowledge of the composition and the reactivity loss of the fuel at the end of its life in the reactor in order to carry out criticality safety analyses, shielding design and radiation protection studies. An important parameter that plays a central role in this context is the fuel burnup. The fuel burnup is a measure of the total amount of thermal energy generated per unit of fissile material in the reactor and is the main indicator of the useful lifetime of fuel in the core. The main question related to burnup is whether there are significant incentives to increase it further and what the limits are with respect to economic, engineering, and physics implications. Longer fuel cycles imply reduction of the outage period and consequently the maintenance costs, because less fuel needs to be replaced. The total cost of the fuel decreases at high burnup, because more full-power days are obtained. However, an accurate estimation of the economic benefit is not a simple task, because of several uncertainties that must be carefully considered. In such an analysis, waste disposal aspects play an important role too, the corresponding costs representing an important factor in the computation of global costs [xu].

For all these reasons, a precise experimental evaluation of burnup is essential and the possibilities to achieve this goal are several. For instance, chemical analysis is a possible but expensive way. An interesting approach is the use of non-destructive assays (NDAs), because these techniques are quite fast, cheaper, and preserve fuel integrity in contrast to destructive approaches. In particular, an

interesting NDA method to evaluate the burnup of irradiated fuel is by performing gamma-spectroscopy, thus enabling the determination of the activity ratios of certain fission product radio-isotopes.

In the process of observing and evaluating fuel performance, the development and application of new techniques of investigation can play an extremely important role. Thus, for example, the implementation of computer tomography, widely used in medical applications, is a very promising non-invasive technique that can be employed successfully in the investigation of single fuel rods as well as entire fuel assemblies. This technique, although not new in nuclear fuel characterisation, is a growth area due to the continued progress of computer science that makes possible the implementation of more sophisticated and better performing algorithms for the reconstruction of images. By its application to nuclear fuel investigation technologies, it is possible to perform tomographic reconstruction of isotopic distributions inside single fuel rods, which is extremely useful for the understanding of fuel performance.

This thesis addresses the design, the construction and the employment of a new gamma detection station assigned to perform non-destructive investigations of highly burnt fuel rods. In particular, the detection station has been designed and deployed for gamma-ray emission and transmission tomography measurements with irradiated fuel rod samples at medium to very high burnup levels.

1.1. General Considerations on LWRs

Complementing the many national initiatives are two major international efforts to promote innovative approaches in nuclear power generation technology: the Generation IV International Forum (GIF), and the International Project on Innovative Nuclear Reactors and Fuel Cycles (INPRO) of the International Atomic Energy Agency (IAEA). Since the 1950s, however, it is light water reactors (LWRs) which have been dominating worldwide nuclear electricity generation, their current contribution being over 80%. As a result, important research trends in nuclear power plant (NPP) technology still need to be directed to such reactors, with the aim of improving safety assessments, fuel cycle efficiency and operational flexibility. The two major categories of commercial LWRs are PWR (pressurised water reactor) and BWR (boiling water reactor), pursued in the United States, for example, by Westinghouse and General Electric, respectively.

PWRs are based on a two-loop design, where the primary loop has water only in the liquid state at high pressure (~150 bar) while in the secondary loop the water is two-phase. A heat exchanger is placed between the two loops to generate steam in the second loop as required by the turbines, which are connected to a generator for the electricity production. BWRs have a single loop and work at

lower pressure (~70 bar) with the water in two phases. Here, it is the steam produced in the reactor core which is fed directly to the turbines.

In LWR cores, the water has a multiple purpose. Thus, it is both the vehicle for conversion of the energy produced by the fuel into electrical energy and also the moderator, to slow down the neutrons released by the fission process (from fast to thermal energy) so that a self-sustained chain reaction is possible with the low enriched uranium used. The fuel design in LWRs involves an optimisation the uranium-to-water ratio. The fuel itself can be UO_2 with uranium enriched to 3-5 wt% or mixed oxide (MOX), a mixture of UO_2 and PuO_2. The fuel pellets are stacked in Zircaloy tubes of ~4 m length with a diameter of about 12 mm. These fuel pins are mounted in relatively large numbers (100-300, depending on the reactor type and fuel design) to form assemblies. Fig 1.1 shows an example of a BWR fuel assembly.

Fig. 1.1: SVEA-96 fuel assembly (BWR).

1.2. Status of Research on LWR Fuels

As indicated in the previous section, considerable efforts are being expended by the scientific community to improve the technology of current and future light water reactors. Many projects are developed in order, for example, to extend the life of NPPs, improve fuel performance, increase the average discharge burnup, up-rate the thermal power, and/or increase cycle lengths. The final goal of such trends, in most cases, is the reduction of power generation costs in an increasingly competitive electricity market.

In modern BWRs, the fuel assembly design is constantly in evolution. A principal aim thereby is to increase the net heat production (power up-rate), while respecting safety limits at the level of the individual fuel pin. This is often achieved with very heterogeneous assembly designs, which permit a relatively flat power distribution to be maintained during the lifetime of the fuel in the core. Furthermore, the cycle economy is improved by using relatively high initial ^{235}U enrichments in order to achieve high discharge burnup levels.

Concerning PWR fuel, increased resistance to corrosion of the fuel in the core is attained by improving the cladding material, the cycle economy is optimised by increasing the ^{235}U enrichment, and the thermal efficiency is improved by increasing the outlet temperature. Separate consideration must be given to the use of MOX fuel in PWRs where the "self-generated recycle" (use of 30-40%

3

MOX fuel in the core) is well established. In this kind of core configuration, there are pronounced changes in pin power between the UO_2 and MOX assemblies. The heterogeneous power distribution can result in significantly larger uncertainties in reactor physics codes predictions. In addition, questions related to plutonium production (current MOX loadings do not result in a global reduction of Pu but rather, in just a slowing down of its production) are of some concern, and a significant R&D effort is required in this context.

In the light of such an evolution of LWR fuel designs, new questions arise. First of all, the increase of the total energy produced per fuel assembly, with the consequent increase of fission products and actinides in spent fuel, introduces problems in the management of the back-end of the fuel cycle. Cladding integrity, radioactive inventories, decay heat, intermediate and final disposal, handling, transport, and reprocessing are the main topics. Accordingly, there is a need to increase the experience with high-burnup fuel and the validation of corresponding prediction methodologies. For this reason, the update of the experimental database is extremely important and, as a consequence, the development of novel techniques for more sophisticated spent fuel investigations represents a crucial field for future development.

In any case, the small number of critical facilities suitable for complex LWR critical experiments worldwide is an important reason for the rather limited experimental database available. In addition, critical facilities can normally handle only fresh fuel, so that investigations using burnt fuel have been really scarce at these facilities. Furthermore, while the use of fresh UO_2 is relatively unproblematic, the investigation of Pu-containing fuel (typically MOX) is very difficult due to safeguards and safety considerations, the implementation of special procedures being required in this context. It is thus no big surprise that very few experimental results are available from critical LWR experiments employing burnt fuel.

1.2.1. Research at PSI

The Paul Scherrer Institute (PSI) conducts basic and applied research in several areas. In particular, a major effort is devoted to nuclear energy and safety. In this section, attention is focused on the research trends in nuclear fuel technology and the latest progress achieved at PSI in the different laboratories concerned.

Among the activities conducted at PSI-West, irradiated fuel rods have been investigated utilising the capabilities of the neutron radiography set-up [koe-bae] at the spallation neutron source facility SINQ [gro]. The main purpose thereby has been the non-destructive examination of the quantity and

distribution of hydride within the fuel cladding. Radioprotection and safeguards requirements, however, considerably limit the use of experimental facilities at PSI-West to study nuclear fuel.

The Laboratory for Materials Behaviour (LWV), in PSI-East, is the only Swiss laboratory with hot cells and the capability to perform a wide range of in-depth investigations of spent fuel rods. The post-irradiation examinations, conducted routinely in the framework of different PWR and BWR programmes, involve the application of a number of different techniques (visual inspection, determination of diameter variation and rod elongation, fission gas release, metallographic structure, oxide layer formation, within-pellet relative isotopic distributions through secondary ion mass spectrometry (SIMS), profilometry for the determination of relative activity variations along the rod, electron microprobe analysis (EMPA), laser ablation integrated with inductively coupled plasma mass spectrometry (LA-ICP-MS), etc.). Thus, LWV has been the centre for a number of experimental programmes for the study of burnt nuclear fuel, e.g. ARIANE [wer].

In the Laboratory for Reactor Physics and Systems Behaviour (LRS), there are a number of activities related to LWR technology. Thus, for example, calculational studies have been carried out for the analysis of the ARIANE experiments using CASMO-4 [ede] and MONTEBURNS [tre], and significant contributions have been made to the high-irradiation, Gd-rod project conducted jointly by NPP-Leibstadt (KKL) and PSI. The analytical expertise applied in this context is that associated with the detailed modelling of the Swiss NPPs, necessary for on-call services for safety-related issues in the framework of the STARS project. Maintaining and upgrading its calculational capabilities to keep pace with the trends of the Swiss utilities (swissnuclear) towards higher burnups has, in this sense, been a central task within LRS.

The active collaboration between LRS and swissnuclear in the area of LWR-physics has enabled the establishment, at PSI, of a high level of expertise in the field of LWR analysis. This comprises the application of both industry-standard codes such as CASMO-4 [ede] for core-follow calculations and the PSI's ELCOS code system [par] for special studies. In addition, the use of Monte-Carlo codes such as MCNP [bri] has proved to be very useful because of their ability to model complex 3D-geometies using continuous-energy cross sections. Furthermore, studies have been conducted to assess the safety and operational impact of increased MOX loadings and the possible introduction of plutonium inert matrix fuel (IMF) in LWRs (see below). Analytical LRS activities of the above type often indicate the areas in which integral reactor physics experiments are required, and the laboratory's versatile critical facility PROTEUS plays a crucial role in this context (see Section 1.2.1.1).

To take a particular example, considerable R&D efforts have been underway at PSI towards establishing the viability of Pu-Er-Zr oxide as an IMF that could be introduced into present-day LWRs without basically changing fuel assembly and core designs [led-sta-cha]. Analytical studies, conducted at the whole core level, have shown that Pu-inventory reductions about twice as high as with MOX fuel would be achieved in once-through operation, the poor isotopic quality of the discharged plutonium as well as the chemical inertness of the irradiated IMF warranting its direct end-disposal [par2-sta2]. Other studies have also been conducted to assess the appropriateness of current LWR codes and their cross section datasets for IMF analysis [par3-par4-pel]. In the above context, first-of-its-kind experimental work has been, and is continuing to be, performed at PROTEUS to assess the reliability of the neutronics design calculations for Pu-IMF utilisation in LWRs [cha2]. These experiments employ a part of the fuel materials which were specially fabricated at the PSI-Hotlab for the comparative IMF/MOX irradiation tests currently underway at Halden [led2-cha3].

The LWR-PROTEUS project [wil-wil2] in LRS is, worldwide, one of the most significant reactor physics research initiatives supporting the sophistication of LWR fuels for optimising channel power, burnup and assembly power distributions. This project was designed to evaluate the capabilities of different modern calculational codes of interest to the utilities using nominal assembly data (*production models*), to qualify the adequacy of such calculations by studying the sensitivity of reactor physics parameters with regard to departure from nominal conditions (geometry and material characterisation), and to validate the codes by developing an ambitious experimental programme, which includes the measurement of rod-by-rod reaction rate distributions, individual fuel rod reaction rate ratios, and the reactivity effects of perturbing a critical lattice by removing individual fuel rods.

1.2.1.1. The LWR-PROTEUS Phase II experiments

PROTEUS is a zero-power research reactor that has been in operation since February 1968 at the Paul Scherrer Institute in Switzerland. During its lifetime, it has been used to carry out experimental reactor physics investigations for a wide range of advanced reactor concepts, like the gas-cooled fast reactor (GCFR), the tight-pitch, high conversion, light water reactor (HCLWR) and the modular high temperature reactor (HTR). It is currently being employed for investigations related to modern and advanced light water reactor fuel for the Swiss nuclear utilities (LWR-PROTEUS programme). Thus, in the LWR-PROTEUS Phase I configurations [mur], the central test zone was composed of 9 (3x3) advanced BWR assemblies (see Fig. 1.2), with the central fuel element being investigated under a wide variety of conditions from the viewpoints of reaction rate distributions, pin removal worths, etc.

In LWR-PROTEUS Phase II [mur2], the central BWR assembly was replaced by a PWR mock-up zone, with a central guide tube where the neutron spectrum was PWR-representative. Different moderators could be used in the mock-up zone to simulate different reactor conditions. From the experimental viewpoint, 13 samples of LWR fuel rods that had been irradiated up to nearly record burnup values in the Swiss NPPs were investigated in Phase II from different research fronts. Thus, the first campaign of reactivity and neutron source strength measurements with the irradiated samples was completed in PROTEUS under three different moderation conditions in the PWR-zone: a mixture of light and heavy water, full-density light water, and borated water.
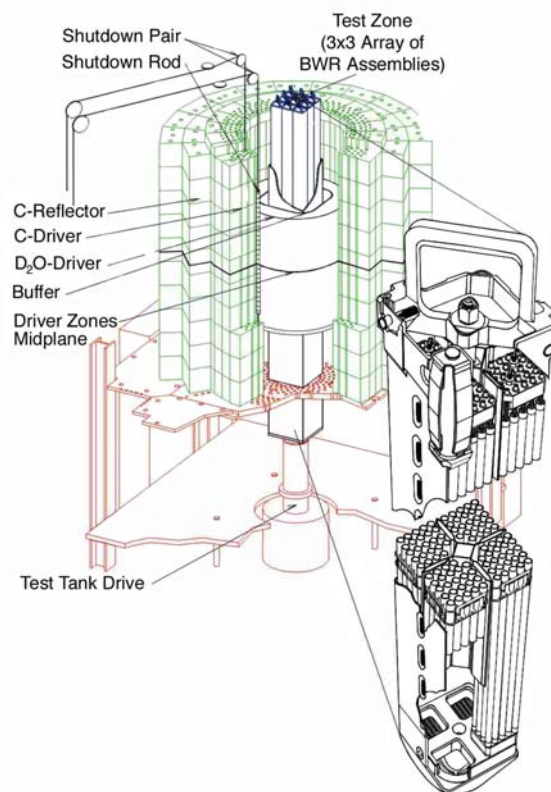
Fig 1.2: Schematic view of the LWR-PROTEUS reactor configuration showing the test zone, the buffer, the driver regions and the reflector. The central BWR assembly was replaced by a PWR mock-up zone in Phase II.

The most important reactor physics measurement in LWR-PROTEUS Phase II was reactivity worth loss due to burnup (reactivity effect in PROTEUS of replacing a fresh, reference sample in the central guide tube by a burnt fuel sample), expressed in each case relative to a well-known reactivity worth (reactivity difference between the fresh reference and a fresh, natural UO_2 sample). The asymptotic period method and the autorod compensation technique were used for the measurements.

Another type of experimental investigation in LWR-PROTEUS Phase II was the determination of the neutron source strength of each irradiated fuel rod sample, which increases dramatically with burnup. This was carried out by inverse kinetics analyses and by sub-critical measurements. The immediate application of these measurements is the accurate estimation of neutron sources for the calculation of radiation shielding. In fact, the total dose rate at the outer surface of spent fuel casks is usually governed by the neutron dose rate, and thus a certified cask design for <50 GWd/t fuel may very well become unusable if burnup is extended. The neutron source is mainly related to the spontaneous fission of ^{244}Cm (especially for fuel with a relatively long cooling time). However, other spontaneous fission and (α,n) sources are also present in the composite sample.

1.3. Scope and Structure of the Thesis

The present doctoral research represents an important extension of the unique, high-burnup related database generated in the framework of the LWR-PROTEUS Phase II experiments. It consists essentially of the development and optimisation of non-destructive assay (NDA) techniques based on gamma-ray emissions from irradiated fuel, useful for the identification of radioisotopes of relatively low abundances but high activity. The knowledge enhancement being aimed at relates to non-invasive absolute measurements of the radionuclide inventory, tomographic reconstruction of samples' density distributions, and tomographic reconstruction of the distribution of certain radionuclides within the fuel samples. This is achieved in three stages, viz.:

1. The design, set-up and operation of a novel gamma-ray detection station for the measurement of photon emission from the burnt fuel samples.

2. Computerised tomography (CT) of high burnup fuel rods, executed in both emission and transmission modes, for the determination of the within-pin distribution of ^{137}Cs, ^{134}Cs and ^{154}Eu, as well as the within-pin density distribution. The purpose thereby is the validation of within-pin activity distributions in general, and the characterisation of the migration of volatile species in particular.

3. The non-destructive determination of burnup though measured radionuclide activities and also though the derivation of appropriate ratios of radionuclide concentrations in the burnt fuel samples, the latter being a feasible option only once detailed distributions and corresponding self-absorption correction factors have been determined.

The experimental data generated through the above types of investigation of four irradiated fuel rod samples of different burnup (from medium to very high burnup) are then compared with calculational results obtained using a modern LWR design code.

The important enhancements achieved by the present research show that:

1) The quantification of radionuclide compositions of spent fuel rods based on tomographic measurements can strongly complement the usual γ-spectrometry based information obtained by non-destructive measurements, viz. that of axial distributions.

2) The compositions obtained non-destructively, i.e. for radionuclides of medium half-lives only, can serve as a useful cross-check of data for these nuclides as derived from chemical assays. In fact, in a certain sense, this information can be considered to constitute a means of "calibration", which will also help to qualify the chemical assays of stable and/or very long-lived nuclides.

3) As a possible good candidate for serving as absolute burnup monitor on its own, ^{154}Eu is to be preferred over both ^{137}Cs and ^{134}Cs.

4) The methodology for non-destructive determination of burnup through the derivation of ^{137}Cs, ^{134}Cs and ^{154}Eu single ratios needs particular attention when extended to very and ultra-high burnups.

5) The non-destructive determination of Cs migration in the fuel rod can complement and cross-check information which is usually obtained only via destructive techniques as SIMS, EPMA and LA-ICP-MS.

6) The absolute density of the burnt pins and the within-pellet density variations, as determined from the transmission tomographic reconstructions, represent valuable supplementary information.

As regards the thesis structure, Chapter 2 briefly describes certain basic aspects of burnt fuel and the common techniques employed worldwide for fuel analysis. Chapter 3 describes the presently developed experimental setup (from the preliminary measurements used for design of the tomographic station, to a description of its application to gamma transmission and emission tomography), and the burnt fuel samples investigated. In Chapter 4, the transmission tomography is described in detail, and the results concerning attenuation and density distribution within the fuel rods are discussed. Chapter 5 concerns the emission tomography, with a technical description of the methodology used and a discussion of the results. The burnup indicators, relative and absolute, and their comparison with other measurement techniques and calculations are the main topic of Chapter 6. Chapter 7 is devoted to the final conclusions.

References

[bae]   S. BÄCHLER *et al.*, "The New Cold Neutron Tomography Set-Up at SINQ", *Nucl. Instr. and Meth. In Phys. Res.* A, **481** p.397 (2002)

[bri]   J.F. BRIESMEISTER, "MCNP – A General Purpose Monte Carlo N-Particles Transport Code, Version 4C" LA-12625-M

[cha]   R. CHAWLA, "Merits and Feasibility of Pu-Er-Zr Oxide as LWR Fuel", *Trans. Am. Nucl. Soc.*, **82** p.229 (2000)

[cha2]   R. CHAWLA, P. GRIMM, P. HEIMGARTNER, F. JATUFF, G. LEDERGERBER, A. LÜTHI, M. MURHY, R. SEILER, and R. VAN GEEMERT, "Integral Measurements with a Plutonium Inert Matrix Fuel Rod in a Heterogeneous Light Water Reactor Lattice", *Prog. Nucl. Energy*, **38** p.359 (2001)

[cha3]   R. CHAWLA, C. HELLWIG, F. JATUFF, U. KASEMEYER, G. LEDERGERBER, B. H. LEE, G. ROSSITER, "First Experimental Results from Neutronics and In-Pile Testing of a Pu-Er-Zr Oxide IMF", presented at ENS TOPFUEL-2001, Nuclear Fuel: Development to Meet the Challenge of a Changing Market, Stockholm, 27-30 May 2001

[ede]   M. EDENIUS, K. EKBERG, B.H. FORSSEN, D. KNOTT, "CASMO-4. A fuel Assembly Burnup Program. User's Manual", Studsvik Report SOA-95/1, Studswik of America (1995)

[gro]   F. GRÖSCHEL *et al.*, "Neutron Radiography of Irradiated Fuel Rod Segments at the SINQ: Loading, Transfer and Irradiation Concept", *Nucl. Instr. and Meth. in Phys. Res.* A, **424** p.215 (1999)

[iae]   "IAEA Annual Report 2003"

[koe]   S. KÖRNER *et al.*, "Design and Optimization of a CCD-Neutron Radiography Detector", *Nucl. Instr. and Meth. in Phys. Res.* A, **454** p.158 (2000)

[led]   G. LEDERGERBER, A. STANCULESCU, C. DEGUELDRE, J.M. PARATTE, M. POUCHON, M. BURGHARTZ, and U. KASEMEYER, "Design, Fabrication and Characterisation of Inert Matrix Fuel for Plutonium Utilisation in LWRs", International Symposium on MOX Fuel Cycle, Technologies for Medium and Long-Term, Deployment: Experience, Advances, Trends; Vienna, Austria, 17-21 May 1999

[led2]   G. LEDERGERBER, P. HEIMGARTNER, Y.W. LEE, H. S. KIM, U. KASEMEYER, W. WIESENACK, C. DEGUELDRE, H. K. JOO, and D. S. SOHN , "Qualifying LWR Inert Matrix Fuel with Plutonium for Irradiation Testing in the Halden Material Test Reactor", GLOBAL '99

Nuclear Technology - Bridging the Millennia, International Conference on Future Nuclear Systems, Jackson Hole, Wyoming, USA, 29 August-3 September 1999

[mur]   M. MURPHY, A. LÜTHI, R. SEILER, P. GRIMM, O.M. JONEJA, A. MEISTER, R. VAN GEEMERT, F. JATUFF, R. BROGLI, R. JACOT-GUILLARMOD, T. WILLIAMS, S. HELMERSSON, R. CHAWLA, "Neutronics investigations for the lower part of a Westinghouse SVEA96+ assembly", *Nucl. Sci. Eng.,* **141** p.32 (2002)

[mur2]   M. MURPHY, F. JATUFF, P. GRIMM, R. SEILER, R. BROGLI, G. MEIER, H.-D. BERGER and R. CHAWLA, "Reactivity and neutron emission measurements of highly burnt PWR fuel rod samples", *Ann. Nucl. En.,* **33**(9) p.760 (2006)

[par]   J. M. PARATTE, P. GRIMM, J.M. HOLLARD, "1996a. ELCOS – the PSI code system for LWR core analysis. Part II: user's manual for the fuel assembly code BOXER", PSI Bericht No. 96-08

[par2]   J. M. PARATTE, R. CHAWLA, R. FRUEH, O. P. JONEJA , S. PELLONI , and C. PRALONG , "Validation Efforts for the Neutronics of a Plutonium-Erbium-Zirconium Oxide Inert Matrix Light Water Reactor Fuel", *Journ. Nucl. Matls.,* **274** p.120 (1999)

[par3]   J.M. PARATTE, H. AKIE, R. CHAWLA, M. DELPECH , J. L. KLOOSTERMAN , C. LOMBARDI , A. MAZZOLA , S. PELLONI , Y. PÉNÉLIAU , and H. TAKANO, "Comparisons of Cell Calculations for Uranium-Free Light Water Reactor Fuels", *Nucl. Technol.,* **130**, p.159 (2000)

[par4]   J.M. PARATTE and S. PELLONI, "Influence of the Thermal Cut-Off Energy on the Calculation of Neutronic Parameters for Light Water Reactor Lattices", *Nucl. Sci. Eng.,* **135** p.48 (2000)

[pel]   S. PELLONI , J.M. PARATTE, A. STANCULESCU, and R. CHAWLA, "Neutronics of Inert Matrix Pu Fuel Rods in a UO$_2$ PWR Environment", OECD/NEA Workshop on Advanced Reactors with Innovative Fuels, PSI Villigen, Switzerland, 235-243, 21-23 October 1998

[sta]   A. STANCULESCU, R. CHAWLA, C. DEGUELDRE, U. KASEMEYER, G. LEDERGERBER, and J.M. PARATTE, "Swiss Research and Development on Uranium-Free LWR-Fuels for Plutonium Incineration", IAEA Technical Committee Meeting on Fuel Cycle Options for Light Water Reactors and Heavy Water Reactors, Victoria, British Columbia, Canada, IAEA-TECDOC-1122, 293-307, 28 April-1 May 1998

[sta2]   A. STANCULESCU, U. KASEMEYER, J. M. PARATTE, and R. CHAWLA, "Conceptual Studies for Pressurized Water Reactor Cores Employing Plutonium-Erbium-Zirconium Oxide Inert Matrix Fuel Assemblies", *Journ. Nucl. Matls.,* **274** p.146 (1999)

[tre]   H.R. Trellue, D.I. Poston, 1999. "User's Manual Version 2.0 for Monteburns, version 5B", LA-UR-99-4999, LANL. (1999)

[xu]   Z. XU., M.S. KAZIMI, M.J. DRISCOLL, "Impact of High Burnup on PWR Spent Fuel Characteristics", *Nucl. Sci. Eng.*, **151** p.261 (2005)

[wer]   B. WERNLI, "Zweites Programm-Komitee Meeting des ARIANE-Programmes, 2-3 Mai 1996", PSI Internal Report AN-43-96-28, 28 May 1996

[wil]   T. WILLIAMS, R. BROGLI, R. CHAWLA, and R. SEILER, "LWR-PROTEUS: New Series of Critical Experiments Starts in Switzerland", *Nuclear Europe Worldscan*, **61** p.1 (1999)

[wil2]   T. WILLIAMS, P. GRIMM, R. SEILER, S. PELLONI, A. STANCULESCU, and R. CHAWLA, "First Criticality of LWR-PROTEUS: A New Programme of Integral Experiments for Current, Advanced and Innovative LWR Fuels", OECD/NEA Workshop on Advanced Reactors with Innovative Fuel, PSI Villigen, Switzerland, 117-125, 21-23 October 1998

2. Characteristics of Highly Irradiated LWR Fuels

During irradiation in a nuclear power plant, the composition and physical characteristics of the fuel change continuously from its initial physical properties, and this has important consequences on the fuel cycle. At the end of its life in the reactor, the fuel needs to be characterised as accurately as possible for reasons related to both safety and economy. The main investigations carried out are oriented towards verifying the fuel cladding integrity and determining the fissile content and the fuel burnup, the latter being an indicator of the fuel cycle efficiency.

This chapter is divided into three main parts. The first section gives a general description of the main characteristics of burnt fuels and the changes which occur during irradiation. Section 2 briefly describes post-irradiation examination (PIE) techniques, with emphasis on destructive testing, while Section 3 covers non-destructive assay (NDA) methodologies.

2.1. General

A fuel rod consists of a stack of fuel pellets loaded into the cladding tube. A radial gap of about 100 μm between the pellet and the inner surface of the cladding allows the introduction of the pellets into the cladding. A spring is placed above the pellet stack to prevent axial gaps forming in the column. The cladding tube is closed at both ends by welded Zircaloy plugs. The rod is pressurised with a fill gas, generally helium. The fuel pellets are cylindrical in shape, with a pellet length-to-diameter ratio in the range of 0.8 to 1.7. The pellet ends can have different shapes, usually with a concave depression called "dish". The function of the dish is to accommodate fuel thermal expansion and swelling in the hot centre of the pellet. The fuel rods are introduced into a Zircaloy structure to form bundles with a square cross section, the "fuel assemblies", which are loaded into the reactor core. During reactor operation the fuel assemblies are cooled by pressurised water (at ~150 bar for PWRs and ~70 bar for BWRs).

2.1.1. Fuel Burnup

The *burnup* of nuclear fuel is related to the lifetime of fuel in the core and it is given by the total amount of thermal energy that it has produced per unit of fissile material in the reactor. The common unit used to measure the burnup is MWd/kg or GWd/t[1]. The burnup relationship is

---

[1] 1 GWd/t = 86.4GJ/Kg in SI units

$$BU[GWd/t] = 1.8563 \times 10^{-24} E \frac{N}{Y} \qquad (2.1)$$

in which

N: number of atoms of burnup monitor formed during irradiation per metric ton of initial heavy metal,

Y: effective fractional fission-yield of burnup monitor,

E: effective energy released per fission [MeV]

Another definition of burnup is the number of fissions per 100 heavy nuclide atoms initially present in the fuel, expressed in percentage. The relationship for this definition is the following:

$$BU[\%] = 100 \frac{P/Y}{P/Y + H} \qquad (2.2)$$

where

P: atom concentration of fission-product burnup monitor,

Y: effective fractional fission-yield value.

H: final atom concentration of heavy nuclides (mass > 232)

The two burnup expressions are related by the conversion BU[GWd/t]=46.977 E BU[%]. Assuming an effective energy release of 202 MeV per fission, a burnup of 1% corresponds to a burnup of 9.489 GWd/t [hsu].

The distinction between a "normal" and "high" burnup value is quite arbitrary and depends on the advances in fuel technology. In fact, the maximum discharge burnup value is always moving upwards. At the current time, it is customary to formulate the following distinctions for burnup in spent LWR fuel rods: *low* (<30 GWd/t), *medium* (30-60 GWd/t), *high* (60-90 GWd/t), *ultra-high* (> 90 GWd/t).

From a reactor operation point of view, the possibilities to modify the energy production without re-designing the full reactor are rather limited. In fact, the constraints are so many that the main parameter which one can vary is burnup. Increasing burnup implies an extension of the in-core time for the fuel, and this has complex practical consequences which need careful analysis before a decision is taken. The affected nuclear design parameters requiring particular attention include reactivity, power peaking factors, control rod worths and reactivity feedback coefficients.

2.1.2. Changes in fuel properties during irradiation

During irradiation, a series of thermal, mechanical, and chemical phenomena modify the fuel structure and control the fuel behaviour. A full description of the phenomena involved is not the purpose of this section, but a generic introduction to aspects which are most relevant to this work will be given.

Heat is generated in the fuel during irradiation in the core, and the radial temperature distribution inside the pellet is characterised by a steep gradient. In general, two fission products are generated for each fission and the total number of medium and heavy atoms increases by about 1% when the fuel burnup increases by 10 GWd/t, contributing to fuel swelling at a rate of about 1% per 10 GWd/t. Another contribution to the fuel swelling comes from the gaseous fission product release. At the same time, the cladding creeps down under the effect of the coolant pressure, which is normally much higher than the rod inner pressure. The cladding creep-down is also dependent on the fast neutron fluence. Fuel thermal expansion, pellet cracking, fuel swelling, and cladding creep-down contribute to close the pellet-cladding gap. The gap closure occurs at a pellet average burnup in the range of 20-40 GWd/t. The above cited phenomena may now be examined in greater detail

2.1.3. Radial power profile in a fuel pellet

The main free path of the thermal and epithermal neutrons in UO_2 fuel is short compared with the pellet diameter. Since most thermal and epithermal neutrons come from outside of the pellet, a large fraction of them are absorbed in the outer regions, the pellet rim[2] region being particularly affected in the case of resonance absorptions (important, for example, for Pu-buildup). Consequently, the neutron flux distribution presents a deep depression at the pellet centre. The radial power profile in the pellet can be directly derived from the flux distribution as:

$$P(r) = \sum_i \left[\varepsilon_i N_i(r) \sigma_{f,i}(r) \right] \Phi(r) \quad i = \text{fissile isotopes} \tag{2.3}$$

where P: power density, r: pellet radius, ε: energy released per fission, N: atomic density, σ_f: microscopic fission cross-section, and ϕ: neutron flux.

In fresh fuel, when the N_i are uniform, the radial power profile is similar to the radial flux distribution. During irradiation, ^{239}Pu is generated to a considerable extent by epithermal neutron capture by ^{238}U, mostly occurring in the outer region of the pellet. As a consequence, the ^{239}Pu concentration at high burnup presents a maximum at the pellet rim and the radial power profile (Eq (1.3)) is significantly peaked at the periphery of the pellet. Under such conditions, for a fuel pellet having a burnup of

---

[2] The outermost (rim) region at high burnups develops a so-called high burnup structure, as described later in this section.

60 GWd/t, for example, the power density at the pellet periphery is 2.7 times the average, and the local burnup is about 2.4 times the average [bil].

2.1.4. Fission gas release

As burnup increases to high levels, the changes in material properties become considerable. The most obvious effect is the large accumulation of fission products in the fuel matrix. These occur as solid, volatile (caesium, iodine) and gaseous (krypton, xenon) species. The volatile fission products contribute to 45% of solid swelling and the gases to about 37% [zim]. At a burnup of 62 GWd/t, about 6.5% of the actinides have been fissioned. The fission product molar concentration then reaches 12% of the heavy atom concentration [bil]. This change in composition modifies the physical properties of the uranium oxide and affects the thermal and mechanical behaviour of the fuel. The cladding properties are also affected.

The gaseous fission products, mainly xenon and krypton, contribute significantly to the rod inner pressure. Each fission generates, on average, about 0.3 atoms of xenon and krypton [zim]. Most of these atoms are generated in the fuel grains and they diffuse in the fuel grain under the effect of both temperature and irradiation. Some gas atoms are eventually trapped by the grain boundary where they accumulate in the form of either bubbles or individual atoms. The grain boundary bubbles are responsible for gaseous swelling. When the bubbles interlink to create tunnels, the gas starts to release to the rod free volumes and contributes to the rod inner pressure. This phenomenon may become unstable. The pollution of the pellet-cladding gap by xenon and krypton contributes to the degradation of the gap heat transfer and the increase of the fuel temperature. A higher temperature accelerates the gas atom diffusion to the grain boundary and the free volumes, increasing fission gas release and rod inner pressure. If the rod pressure significantly exceeds the coolant pressure, the cladding starts creeping out, increasing the gap size and degrading further the gap conductance. This phenomenon is called cladding lift-off and may also cause cladding failure.

The large amounts of fission products (not only the gases) that accumulate in the fuel matrix at high burnup considerably affect the diffusion processes in the nuclear fuel. In particular, the diffusion coefficients at constant temperature, of the krypton and xenon atoms in the fuel matrix, strongly increase with the local burnup. At the same time, the fuel temperature at constant power increases with burnup due to fuel conductivity degradation. The result is the enhancement of gaseous swelling and fission gas release at high burnup [whi].

2.1.5. High burnup structure

At high burnup, the microstructure of the ceramic fuel changes to the so called "high burnup structure" or rim structure. This structure is characterised by the formation of small grains, less than 1 μm in diameter, a high fraction of porosity (10 to 20%), and relatively low fission gas concentration within the grains. The grain subdivision is the result of high internal stresses due to the accumulation of xenon and krypton at the lattice defects. This hypothesis is supported by the fact that the orientation of the lattice is almost the same in the sub-grains as that in the larger original (as-fabricated) grain. The new structure is characterised by a large inter-granular porosity. This porosity collects a large fraction of the gas initially present in the "old" grains. The high burnup structure starts developing when the local burnup reaches values in the range of 65 to 70 GWd/t. The kinetics of the fuel restructuring is relatively fast. As the burnup increases beyond 70 GWd/t, the high burnup structure develops in more central regions of the pellet. The high burnup structure does not develop when the local temperature exceeds 1100 °C. A region of high inter-granular porosity in the outer part of the pellet constitutes a thermal resistance and, therefore, contributes to the increase in the fuel temperature in the central part of the pellet [bil].

2.1.6. Caesium behaviour at high burnup

Special attention has to be given here to the behaviour of caesium, since this is an important subject of investigation in the present research.

The caesium boiling temperature is close to 685 °C at a pressure of 0.1 Mpa [ola]. Because of the high yield of this element, a substantial pressure ($\cong 0.1$ MPa) of caesium may develop locally. Like xenon and krypton, caesium diffuses in the grain and is trapped by the grain boundary. As soon as it is in contact with the open porosity, it is transported by distillation to the cold surfaces. Since the temperature at the inner surface of the cladding is lower than the caesium boiling point, caesium vapour condenses in the pellet-cladding gap, where it forms compounds such as caesium uranate $Cs_2UO_{3.56}$). At high burnup, when the pellet average burnup reaches typically 45 GWd/t, the mixture of chemical compounds, which are present between the pellet and the cladding, forms a soft bonding. Since the thermal conductivity of the bonding is much better than that of the mixture of helium and xenon in the pellet-cladding residual gap, bonding contributes to the reduction of the fuel temperature. Since the bonding is much softer than UO_2, it also has a beneficial mechanical effect, contributing to ease the stress peaks at the inner surface of the cladding. These stress peaks are common and result from the development of wide radial cracks in the pellet and irregularities in the pellet and cladding surfaces. Consequently, the chemical bonding between the pellet and cladding improves the so-called pellet cladding interaction (PCI) resistance of the fuel at high burnup [bil].

2.1.7. Transient fuel behaviour

During a power release at high burnup, when the local power typically exceeds 40 kW/m, fuel gaseous swelling starts loading the cladding. The resulting cladding deformation may be as large as 1% and lead to cladding failure. The rate of contribution to fuel solid swelling by the fission product accumulation may be considered constant (1% per 10 GWd/t) as long as all the fission products remain in the fuel matrix. However, a considerable amount of xenon, krypton and caesium can be released from the fuel. Taking into consideration the caesium, iodine and fission gas release, the solid or matrix swelling is described by the following relation:

$$\left(\frac{\Delta V}{V}\right)_{mat} = A_{mat}(1 - \alpha_{FG}FGR - \alpha_{CS}CSR)Bu \tag{2.4}$$

A_{mat} : solid swelling constant $= 10^{-3}$ (GWd/t)$^{-1}$ [zim-bil2]

FGR : local fractional fission gas release from the grain

CSR : fractional release of the volatile fission products from the grain

Bu   : local burnup (GWd/t)

α FG   : fraction of gaseous fission products $= 0.37$

αCS   : fraction of volatile fission products $= 0.45$

At low burnup, high tangential stresses may develop in the cladding during a power ramp due to pellet thermal expansion and, at very high power, gaseous swelling. If the power is then maintained constant at the ramp terminal level, these stresses relax by thermal creep of the cladding. At high burnup, gaseous swelling occurs at lower power and its contribution to PCI is more important. However, fission product release during and immediately after the power ramp contributes to making the pellet softer due to negative matrix swelling and volume recovery (Eq. 1.4). This effect mitigates the effect of gaseous swelling.

2.2. Post-Irradiation Examination

A variety of post-irradiation examination (PIE) methods have been developed for verifying the reactor-operator-declared burnup values and the status of the fuel at the end of its life in the reactor. These methods can be based on a combination of destructive and non-destructive approaches. Emphasis is placed in this section on destructive techniques.

2.2.1. Typical investigations

Post-irradiation examinations can be applied either at fuel assembly level or at single rod level. A variety of investigations are carried out, ranging from the verification of fuel cladding to the measurement of parameters such as the heat released, the power distribution and the fissile/fertile content. Other techniques make possible advanced studies via measurements, for example, of elemental radial distributions employing electron probe microanalysis (EPMA) and of changes in the UO_2 microstructure across the fuel pellet employing scanning electron microscopy (SEM).

As indicated earlier, a parameter of prime interest is the burnup value itself. This is so for a variety of reasons, e.g. from the viewpoint of so-called "burnup credit". The latter essentially implies, in the context of criticality safety, the accounting of burnup in terms of fissile material depletion and accumulation of neutron absorbing actinides and fission products. The principal aim thereby is to reduce unnecessary conservatism in various operations related to irradiated fuel, e.g. transport (to optimise cask design), in-pond storage (to be able to store more enriched fuel assemblies in existing installations), the design of new storage installations for (to propose denser configurations), and reprocessing (e.g. to maintain the material throughput despite increases in initial enrichment).

2.2.2. Standard burnup measurement techniques

Typical destructive methods are based on chemical analysis. Among the different chemical assays available based on mass spectrometric techniques [bec-pla], such as glow-discharge, spark-source, resonance-ionisation, accelerator-laser-ionisation, thermal-ionisation, or inductively-coupled-plasma (ICP) mass spectrometry (MS), the most commonly used technique is ICP-MS, where a fuel amount corresponding to 1-3 pellets is dissolved in an acid. This solution is nebulised into a plasma and then analyzed. ICP-MS offers very low detection limits, is also applicable for long-lived radionuclides, provides information on the isotope composition of fission products and actinides, and is capable of measuring stable as well as radioactive nuclides with similar sensitivity. Generally, with ICP techniques, the burnup can only be determined as the average burnup of the pellets. The principal burnup monitors that are suitable are: ^{148}Nd, ^{139}La, ^{99}Tc and ^{236}U.

While ICP-MS is an accepted technique for routine measurements in the nuclear industry, the technique of multicollector inductively coupled plasma mass spectrometry (MC-ICP-MS) is attracting much attention because it permits the precise measurement of the isotope compositions for a wide range of elements combined with excellent limits of detection due to high ionisation efficiencies [gue].

With laser ablation (LA) ICP-MS, on the other hand, there is the theoretical possibility to determine local burnup, measurements being carried out in combination with standard ICP-MS. The technique is destructive as well, but not as strongly as ordinary ICP-MS. Another variation of the method is fiber-optic, high-resolution, inductively coupled plasma atomic emission spectroscopy (FO-HR-ICP-AES), where a fuel segment is dissolved in acid and a dilute solution of this is used to optically determine the ^{139}La content [gig], a widely used burnup monitor. The accuracy of this kind of burnup determination is better than 4%.

To determine local burnup in the fuel, another approach is the use of secondary ion mass spectrometry (SIMS), in combination with ICP-MS data on the same fuel. These techniques are relative, and a quantitative cross-checking must be carried out by another method, via a local analysis of ^{148}Nd or by using a calibrated fuel sample. Analysis of ^{148}Nd concentration yields values for the burnup with an accuracy of 2-3%.

2.3. Non-Destructive Assay (NDA) Methods

2.3.1. General

Non-destructive measurement techniques have been applied to a variety of parameters associated with the characterisation of irradiated fuel materials. Among the different types of non-destructive methods used for measurement on the radioactive components of burnt fuel rods (such as gamma-ray spectrometry [iae], neutron measurements, reactivity and calorimetric measurements), great interest is given by [phi]:

1. Gamma spectrometry, allowing:

   - the identification and quantification of gamma-emitting radio-nuclides

   - the calculation of the isotopic composition of the plutonium and/or uranium present

   - the derivation of fuel burnup using fission products concentration or radio-nuclide isotopic ratios

2. Passive neutron assay, giving:

   - the total neutron emission rate

   - the coincident neutron emission rate

3. Active neutron assay, giving the fissile mass content

In the following sections, a distinction is made between non-destructive active and passive investigations, giving more prominence to passive methods, especially the techniques devoted to fuel burnup investigation.

2.3.2. Invasive methods

In the context of neutron and gamma-ray measurements, one should differentiate between invasive methods, using an external source, and non-invasive or passive methods. Some examples of standard invasive techniques are the active neutron interrogation methods to quantify the low α-activity fissile masses in the fuel employing a very high activity neutron source to override the passive neutron signal. Neutron radiography applied to burnt fuel rods is another example of recent developments [koe-bae].

Concerning gamma-ray spectrometry, the employment of an external gamma source for invasive analysis is widely used for radioactive waste drums investigations, as a fast and efficient way to derive material densities.

2.3.3. Non invasive methods

As non-invasive methods for burnup measurement, the most used techniques are gamma spectrometry and passive neutron counting. Ideally the result can be obtained by measuring the amount of fissile material left in the fuel when the initial enrichment of the fuel assembly is known. Practically the procedure is not so easy. If gamma spectrometry is employed, the burnup measurement can be performed indirectly using the spontaneous emission of gamma-rays by the fission products. In fact, the buildup of specific fission products can be used as a quantitative measure of burnup, if the following conditions are met [phi-hsu]:

- The fission product should be characterised by near-to equal fission yields for the major uranium and plutonium fissioning nuclides. If the yields are substantially different, the effective fission yield will depend on the reactor's operating history.

- The neutron capture cross section of the fission product must be low enough so that the observed fission product concentration is due only to heavy element fission and not to secondary neutron capture reactions. This requirement can be circumvented employing isotopic ratios where a linear dependence on the neutron fluence (and hence on the burnup) can be assumed.

- The fission product half-life should be long compared to the fuel irradiation time, so that the quantity of fission products present is approximately proportional to the number of fissions.

- The fission product gamma rays must be of relatively high energy (above 500 keV) so as to be able to escape to a useful degree from the fuel pin. In practice, passive gamma-ray measurements are more restricted to the outer regions. A further complication is due to the non-uniform neutron flux during the irradiation that can lead to non-uniform burnup.

- Low migration (including precursor) in the fuel.

Following the above basic rules, one can have a very accurate and fast comparative method, based on the use of a single radionuclide, viz. ^{137}Cs, which has nearly identical fission yields for ^{235}U and ^{239}Pu, and is hence representative of the total number of fissions. Moreover, the ^{137}Cs neutron absorption cross section is negligible. A limitation of this method concerns the intrinsic assumption of no migration of caesium and this makes its application difficult in the case of high burnup fuels. Furthermore, it requires a large number of calibrated fuel samples for adaptation to the different geometries investigated. Basically, if the burnup is known for a given irradiated sample, then the amount of ^{137}Cs formed can be derived [iae2]. In addition to ^{137}Cs, short lived isotopes, when applicable, can be employed as burnup monitors, e.g. ^{140}La (40.2 h), is used to determine the amount of ^{235}U left in the fuel element, which can easily be converted to the burnup value [wan].

Another approach for burnup determination is using the activity, or concentration ratios, of long-lived fission product isotopes [kri]. This is a peak-ratio technique which produces results independent of the detector and geometrical efficiency, and for this reason is very accurate. This standard method, the so-called intrinsic calibration method [dra], has been extensively tested in the use of ^{144}Ce/^{144}Pr (for cooling time less than 2 years), ^{134}Cs/^{125}Sb (for cooling time ~1.5 years) [iae], ^{134}Cs/^{137}Cs or ^{154}Eu/^{137}Cs (for cooling time > 2 years) as burnup indicators at low and medium burnups. Many other ratios can be built to determine cooling time and irradiation time (i.e. ^{133}I/^{132}Te, ^{133}Ce/^{137}Cs, etc.) [iae]. The ratios containing caesium could be affected by its migration, and this effect must be considered in order to apply a correction[3] or an increment of the relative uncertainties. Combined functions of individual nuclide ratios, e.g. $(^{134}$Cs/^{137}Cs$)^2$/$(^{106}$Ru/^{137}Cs$)$ are additional options [nak]. Monitors suitable for high and ultra-high burnup levels, however, still need to be identified, and this can only be done through the qualification of appropriate experimental methods.

It should be noted that these methods require the use of reactor physics codes in order to establish correlations between the ratios and the burnup. Further, the employment of depletion codes needs valid and updated basic cross section data (which are still not very suitable for high burnup fuels) and,

---

[3] The application of such a correction is not simple because of large uncertainties in the caesium within-pin distribution, depending on the burnup itself.

furthermore, a detailed irradiation history of the sample during its life in the reactor is not always available.

The non-invasive methods for burnup measurement employing passive neutron counting are based on the neutron generation process due to spontaneous fission of heavy actinides or from (α,n) reactions taking place in the fuel. However, in most cases, the (α,n) component is negligible compared to the contribution of spontaneous fission. Moreover, at fuel discharge time the spontaneous fission component is dominated by the contribution from ^{242}Cm (~0.45 year half-life[4]), as well as from ^{244}Cm (~18 years half-life), which remains the main neutron source for longer cooling times. Burnup measurements can be done by establishing a correlation between the total number of neutrons emitted by the fuel and its calculated burnup utilising a mathematical fit.

A commonly used expression is the following empirical power function:

$$\text{Neutron rate} = a\,(\text{Burnup})^{b} \qquad\qquad (2.5)$$

where b is usually a number between 3 and 4 [phi-tou].

The rapid buildup of ^{244}Cm with burnup is well known, and has been identified as a potential problem for high-burnup fuel. It increases approximately as the burnup to the power 4. The dominant production route is multiple captures in plutonium isotopes, then decay through ^{243}Am to produce ^{243}Cm, and finally neutron capture to create ^{244}Cm. It should be noted that, at very high burnups, ^{252}Cf becomes an important contributor to the neutron emission rate.

Other non-destructive techniques, based on gamma spectrometry, are commonly used to investigate the power distribution in nuclear fuel, e.g. by determining the concentration of ^{140}Ba, for which the production rate is very nearly proportional to the thermal power [jan1], or by measuring and correlating the ^{137}Cs activity to the decay heat [jan3].

In the following section, the application of tomography for the investigation and characterisation of nuclear fuel in a single fuel pin or full assembly is described.

---

[4] The decay information (half-life, branching ratios, etc) used in this thesis is that provided by JEFF-3.1 data [jef].

2.3.4. Tomography applied to nuclear fuel

Computer tomography (CT) is the process of obtaining sectional images of the interior of objects by performing external measurements, namely multiple radiation projections, which can be of X-rays, γ-rays or neutrons. CT is widely applied in the medical field and, in the context of non-destructive testing, is used in many other fields, e.g. industrial applications. Several tomographic techniques have been developed: single photon emission computerised tomography (SPECT), positron emission tomography (PET), ultrasonic tomography and magnetic resonance tomography (MR).

Computer tomography can be applied successfully in nuclear technologies as well, in particular in the process of investigation and characterisation of nuclear fuel. In this particular case, the method applied is SPECT. Two-dimensional SPECT is a non-destructive technique that generates cross-sectional images of an object on the basis of measurements of γ-rays emitted by separate "portions" of this object. The γ-rays collected from a single portion constitute a "projection element". A set of projection elements obtained for a particular direction of propagation of the gammas – as defined by a certain direction of a collimator slit – is called a "projection".

In the literature, various experiments have been reported related to emission tomography applied on single fuel rods. Precision gamma scanning has frequently been used to measure the axial isotopic distribution of fission products and actinides, and also successfully for determining the radial distribution. One of the first and very interesting applications of two-dimensional gamma-ray scanning on spent fuel rods, measuring the spatial distribution of radioactive isotopes (fission and activation products), was made at Los Alamos National Laboratory by Barnes [bar-bar2] and Phillips [phi]. Also of note is the ISARD programme [duc], developed at Grenoble. More recently, fuel rods and irradiated pellets have been measured at the VENUS facility [bor], whilst tomographic analysis on fuel cladding to verify its integrity has been performed by Dobrin [dob]. Interesting as well is the work of Buurveld et al. [buu], where within-pin distributions of ^{134}Cs, ^{137}Cs, and ^{106}Ru are investigated in spent fuel, and Tanke et al. [tan2], with ^{137}Cs and ^{106}Rh distributions. Very recently, SPECT has been applied to lightly activated fuel rods, for the determination of within-pin reaction rates distribution by Pralong at PSI [pra]. The application of tomography on spent fuel assemblies, developed at Uppsala [jan2], with the main purpose of cladding failure detection, is another example concerning nuclear fuel.

Table 2.1 documents the main parameters characterising interesting earlier SPECT investigations of nuclear spent fuel segments. These investigations have certain common features with those conducted in the present research, so that the information provided in the table can serve as a useful reference. Although the mentioned studies do not constitute an exhaustive list, they probably do represent the major contributions made in the field to date[5]. It should be made clear, however, that in none of the cited studies has there been a strict, quantitative reconstruction of the tomography measurements.

As a complement to emission tomography, transmission tomography is a very valuable option which has been applied earlier to nuclear wastes (quality control of radioactive waste packages) [cam]. This technique, based on the use of absorption of a physical entity (gamma ray, X-ray, light, ultra-sound) crossing a body, is relevant to study the internal morphology of an object (the evaluation of density distribution, precipitates, voids and cracks), while emission tomography uses the observation of events that take place inside the body and which help to characterise the object itself. Consequently, the combination of the two methodologies can be instrumental for obtaining maximum information, using the results of the first (e.g. a map of linear attenuation coefficients) as additional input for the analysis of the second. However, such an approach has never been applied before to the investigation of single fuel rods[6].

A separate section could be devoted to describe the application of the artificial neural network (ANN) method in tomographic analysis, but being a huge topic in itself, just a short description is being given here. Nowadays, a new trend in image processing is working on the implementation of feed-forward, back-propagation artificial neural network analysis for tomographic reconstruction. The main idea is to build a network with nodes and connections, then to train the network to reconstruct known images from their projections, trying to determine each nodal weight, and finally to use the trained network to reconstruct an unknown image from its measured projections. This technique has been applied to the case of irradiated nuclear rods recently [cra2].

---

[5] The selection made in Table 2.2 is essentially restricted to the application of emission tomography to fuel rods. An extension to waste analysis and/or fuel assembly analysis would be too voluminous and not of great relevance to the present research.
[6] At least, to the knowledge of the author.

Table 2.1**:** Overview of gamma emission tomography applications for nuclear fuel rod investigation.

Paper reference	Burnup	Slit dimensions (WxHxL) [mm]	Number of lateral steps	Step size [mm]	Number of angles	Angular interval [°]	Acquisition time [s]	γ-lines (isotope / energy [keV])	Basis functions	Reconstr. Method
[buu]	24 GWd/t	0.3x15x1400	121 or 146	0.1	20	18	250	^{134}Cs/605 ^{106}Ru/622 ^{137}Cs/662	32x32 pixels	Least squares, preconditioned conjugate gradient
[mue]	26 GWd/t	0.2x8x ?	50	0.2	8	45	1000 (total ~110 h)	^{137}Cs/662	50x50 pixels	ART[1]
[cra]	?	0.25x ? x ?	50	?	5	? (equidistant)	?	^{137}Cs/662	50x50 pixels	ML[2], ME[3], ART, Monte Carlo BP[4]
[dob]	19.5 GWd/t	0. 5x ? x ?	25	0.5	5	? (equidistant)	60 (total ~2 h)	^{137}Cs/662 ^{95}Zr/725 [5]	25x25 pixels	ME
[ale]	18.3 GWd/t	0.25x ? x ?	50	0.25	5	? (equidistant)	?	^{137}Cs/662 ^{140}La/1596	50x50 pixels	ME
[tan2]	23 GWd/t	0.05x?x2000	?	?	?	?	?	^{106}Rh/? ^{137}Cs/662		ML/ART
[bar]	19.2 GWd/t		?		6 (?)		?	^{137}Cs/662 ^{60}Co		FBP[6]
[phi]			>100		~2	90		^{140}La/487 ^{106}Ru/497 ^{137}Cs/662		Analytical method
[duc]	fresh	0.3x10	35		6	45	600	activation products		Least squares

[1]Algebraic Reconstruction Technique; [2]Maximum Likelihood; [3]Maximum Entropy; [4]Back Projection; [5]probable interference with signal coming from the Zircaloy cladding; [6]Filtered Back Projection (A description of the reconstruction techniques is given in Chapters 4 and 5).

2.3.5.   Radioisotopes suitable for emission tomography

As indicated earlier, the choice of gamma-emitting isotopes that can be used for emission tomographic measurements in spent fuel depends on their concentrations, half-lives and decay modes. As a consequence, a principal constraining factor is the cooling time of the fuel. Further, the relevant γ-rays are limited to a certain energy range (> 0.5-0.6 MeV) from the viewpoint of moderate attenuation, while intensity is still another constraint with counting statistics needing to be adequate for the reconstruction model used (desired uncertainty of <1%).

The isotopes currently employed for emission tomography are ^{134}Cs, ^{137}Cs and ^{154}Eu, as listed in Table 2.2, which also provides relevant information on the individual γ-rays.

Table 2.2: Radioisotopes used currently for gamma emission tomography.

Isotope	Gamma energy [keV]	Branching ratio(*) [%]	Half-life [years]	Relevant cooling time(**) [years]
^{134}Cs	604.69 795.84	97.6297 85.5197	2.0651	1-10
^{137}Cs	661.657	85.0256	30.04	2-100
^{154}Eu	1274.69	35.00	8.593	2-30

(*) [jef]; (**) Cooling time adequate for the measurements.

A description of the production of these radionuclides is given in the following paragraphs, whilst detailed calculations performed to study their buildup with burnup are presented in Chapter 6.

^{134}Cs

This isotope is not produced directly from fission, but from neutron capture in ^{133}Cs, which is a stable isotope. ^{133}Cs is mainly obtained from a combination of repeated beta decays of its isobaric parents (^{133}Sb→^{133}Te→^{133}I→^{133}Xe→^{133}Cs), as illustrated in Fig. 2.1[7]. For this reason, ^{134}Cs can be correlated to the square of the neutron fluence, and hence to the square of burnup. ^{134}Cs has a shorter half-life (2.065 years), compared to ^{137}Cs.

---

[7] Figs. 2.1-2.3 have been produced by manipulation of basic graphics from Janis vs. 2.1[jani].

Fig. 2.1:   Production scheme for ^{134}Cs.

$\underline{^{137}\text{Cs}}$

The production of ^{137}Cs is dominated by direct fission in mass chain 137, as illustrated in Fig. 2.2, in combination with repeated beta decays of its isobaric parents (^{137}Te→^{137}I→^{137}Xe→^{137}Cs). Another possible production path is neutron capture in the stable isotope ^{136}Xe (^{136}Te→^{136}I→^{136}Xe+n→^{137}Xe→^{137}Cs), but in this case the neutron capture cross section is quite small (0.26 b) and, furthermore, the loss of ^{137}Cs through neutron capture is of similar magnitude (0.25 b). The combination of the relatively long half-life and the production through direct fission implies that the abundance of ^{137}Cs can be strongly correlated to the neutron fluence, and hence to burnup. Because of its half-life of 30.04 years, this isotope has relatively insignificant decay during the irradiation time and dominates the gamma-ray emission spectra when the fuel is cooled for several years.
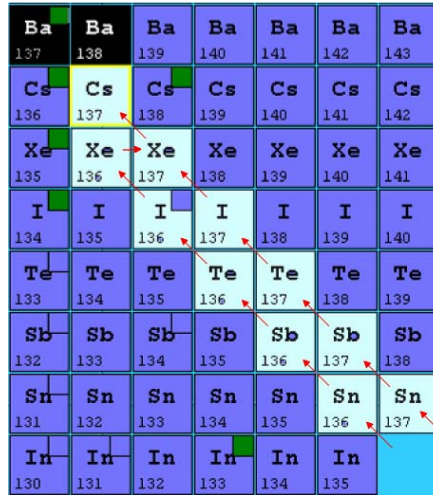
Fig. 2.2: Production scheme for ^{137}Cs.

^{154}Eu

The buildup of this isotope is similar to that for ^{134}Cs, i.e. it is not produced directly through fission, but mainly from neutron capture in ^{153}Eu, which is a stable isotope (see Fig 2.3). ^{153}Eu is obtained from the beta decay of ^{153}Sm (^{153}Sm→^{153}Eu). ^{154}Eu has a half-life of 8.593 years, which makes the use of this isotope interesting as a burnup monitor for fuel with a cooling time > 3 years. Further, this element is not volatile, in contrast to caesium (which migrates), making it attractive as a within-pin burnup distribution indicator.
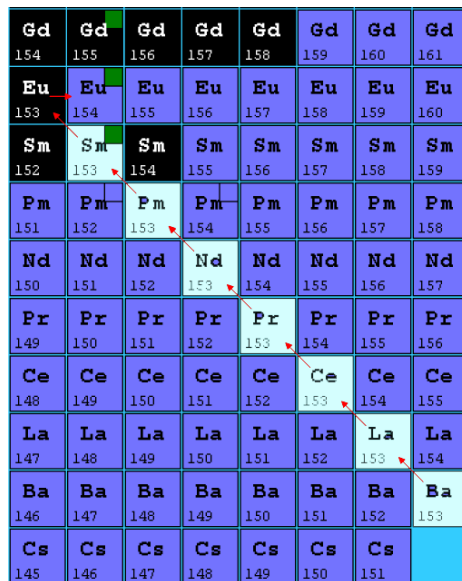
Fig. 2.3: Production scheme for ^{154}Eu.

References

[ale]   A. ALEXA, T. CRACIUNESCU, G. MATEESCU, R. DOBRIN, "The Tomographic Maximum Entropy Method in the 3-D Analysis of Nuclear Fuel Pins", *J. Nucl. Mat.*, **218** p.139 (1995)

[bae]   S. BÄCHLER *et al.*, "The New Cold Neutron Tomography Set-Up at SINQ", *Nucl. Instr. and Meth. Phys. in Res.* A, **481** p.397 (2002)

[bar]   B.K. BARNES, J.R. PHILLIPS, M.L. BARNES, "Reconstruction of radial fission product distributions in reactor fuels from a small number of projections", *J. Nucl. Mat.*, **106** p.147 (1982)

[bar2]   B.K. BARNES, D.M. HOLM, W.M. SANDERS, D.D. CLINTON, J.E. SWANSEN, "Techniques for two-dimensional gamma-ray scanning of reactor fuel element sections", *Nucl. App. & Tech.,* **9** p.746 (1970)

[bec]   J.S. BECKER, *J. Anal. Atom. Spectr..* **17** p.1172 (2002)

[bil]   M.R. BILLAUX, "Fuel Performance, Limits, Operational and Safety Issues", The 2005 Frédéric Joliot/Otto Hahn Summer School, Forschungszentrum Karlsruhe, Aug 24- Sep 2, (2005)

[bil2]   M.R. BILLAUX, V I. ARIMESCU, F. SONTHEIMER, H. LANDSKRON, "Fuel and Cladding Properties at High Burnup", International Topical Meeting on Light Water Reactror Fuel Performance, Park City, Utah, April10-13, (2000)

[bor]   L. BORMS, J. OEYEN "The design of a multipurpose tomography installation", *Nucl. Instr. and Meth. in Phys. Res.* A, **422** p.489 (1999)

[buu]   H. A. BUURVELD, G. DASSEL, "Emission Computer Tomography on a Dodewaard Mixed Oxide Fuel Pin", *Report ECN-C—93065*, Petten (1993)

[cam]   D. CAMP, H. MARTZ, G. ROBERSON, D. DECMAN, R. BERNARDI, "Nondestructive waste-drum assay for transuranic content by gamma-ray active and passive computed tomography", *Nucl. Instr. and Meth. in Phys. Res.* A, **495**(1) p.69 (2002)

[cra]   T. CRACIUNESCU, C. NICULAE, G. MATEESCU, C. TURCANU, "A Comparison of Four Tomographic Methods for Nuclear Fuel Pin Analysis", *J. Nucl. Mat.*, **224** p.199 (1995)

[cra2]   T. CRACIUNESCU, "A neural network model for the tomographic analysis of irradiated nuclear fuel rods", *Nucl. Tech.*, **146** p.65 (2004)

[dob]   R. DOBRIN, T. CRACIUNESCU, I.L. TUTURICI, "The Analysis of Failed Nuclear Fuel Rods by Gamma Computed Tomography", *J. Nucl. Mat.*, **246** p.37 (1997)

[dra]   T.N. DRAGNEV, *J. Radioanal. Chem.* , **36** p.491 (1977)

[duc]   G. DUCROS, "ISARD, a method of tomographic reconstruction of the position of gamma emitters in a nuclear fuel pin from transversal gamma scanning", *Nucl. Tech.*, **68** p.370 (1985)

[gig]   J.J. GIGLIO et others, "Determination of burnup in spent nuclear fuel by application of fiber optic high-resolution inductively coupled plasma atomic emission spectroscopy (FO-HR-ICP-AES)", *Nucl. Instr. and Meth. in Phys. Res.* A, **396** p.251 (1997)

[gue]   I. Günther-Leopold, B. Wernli, Z. Kopajtic, D. Günther, *Anal. Bioanal. Chem.*, **378** p.241 (2004)

[hsu]   S.T. HSUE, T.W. CRANE, W. L.TALBERT, J.C. LEE, "Nondestructive Assay Methods for Irradiated Nuclear Fuels", Los Alamos National Laboratory report LA-6923 (1978)

[huv]   M.HUVER, C.PASSARD, P.FLEURY, "Radioactive waste measurement SIMENON, a new software for interpretation and production of results issued from combined measurements", Présentation lors de la conférence INMM, Phoenix, July 1999.

[iae]   "Determination of research reactor fuel burnup", IAEA-TECDOC-633, (1992)

[iae2]   "Guidebook on Non-Destructive Examination of Water Reactor Fuel", IAEA-TECDOC-322, (1991)

[jani]   "Janis 2.1" (07/2004) from NEA. http://www.nea.fr/janis/

[jan]   P. JANSSON, S. JACOBSSON SVÄRD, A. HÅKANSSON, A. BÄCKLIN, "A Device for Nondestructive Experimental Determination of the Power Distribution in a Nuclear Fuel Assembly", *Nucl. Sci. & Eng.*, **152** p.76 (2006)

[jan2]   S. JACOBSSON, A. HÅKANSSON, A. BÄCKLIN, O. OSIFO, C. WILLMAN, P. JANSSON "Nondestructive experimental determination of the pin-power distribution in nuclear fuel assemblies", *Nucl. Sci. & Eng.*, **151** p.70 (2005)

[jan3]   P. JANSSON, A. HÅKANSSON, A. BÄCKLIN, S. JACOBSSON, "Gamma-Ray Spectroscopy Measurements of Decay Heat in Spent Nuclear Fuel", *Nucl. Sci. & Eng.*, **141** p.129 (2001)

[jef]   The Joint Evaluated Fission and Fusion file (JEFF-3.1). *http://www.nea.fr/html/dbdata/JEFF/*.

[koe]   S. KÖRNER *et al.*, "Design and Optimization of a CCD-Neutron Radiography Detector", *Nucl. Instr. and Meth. in Phys. Res.* A , **454** p.158 (2000)

[kri]   E. KRISTOFF, G. PREGL, "Gamma Spectrometric Assessment of Nuclear Fuel", *Nucl. Instr. and Meth. in Phys. Res.* A, **297** p.507 (1990)

[mat]   Hj. MATZKE, "On the Rim Effect in High Burnup UO_2 LWR Fuels", *J. Nucl. Mat.*, **188** p. 19 (1992)

[man]   R. MANZEL, C.T. WALKER, "EPMA and SEM fuel samples from PWR rods with an average burn-up of around 100 MWd/kgHM", *J. Nucl. Mater.* , **301** p.170 (2002)

[mue]   J. MUELLHAUER, "Kernbrennstoffanalyse mittels Gamma-Emissions-Computer-Tomografie", Seminar Computertomografie, *Deutsche Gesellschaft für Zerstörungsfreie Prüfung e.V.*

[nak]   Y. NAKAHARA et al., Experimental Verification of Availability of $(^{134}Cs/^{137}Cs)^2/(^{106}Ru/^{137}Cs)$ Gamma-ray Intensity Ratio as a Burn-up Monitor for LWR Fuels, *Sixth International Conference on Nuclear Criticality Safety*, ICNP'99, Versailles, France, Sep 20-24 1999.

[ola]   D.R.OLANDER, "Fundamental Aspects of Nuclear Reactor Fuel Elements", TID-26711-P1, ERDA Technical Information Center, Oak Ridge, Tennessee, (1976)

[phi]   J.R. PHILLIPS, "Passive Nondestructive Assay of Nuclear Materials", LA-UR-90-732, p. 529

[phi2]   J.R. PHILLIPS, "Improved nondestructive determination of two-dimensional radial isotopic distributions in irradiated fuel pins", *Nucl. Techn.*, **28** p.282 (1976)

[pla]   I.T. PLATZNER (Ed.), *Modern Isotope Ratio Mass Spectrometry,* Wiley, Chichester, (1997)

[pra]   C. PRALONG, "Investigation of Within-Pin Reaction Rate Distributions in a Highly Heterogeneous BWR Fuel Assembly", *Thèse EPFL No 2663* (2002)

[tan]   R.H. TANKE, A.J.B. DE ROOY, "Three-dimensional gamma tomography as part of KEMA Source-Term Research", *KEMA Scientific & Technical Reports,* **7** (1) p.11 (1989)

[tan2]   R.H. TANKE, J.E. JASPER, P.A.M. GAALMAN, D. KILLIAN, "Applications of tomography in nuclear research", *Kerntechnik,* **56(**5) p.283 (1991)

[tou]   H. TOUBON et al., "Burn-up measurements coupling gamma spectrometry and neutron measurement", CANBERRA Tec. Doc. (2003)

[zim]   H. ZIMMERMANN, "Fission Gas Behaviour in Oxide Fuel Elements of Fast Breeder Reactors", *Nucl. Tech.*, **28** p.127 (1978)

[wan]   T. WANG, D. HSU, C. TSENG, "Feasibility Studies on Iterative Methods of Fuel Burnup Estimation Using Gamma-ray Spectrometry", *App. Radiat. Isot.,* **41**(1) p.41 (1990)

[whi]   R.J. WHITE, M.O. TUCKER, "A New Fission-Gas Release Model", *J. Nucl. Mat.,* **118** p.1 (1983)

3. <u>Measurement Station and Experimental Setup</u>

This chapter describes the experimental setup developed and used in the course of the present research. While Section 3.1 briefly covers the preliminary experiments performed, Section 3.2 relates to the exploratory design calculations. The gamma tomography station is described in Section 3.3, while the last section deals with the irradiated fuel rod samples investigated.

3.1. Preliminary Experiments

As indicated in Section 1.2.2, 13 spent fuel segments coming from the Swiss nuclear power plants have been investigated in the framework of the LWR-PROTEUS programme [mur], using several different techniques (reactivity measurements, etc). Some of these burnt fuel rod samples were selected for a preliminary series of high-resolution gamma spectroscopy measurements at PSI. The goals thereby were two-fold, viz. (a) to have an initial assessment of the activity and burnup of the most highly burnt fuel segments, and (b) to gain experience and data for the development of a simulation model for the estimation of photonic efficiency and optimisation of design parameters of the new gamma tomography station.

The experiments were conducted using shielding setups at two different PSI facilities, viz. at PROTEUS [mur] and at the NEUTRA facility of the spallation neutron source SINQ [leh]. In each case, the measurement equipment consisted of an EG&G ORTEC HPGe (high-purity germanium) detector, cooled with liquid nitrogen, and an EG&G ORTEC DSPec digital gamma-ray spectrometer [dsp] (a comprehensive unit containing an analogue-to-digital converter, a digital shaping amplifier, high voltage power supply, etc.).
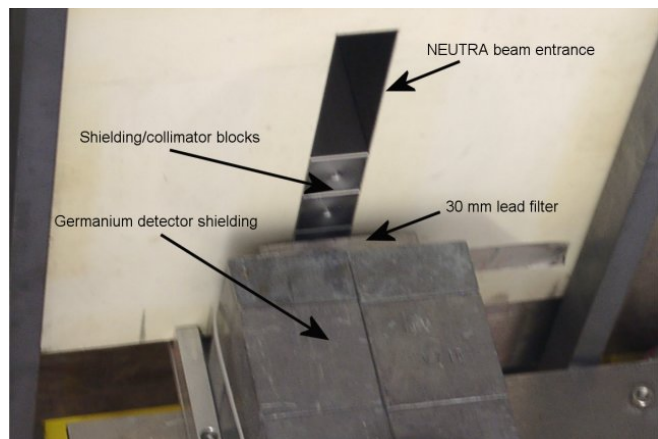

Fig. 3.1: Gamma measurement setup at the NEUTRA facility

Fig. 3.2: PROTEUS transport flask/sample changer used for preliminary measurements of spent fuel rod segments.

The fuel rod segment S#3 (see Section 3.4) was chosen for the measurement at the NEUTRA facility. The sample was placed in a vertical position at the centre of a block of steel of 100x100x100 cm^3, with a vertical cylindrical hole of 20 cm diameter in the middle and provided with a lateral window (see Fig. 3.1). A collimator of 40 cm of steel was employed with a horizontal slit of 1 mm height and 50 mm width. The collimator was inserted in this window, and a lead filter of 3 cm was used in front of the detector to reduce the effect of low-energy scattered photons. By using the NEUTRA flask drive to displace the rod segment vertically, it was possible to perform measurements corresponding to several different axial positions. The presence of a window in the steel block was used for activation measurements employing the neutron beam of NEUTRA, but this was in relation to another research activity and, for this reason, is not discussed further.

The fuel segment S#4 (see Section 3.4) was investigated at the PROTEUS facility. In this case, a different approach was taken, the rod segment being driven out of the bottom of the PROTEUS transport flask/sample changer (Fig. 3.2), such that the protruding length of a few centimetres could be used for the gamma measurements. These were conducted in the reactor's upper shielded cavity, the HPGe detector being located at the bottom level of the flask, ~1 m from the rod segment.

3.2. Exploratory Design Calculations

The experiment performed at NEUTRA was simulated afterwards using the Monte Carlo code MCNP-4C [bri]. A model has been developed to study the photonic efficiency of the system, simulating in detail the geometry of the relevant parts of the apparatus involved, special attention being given to the HPGe detector, the collimator, the within-pin source distribution and the radiation shielding. As indicated earlier, the resulting comparison of calculations and measurements was the basis for the modelling of the collimator and detection geometry for the new gamma tomography station.

3.2.1. Modelling of an HPGe detector

MCNP is a multi-purpose Monte Carlo N-particle code commonly used to model neutron, photon and electron transport for a wide range of applications. In the present study, the MCNP version 4C [bri] was used to model the photon transport through the shielding and collimator system. Single photons were followed during their entire history, from birth inside a fuel pin until absorption, if successful, inside the detector.

Two different tallies[8] were employed and compared: the "surface current tally *f1*", which is the number of particles crossing a surface, and the "pulse height tally *f8*", which provides the energy distribution of pulses created in a detector by radiation. The pulse height tally is very attractive for its capability to compute all the energy deposited in the detector by the single incoming photon (including all progeny created during the travel) [hen]. For this reason, a reasonable *f8*-tally prediction of the code is strongly related to a correct geometrical description of the active crystal detector volume. As an immediate consequence, detailed and accurate information on the crystal detector geometry is very important, especially the following details: shape, dimensions, position and thickness of the window, presence of an axial cavity, exact location of the cavity and its dimensions, the region capable of conversion of incoming radiation to countable pulses, and the dead layer. Other parameters for the detector, such as dimensions and material of the casing, electrical components, etc., are much less important in comparison with those cited above.

---

[8] Tally denotes the score count of particles that reach the final point (detector zone).

Usually some of these data are provided by the manufacturer, but the most important information, the volume and shape of the germanium crystal, is not detailed enough, particularly for a coaxial detector with its axial cavity, the dimensions of which are usually not well known. Sometimes the crystal could have been reprocessed, and this is another source of uncertainty because it influences the cavity dimensions. Because the successful use of the pulse height tally is strongly related to the knowledge of the active volume of the crystal, a further effort was necessary to study the most critical detector components. For this reason, an X-ray radiography of the detector, shown in Fig. 3.3a, was made at PSI to investigate the internal structure. This did not, however, resolve definitively all of the uncertainties. The radiography gave some insight about the external casing, some secondary components and, most interestingly, the shape of the crystal at the edge, but no information was available about the axial cavity of the crystal because of the high density of germanium.

(a)   (b)
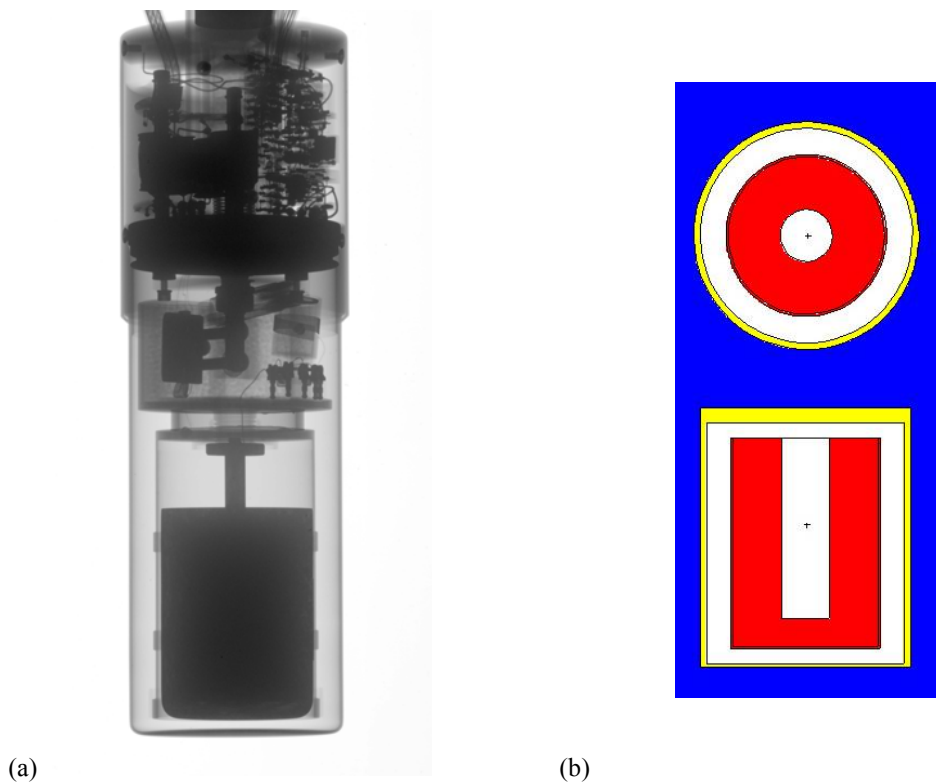
Fig 3.3: On the left (a) an X-ray radiography of a HPGe detector; on the right (b) a simplified model of the detector used for Monte Carlo calculations, in radial (upper) and longitudinal (lower) sections.

The final detector model has been built using the information from the manufacturer and from the radiography, improved with cross-check tests between an experimental calibration and the simulation done with the two different MCNP tallies. In Fig. 3.3b, a simplified detector geometry model employed for the MCNP calculations is shown. In this rather extreme simplification, the electronic components are neglected because the main objective was the accurate definition of the active volume of the germanium crystal (red region). The yellow region is the aluminium casing, whilst the white is just empty space.

As a first test, the detector intrinsic efficiency was determined experimentally and then predicted using MCNP, with the model described above. The detector calibration was performed in the PROTEUS reactor hall, using a ^{152}Eu gamma source with an activity of 391 kBq. This source, very attractive for calibration purposes due to its wide gamma energy range [50-1500 keV], was placed at a distance of 63 cm from the front window of the detector. From the spectra measured with the HPGe detector, gamma peaks at different positions in the energy spectrum were chosen and the relative count rates recorded in order to derive the intrinsic efficiency. By least square fitting, an exponential function versus energy was derived.

The calibration setup was afterwards reproduced with MCNP following the above illustrated detector model. The photons crossing the surface and entering into the active region of the detector were calculated using the "surface current" tally (*f1*), while the photons giving a contribution to the detector signal were computed using the "pulse height" tally (*f8*). The intrinsic efficiency was derived as the ratio *f8/f1*. Calculations were run using different dimensions of the cavity, comparing each time with measurements. Final dimensions were decided upon on this basis, and the detector model could thus ultimately be defined.

3.2.2. Modelling the NEUTRA setup

The experiment performed at the NEUTRA-SINQ facility was also simulated using MCNP-4C. The geometry[9] of the measurement set-up, the fuel pin composition and the detector (see previous section) were accurately reproduced.

---

[9] The fuel pin has an axial length of 40 cm and an external radius of 0.5375 cm. The distance between the collimator (steel) and pin was ~10 cm and the collimator slit was 5 cm x 1 mm. The collimator thickness was 40 cm. The detector (HPGe) had a 3 cm lead filter located in front of its window.

Several MCNP predictions were made using different within-pin source distributions. As an illustrative example of the MCNP model, reproducing the within-pin source distribution, Fig. 3.4 shows (on the left side of the picture) the fuel pin composition represented by different colours (fuel matrix, cladding and over-cladding) and divided into 10 radial regions (10 zones are typically used in pin-cell depletion calculation codes). On the right of the picture, the gamma-source distribution is represented in a longitudinal view and the active source is visible. It was modelled over 5 cm of a total fuel length of 40 cm, vertically centred on the collimator slit.

(a)   (b)

Fig. 3.4: Fuel pin in MCNP model of the NEUTRA setup: on the left (a) the internal composition described using different colours (fuel matrix, cladding and over-cladding) and on the right (b) the simulated vertical source distribution.

The count rates corresponding to the main γ-peaks of ^{137}Cs (0.662 MeV), ^{134}Cs (0.569, 0.605, 0.796, 1.039, 1.168, 1.365 MeV), and ^{154}Eu (0.723, 0.873, 0.996, 1.005, 1.275, 1.597 MeV) have been predicted in two different ways: in one case using the *f1* tally and the measured intrinsic detector efficiency, calculated as c/s = *f1* ε_{exp} *Y* A (where ε_{exp} is the measured intrinsic efficiency of the detector, *Y* the branching ratio and A the activity of the sample); in the other case using the *f8* tally and the MCNP-calculated intrinsic detector efficiency (implicitly contained in the *f8*-tally), as c/s = *f8* *Y* A. Some variation reduction techniques have been applied in the MCNP calculations. However, for the *f8* tally, it was not possible to use the standard techniques, which are not allowed in this special case. To overcome this limitation, the photon source was biased by the direction of the detector and in the longitudinal length distribution (as shown in Fig. 3.4b).

The parallel use of two different tallies is a way to confirm the validity of the germanium detector model applied, the *f1* tally not being influenced by the volume of the crystal (and the presence of the hole inside) as is the *f8* tally. In fact, using *f1*, one tallies the photons entering into the active zone of the detector and

giving a contribution only if the energy is beyond the single photo-peak (no Compton contributions). In contrast, the *f8* simulates even the conversion of the particles into the final electronic pulse, meaning that the precise dimensions of the active volume of the germanium crystal are rather crucial [soo]. The discrepancies between the two approaches for the calculation of counts/s were found to be within 2-3% in the energy range 0.6-1.4 MeV, becoming larger at lower and higher energies.

From the spectroscopic analysis of the experimental results, three main isotopes ([134]Cs, ^{137}Cs, and [154]Eu) were detected with a total number of 14 gamma peaks. The within-pin radial source distribution used in the simulation was modified several times to quantify any consequences on the final results, a flat distribution and centre-depressed distributions (of different degree) being employed for the purpose.

Calculations and experimental results have then been compared. In Fig. 3.5 the intrinsic detector efficiency predicted in this configuration (derived as the ratio *f8/f1*) is plotted as a function of photon energy and for two different source distributions, together with the efficiency derived experimentally. The agreement between measurements and calculation in the middle energy range (between 0.7-1.4 MeV) is within 1%, but larger discrepancies are present for some peaks below and above this region.
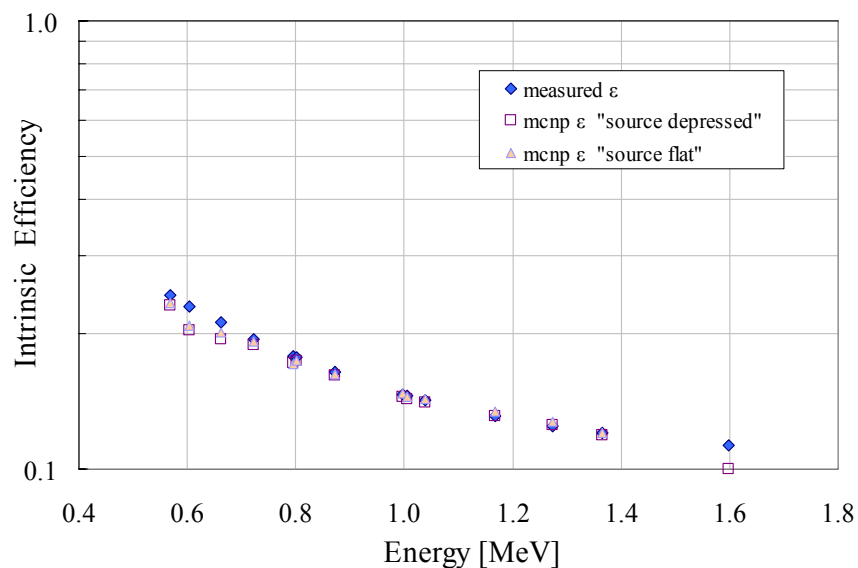
Fig.3.5: Experimental and calculated intrinsic detector efficiency.

Another interesting application of the MCNP pulse height tally (*f8*) is in the realization of a simulated spectrum ("detector pulse-height spectrum"). The procedure consists in computing several separate runs for each gamma line, using a specific card to set the virtual number of channels desired (i.e. tally energy specification "e8 0 1e-5 0.4 5089i 1.6" to select 5090 energy bins between 0.4 - 1.6 MeV). For each run a separate spectrum is generated, such that the final spectrum can be obtained by addition of all the other spectra. As an example, a simulated gamma-ray pulse-height spectrum is shown in Fig. 3.6. In the development of this spectrum, not all the contributions from other gamma emitters present in the fuel rod have been taken into account. Only the main gamma-emitters, i.e. [134]Cs, ^{137}Cs, and [154]Eu, with their more prominent gamma-rays, have been considered.
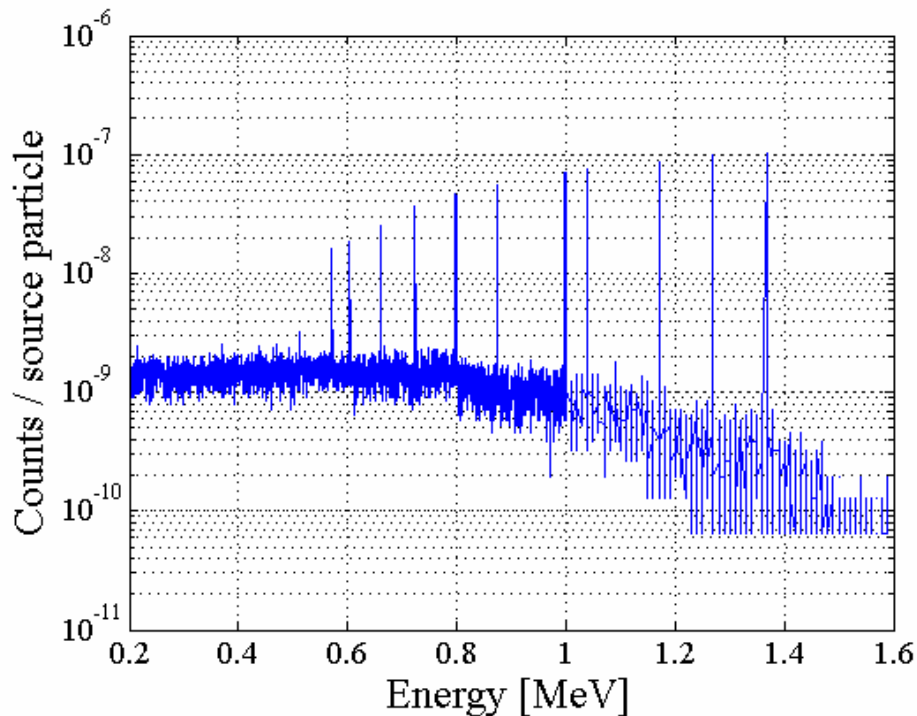
Fig.3.6: Simulated gamma-ray pulse-height spectrum with contributions from main gamma-emitters, i.e. [134]Cs, ^{137}Cs and [154]Eu.

3.2.3. Modelling of a new setup

The experience gained during the preliminary campaign was used to model a new experimental setup, focusing attention on the photonic requirements necessary for a 2D tomography system. The main requirements for a valid radio-isotopic reconstruction are:

- Accuracy better than 1% for all the main gamma-rays

- Accuracy better than 0.1% for the gamma-rays suitable to be used for tomography reconstruction

- Count-rate low enough to preserve the peak shape and resolution

- Measurement time (MT) short enough to allow realistic tomographic measurements

- Collimator slit width (ΔL) as narrow as possible in order to increase the spatial resolution for tomography. This choice limits the final image resolution.

As a first assumption, the collimator slit was assumed to be rectangular and with a height of 2 cm, such that the detector could see about two pellets, limiting the longitudinal uncertainties. A small slit height is usually necessary when a 3D tomography must be performed, and in that case several solutions for high performance collimators exist. This, however, corresponds to needs in certain medical applications.

To match the above described requirements, detailed simulations have been performed, trying to find a good compromise between accuracy of the measurements and count-rate. The MCNP model developed for this study comprised a complete geometrical description of the shielding, collimator, detector, detector filter, the main steel support, the transport flask/sample changer containing the experimental samples, and the external gamma source. The simulations had the additional goal of characterising the required activity of an external gamma source (^{60}Co) to be used for the transmission tomography application.

Fig. 3.7, a diagram of the MCNP model of the setup, shows the experimental sample position (very close to the collimator) and the shielding, in two different views (vertical view on the left and horizontal view on the right).

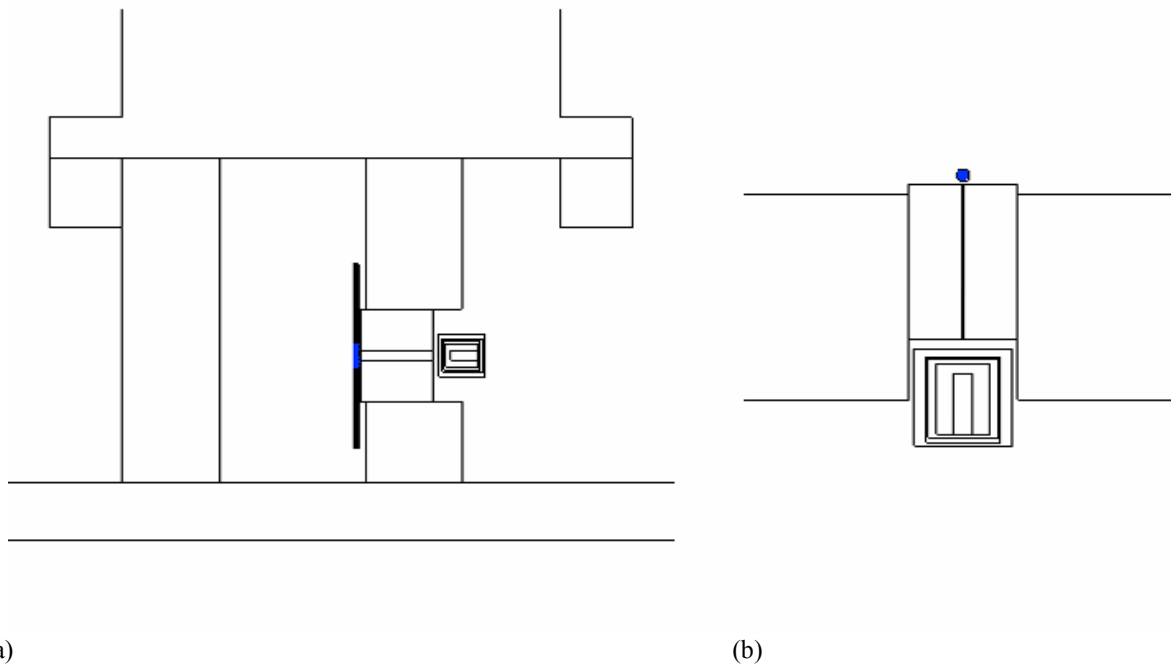(a)   (b)

Fig.3.7: MCNP model for photonic analysis of a tomographic station; on the left a vertical view of the station, and on the right a detail of the horizontal section.

As a conclusion of this calculational study, the collimator material was chosen to be tungsten and its thickness was fixed at 15 cm and the slit width at 0.02 mm, because the accuracy of the ^{137}Cs gamma-peak was satisfactory (uncertainties < 0.1%) in this condition. However, a wide range of sample activities needed to be investigated. This factor influenced the final design, suggesting the use of a variable slit, such that the width could be reduced or increased depending on the sample. The possibility to move the detector further from the collimator in case of too high a dead time was considered as well.

3.3. Gamma Tomography Station

A measurement station has been built for the non-destructive investigation of highly active samples, viz. spent fuel rod segments of 400 mm length. The station also allows gamma-spectrometry and neutron emission measurements to be made, but it is designed principally for tomographic investigations.

The measurement station is a structure consisting of a lead shielding enclosure, a tungsten collimator, a remote handling system with the associated control system, a gamma detector, a system for the injection of an external gamma source and a set of neutron detectors. The station is operated in combination with the PROTEUS transport flask/sample changer [mur], which loads the fuel segment into the station from the top, after which a remotely controlled clamping system ensures that the sample is secured in an accurately known position in a 'V' channel. The full assembly weighs 2 tonnes, sample flask changer not included (an extra ~ 6 tonnes).

The working principles of the station and the engineering drawings are explained in the next sections, followed by descriptions of the individual components.

3.3.1. Working principles

The basic capability needed for a tomographic station is to generate cross-sectional images of an object – a fuel rod in this case – on the basis of measurements of γ-rays emitted by separate "slices" of this object. For this reason it is necessary to traverse the fuel rod laterally with respect to the collimator slit, making many steps across the whole width of the fuel rod and measuring the intensity of the γ-rays at each step. The set of intensity data collected for all the steps of a particular traverse is called a projection (see Fig. 3.8). In order to reconstruct the "image" of the object, a number of "projections" need to be recorded. This is done by rotating the object on its centre and collecting the "projections" at different angular positions.

As indicated in Fig. 3.8, the tomographic station can operate in two different ways: using an external γ-source, such that the projections coming from the source can give information about the internal morphology of the object (transmission), or without the external source, such that the projections

collected belong only to the internal source distribution (emission), giving information about the within-pin activity distribution.
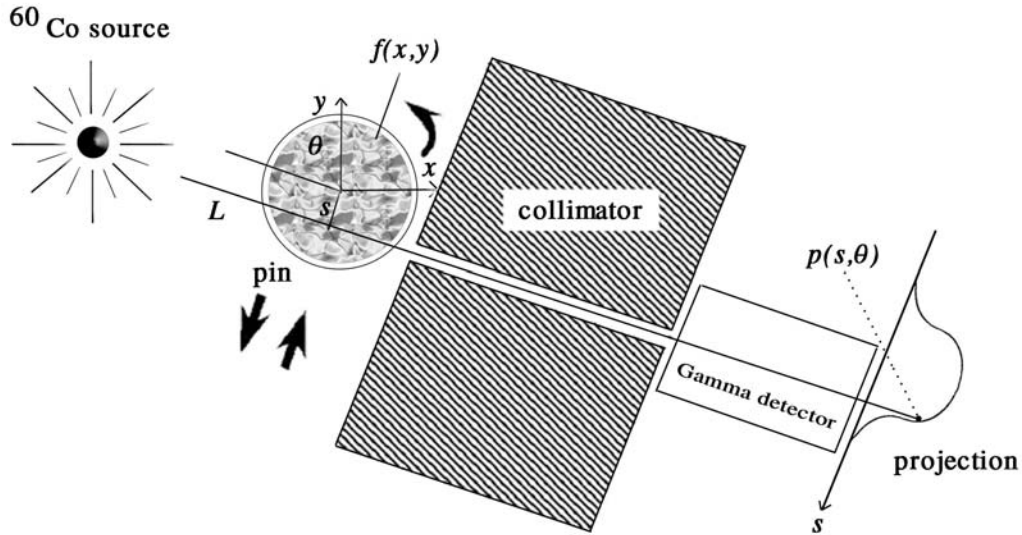

Fig. 3.8: Schematic illustration of the basic principles of the tomographic station.

If one refers strictly to emission tomography, one can denote with $f(x,y)$ the unknown distribution of the γ-source within the object, and with $p(s,\theta)$ the projection element, function of the lateral displacement s of the object respect to the collimator slit, and its angular rotation θ. The mathematical relationship between $p(s,\theta)$ and $f(x,y)$ is described using a projection operator $W(s,\theta)$, which essentially models the transport of the photons of interest through the different materials of the system in a geometry corresponding to the measurement configuration, given by (s,θ). The problem to be inverted may be posed in the following matrix form:

$$W\vec{f} \cong \vec{p}$$

Reconstructing $\vec{f}$ from the measured projection elements reverts to inverting the system matrix W.

To determine the unknown distribution $\vec{f}$, it is necessary to have:

- o a set of measured projection elements $p(s,\theta)$
- o a system matrix W properly modelling the involved physics processes, according to the type of discretisation chosen, i.e. according to the type of basis functions chosen
- o a reconstruction technique, i.e. a way of performing the inversion of the direct problem described above.

In transmission tomography the problem is slightly different, because here the unknown f is the attenuation inside the object:

$$f = \int_L \mu(x,y)dl$$

In this case, the development of an efficiency system matrix (W) is not necessary, as explained in Chapter 4. The goal of the transmission tomography is to reconstruct the attenuation map of the object, and use this map to correct the emission tomography for the effect of attenuation. The attenuation map leads directly to a material density map, which is of interest in its own right.

Details of the various reconstruction techniques used are discussed in Chapters 4 and 5.

3.3.2. Engineering drawings

The tomographic measurement station consists of several components, described in detail in the following section, and can be thought of as consisting of three main entities. In the vertical-view engineering drawings (Figs. 3.9 and 3.10), one sees a 5-cm thick steel plate, which is the foundation of the station. The main body of the station, consisting of the steel pedestal, the shielding enclosure, the remote handling system, the supports of the γ-detection system and the external source injection guide, is fixed to the steel plate. The third part (the PROTEUS transport flask/sample changer) is positioned on the top of the main body, supported by the steel pedestal, and accurately fixed to the main body such that the fuel handling can be performed safely. As mentioned earlier, the total weight of the station (main body and steel plate) is about two tonnes, whilst the transport flask/sample changer weighs 6 tonnes. The station was designed such that any direct γ-radiation beam can be avoided. The measurement campaign has been carried out in the PROTEUS "fuel laboratory" – a secure underground room designed for fuel handling.
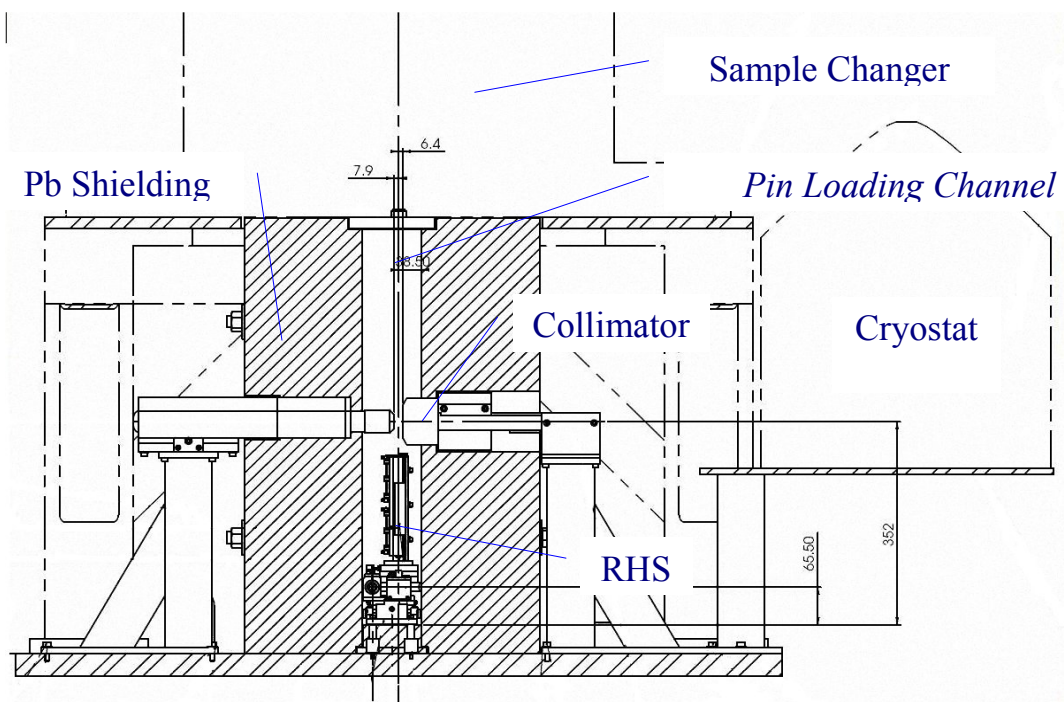
Fig. 3.9: Engineering drawing (<yz> view); RHS: remote handling system.
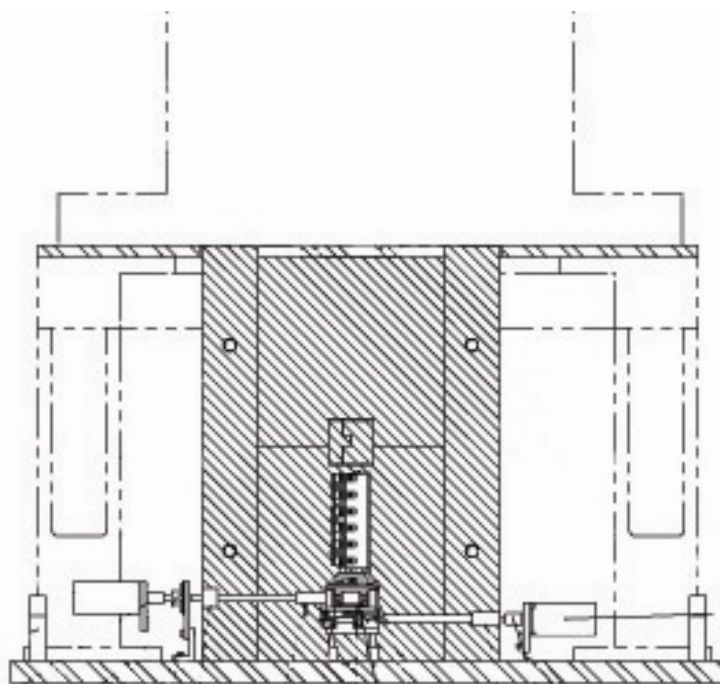

Fig. 3.10: Engineering drawing (<xz> view).

3.3.3. Components

Lead shielding

The lead shielding enclosure is 200 mm thick and designed such that the burnt fuel segments are well shielded when in the measurement position. The shielding is fabricated from lead "T" bricks secured by steel rods, as seen in Fig. 3.11. The shielding has two main lateral openings to host the collimator and the external source injection system on opposite sides. The openings have stepped sides to avoid direct radiation paths. The enclosure has a central cavity large enough to host the clamping system and the remote handling, as is evident from Fig. 3.11b, where a side of the enclosure has been removed to install the remote handling system.
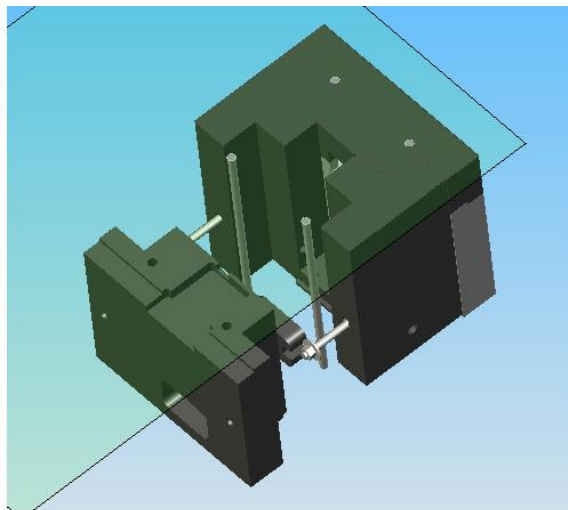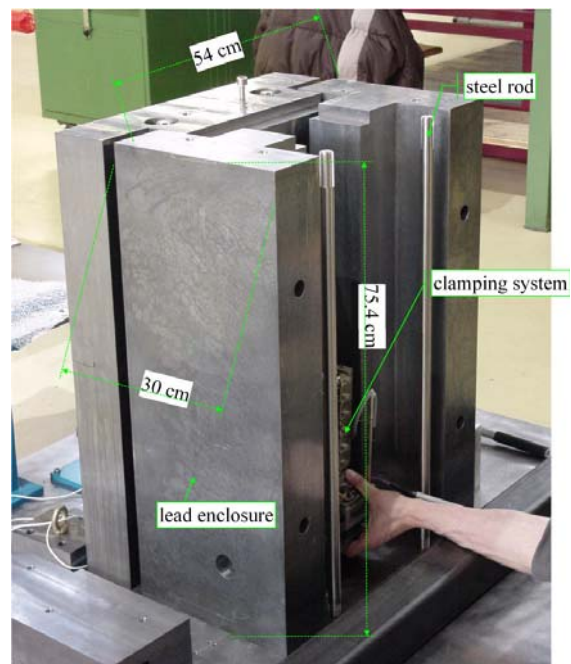
(a)   (b)

Fig 3.11: (a) A horizontal section of the 3D drawing of the shielding enclosure; the lead bricks and the steel rods are clearly visible. (b) View of the shielding during the assembly. A side of the station is open, corresponding to the collimator/γ-detector sector.

Collimator

The collimator is a block of tungsten of 150 mm length, with an internal slit of 0.2x20 mm (Fig. 3.12; 3D drawing and view of the collimator before assembly) with a capability to modify the slit width as required. In Fig 3.13a, the blades of tungsten used to modify the slit are shown; different thicknesses of the blades allow different slit widths (thicknesses in the range of 200-1000 μm have been prepared). The collimator is located in an opening through the shielding wall, with an external support, outside the shielding enclosure and fixed on the steel base plate to guarantee its stability. The collimator is positioned such that it is protruding from the internal side of the lead wall and almost touching the surface of the pin but without any contact. In Fig. 3.13b, a view is shown (top view) of a dummy rod gripped in the clamping system just in front of the collimator slit.

(a)   (b)
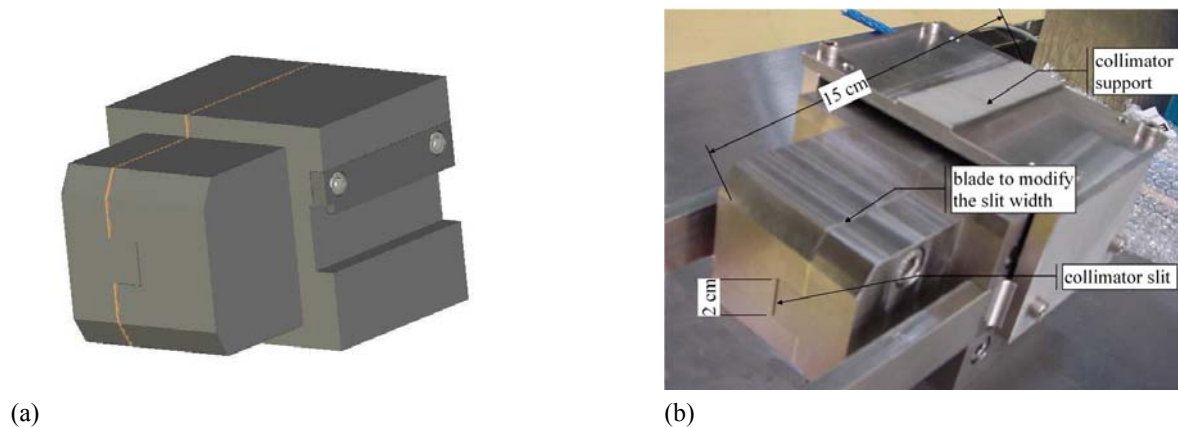
Fig. 3.12: The tungsten collimator with adjustable slit width. (a) 3D drawing of the collimator. (b) A view of it before the assembly of the station.

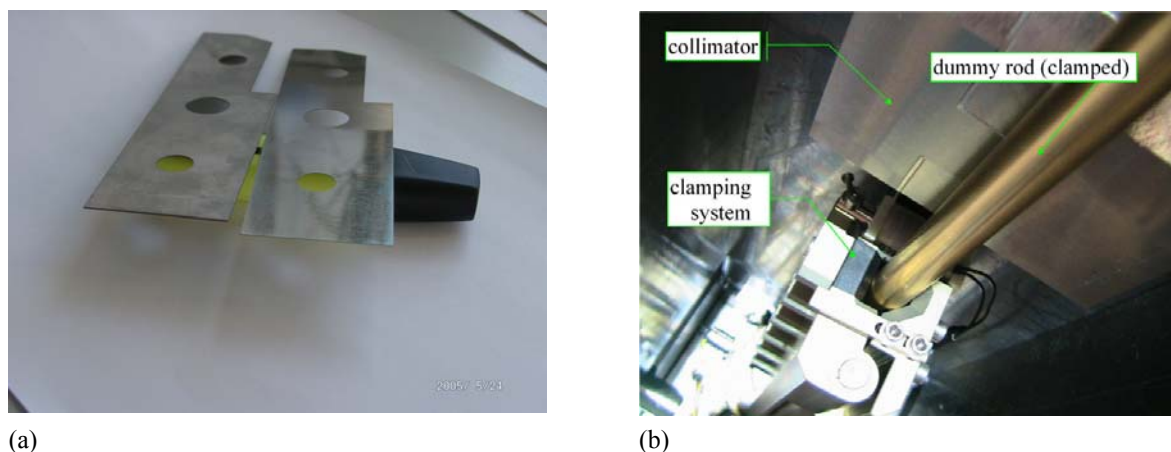(a)   (b)

Fig. 3.13: (a) The tungsten blades used for slit width modification. (b) A detail of the loading of a dummy rod into the clamping system such that the rod and the collimator are very close but not in direct contact.

<u>Clamping system</u>

The system for clamping the spent fuel pins consists of a V-channel, with a securing plate driven by 6 magnets. After the pin is lowered from the top (from the transport flask/sample changer) into the channel, the magnet mechanism is set in action to close the securing plate onto the V-channel to clamp the pin softly but exactly (Fig. 3.14). The clamping strength is enough to grip the pin such that its position is stable, but not so excessively strong as to risk any damage to the fuel (the global strength is 7N). During operation, the pin is always supported by a wire from the transport flask/sample changer so that, in case of loss of power in the system, the magnetic clamp opens and leaves the pin held by the transport flask/sample changer wire.

(a)   (b)
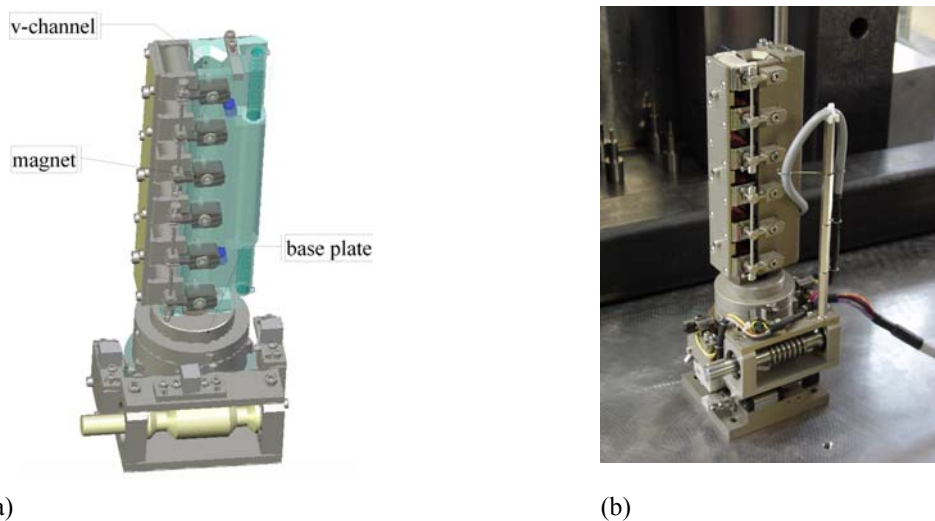
Fig. 3.14: The clamping system. (a) 3D drawing of the clamping system. (b) A view of the system before its assembly into the station.
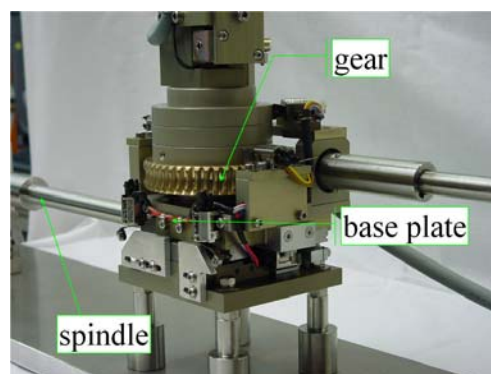

Fig. 3.15: Details of the base plate and the gear at the bottom of the clamping system. The spindles for the connection to the stepping motors are visible as well. Note the stepped shafts to avoid direct radiation paths.

The clamping mechanism is mounted on a base plate, which can be moved by a system of gears and stepping motors (see Fig. 3.15) to traverse the sample past the collimator and to rotate it to different angular positions, as described below.

Remote handling system: magnetic clamping and traversing system

This system is completely remote-controlled. The mechanism consists of a plate allowing a lateral displacement of the entire clamping system and a gear system for its rotation. The lateral movement (the total spacing for the lateral movement is $\Delta L_{tot}=\pm 8.625$mm, whereas the single steps are flexible, e.g. 0.2 mm) and the rotation (steps of 45°) are ensured by two stepping motors placed outside the lead wall, each of them connected by a spindle to the main plate. Further, the system is provided with a certain flexibility regarding the measurement of different axial positions of the pin. In fact, the flask/sample changer can move the pin vertically such that the clamping system can grip it at different axial positions. In Fig. 3.16, a 3D drawing of the remote handling system is shown.

The main console of the station is placed outside of the fuel laboratory at a distance of 10 m from the cell, in the reactor hall. It is important to note that, during operation with burnt fuel samples, there is no necessity to enter the measurement room.

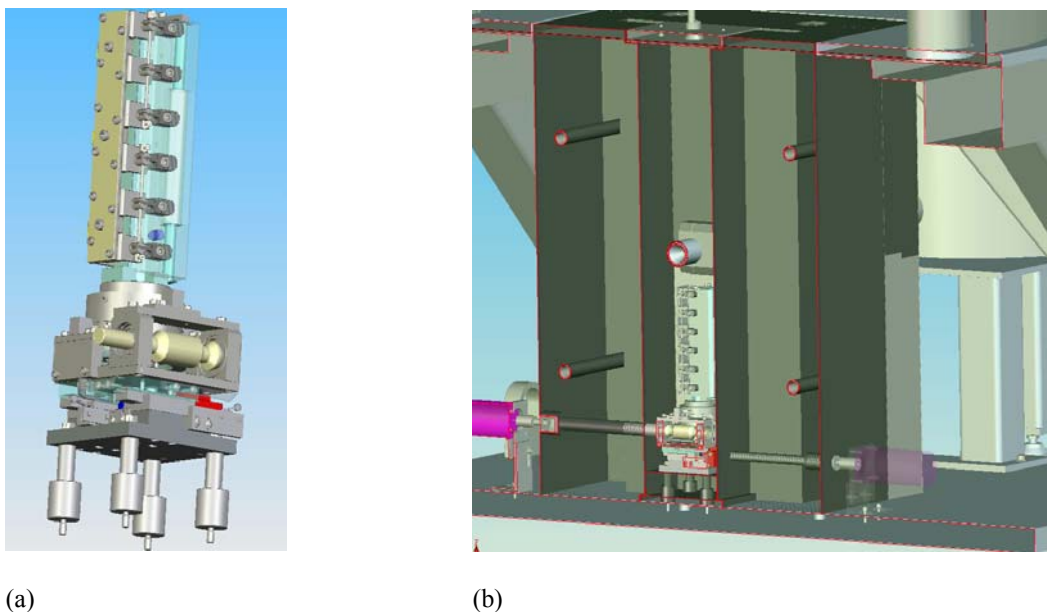(a)   (b)

Fig. 3.16: 3D drawing of the remote handling system. (a) The clamping system, located on the plate-gear with the supports for the fixing on the basic steel plate. (b) A vertical-cut view of the shielding enclosure, showing the remote handling system and the stepping motors connected through the shielding.
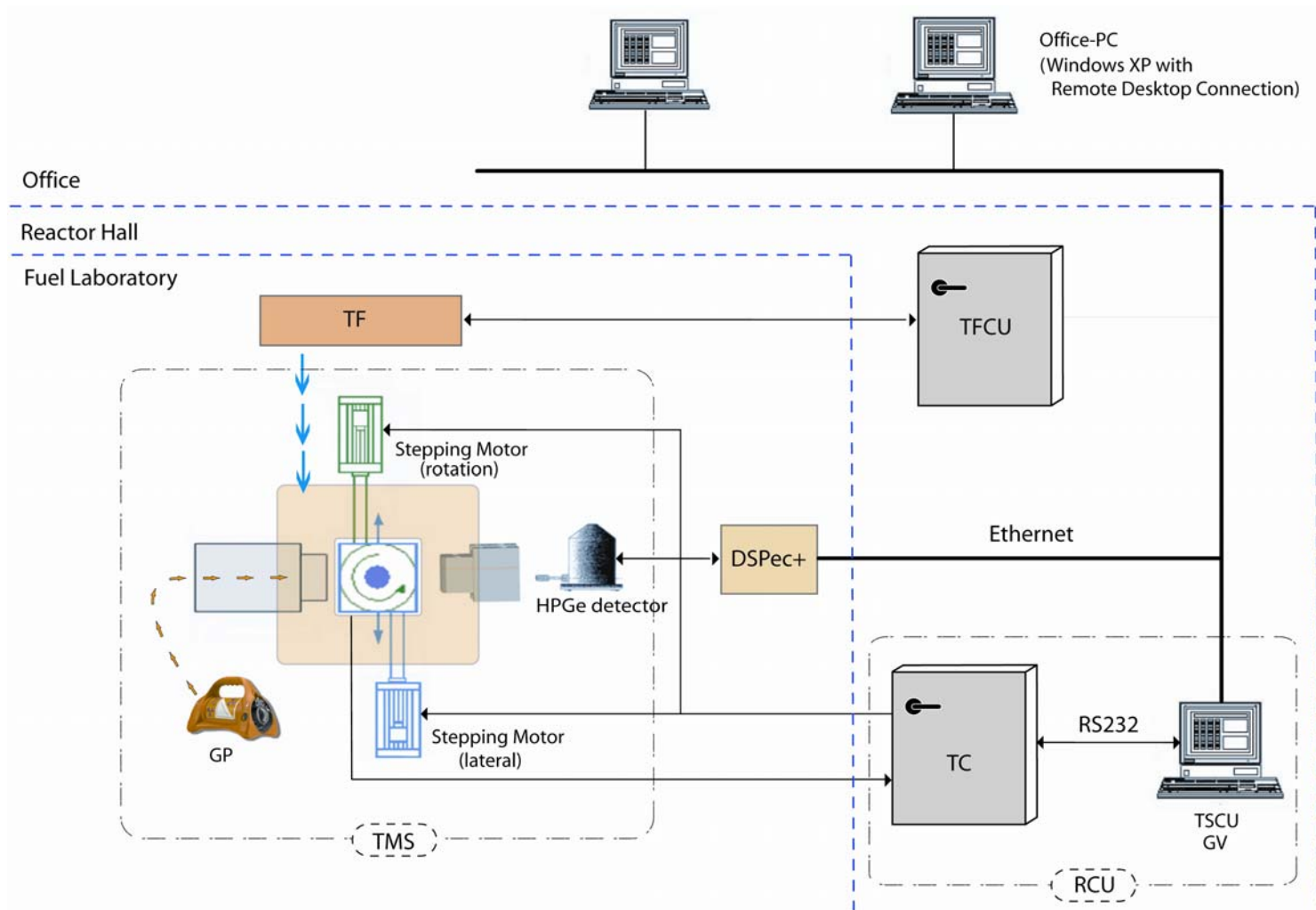
Fig 3.17: Schematic drawing of the tomography system designed for spent fuel rod investigations. Here, the subdivision into three layers is visible: (1) the "fuel laboratory" layer where the tomographic station with the fuel rods (TMS) and the gamma projector (GP) are placed, (2) the "reactor hall" which hosts the control cabinets of the "remote control unit" (TC) and the transport flask/sample changer (TFCU), and (3) the "office" layer where the system can be operated via a PC.

Remote control unit of the TMS

The "remote control unit" (RCU) is connected by cables penetrating the lead shielding (through labyrinthine paths) to the "tomographic cabinet" (TC). The cabinet is connected, via a serial cable (RS232), to the PC. A technical schematic of this is shown in Fig. 3.17, in which the subdivision into three layers is visible: (1) the "fuel laboratory" layer where the tomographic station ("tomographic measurement station", TMS) with the fuel rods, the detector and the "gamma projector" (GP) are placed, (2) the "reactor hall" layer which hosts the control cabinets of the "remote control unit" (TC) and the transport flask/sample changer ("transport flask control unit", TFCU) and a PC, and (3) the "office" layer where the system can be operated via another PC.

From a normal PC, the TMS is operated using a special programme ("tomographic station control unit" TSCU) [pie]. With this application, it is possible to perform the following operations: system settings definition (to define the parameters for the displacement and rotation of the samples), clamping/unclamping of the pin, lateral displacement and rotation of the pin, programming of tomography cycles, and control of the HPGe detector through the ORTEC DSPEC+ unit [dsp]. In Fig. 3.18, the main window of the TSCU programme is shown. In Fig 3.19, the two main windows for "manual mode" and "run auto mode" operations are shown as well. The run auto mode allows one to configure and run tomography measurement cycles.
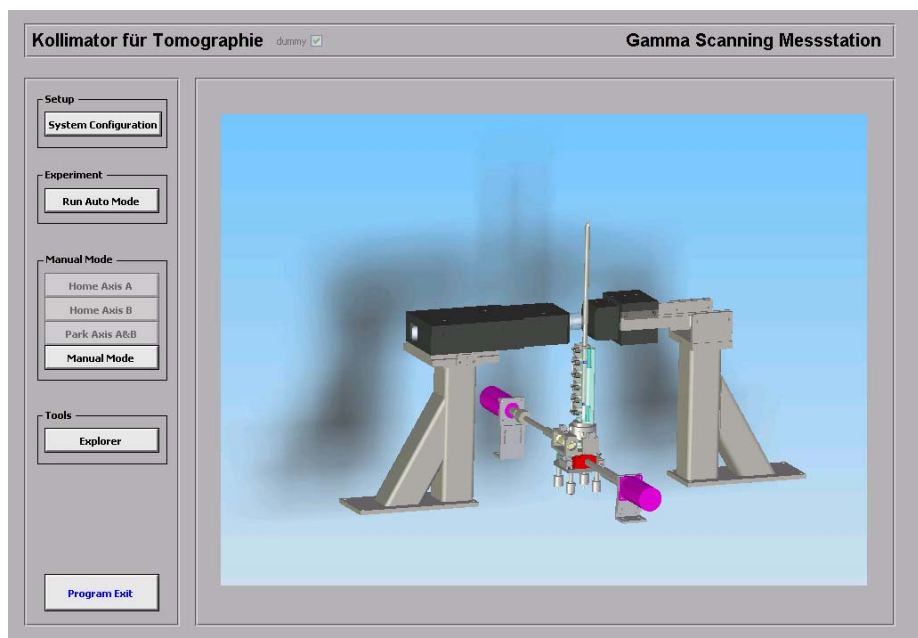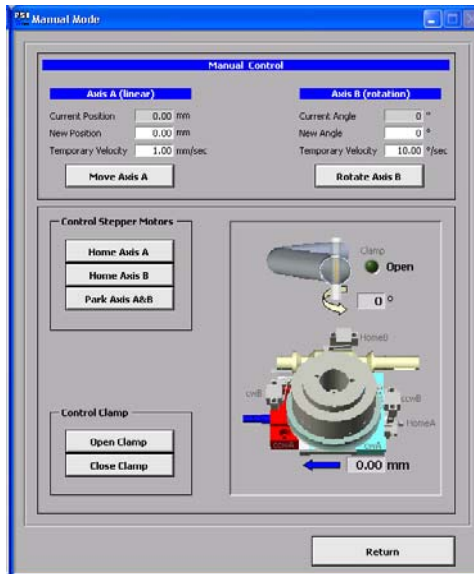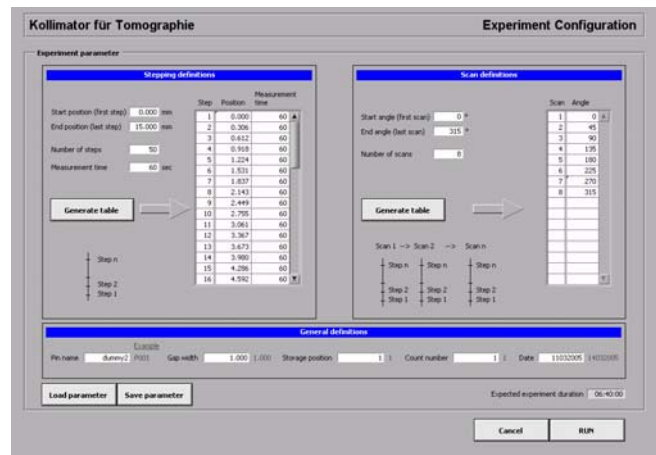

Fig. 3.18: Main frame of the programme (TSCU) for the control of the tomographic station. It is possible to distinguish the two operation modes: manual mode, run auto mode.

(a)   (b)

Fig. 3.19: TSCU programme for the control of the tomographic station. (a) "Manual mode" frame. (b) "Run auto mode" frame.

PROTEUS transport flask/sample changer

The transport flask/sample changer is a unit used for the managing of spent fuel rods of 40 cm length and has been employed principally for reactivity measurements in the framework of the PROTEUS Phase II programme [mur]. The flask does not rest directly on the shielding enclosure, but is supported by a special structure used earlier in the context of standard Phase II operations. The support is fixed to the steel plate such that the whole assembly is rigidly locked together.

During the measurements, the pin is loaded into the tomographic station using the flask control unit (TFCU), at "reactor hall" layer, in combination with the tomographic control unit (TC). The two units are not synchronized; the first unit drives the samples vertically, whilst the second ensures the gripping of the pin and the displacement operations. In particular, the TC unit, through the TSCU, allows to programme sessions of tomographic measurements remotely, as described earlier.

In Fig. 3.20a, the bottom of the sample flask changer is shown during the loading of a dummy rod into the V-channel of the clamping system, during the first campaign of cold tests. From the picture, the details of the inside of the tomographic station are visible. Fig. 3.20b gives an external view, showing the flask with its pedestal and the station with its front side completely open for cold test operations.

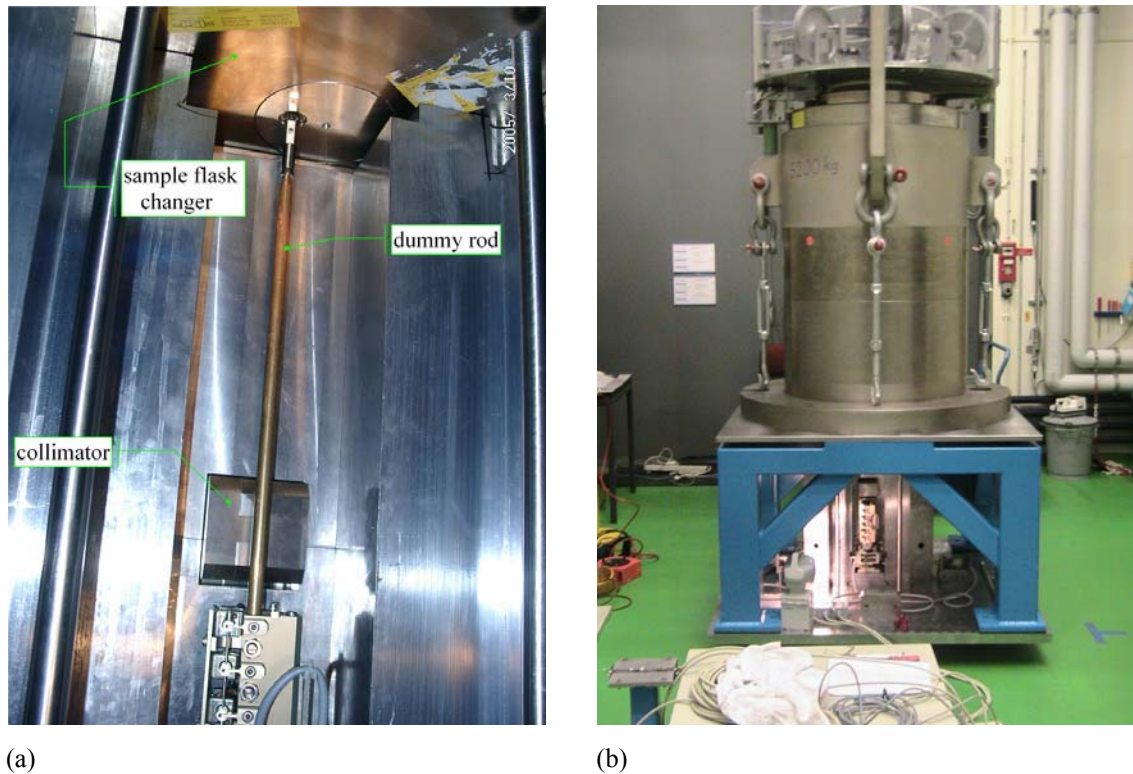(a)   (b)

Fig. 3.20: (a) Inside the tomography station, during the loading and clamping of a dummy rod. (b) External view of the station with the sample flask changer, the pedestal, and the station with the front side completely open for cold test operations.

External gamma source insertion system

The possibility to drive a γ-source into the internal cavity of the station is a fundamental requirement for transmission tomography measurements. For this purpose, a commercial gamma projector (Fig. 3.21a) was hired and used for the measurements. The gamma-ray projector (GP), Model Delta 880 of CONTROLTECH [sen], is a compact exposure device normally used for industrial gamma-radiography. It is designed to host different source types and projects the source through a guide tube of 2 m length. The exposure device body is made of depleted uranium and weights 22 kg. It is provided with a 10 m long remote control cable.

The γ-source used was ^{60}Co of 65.2 mCi (2412 MBq) activity with a size of 2 mm x 1 mm diameter. In order to use the cobalt source in the tomography station, a special device was built. This device (see Fig 3.21b for a sectional view) allows the penetration of the source guide tube into the enclosure shielding and ensures the location of the source in a final position as close as possible to the sample and in line with the collimator slit opening. The indirect path (designed to prevent a direct radiation beam to the outside), which hosts the source guide tube, is clearly visible in the 3D drawing of Fig. 3.21b. Fig. 3.22 shows the view from the top of the internal part of the shielding enclosure during a cold tests campaign, with the gamma projector device terminal, the dummy rod gripped into the clamping system, and the tungsten collimator.
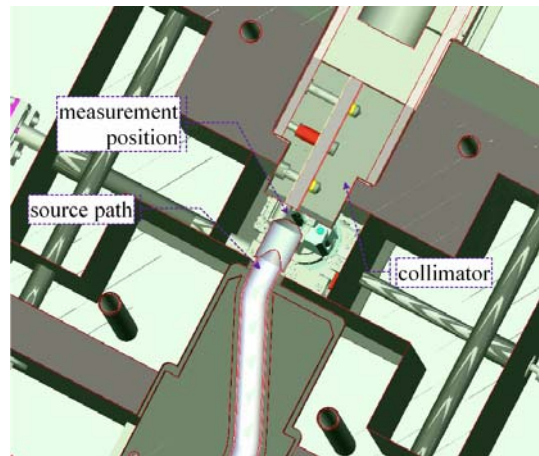
(a)   (b)

Fig. 3.21: (a) The gamma ray-projector (GP) Model Delta 880. (b) Sectional view of the device hosting the source guide tube with the end stop.
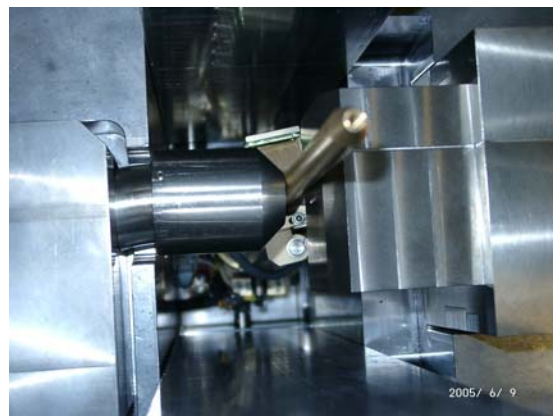

Fig. 3.22: View from the top of the internal part of the shielding. The gamma projector device terminal, the dummy rod gripped into the clamping system and the tungsten collimator are shown.

The gamma projector is provided with a remote winding gear, which can be operated at a distance of 10 m (maximum length of the cable) from the source container.

High-resolution gamma spectrometry system

The gamma measurement equipment consists of an EG&G ORTEC high-purity germanium (HPGe) coaxial detector, cooled with liquid nitrogen. The germanium detector employed in the first part of the measurement campaign belongs to the ORTEC GEM series [egg]. It is a p-type detector with detection energy range from 40 keV to 10 MeV and has an 18% relative efficiency with 1.67 keV resolution for the 1332 keV photopeak of ^{60}Co. The crystal has a diameter of 47 mm, is 61 mm long and has a 0.7-mm thick inactive germanium layer. Its distance from the end cap is 3 mm. The end cap of the detector is a 1.27-mm thick aluminium layer. The detector was shielded with a cadmium-and-copper casing to stop the X-rays produced by fluorescence in the lead. The detector is connected to an EG&G ORTEC DSPec Plus digital gamma-ray spectrometer [dsp], a comprehensive unit containing an analogue-to-digital converter, a digital shaping amplifier, high voltage power supply, etc. The DSPec module provides a 3500 V high voltage for this detector. The rise time, flap top, cusp (rise and fall curvature) and tilt (flat top curvature) of the filter functions have been adjusted, depending on the sample under measurement, to keep the dead time reasonable low. The DSPec automatic baseline restore (pole zero and tilt selection) was used in order to optimize the peak resolution. The DSPec+ is located at the "fuel laboratory" layer and connected to the hub in the reactor hall.

The spectra acquisition and analysis software is the Gamma-Vision multi-channel analyser programme from EG&G ORTEC [gam].

The detector can be optionally protected by an additional lead filter of 3 cm thickness (to reduce the low energy gammas coming from scattered γ-rays, and thus reduce the dead time) and a paraffin wax filter of ~3 cm thickness to reduce the neutron contribution. Both these filters are located within the shielding wall, as seen in Fig. 3.23a, between the front of the detector and the collimator. The body of the detector is further protected along its lateral profile with additional lead shielding, as shown in Fig. 3.23b.

During the second part of the measurement campaign, the germanium detector had to be replaced because of the radiation damage on the germanium crystal, induced mainly by the strong intrinsic neutron source of the fuel rod segment with the highest burnup. Another detector of the same kind (GEM series, p-type), having very similar characteristics, was used as a substitute for the damaged detector.
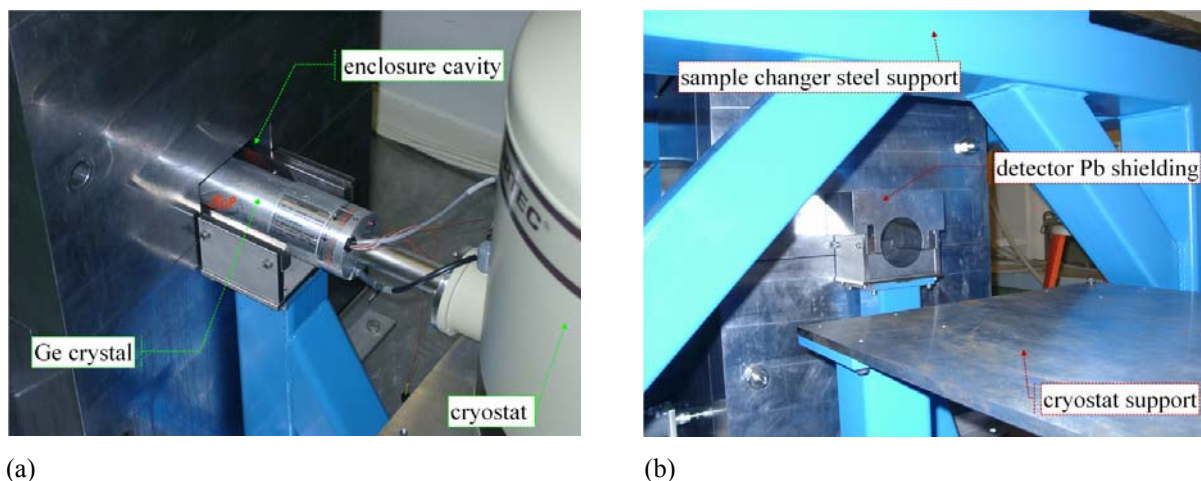
Fig. 3.23: (a) The HPGe detector and its location inside the shielding enclosure. (b) View of the detector aperture surrounded by lead shielding. The steel support for the cryostat is also visible.

3.3.4. Assembly and operation

The first partial assembly of the measurement station was done at the PSI workshop and the station was moved to PROTEUS afterwards. The main components were assembled in the reactor hall of PROTEUS and the flask/sample changer was fixed to the main body of the station, supported by the steel pedestal, as shown in Fig. 3.24a.

Cold tests were performed before operation with active samples [car], in order to verify the functionality of the measurement station in itself and in combination with the flask. In Fig. 3.24b, a view of the alignment operation is shown, with a dummy sample being loaded from the flask to the clamping system of the station. As a preliminary measurement, the station was then loaded manually with a low intensity ^{137}Cs source and subsequently with an IMF fuel rod, in order to test the detector acquisition system and the effectiveness of the collimator in such a geometry. Finally, the full assembly was moved to its location in the PROTEUS fuel laboratory, for the measurement campaign with highly active fuel rods.

As indicated earlier, the fuel laboratory is an underground room, with thick concrete walls, designed for fuel handling operations. Once the measurement station was located in this room, there was no need for manual interventions, except for the operation of the gamma projector (the consol being 10 m away from the source) and the filling of the detector cryostat with liquid nitrogen. Fig 3.25b shows the station in its final operating location. The cryostat of the germanium detector and the gamma projector are clearly visible.

Although the basic experimental set-up was maintained as described above for the entire measurement campaign, the distance between detector and sample, as also the filter in front of the detector, were modified according to the requirements for best performance. The preferred configuration consisted of a lead filter of 30 mm in front of the detector to attenuate the low energy gammas, and consequently to reduce the detector dead time, and a paraffin wax neutron filter to reduce the neutron damage to the detector.

Principally, three kinds of measurement procedures have been employed:

- A long spectrometric measurement of the four samples (3000-10000 s), with the pin clamped right at the centre of the collimator slit, followed by a long measurement with the pin clamped at a side, not in line with the collimator (background measurement)

- A session of transmission tomography measurements. The cobalt source was introduced into the station and a cycle of tomographic measurements, programmed with the previously described software, was run, e.g. typically performing between 60-70 lateral steps for each of 4-8 angular positions. In this case, the measurement time for each spectrum was short (~500-1500 s).

- A session of emission tomography measurements. The procedure is the same as described above, but with the gamma source outside of the cell. In principle, the transmission and emission measurements can be performed in the same session, because the ^{60}Co peaks do not interfere particularly with the peaks of interest, and the Compton background is negligible if compared to the background coming from the samples loaded in the sample flask changer.
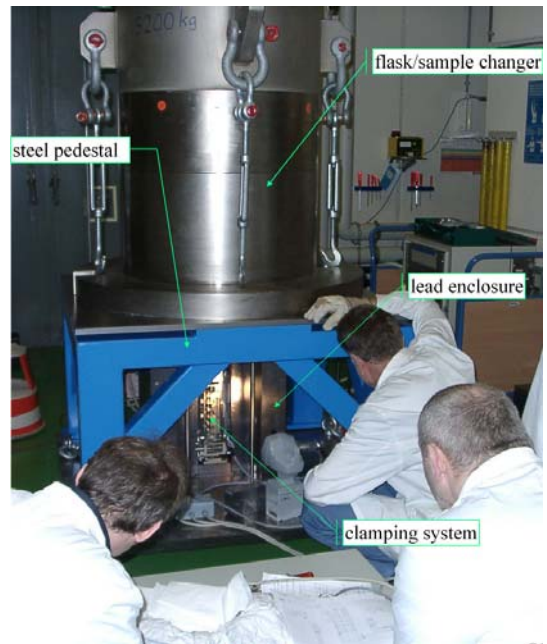
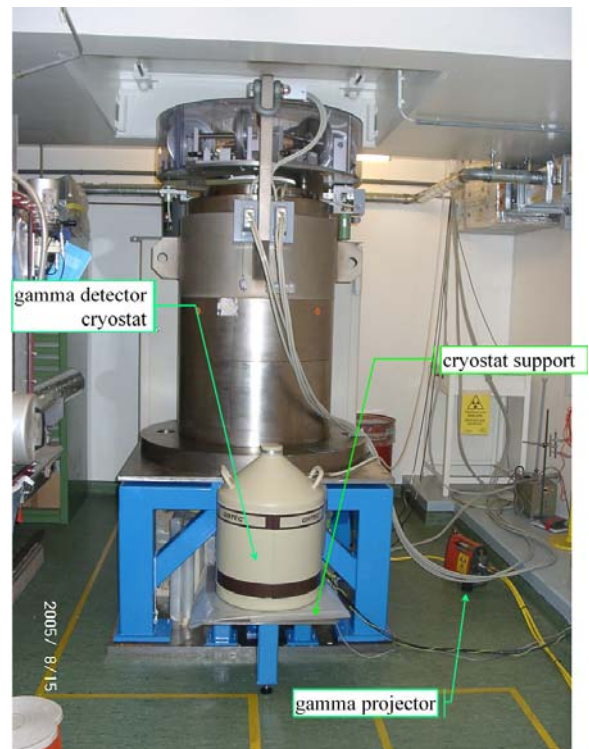(a)   (b)

Fig. 3.24: (a) Sample flask changer and measurement station during the assembly at the PROTEUS reactor hall. (b) Alignment between the two main bodies while testing the loading of the sample into the clamping system.

(a)   (b)

Fig. 3.25: (a) The measurement station during its installation into the fuel laboratory. (b) The measurement station finally operative.

3.4. Burnt Fuel Rod Samples

Four highly burnt UO_2 segments with different burnups, from PWR fuel rods used in a Swiss nuclear power plant, have been investigated experimentally with non-destructive techniques using the previously described measurement station. The fuel segments are UO_2, with a length of 400 mm. In Table 3.1, the main characteristics of these fuel rods are described, in terms of the irradiation time of the samples (expressed in reactor cycles), the burnup estimation through CASMO-4 [ede] calculations, the cooling time, and the life-average temperature of the moderator. All the pins have been encapsulated in Zircaloy over-cladding (400 μm of thickness) to prevent their being damaged and to guard against contamination. Besides the burnt samples, a fresh 3.5% UO2 sample was loaded into the flask to act as a reference for the gamma-ray transmission measurements.

Table 3.1: Characteristics of the experimental samples.

Sample Designation	Fuel Type	Reactor Cycles	CASMO-4 Burnup Estimation [GWd/t]	Cooling Time[1] [years]	Moderator Temp [°K]
S#1	UO_2	3	52	~10	~590
S#2	UO_2	5	71	~10	~580
S#3	UO_2	7	91	~10	~570
S#4	UO_2	10	126	~4	~580

[1] Time between discharge and measurement

References

[bri]   J.F. BRIESMEISTER, "MCNP – A General Purpose Monte Carlo N-Particles Transport Code, Version 4C", LA-12625-M

[car]   S. CARUSO, "Cold test planning for the tomography measurement cell at Proteus**,** *PSI Internal Report* AN-41-05-05 (2005)

[dsp]   "DSPECTM. Digital Gamma-Ray Spectrometer", EG&G ORTEC Catalog, Oak Ridge.

[ede]   M. EDENIUS, K. EKBERG, B.H. FORSSEN, D. KNOTT, "CASMO-4. A Fuel Assembly Burnup Program. User's Manual", Studsvik Report SOA-95/1, Studsvik of America, 1995

[egg]   "Modular pulse-processing electronics and semiconductor radiation detectors". EG&G ORTEC Catalog 1997-1998

[gam]   "GammaVisionTM-32. Gamma-Ray Spectrum Analysis and MCA Emulation for Microsoft®Windows® 95 and Microsoft Windows NT. A66-B32 Software User's Manual", EG&G ORTEC Part No. 774780 Manual Revision A, Oak Ridge

[hen]   P.H.G.M. HENDRIKS, M. MAUĆEC, R.J. DE MEIJER, "MCNP modelling of scintillation-detector γ-ray spectra from natural radionuclides", *Applied Radiation and Isotopes,* **57** p.449 (2002)

[key]   R.M. KEYSER, "Resolution and sensitivity as a function of Energy and incident geometry for germanium detectors", *Nucl. Instr. and Meth. in Phys. Res. B*, **213** p. 236 (2004)

[leh]   E.H. LEHMANN, P. VONTOBEL, L. WIEZEL, "Properties of the Radiography Facility NEUTRA at SINQ and its Potential for Use as European Reference Facility", Proc. 6th World Conf. on Neutron Radiography, Osaka 1999

[mur]   M. MURPHY, F. JATUFF, P. GRIMM, R. SEILER, R. BROGLI, G. MEIER, H.-D. BERGER and R. CHAWLA, "Reactivity and neutron emission measurements of highly burnt PWR fuel rod samples", *Ann. Nucl. En.,* **33**(9) p.760 (2006)

[pie]   R. SCHUPPISSER, "Tomographiesystem. Short information for operating with the software", TN-369-05-001 PI Electronics AG

[sen]   "SENTINEL GAMMARAY PROJECTOR MODEL DELTA 880 Technical Manual", AEA TECHNOLOGY

[soo]   A. SOOD, R.A. FORSTER, B.J. ADAMS, M.C. WHITE, "Verification of the pulse height tally in MCNP 5", *Nucl. Instr. and Meth. in Phys. Res. B*, **213** p.167 (2004)

4. Gamma-Transmission Measurements and Results

Computerised tomography (CT), in essence, is the reconstruction of an internal image of an object from external observations. More precisely, it is the *"process of producing an image of a two-dimensional distribution (usually of some physical property) from estimates of its line integrals along a finite number of lines of known locations"* [her].

The aim of computerised tomography is to obtain information regarding the nature and position of materials inside a body. A distinction must be drawn between transmission and emission tomography. Transmission tomography, using the absorption of a physical entity (gamma-ray, X-ray, light, ultra-sound) crossing a body, is relevant for studying the internal morphology of an object, whilst emission tomography uses the observation of events that take place inside the body to characterise the object.

In the case of transmission tomography applied to nuclear fuels, this technique can be considered both as a non-destructive analysis method for fuel pin density investigations and as a way to determine within-pin spatial distribution maps of the linear attenuation coefficients. This technique has been applied previously to radioactive waste packages [tan-cam], but never, to the author's knowledge, in irradiated fuel rods as are investigated here.

Transmission tomography can be used in combination with emission tomography. In fact, the morphological map obtained can be used in the emission reconstruction process to increase the final image quality. Emission tomography, in the context of nuclear fuel, can be used to estimate the internal distribution of gamma-emitting radionuclides, e.g. the fission products ^{134}Cs, ^{137}Cs, and ^{154}Eu.

This chapter, apart from providing a general introduction to computerised tomography, presents the applied procedures and results obtained for the gamma-transmission tomography conducted on the burnt and fresh fuel samples previously investigated in the LWR-PROTEUS Phase II experiments. The first section gives a brief historical account of the principal developments in computerised tomography, Section 4.2 reviewing the main methods employed for the reconstruction of images from projections. The currently applied procedures for transmission tomography are presented in Section 4.3, while the principal results obtained in terms of reconstructed 2D images, e.g. of fuel density distributions, are reported in Section 4.4.

4.1 Principal Developments in Computerised Tomography

The problem of image reconstruction from projections has been studied over many years in a large number of scientific, medical and technical fields. Of all the applications, having the same mathematical and computational foundations, the one with the greatest impact worldwide has been in the field of diagnostic medicine, computerised tomography having in effect revolutionised radiology.

The mathematical basis for tomography was first developed by Radon in 1917 [rad]. However, it was not implemented until 1972, when the first CT scanner was invented, for which G. N. Hounsfield and Alan McCormack received the Nobel Prize [hou]. Since then, many advances have been made in scanner technology, as well as in the algorithms used for CT reconstruction.

The two major classes of reconstruction methods[10] can be characterised as analytical or iterative (see Fig. 4.1). In the first class, the filtered back projection (FBP) algorithm is an analytical method (transform method), based on the direct inversion of the Radon formula using Fourier transforms. Although developed as early as in the sixties, it remains the most widely used reconstruction method in CT up to the present day, because of its high speed and easy implementation. The method, due originally to Bracewell and Riddle [bra], was improved independently by Ramanchandran and Lakshminarayanan [ram], who are also responsible for the convolution back-projection algorithm, and by Herman [her].
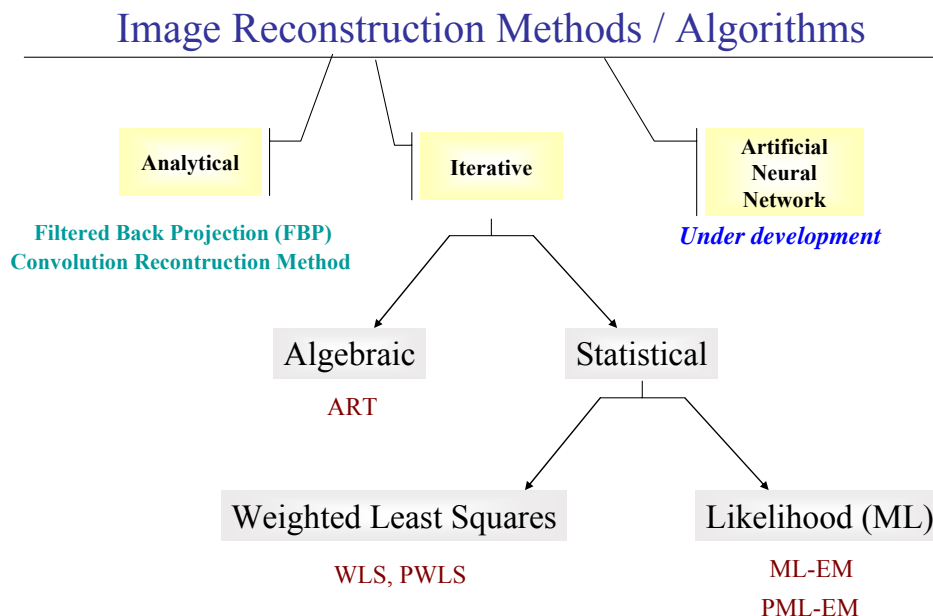
Fig. 4.1: Schematic tree representing the most common image reconstruction methods.

---

[10] This classification is not limited to transmission, but to all tomography.

The iterative approaches, can be based on the algebraic reconstruction technique (ART) [gor-her], or on statistical models. The latter algorithms take into account the statistical nature of the acquired projection data and incorporate the physical model into the reconstruction. A typical iterative method is the maximum likelihood approach. Statistical modelling for tomographic image reconstruction has been an active research field in recent years, and for this reason many different approaches have been developed. Rockmore and Macovski [roc] proposed, in 1976, an improvement for image reconstruction, in which radioactivity distributions were obtained using a maximum likelihood (ML) estimation, based on Poisson statistics. Shepp and Vardi [shep], and Lange and Carson [lan], independently proposed computing the maximum likelihood estimate of emission images by an expectation maximisation (EM) algorithm, again based on Poisson distributed random variables. Lange et al. [lan2] subsequently proposed a simple gradient algorithm for computing the maximum likelihood estimate. Sauer and Bouman [sau-sau2] developed an algorithm for finding the maximum a posterior estimate based on a Markov random field model. Fessler [fes2] proposed a weighted least square method based on an iterative coordinate descent algorithm. A fast in-plane scatter computation was proposed by Mumcuoglu et al. [mum], and the algorithm was optimised with a gradient descent method.

The well-studied maximum likelihood expectation maximisation (ML-EM) algorithms have been found to produce good results in various applications, but they require a large number of iterations, requiring intensive computer usage. One of the main reasons for this is that EM algorithms have a very slow convergence, and thus a large number of iterations may be required to achieve an acceptable reconstructed image. Several modifications have been suggested to accelerate the convergence of these algorithms using line search [lew] and vector extrapolation [raj] techniques. Of interest here, is the implementation of penalisation functions to regularise the ML (Penalised Maximum Likelihood [PML-EM]), for example the Space-Alternating Generalised EM (SAGE) algorithms for image reconstruction, by Fessler and Hero [fes-fes1].

Recognising the limitations of the ML-EM algorithm, researchers began considering maximum *a posteriori* (MAP) methods [lev]. These methods are based on the observation that neighbouring spatial elements generally have similar intensities. It has been observed that MAP methods tend to produce overly smooth estimates, which may obscure important boundaries. Daube-Witherspoon and Muehlleher [dau], and Kaufman [kau], developed reconstruction algorithms for obtaining least-squares (LS) estimates. The least-squares method is computationally efficient and guarantees non-negative estimates and converges rapidly. However, studies indicate that it produces less accurate estimates than the ML-EM algorithm, especially in the presence of severe noise. Other faster alternatives have been proposed to speed up the convergence. One popular and effective method for accelerating the reconstruction process involves the use of ordered subset (OS) [hud] or block-iterative

methods [byr]. The ML-EM method combined with the OS algorithm, and called the OS-EM method, can accelerate the ML-EM algorithm by up to 10 times or more. This method is widely used in commercial CT applications. The great interest in CT imaging has prompted the development of several ordered subset or block iterative algorithms with the intent of accelerating the iterative convergence process. In particular, Erdogan and Fessler developed a fast and monotonic algorithm by applying the ordered subset principle to paraboloidal surrogate functions (PSCA[11] method), and produced an approach very suitable for transmission tomography, the ordered subset transmission (OSTR) [erd-erd2].

In 1995, De Pierro published a clever modified EM algorithm [dep] for handling the regularised case, implementing the ordered subsets principle to accelerate the convergence (PL-DP). Another completely new and independent research area in image reconstruction is growing nowadays and is based on artificial neural networks. This approach is still not really optimised for this kind of problem and the results are not yet as satisfactory as for the commonly used tomographic methods. However, Craciunescu has recently applied the neural network model to irradiated nuclear fuel rods, comparing the results with the ML-EM method [cra].

4.2   Methods for Image Reconstruction

As already mentioned, in transmission tomography, beams of radiation are passed through the body being investigated, from various positions and at various angles. Each beam is detected on the side of the body opposite from the beam source, and its detected intensity is compared to its unattenuated intensity. These data are collected at various angles, from 0 to 360 degrees. The property that is computed in transmission tomography is the linear attenuation coefficient, at various points in the object's cross-section.

In our measurements, with an external radiation source of ^{60}Co being used (see Chapter 3 for a more detailed description of the external source and the source projector used), the beam implies two γ-rays with energies of 1.173 MeV and 1.332 MeV. The body, viz. the fuel pin, can be assumed to be a regular cylinder, as shown in Fig. 3.8. Considering the intensity of the emitted beam I_0, the intensity I of the detected beam is $I_o e^{-\mu l}$. We can define a function f, the *transmittance* of the object, as the logarithm of the ratio of these intensities, so that f is given by the linear transformation:

$$\ln(I_0 / I) = f(x, y) = \int_L \mu(x, y)dl \qquad (4.1)$$

where $\mu(x,y)$ is the absorption coefficient of the object at the point (x,y) and L is the line along which the beam travels.

---

[11] Paraboloidal Surrogate Coordinate Ascent

In the two-dimensional case, the line *L* can be represented uniquely by the parameters *r* and θ (see Fig 4.2), where θ measures the anti clockwise angle of the line from the *x*-axis, and *r* measures the distance of the line from the origin of the (*x,y*) plane. Thus, we can use Equation (4.1) to define a transform which maps the function $\mu(x,y)$ to a function *f(r,θ)*, where *f(r,θ)* is the line integral of $\mu(x,y)$ over the line defined by *r* and θ. This transform is known as the Radon[12] transform and denoted **Rf**. It corresponds closely to an "ideal" parallel-beam imaging system since, in such a system, each projection of the image corresponds to a slice through the radon transform at constant θ. The basic, idealised problem of tomography is to reconstruct an image from its Radon transform. Fortunately, the Radon transform, when properly defined, has a well-defined inverse [gar]. In order to invert the transform, one needs projection data spanning 180 degrees.
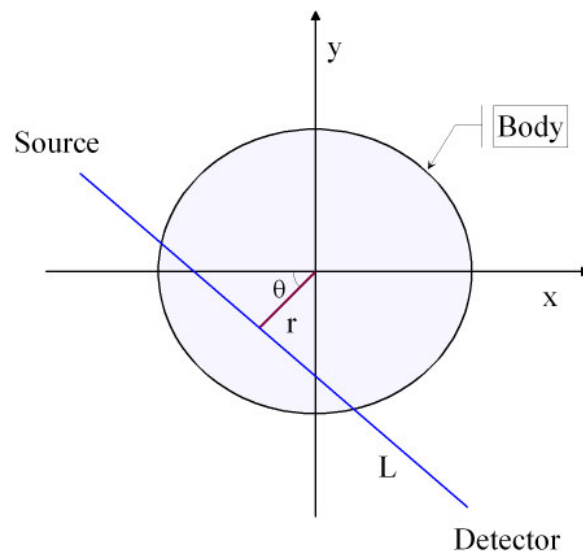
Fig. 4.2: Schematic sketch of a sample, with the variables *r* as measure of its lateral displacement and θ , that of its rotation.

4.2.1   Transform methods

Let us consider a source-sample-detector geometry in the <xy> plane, or better, using polar coordinates, in the plane *(r,θ)*, and the function *f(r,θ)* representative of the internal density distribution of the sample (null outside the sample boundaries). This function must satisfy the conditions of continuity and integrability, so that we can consider it our "picture function". In addition, *f(r,θ)* is our relative linear attenuation function. The Radon transform **Rf** is the collection of line integrals of the function *f* along all lines in the plane (in the literature defined as the "raysum"):

---

[12] Transmission computer tomography (TCT) has its basis in the formulation of the Radon theorem of 1917.

$$[Rf](r,\theta) = \int_{-\infty}^{\infty} f(\sqrt{r^2 + z^2}, \theta + arctg\frac{z}{r})dz \qquad (4.2)$$

The goal of the reconstruction is to estimate the value of the function at given points (no device being able to provide a direct measure), from a partial knowledge of its Radon transform. A set of raysums, computed on parallel lines for a fixed rotation angle θ, is called a projection.

For $r=0$, θ+arctg(z/r) = θ+π/2, the following equations are valid:

$$[Rf](r,\theta) = [Rf](-r,\theta + \pi) = [Rf](r,\theta + 2\pi)$$

$$[Rf](r,\theta) = 0 \text{ if } |r| \geq E$$

It is possible to calculate a function from the computation of all its line integrals, as shown by the following relationship (*Radon Inversion Formula*):

$$f(x,y) = -\frac{1}{2\pi^2}\lim_{\varepsilon \to 0}\int_{\varepsilon}^{\infty}\frac{1}{r}\int_{0}^{2\pi}\frac{\partial}{\partial l}[Rf](x\cdot\cos\theta + y\cdot\sin\theta + r,\theta)d\theta \cdot dr \qquad (4.3)$$

This implies that the distribution of relative linear attenuations in an infinitely thin slice is uniquely determined by the set of all line integrals. The important point is that for a function such as $[Rf](r,\theta)$ of $f(r,\theta)$, an operator R^{-1} exists such that $R^{-1}[Rf] = f(r,\theta)$, but complications arise in the practical application of the theorem because we only have a finite set of measurements. Further, inaccuracy in the measurement process affects the Radon Inversion Formula. The most common approach to solve the problem is called the *Filtered Back-Projection* method, and it consists of taking the inverse of the Radon transform. Briefly, the image is first back-projected and then filtered with a two-dimensional ramp filter[13].

Another approach is based on the so-called convolution method, based on the projection slice theorem, which links Fourier transforms to cross-sectional images of an object. The latter theorem states that the one-dimensional Fourier transform, with respect to r, of $f(r,\theta)$ is equal to the central slice at angle θ of the two-dimensional Fourier transform of f(x,y). The projection slice theorem implies that the Radon transform of the two-dimensional convolution of two functions is equal to the one-dimensional convolution of their Radon transforms. Using the property of symmetry of convolution, a closed formula for the inverse Radon transform can be found. This means first carrying

---

[13] Several filter options exist, i.e. Gaussian, Ram-Lak, Shepp-Logan, hamming, cosine, etc

out a one-dimensional high-pass filtering of each projection using a ramp filter and then a back projection of the outputs of the filter [her].

The filtered back-projection (FBP) method has been applied extensively in the present research because of its fast implementation and its realistic reconstruction that make it a very efficient tool for producing a "first guess" of the image, for use as input to more sophisticated iterative methods.

As indicated in Section 4.1, there is a wide range of reconstruction techniques which have been proposed over the years, and one can clearly not describe each of them in detail. In the context of the present research, several different iterative techniques have been tested and used and, accordingly, following a general description of statistical methods, an explanation is provided of the best performing of these techniques.

4.2.2   Statistical iterative methods

Measurements in an application limited to single photon detection can be modelled appropriately as Poisson random variables but, considering the presence of background counts and Compton scattering contamination, etc., the data may be no longer Poisson. However, in single photon detection problems, more than in positron emission tomography (PET) systems, it is still reasonable to assume the following Poisson model [erd]:

$$y_i \sim Poisson \left\{ b_i e^{-[\overline{A}\mu]_i} + r_i \right\} \quad i = 1,....,k \tag{4.4}$$

where r_i is the mean value of background events, b_i is the blank scan count[14], y_i the measured counts, k the number of measured γ-rays and

$$[\overline{A}\mu]_i = \sum_{j=1}^{N} a_{ij}\mu_j \quad \text{with} \quad j = 1,....,N \quad (N: \text{number of pixels}) \tag{4.5}$$

represents the line integral of the attenuation map μ, and $\overline{A}$ is the $k*N$ system matrix.

For the specific case of transmission tomography, the Poisson-model assumption described above can be considered appropriate. In contrast, for emission tomography, the Poisson nature of the measured data cannot be guaranteed after various corrections have been applied (radioactive decay, branching ratio correction, cladding and filter attenuation compensation, etc.), since these affect the frequency distribution [erd]. To overcome these problems in the emission tomography, the data have been processed without corrections, as described in Chapter 5. In that way, the Poisson-model assumption remains acceptable.

---

[14] The blank scan is a measurement recorded when the sample is not between the external source and the collimator slit, such that the detector can measure the direct unattenuated incoming radiation.

Irrespective of the type of tomography or of the nature of the measured data (Poisson, Gaussian), statistical methods base the solution of the ill-conditioned problem on the development of a cost function (or object function) $\Phi(f)$, which has to be maximised. A simple scheme for this process is shown in Fig. 4.3. How the objective function is built depends on the specific approach adopted.
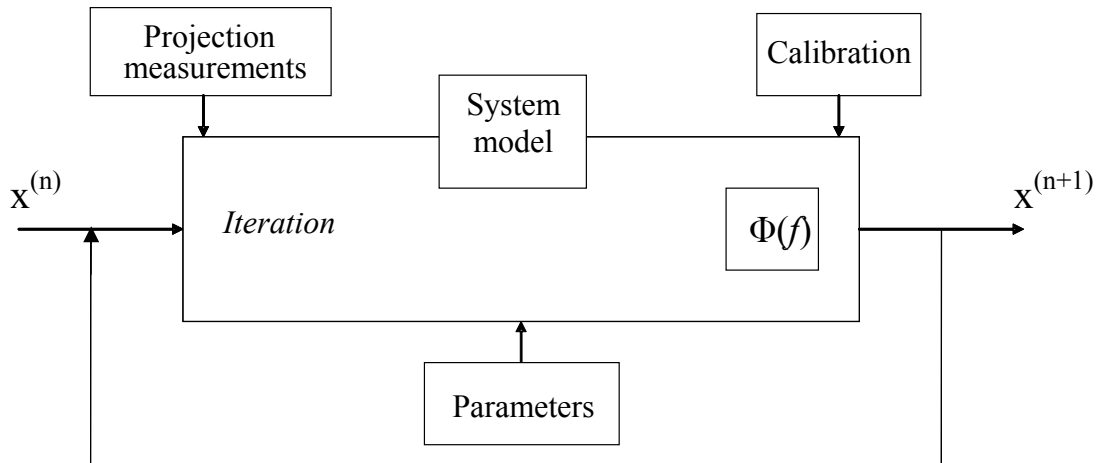

Fig. 4.3: Schematic representation of an iterative method for tomography.

The statistical iterative techniques tested in the framework of this thesis are the following:

- Maximum-Likelihood Expectation-Maximisation (ML-EM)
- Ordered Subset Expectation Maximisation (OSEM) [for emission]
- Ordered Subset Transmission (OSTR) [for transmission]
- Penalised Maximum-Likelihood Expectation-Maximisation (PML-EM)
    - Space-Alternating Generalised EM (SAGE)
    - Ordered Subset De Pierro (OSDP)
    - Paraboloidal Surrogates Coordinate Ascent (PSCA)
- Penalised Weighted Least Square (PWLS)

In the following, an overview of the most important of these methods is given.

4.2.2.1   *Maximum-Likelihood Expectation-Maximisation*

Iterative image reconstruction algorithms have the potential to produce low-noise images. They are essentially based on maximum-likelihood expectation-maximisation (ML-EM) techniques [shep-lan], which assume Poisson-distributed measurements. Such an algorithm consists of a series of forward and backward projections starting from the initial estimate (usually a FBP image) until an acceptable level of accuracy of the image is achieved.

Let x_k denote the kth projection element, K the total number of projection elements and $\vec{x}$ the corresponding vector (it is always possible to arrange the elements of all the projections in a single vector). Let f_i be the linear attenuation in the object (in the case of transmission) or the unknown distribution of the γ-source within the object (in the case of emission tomography), after discretising the object area into a number of pixels, indexed by i. The mathematical relationship between x_k and f_i can be described using a projection operator $\mathcal{W}_k$, which essentially models the transport of the photons of interest through the different materials of the system in a geometry corresponding to the kth measurement configuration:

$$\mathcal{W}_k f_i \cong x_k \tag{4.6}$$

Reconstructing f_i from the measured projection elements reverts to inverting this operator. With a vector formulation we have:

$$W\vec{f} \cong \vec{x} \tag{4.7}$$

$\vec{f}$ is the vector of parameters f_i and W is the "system matrix" with elements w_{ik}.

The likelihood function $L(\vec{f})$ is a probability distribution and is given by

$$L(\vec{f}) = P(X \mid f) = \prod_i \prod_k e^{-w_{ik} f_i} \cdot \frac{(w_{ik} f_i)^{X_k}}{X_k!} \tag{4.8}$$

ML is based on minimising the cost function, the natural logarithm of the likelihood

$$\ln(P(X \mid f)) = \sum_i \sum_j [(-w_{ik} f_i) + X_k \ln(w_{ik} f_i) - \ln(X_k!)] \tag{4.9}$$

The algorithm is based on two different steps. The first, the E-step, consists of forming a conditional expectation

$$E(X_k \mid Y_i, f^{(n)}) = \frac{w_{ij} f_j^{(n)} Y_i}{\sum_k w_{ik} f_k^{(n)}} \tag{4.10}$$

The second step, M-step, is a maximisation search:

$$\frac{\partial}{\partial f_i} E(\ln(P(X \mid f)) \mid Y, f^{(n)}) = -\sum_k w_{ik} + \sum_k E(X_{ik} \mid Y_i, f^{(n)}) f_i^{-1}$$
(4.11)

The maximum found is chosen as the next iterate:

$$f_j^{(n+1)} = \frac{\sum_i E(X_k \mid Y_i, f^{(n)})}{\sum_i w_{ij}} = \frac{f_i^{(n)}}{\sum_k w_{ki}} \sum_k \cdot \frac{w_{ik} Y}{\sum_j w_{kj} f_j^{(n)}}$$
(4.12)

The main drawback of the basic maximum-likelihood expectation-maximisation algorithm is its slow convergence. Consequently, noise is usually strongly amplified before convergence has been reached.

4.2.2.2 *Penalised Maximum-Likelihood Expectation-Maximisation*

Objective functions based solely on the measurement statistics perform poorly due to the ill-conditioned nature of tomographic reconstruction. Unregularised methods produce increasingly noisy images with iteration. To overcome this problem, several regularisation methods have been investigated, that impose smoothness constraints on the image estimate. This means that a penalty term can be included in the optimisation process, i.e. in the objective function. This penalty, or regularisation, term (accounting for *a priori* information such as smoothness) may be added to the function to be maximised, and this is the specificity of the penalised maximum-likelihood expectation-maximisation techniques [fes], as well as of all the so-called "penalised", or "Bayesian", methods.

The new objective function to be maximised is the difference of the log-likelihood and the penalty function, the trade-off between the two being controlled by a parameter β [fes]:

$$\Phi(f) = \ln L(\vec{f}) - \beta R(\vec{f})$$
(4.13)

This technique introduces an additional unknown parameter β, which "tunes" the importance given to the penalty term. This is a regularisation parameter which controls the trade-off between resolution and noise. It must be either estimated subjectively beforehand, or calculated via an additional iterative process to be developed [fes5]. Moreover, it may be sometimes difficult to find a mathematical penalty formulation that expresses all the constraints one wishes to account for (smoothness in the central region of the pin but not at the edge, radial increase, etc.). On the other hand, the use of well-chosen penalties may improve the "ill-conditioned state" of the minimisation problem.

Fessler and Hero proposed to use a quadratic smoothness penalty in their Space-Alternating Generalised EM (SAGE-3) implementation of PML-EM [fes]. This is the fastest monotonic algorithm known [fes3]. It is based on a sequential update of the parameters using a sequence of small "hidden" data spaces, rather than simultaneously using one large complete data space.

The penalty function used in SAGE is a quadratic smoothness function, viz.:

$$R(\vec{f}) = \frac{1}{2}\sum_i\sum_j n_{ij}\frac{1}{2}(f_i - f_j)^2 \qquad (4.14)$$

where n_i are the neighbours of pixel i and consist of the 8 pixels adjacent to pixel i, n_{ij} =1 for horizontal and vertical neighbours and n_{ij} =1/$\sqrt{2}$ for diagonal neighbours. In this case, one can choose the order of neighbourhood as desired.

A very interesting improvement of the penalised-likelihood image reconstruction technique is the Paraboloidal-Surrogates Coordinate Ascent (PSCA) method [erd2]. In brief, it uses a global surrogate function for the original objective function, which is not separable but has a simple quadratic form. Effectively, the method is based on finding 1-D parabolic functions that are tangent to, and lie above, the terms in the log likelihood. It has several variations depending how one chooses the parabola curvatures and, for its application to nuclear fuel rods, a "fast pre-computed" curvature [erd2], usually monotonic, is recommended. This algorithm has been extensively applied in the present work, for both transmission and emission, of course with different parameters.

Several different kinds of penalty function can be adopted. For our particular case (fuel pins), a very well performing penalty function has been found to be the Huber function, because it preserves the smoothing at the edge of the pin. It reduces noise without any significant loss of contrast, giving accurate images. The prior function, used by Fessler in image restoration [fes4], has a shape similar to that of log cosh*(t)*. The Huber function [hub], a parabola in the vicinity of zero and increasing linearly above a given level $|t| > \delta$, has the following form:

$$H(t) = \begin{cases} t^2/2 & |t| \leq \delta \\ \delta|t| - \delta^2/2 & |t| > \delta \end{cases} \qquad (4.15)$$

The Huber function penalises the differences between neighbouring pixel values. In the range [-δ, δ], it does so at an increasing rate as the difference in value increases, without strongly penalising the larger differences of $|t| > \delta$, which usually occur at the edge of two different regions of the image. If δ is higher than the maximum difference, the Huber function is just a pure quadratic penalty.

This estimator is so satisfactory that it has been recommended for almost all situations. Very rarely has it been found to be inferior to some other function. However, from time to time, difficulties are encountered, which may be due to the lack of stability in the gradient values of the function because of its discontinuous second derivative.

The drawback of the Penalised ML-EM methods is the difficulty in finding optimal values of the two parameters δ (which sets the resolution properties of the method) and, as explained earlier, β. The iteration number is another parameter which needs to be chosen properly for ensuring the quality of the final image. In fact, early stopping of the iteration process is problematic because some features of the image may converge slowly. On the other hand, there may be noise build-up with an increased number of iterations.

4.2.2.3   *Ordered Subset Algorithms*

An accelerated version of the ML-EM, but just for the emission case, is the Ordered Subset Expectation Maximisation (OSEM) [hud], which is widely in use today in emission computer tomography, especially in the medical field.

Ordered Subset methods group projection data into an ordered sequence of subsets. An iteration of OSEM is defined as a single pass through all the subsets, the current estimate being used to initialise the application of EM to the data in each subset. This method is actually not regularised, but there is a modified version for handling the regularised case, which is the Ordered Subset version of the De Pierro (OSDP) modified EM algorithm [dep]. The convergence of these methods is not always achieved.

The Ordered Subset principle has been applied by Erdogan in the Separate Paraboloidal Surrogates (SPS) method for transmission tomography to accelerate convergence. This approach is called Ordered Subset Transmission (OSTR) [erd]. SPS is a simultaneous update algorithm which converges much faster than the transmission EM algorithm.

4.2.2.4 *Penalised Weighted Least Square (PWLS)*

Another widely used iterative method, implemented by Fessler, is the Penalised Weighted Least Square (PWLS) algorithm, which employs a quadratic smoothness penalty [fes2]. The simplest regularised method uses the penalised least-squares cost function:

$$\Phi(x) = \frac{1}{2}\|y - Wx\|^2 + \beta R(x) \tag{4.16}$$

where the roughness penalty R(x) has the form:

$$R(x) = \frac{1}{2}\sum_i \sum_j w_{jk}\psi(x_j - x_k) \tag{4.17}$$

where ψ is a convex cost function. For a "1st-order neighbourhood", w_{ij} is 1 for horizontal and diagonal neighbours and zero otherwise, and for a "2nd-order neighbourhood" w_{ij} is $1/\sqrt{2}$.

A suitable PWLS cost function is:

$$\psi(x) = \frac{1}{2}(y - Gx)diag\{u_i\}(y - Gx) + \beta R(x) \tag{4.18}$$

where the u_i are appropriate weights (inverse of variances).

4.3 Data Collection and Processing for Tomography

This section gives a detailed description of the various phases of the current development of tomographic images through γ-transmission. The section is structured in the following way:

- γ-spectrometry acquisition (projections collection)

- Photo-peak treatment

- Tomography planning

- Corrections to the data

- Sinogram development

In Section 4.4, the results obtained from transmission tomography are presented in the context of the two main goals: density determination and attenuation maps evaluation.

4.3.1   Projections acquisition with high resolution gamma-spectrometry

As described in Chapter 3, high resolution γ-spectrometry has been implemented to investigate burnt and fresh fuel pins. Photons emitted by the external ^{60}Co source, together with photons from fission products (gamma emitters) present in the burnt samples, were recorded by an HPGe detector, for different lateral positions r and angular positions θ of the sample. Each recorded spectrum was analyzed in order to derive, for each measurement step, the count rate corresponding to the different γ-lines of interest.

It was found to be possible to acquire transmission and emission projections in the same measurement session. The acquisition procedure as followed during the experiment is detailed below:

- At the beginning, the fuel pins are inside the flask/sample changer, which is fixed to the tomographic station located in the fuel laboratory. All the equipment and the detector have been tested previously [car].

- The station is operated using a standard procedure [car2]. The pin is loaded into the V-channel inside the station, using the flask/sample changer control unit (see Fig. 3.17) and then clamped employing the "Tomographic Station Control Unit" (TSCU). The TSCU program, accessible from the PC, can be operated in manual mode for positioning (moving the clamping system to the loading position) and pin clamping.

- The external source is injected through the shielding wall of the station opposite to the collimator and detector, using the gamma-projector with a remote control cable. Fig. 4.4 (a) gives a detailed view of this system.

- The amplifier (DSPec+) parameters [dsp] are set using the GammaVision software [gam], in order to optimise the pulse shape for the spectra acquisition for each sample [kno].

- The tomographic measurements can be programmed with the TSCU operating in "auto mode", setting the number of lateral steps, lateral starting position, end position, step width, angular steps and "single" measurement time.

- Once the program is running in "auto mode", the spectra are acquired and saved on the hard disk for each position automatically, because of the interconnection between the TSCU and the GammaVision software.
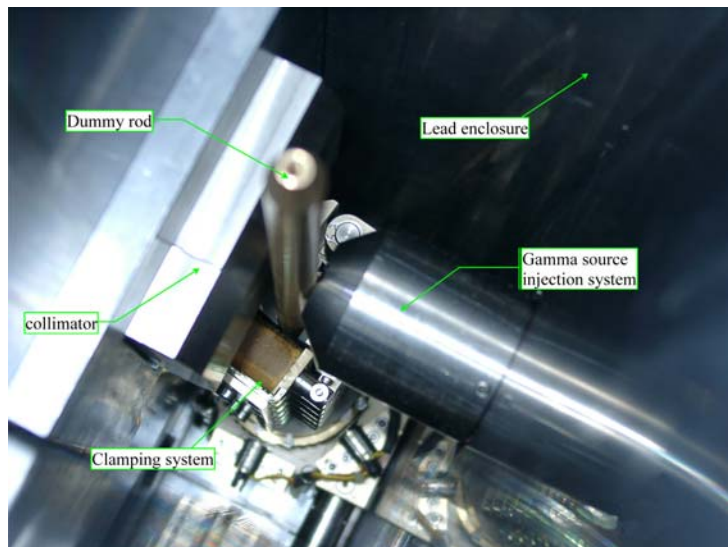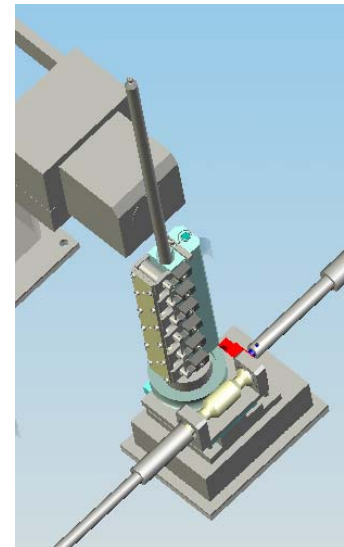
(a)   (b)

Fig. 4.4: (a) Detailed view of the inside of the measurement station. It is possible to distinguish the gamma source injection system, the rod (dummy), the collimator, and the clamping system. This picture provides useful indication of the distance between the pin and the external gamma source, as also between the pin and the collimator. (b) Details of the pin-collimator clamping system, in a 3D technical drawing.

4.3.2   Photo-peak treatment methodology

GammaVision is software that can be used in both data acquisition and data processing modes. Currently, it has been employed for spectrum acquisition but not for spectrum analysis, since the high counts-rates rendered the peaks non-Gaussian and this led to difficulties with the peak fitting algorithms (see Appendix A for more details). The analysis approach used instead is based on a three-window analysis, such that a main window, "region of interest" (*ROI*), is first chosen for the photopeak of interest (both peaks of the ^{60}Co, in the case of transmission). The ROI limits were extended down the sides of the peak to the background continuum level, whilst ensuring that the effect of neighbouring peaks was minimised. The gross area was then calculated and corrected for live time, in order to estimate the count of primary photons. Because some peaks sit on an obviously non-linear background (such as the case of 1.173 MeV ^{60}Co peak affected by the 1.167 MeV peak coming from the ^{134}Cs), a precise background continuum correction was necessary. The method of normalisation of the continuum is illustrated in Fig. 4.5, where *Cl* and *Cr* illustrate the two continua windows, at the low energy and high energy of the peak, respectively.

The net count-rate in the photo peak is given by the following expression:

$$NetArea = ROI - \left[\frac{(Cl + Cr)}{2(n + m)} k \right] \qquad (4.19)$$

where *n*, *m* and *k* are the channels numbers of *Cl*, *Cr* and *ROI*, respectively. *Cl, Cr* and *ROI* are gross areas. The choice of non-contiguous background continua (Cl and Cr) is basically necessary for both transmission and emission tomography because of the presence of numerous interfering peaks that affect the spectra. The peak treatment, however, is more complex for emission tomography than for transmission, and this will be explained separately in Chapter 5.

A C++ program was written to automate the above analysis, because of the large number of spectra to be processed.
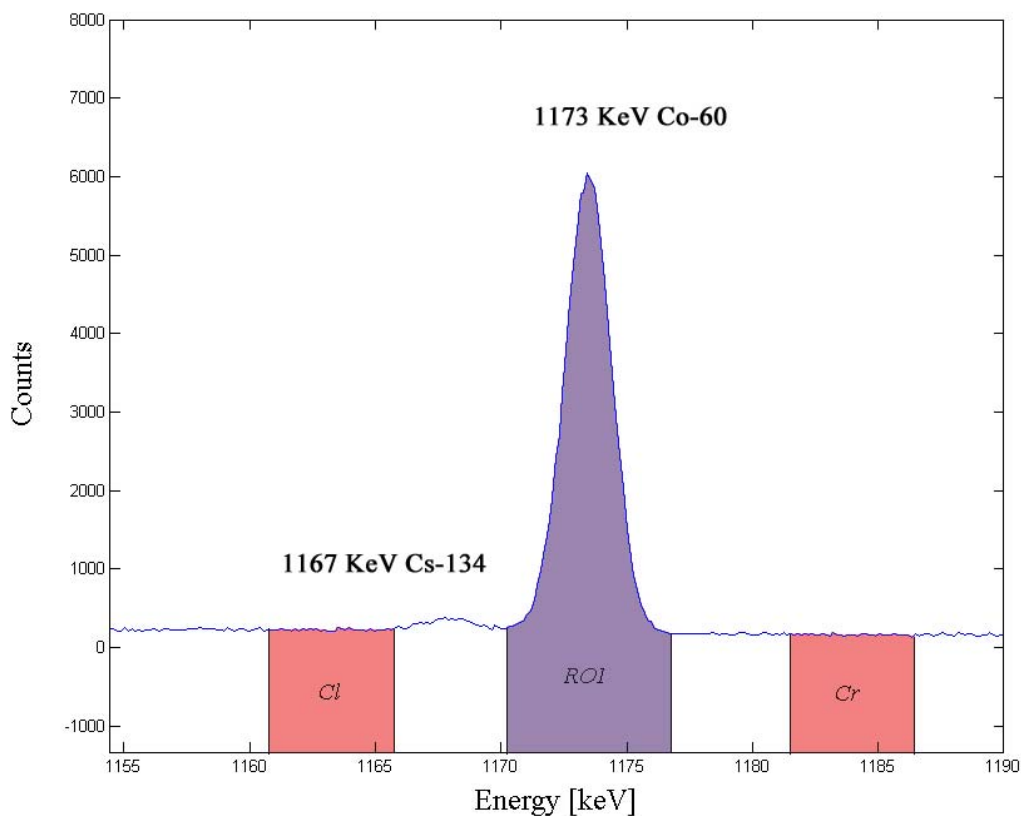
Fig. 4.5: Illustrative portion of a gamma spectrum, with the three windows (*Cl, Cr* and *ROI*) used for net counts determination. The 1173 keV ^{60}Co peak is marked, together with the 1167 keV peak of ^{134}Cs on its low-energy side.

In Fig. 4.6, two acquired spectra are shown, for the fresh sample S#0 (upper part) and sample S#1 (lower). Zooms on the two photopeaks of the external ^{60}Co source, as used for the transmission tomography, are provided in each case.
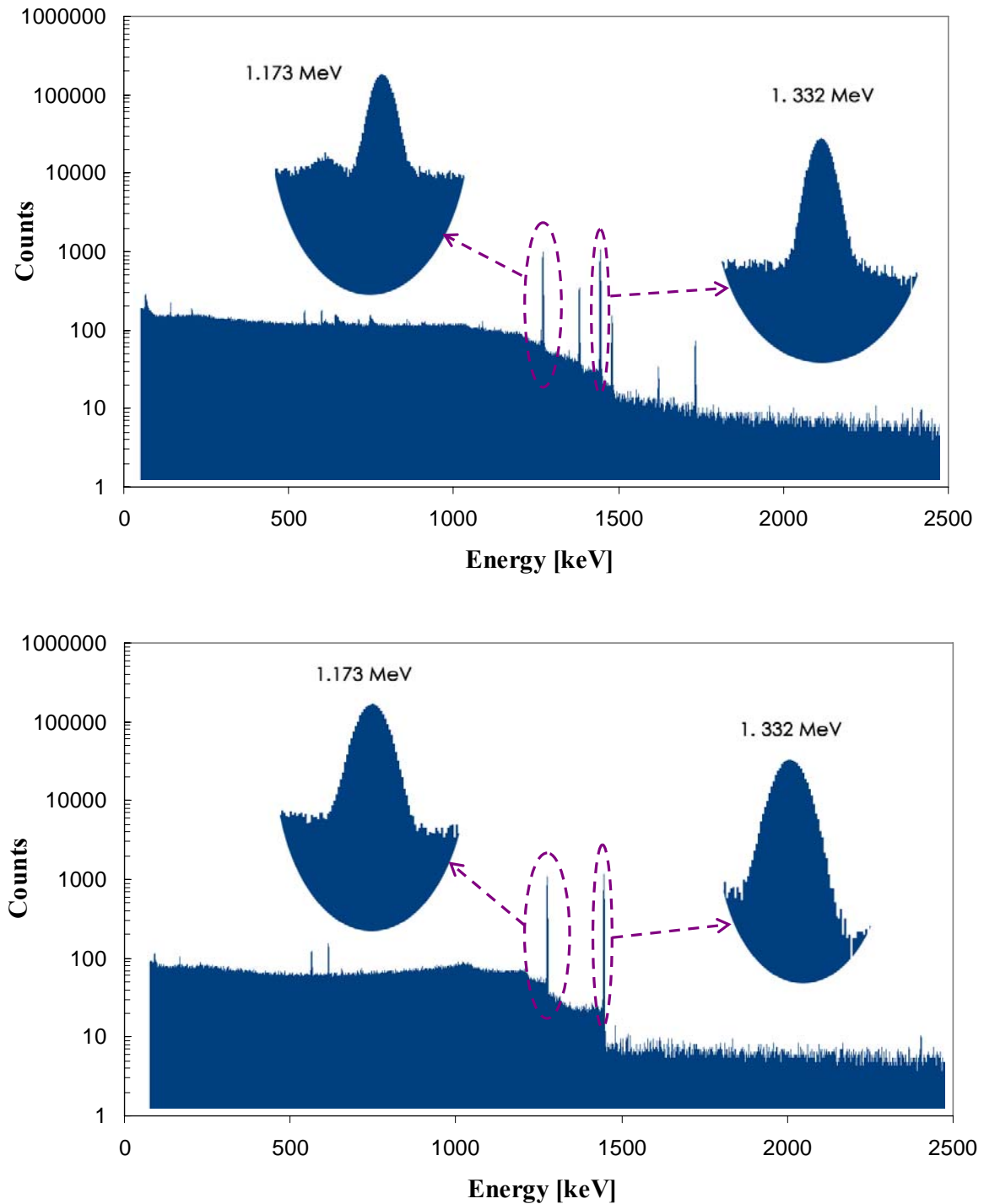
Fig 4.6: In the upper part of the figure is a gamma spectrum acquired from the fresh fuel sample S#0, in the lower part that for the spent fuel sample S#3. In both the cases, zooms are shown for the two photopeaks of the external ^{60}Co source used for the transmission tomography.

4.3.3 Tomography planning

The intensities in counts/s have been measured for the four spent fuel rods (see Section 3.4) and one fresh pin, using the measurement plan shown in Table 4.1. Transmission tomography was employed in each case by measuring the relative intensities of the 1.173 and 1.332 MeV gamma rays, produced by the ^{60}Co. Each session of tomographic investigations comprised a total number of measurements [k x m], where k is the number of lateral displacements of the pin with respect to the collimator slit and m the number of rotations of the pin. In each case, the lateral step size used was 0.02 mm and the angular interval 45°. Table 4.1 includes details concerning the main sample characteristics, the lateral and angular steps, the acquisition time of each single measurement, and the mean dead time.

Table 4.1: Measurement plan used for the tomographic acquisition for the four spent fuel pins and the fresh pin.

Sample Designation	Fuel Type	Burnup CASMO-4 Estimation [GWd/t]	Lateral steps "k"	Angular Steps "m"	Acquisition time [s]	Dead Time [%]
S#0	fresh	-	70	4	600	~8.5
S#1	spent	52	70	8	1200	~11
S#2	spent	71	70	8	550	~13
S#3	spent	91	66	8	500	~16
S#4	spent	126	70	8	600	~35

4.3.4 Projection data corrections

Before starting with the application of tomographic reconstruction algorithms, some operations are necessary to generate the final sinograms from the acquired projections. The sinogram is a way of storing the data in a suitable way for image reconstruction. A single projection view, corresponding to parallel lines relative to a specific angle, is stored in the sinogram as a single column. All columns in the sinogram are projection views at different angles (see Fig. 4.9). In practice, this means a change in domain from a Cartesian <xy> system to a polar <rθ> system. After the acquisition process, an

accurate correction on each angular projection data set is necessary. The reason is that the pin, once clamped in the V-channel by the remote handling system, is not perfectly parallel to the collimator slit, but exhibits a small angular deviation due to mechanical tolerances. This deviation, during a rotation of the pin, provokes a small precession. The consequence is a mis-alignment between the angular projections acquired at different angles. Further, because of irregularities in the pin surface and some uncertainty about the segment position within the overcladding, this problem cannot be solved purely mechanically. An operation of numerical re-alignment needed to be performed for each angular projection dataset and for each pin. The transmission tomography data have been used as an indicator of the relative position of the pin with respect to the collimator slit, allowing a quantification of the misalignment.

The data sets were corrected accordingly, and these corrections were also applied afterwards to the corresponding emission tomography projections in order to ensure an objective correction preserving the azimuthal information. Fig. 4.7 provides an illustrative example of the impact of these corrections on the projections. On the left are shown the intensities of the 1.332 MeV ^{60}Co γ-ray, recorded at 70 different lateral positions (in steps of 0.02 mm) and for 8 different angles (in steps of 45°), for the sample S#1, before the application of the correction. The right hand side of Fig. 4.7 shows the counts/s after the alignment. In the latter plot are also indicated the dimensions of the fuel pellet, cladding and over-cladding.
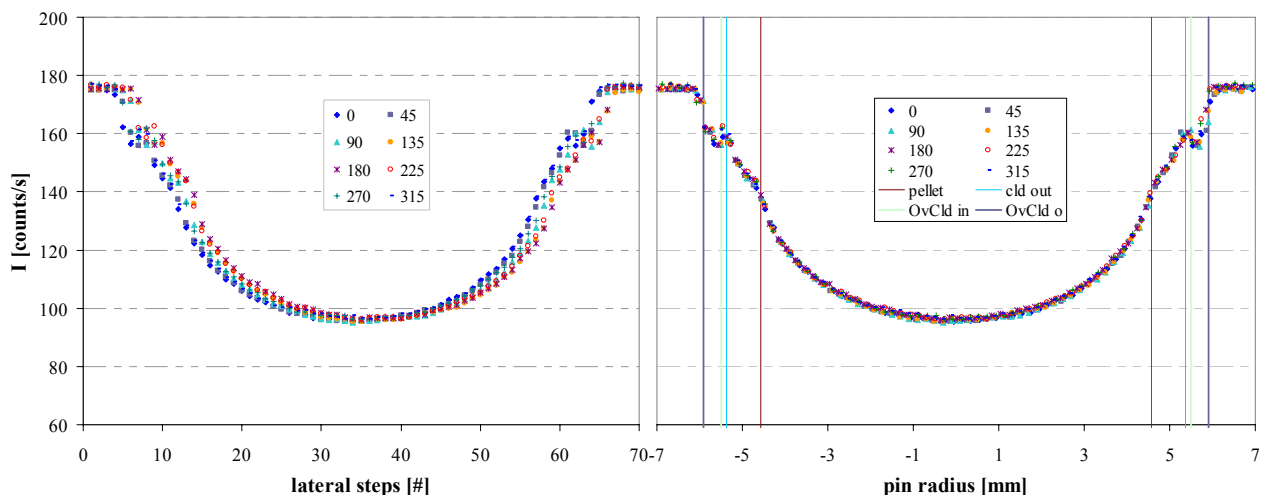
Fig. 4.7: Intensities of the 1.332 MeV ^{60}Co γ-ray, recorded at 70 different lateral positions (in steps of 0.02 mm) and for 8 different angles (in steps of 45°), through the sample S#1, before application of the alignment correction (left) and after the correction (right).

4.3.5 Reduction of the problem in 2D and sinogram preparation

Another correction, which must be applied to the measured data before the generation of the sinograms, is described in this section.

Transmission tomography reconstruction techniques are based on the assumption that the phenomena take place in a two-dimensional system, whilst in reality the projections collected belong to a three-dimensional system. As a consequence, an inconsistency between a cross-section area traversed by the photon beam in the real system and that considered in the analytical solution[15] results in a discrepancy in the attenuation effect. In other words, given a point source, or better a source of 2x1 mm size as it is in reality, positioned at ~1 mm from the sample surface, the area crossed by the photon beam is a trapezoid, defined by the intersection of the fuel pin and the solid angle from the source to the detector end of the collimator (20 mm high). In Fig. 4.8, the technical drawing of the V-channel, pin and collimator is shown together with a γ-ray beam crossing the pin. On the left of the picture is shown the trapezoidal cross-section area *T,* produced by the 2x1 mm source, with the angle of departure exaggerated for illustration. Contrary to reality, in the analytical solution, the basic assumption is that the source is uniformly distributed along a vertical line, parallel to the pin. It is an infinite line along the z axis. As a consequence, the cross-section area of this beam for such a source is a finite trapezoid *S,* different in shape from *T*, as shown in Fig. 4.8 (right), again with the angle exaggerated, and limited by the vertical dimensions of both ends of the collimator slit (20 mm) and the intercept with the fuel pin.
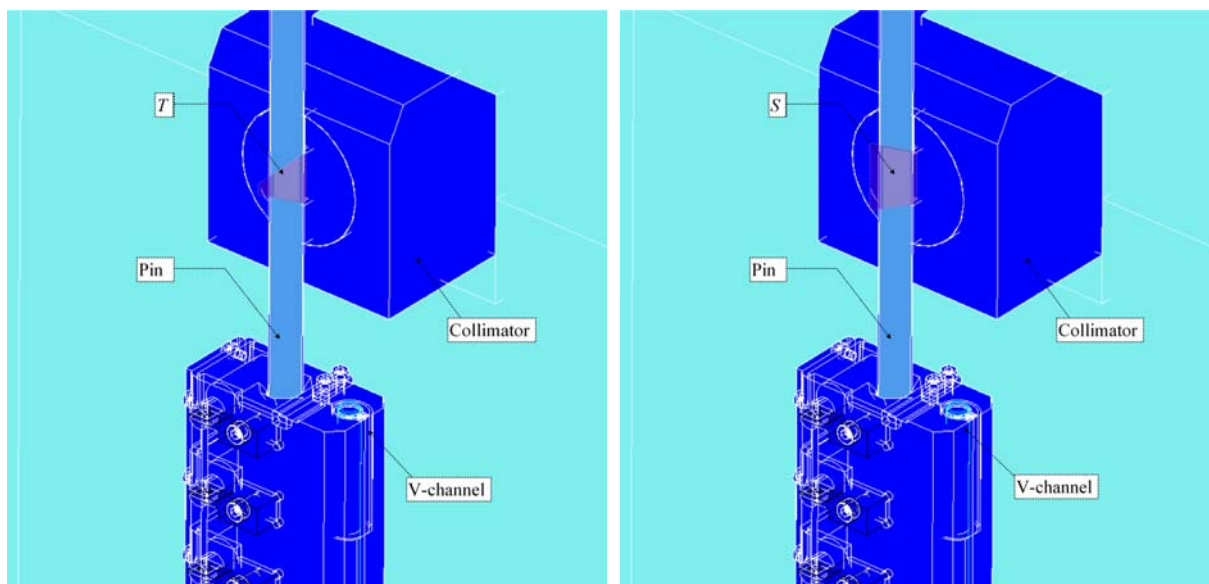
Fig. 4.8: Technical drawing of the V-channel, pin and collimator, shown together with a γ-ray beam crossing the pin. On the left of the picture, one sees the cross-section area *T* produced by the 2x1 mm source, on the right the cross-section area *S* produced by an infinite line source.

---

[15] In this case the word "analytical" is applied to all the reconstruction techniques, analytical or iterative.

In practice, currently, the difference in mean path length for the two models is very small, and that between the transmissions equally so. The measured data have been corrected by < 1% for all the projections. Of course, the correction is applied only in the transmission case (in the case of emission, there is no assumption of infinite source, the location of the γ-source being our unknown).

Eight basic sets of angular projections m have been used to build the sinograms in most of the cases, each projection consisting of 60 values k, representing the counts per second (I) acquired from a photon beam traversing a chord of the sample. Actually, just eight sets of angular projections are not enough to ensure a sufficient quality to the final image. For this reason, an angular interpolation was made, splitting each original angular projection into another eight, such that a total number of $m=64$ projections could be used in the reconstruction algorithm. This value yields a better image quality. The sinogram values between one main angular projection and the following one were averaged to avoid steps in the final sinogram. An example of a sinogram is shown in Fig. 4.9, for a fresh fuel pin, where this step effect has been consistently removed. On the left axis, r, of Fig. 4.9 (a), we have the 60 lateral positions, and on the horizontal axis, θ, of the same figure, the 64 angular projections. In Fig. 4.9 (b), a three-dimensional view of the sinogram is shown, where a light presence of steps is easier to observe.

The slit width of the collimator is 0.2 mm, which allowed the obtaining of an image of 64x64 pixels. Together with the main sinogram containing the modulated intensities I, another complementary sinogram must be built, with the same size as the other, but containing the counts/s acquired when the sample is not between source and collimator slit, i.e. corresponding to the direct beam (I_o).

(a)   (b)
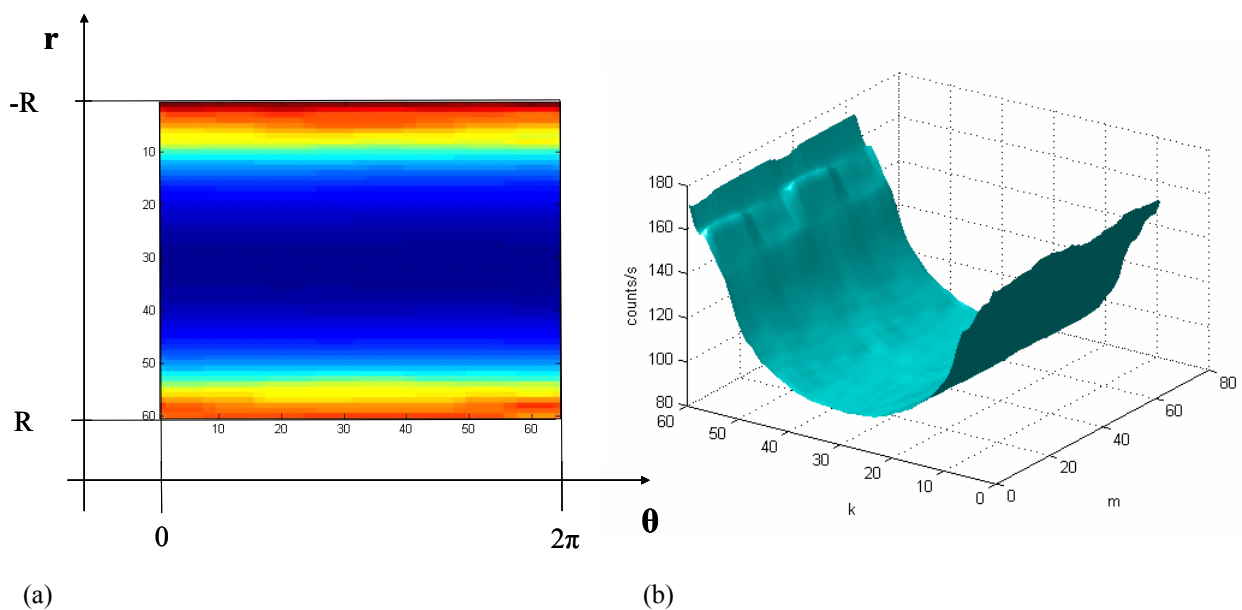
Fig. 4.9: Illustration of a sinogram (a) in $<r,\theta>$ plane, and (b) as 3D image (b). The variables r and θ are described in Fig. 4.2

4.4   Reconstruction of 2D Cross-Sectional Image and Results

The implementation of the computerised tomography was made with the Aspire 3.0 code, developed by J. Fessler at the University of Michigan [fes3]. This is a sparse iterative reconstruction library, for image reconstruction, which implements several reconstruction techniques, analytical and iterative, and allows the use of different penalties and resolution properties. The version used was that for running on a Linux platform. The format of the input data and the output images is the AVS standard *".fld"*. The preparation of the data, the format conversion, and the visualisation of the data was done using Matlab [mat]. The visualisation of reconstructed images was achieved using the AVS/Express 7.0 software [avs].

4.4.1   Attenuation maps

Within-pin linear attenuation coefficient distributions have been derived using the reconstruction methods described in the above sections. As discussed earlier, intensities of both the 1.173 and 1.332 MeV ^{60}Co gamma rays could be used. In fact, the 1.332 MeV γ-ray has been preferred due to its slightly higher energy and better statistics, and it is for this γ-peak that all results are shown from now on.

The filtered back-projection method was used to generate the first-guess image. The penalised likelihood expectation maximisation with paraboloidal-surrogates coordinate ascent (PSCA) algorithm [erd2], for transmission tomography, was used to iterate and generate the final linear attenuation ($\mu(l)$) maps. All the images generated are 64x64 pixels, where each pixel width is 0.2 mm. In Fig. 4.10 is shown the within-pin distribution of the $\mu(l)$ [cm^{-1}] values derived for sample S#1. On the left is the FBP image, and on the right the PSCA-PML image. The FBP image is a noisy but realistic image. The noise was not immediately suppressed to avoid alteration of the physical properties of the object (especially at the edge of the pin). The noise treatment is carried out using statistical methods. Using the PSCA algorithm, the noise is suppressed during the iterative process without compromising the validity of the reconstruction. Observing the PSCA-PML image, the difference in the attenuation values between the Zircaloy material and the UO$_2$ fuel matrix is evident. From this image, it is not possible to distinguish the air gap between the cladding and the over-cladding. This is more visible with a higher resolution of the image and after converting the $\mu(l)$ to density, as shown in the next section.
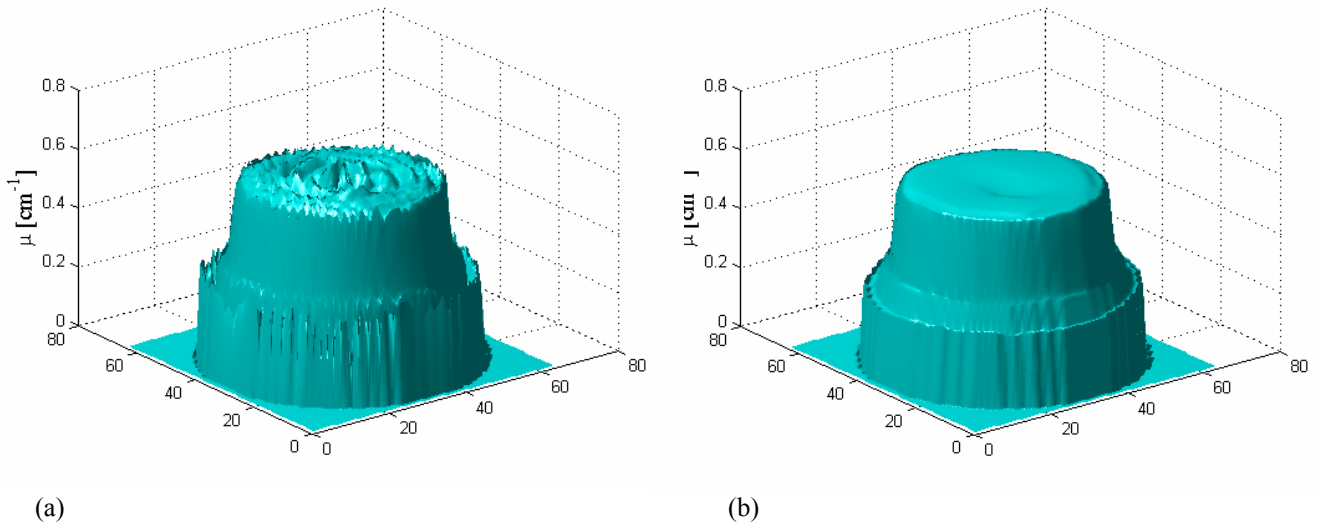
(a)   (b)

Fig. 4.10: The linear attenuation $\mu(l)$ [cm^{-1}] within-pin distribution (64x64 pixels) for sample S#1. On the left the FBP image, and on the right the PSCA-PML image.

The most important goal of the attenuation map, however, is the investigation of inhomogeneity in the physical structure of the fuel matrix, in order to use these maps to apply appropriate attenuation corrections in the emission tomography. In Fig. 4.11, the PSCA-PML images illustrate the linear attenuation reconstructions for (a) the fresh sample S#0, and (b) to (d) for the burnt samples S#2, S#3 and S#4, respectively. These reconstructions have been obtained using an edge-preserving Huber penalty function with a "2nd-order neighbourhood", with $\delta = 0.0008$/mm, and $\beta=9$, performing a total number of 30 iterations.

A global plot of the linear attenuation for all the samples is shown in Fig. 4.12. The plots refer to the vertical cut view at the centre of the pin. The dependence of $\mu(l)$ on burnup is evident from this plot: as the burnup increases, $\mu(l)$ decreases.

The uncertainty bars on the plot, for the two distinct regions, centre and periphery, are derived from the results of a sensitivity study (see Section 4.4.4). In order to use these distributions as attenuation maps for emission tomography, they must be scaled to the energy of the emitted gamma-ray.
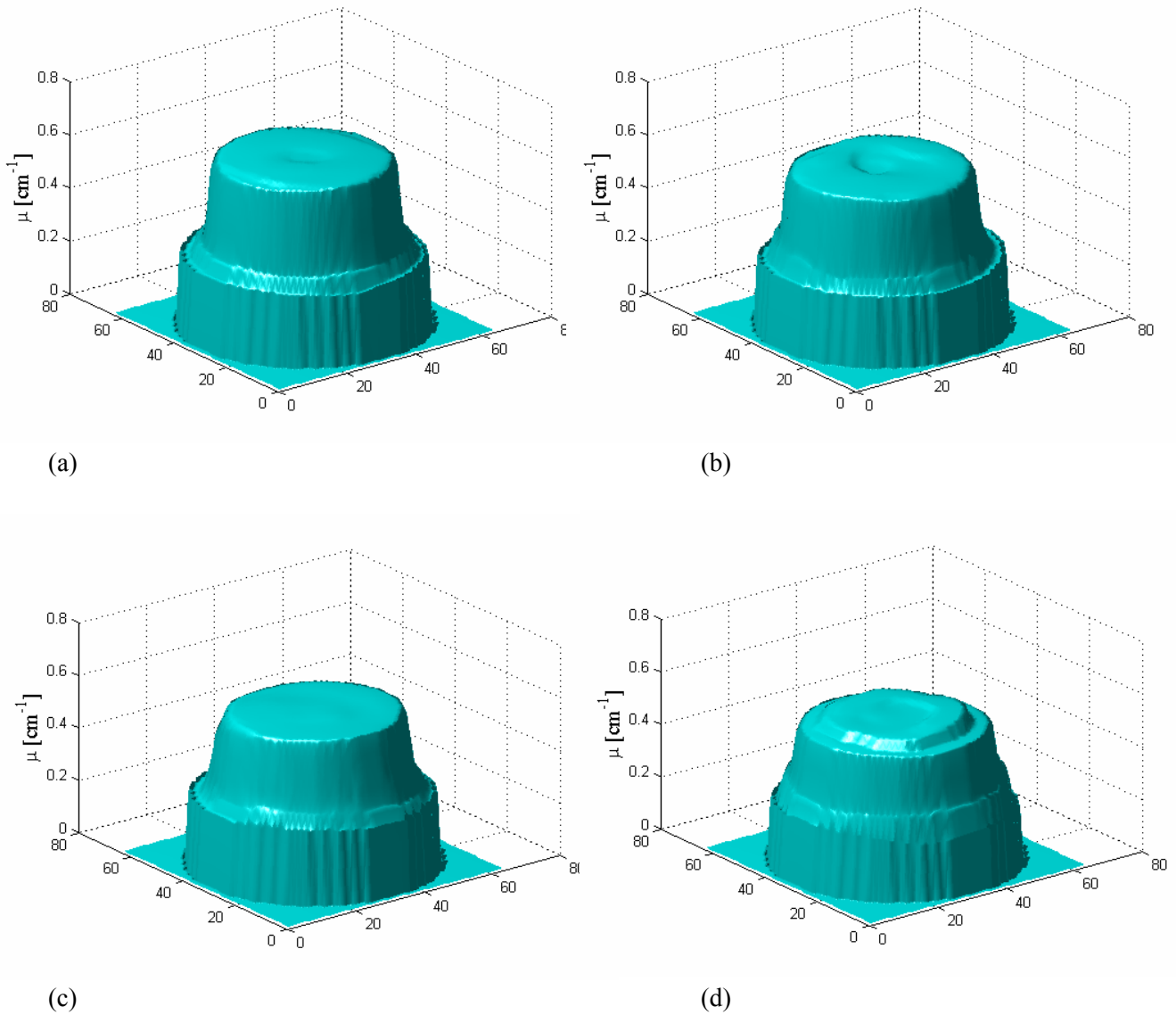
Fig. 4.11: The linear attenuation $\mu(l)$ [cm^{-1}] within-pin distribution for (a) sample S#0, (b), S#2, (c), S#3 and (d) S#4, derived using the PSCA-PML algorithm.

In Fig. 4.13, a 3-D reproduction of the linear attenuation coefficient reconstructions for sample S#4 is presented to provide more visual details. In this figure (image produced using AVS/Express program [avs]), a vertical section is shown together with iso-lines and multidimensional graphics. The details of the peripheral and central regions are better visible because of the advanced graphic tracings of AVS/Express.
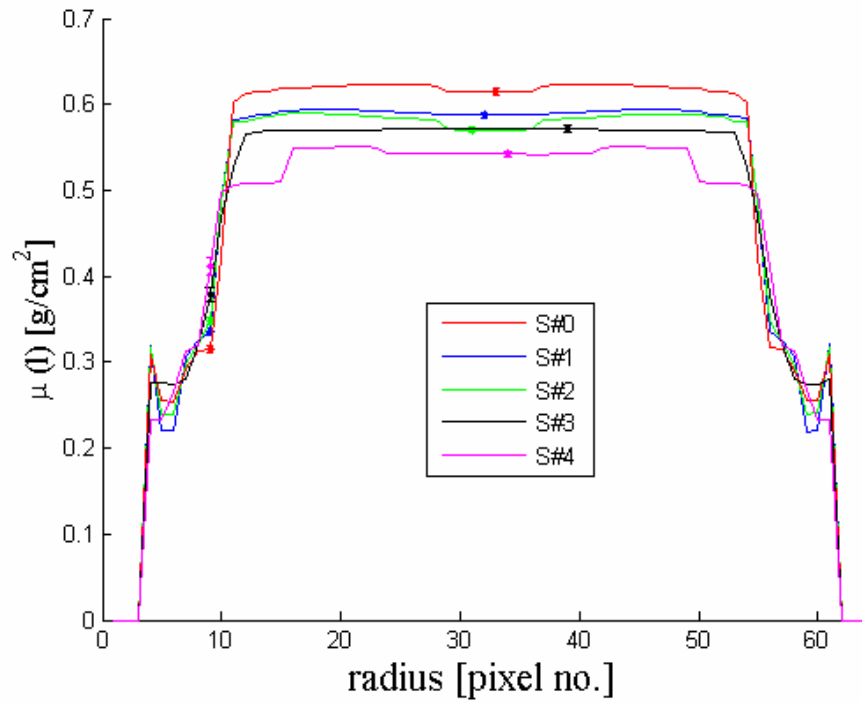
Fig. 4.12: Global plot of the linear attenuation $\mu(l)$ [cm^{-1}] for the various samples, as a vertical cut view (64 pixels) at the centre of the pin.
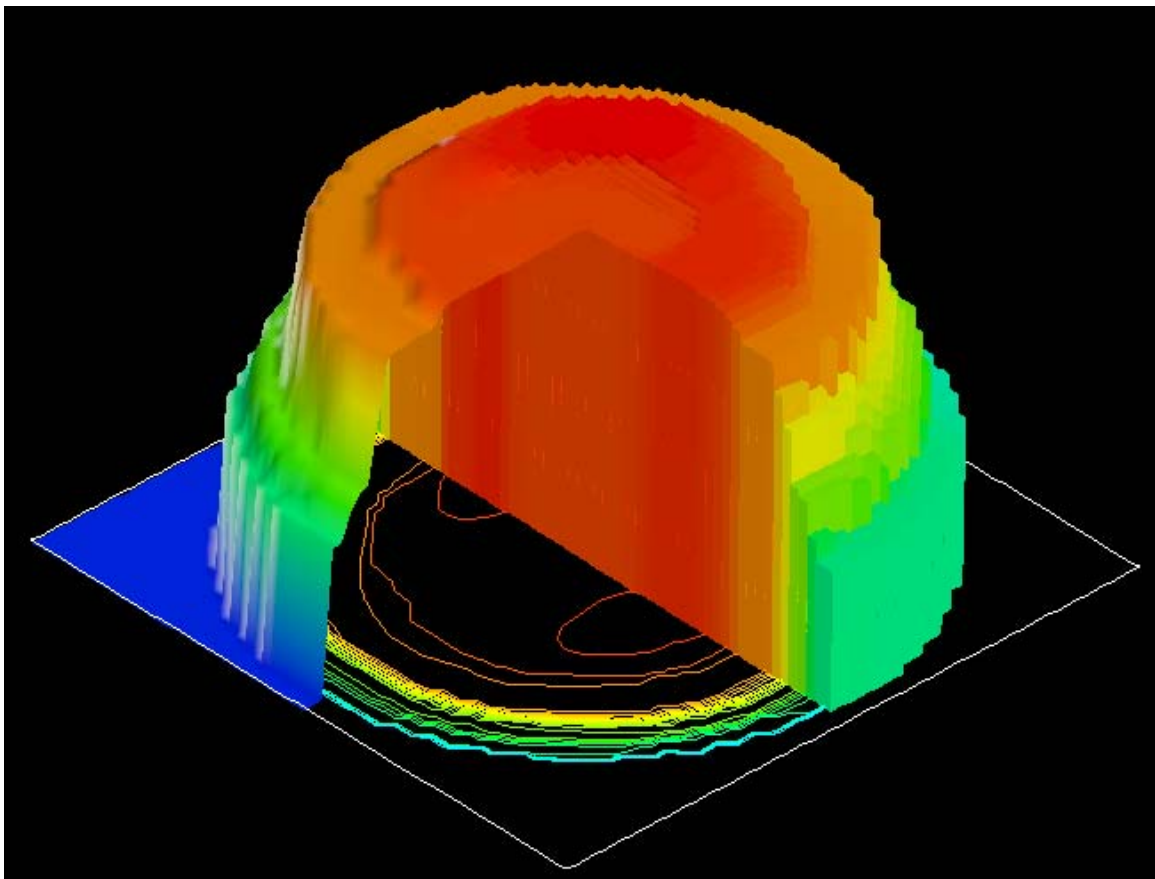
Fig. 4.13: 3-D image of linear attenuation coefficient reconstruction for sample S#4. A vertical section is shown together with iso-lines and multidimensional graphics.

4.4.2   Average density determination

The fuel pin average density was derived by directly using the data from the projections, without tomographic treatment. The reconstructed tomography images can also be used for the average density determination, but the accuracy in the density is much better when the original data are used and the propagation of errors is much simpler. Of course, as shown later, the pin density profiles are produced from the reconstructed images of within-pin linear attenuation.

The density is derived from the calculation of the attenuation in the fuel, as well as in the cladding and over-cladding:

$$I/I_0 = e^{-\mu(l)_{UO_2} x_{UO_2}} e^{-\mu(l)_{zry} x_{cl}}$$
(4.20)

The density ρ is given by:

$$\rho = \frac{-\ln(I/I_0)}{e^{-\mu(l)_{zry} x_{cl}}} \frac{1}{x_f \mu(m)_{UO_2}}$$
(4.21)

where $\mu(l)$ is the linear attenuation in the fuel pellet (UO_2), and in the cladding and over-cladding material (zry), and $\mu(m)$ is the mass attenuation in the fuel pellet (UO_2).

The density derivation was made with the central 36 measurements of each projection data set. The final value has been obtained as a weighted mean of all the projections. The results are shown in Table 4.2. A clear decrease of density with burnup is observed. The uncertainty is an average sigma (σ) derived using the net measured counts, as given by:

$$\sigma_k = \sqrt{\left(\frac{1}{\sqrt{I_k}}\right)^2 + \left(\frac{1}{\sqrt{I_0}}\right)^2}$$
(4.22)

where I_k is the net area measured at position k and I_0 is the net area measured directly with the beam (i.e. without a sample in between). These two errors are added in quadrature as the quotient of I_k/I_0 is the major term responsible for the total error.

Table 4.2: Average density derived for the four spent fuel pins and the fresh pin.

Sample Designation	Fuel Type	Burnup [GWd/t]	Density [g/cm^3]	σ [%]
S#0	fresh	-	10.43	0.5
S#1	spent	52	10.10	0.4
S#2	spent	71	10.04	0.6
S#3	spent	91	9.80	0.6
S#4	spent	126	9.43	0.6

4.4.3   Fuel pin density distribution

The reconstruction was based on the same techniques and routine as those of Section 4.4.1, with the same penalty parameters, but changing the regularisation parameter β (β=7) such that the noise is slightly increased in the final image as the resolution at the edge of the pin is improved. In this way, it was possible to differentiate the over-cladding from the cladding region. Because the collimator slit width is only 200 μm, it is not easy to distinguish regions of 125 μm (the air gap between cladding and over-cladding) or 300 μm (the thickness of the over-cladding for sample S#4). In order to increase the displayed resolution, the image was converted from 64x64 to 128x128 pixels (pixel width of 100 μm). The results (PSCA-PML images) are shown in Figs. 4.14 to 4.18 for all the samples.
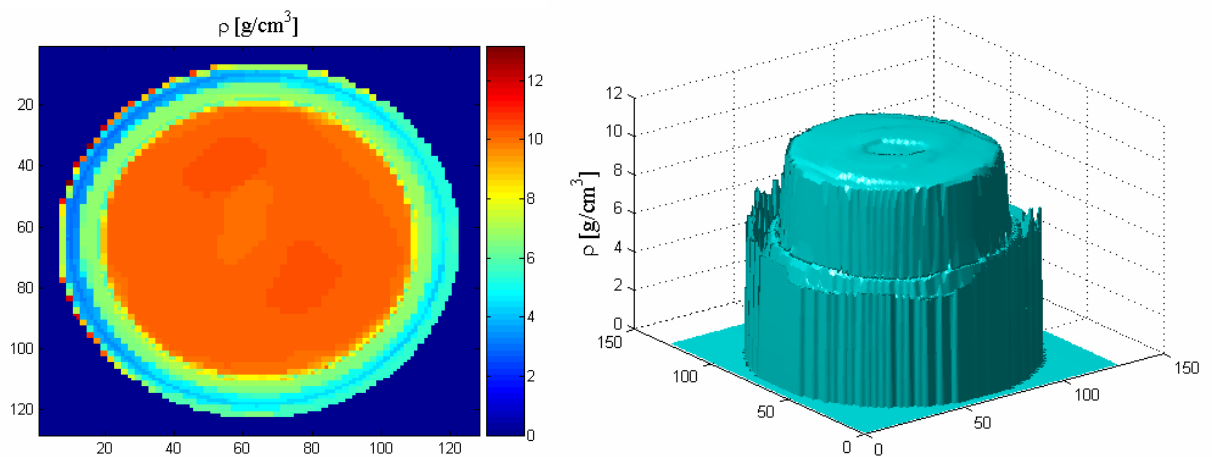
Fig. 4.14: Density [g/cm^3] distribution for sample S#0 (fresh). Horizontal view on the left, 3D image on the right.
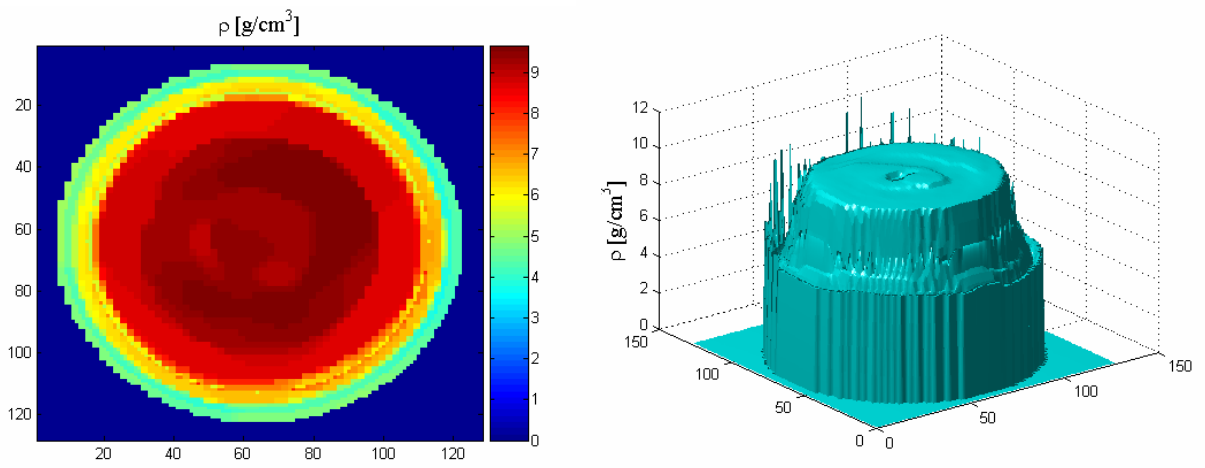
Fig. 4.15: Density [g/cm^3] distribution for sample S#1. Horizontal view on the left, 3D image on the right.
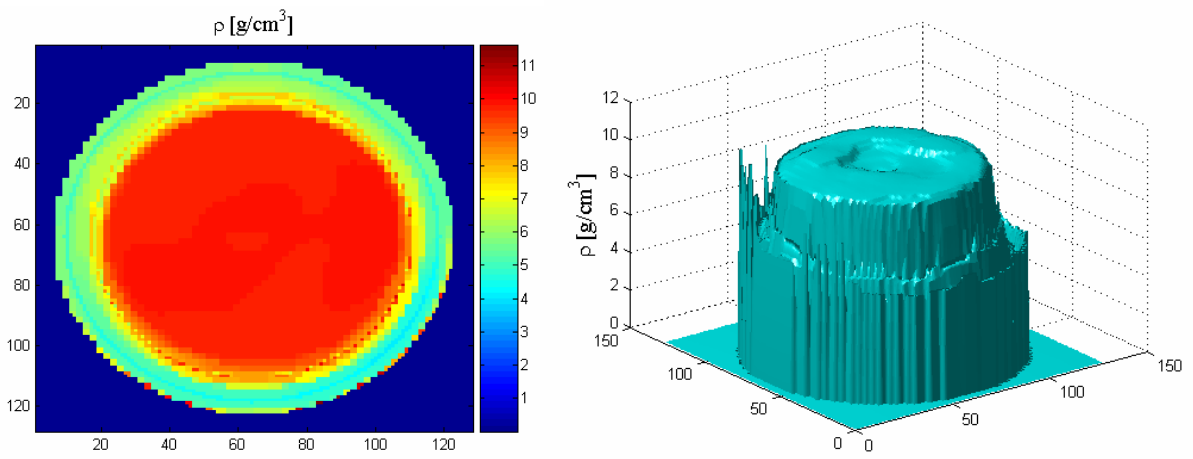
Fig. 4.16: Density [g/cm^3] distribution for sample S#2. Horizontal view on the left, 3D image on the right.
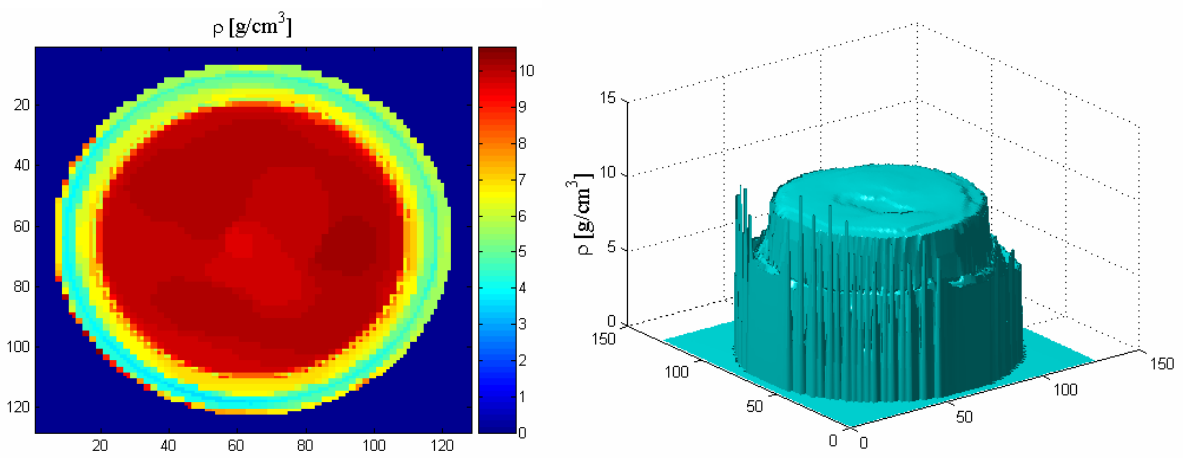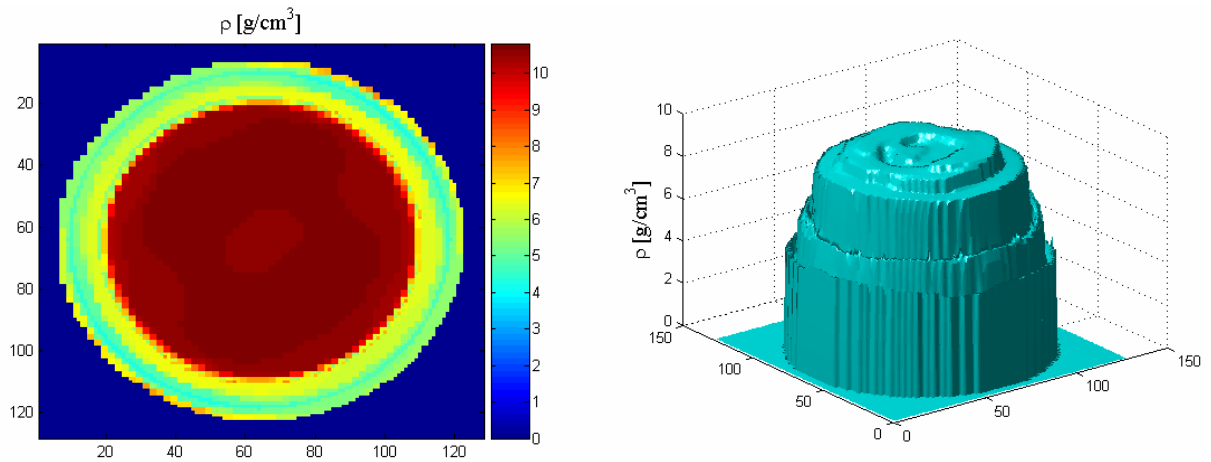

Fig. 4.17: Density [g/cm^3] distribution for sample S#3. Horizontal view on the left, 3D image on the right.

Fig. 4.18: Density [g/cm^3] distribution for sample S#4. Horizontal view on the left, 3D image on the right.

The values chosen for the reconstruction parameters are common for all the samples investigated. This means that the produced noise effect may be greater in some cases than in others. To properly clean each image, a customised treatment needs to be done. Currently, however, it has been considered more important to keep the parameters constant for the reconstruction of all the samples, such that comparisons may be made in a consistent manner. It can be seen that some noisy spikes are present in the images of samples S#1,2 and 3, but these do not conflict with the density evaluation.

In Fig. 4.19, a vertical cut view of density distributions for all the samples, derived using azimuthally averaged sinograms, is shown. Again here, the decrease of density with burnup can be easily observed. The density of the cladding, which should be identical for all the cases, shows discrepancies between the samples. This is because the slit of 200 μm cannot properly resolve the air gap zone and, as a consequence, this region is seen as a mixture of Zircaloy and air, producing as a result a lower density in the image. Indeed, from this plot and from the other 3D images, it is possible to distinguish the over-cladding and the cladding of the pin. The uncertainty bars in the plots, for the two distinct regions, central and peripheral, are derived from the results of the sensitivity study referred to earlier and described in the next section.
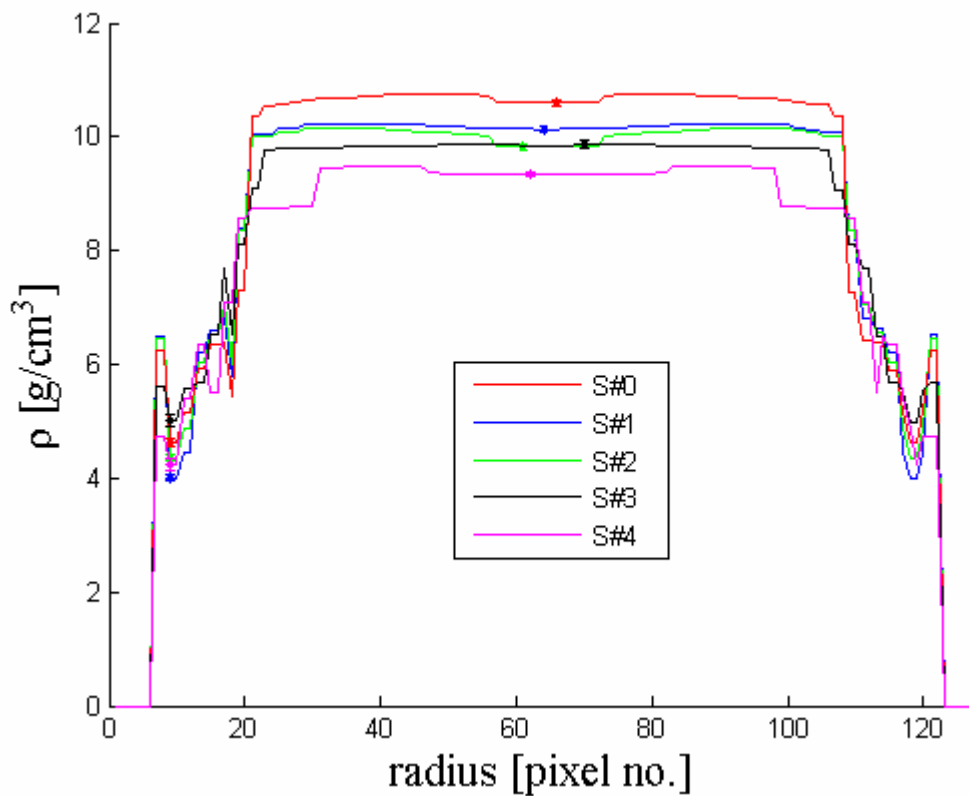
Fig- 4.19: Density [g/cm^3] distribution profiles for all the samples. Each plot is a vertical cut view of density distribution derived with azimuthally averaged images. The original image has 128x128 pixels.

Special attention needs to be given here to sample S#4, which shows a very singular density profile. We can observe a lower density zone at the periphery of the pin, then a step with a higher density region (a factor of ~10% between the two), followed by decrease of density going towards the centre of the pin. The radial extension of this lower density peripheral region (~1 mm) may correspond to the high burnup structure extension as estimated with EPMA [hor], the level of porosity of the fuel being much higher in this region such that it yields a lower overall density. This is better visible from Fig. 4.20 where the density of sample S#4 is plotted versus the radius of the pin, and where the dimensions of the fuel pellet and cladding regions are explicitly indicated.
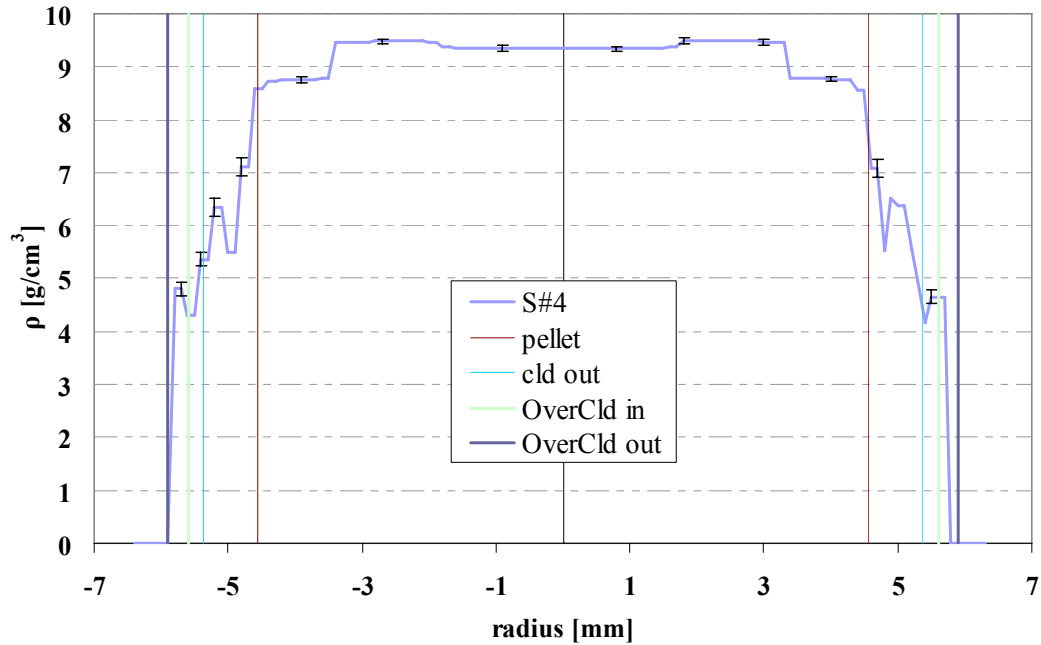
Fig- 4.20: Density of sample S#4 plotted versus the radius of the pin, with explicit indication of the pellet and cladding regions. The errors bars give an indication of the errors at different radii and are not data points in themselves.

4.4.4   Sensitivity study

The treatment of errors in image reconstruction from projections is a complex problem. A sensitivity study was carried out in order to provide a realistic and conservative estimation of the uncertainty on the reconstruction performed. The procedure is based on the introduction of noise into the input sinograms. These new sinograms were derived using the following law:

$$S_{noisy} = S_{clear}(1 + n\sigma P)$$

(4.23)

where S_{clear} is the sinogram without perturbation (60x64 matrix for transmission), σ is the statistical uncertainty of the measurements, n is the order of σ to be tested and P is a Gaussian probability function, all in matrix form. The noisy sinograms (S_{noisy}) have been processed and the image obtained compared with the image reconstructed without perturbation.

In Fig. 4.21, the perturbed sinogram (left) and the consequent PSCA-PML image generated (right) are shown for n=1 *(1σ)* and, in Fig. 4.22, for an extreme case with n=5 *(5σ)*. The case illustrated here is that of the fresh sample, S#0. One can observe that the quality of the image is not affected significantly for n=1, whilst for n=5 the perturbation heavily distorts the final result.
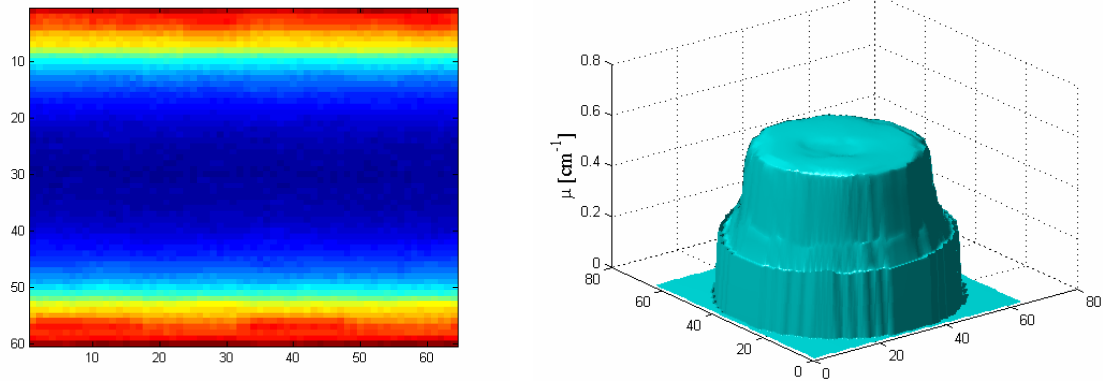
Fig- 4.21: Sinogram of sample S#0, perturbed with 1σ error (left), and image generated (right). The perturbation is not really affecting the quality of the image.
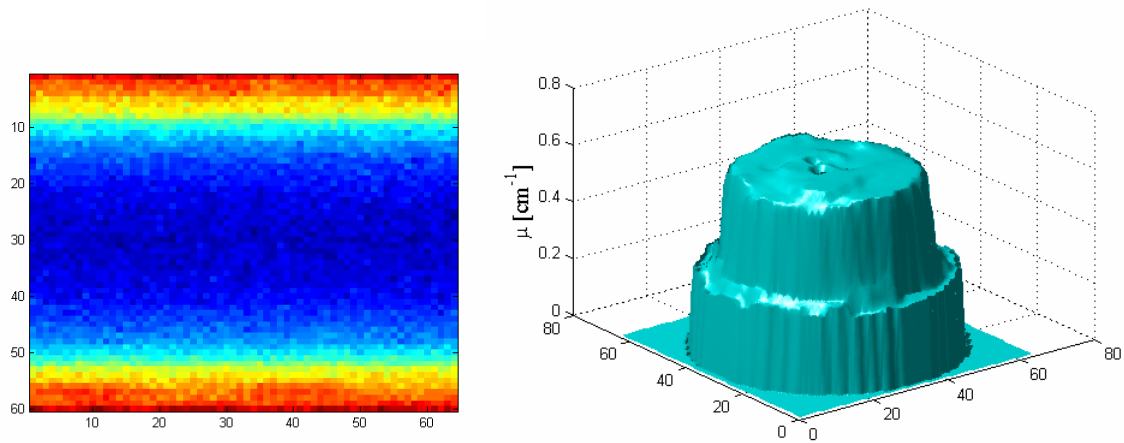

Fig- 4.22: Sinogram of sample S#0, perturbed with 5σ error (left), and image generated. The perturbation is seriously affecting the quality of the image, producing holes and irregularities.

Fig. 4.23 shows the quotient between the unperturbed PSCA-PML image and the 1σ perturbed image for sample S#0. It is clearly seen that the region at the periphery of the pin (cladding and edge of fuel pin) is the most sensitive, whilst the central part has a mean discrepancy of only about 1.5%.
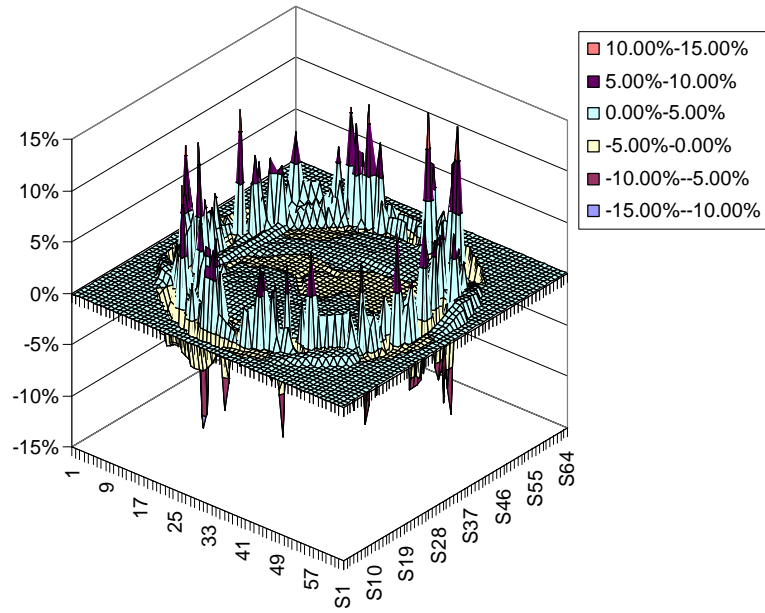
Fig. 4.23: Quotient between the unperturbed PSCA-PML image and the 1σ perturbed image for sample S#0.

Table 4.3 gives the uncertainties for all the samples, as estimated from the described approach with *1σ, 2σ* and *3σ* perturbations, respectively.

Table 4.3: Uncertainty estimation (1σ, 2σ, 3σ) for all samples, in the central region and at the periphery.

Samples	$1\,\sigma$		$2\,\sigma$		$3\,\sigma$	
	Central region	Peripheral region	Central region	Peripheral region	Central region	Peripheral region
S#0	0.6 %	1.5 %	1.1 %	2.3 %	1.5 %	3.6 %
S#1	0.5 %	1.2 %	0.8 %	2.4 %	1.1 %	2.9 %
S#2	0.6 %	1.7 %	1.1 %	2.9 %	1.2 %	4.3 %
S#3	0.7 %	2.1 %	1.1 %	3.4 %	1.2 %	4.8 %
S#4	0.5 %	2.5 %	1.0 %	4.5 %	1.3 %	6.1 %

4.4.5   Density versus burnup

The average fuel density, evaluated from the gamma transmission measurements for each sample, is plotted in function of the burnup in Fig. 4.24. These results are compared with the manufacturer's data for the fresh sample S#0 and a PSI-Hotlab Archimedes measurement [gue] for sample S#4. The assumption of a linear relationship between the density and the burnup is seen to be not unreasonable.
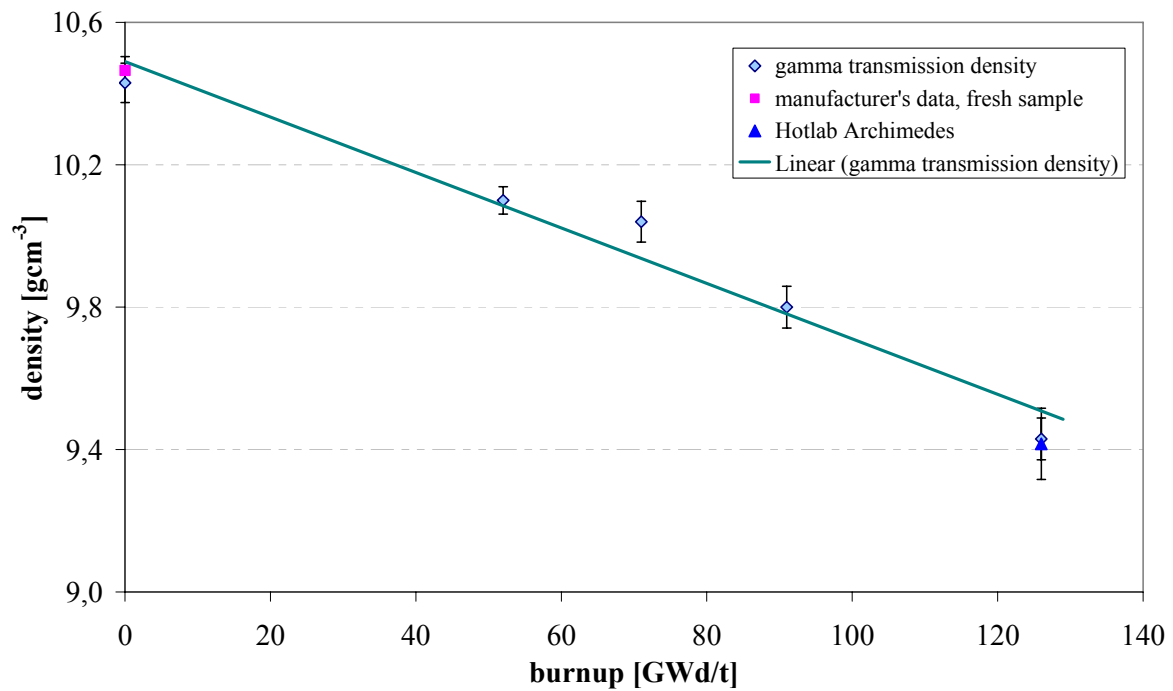

Fig. 4.24: Density measured by gamma transmission and PSI-Hotlab Archimedes.

References

[avs]   AVS/Express Visualization Edition, Version 7.0

[bra]   R.H. BRACEWELL & A.C. RIDDLE, "Inversion of fan beam scans in radio astronomy," *Astrophysics Journal*, **150** p.427 (1967)

[byr]   C.L. BYRNE, "Block-iterative methods for image reconstruction from projections", *IEEE Trans Image Process,* **5** p.792 (1996)

[cam]   D.C. CAMP, H.E. MARTZ, G.P. ROBERSON, D.J. DECMAN, R.T. BERNARDI, "Nondestructive waste-drum assay for transuranic content by gamma-ray active and passive computed tomography", *Nuc. Instr. and Meth. In Phys. Res. A*, **495**(1) p.69 (2002)

[car]   S. CARUSO, "Cold test planning for the tomographic measurement cell at Proteus", PSI Internal Report AN-41-05-05 (2005)

[car2]   S. CARUSO, "Procedure for the operation of the tomography measurement cell at Proteus", PSI Internal Report AN-41-05-04 (2005)

[cra]   T. CRACIUNESCU, "A neural network model fort he tomographic analysis of irradiated nuclear fuel rods", *Nuc. Techn.,* **146** p.65 (2004)

[dau]   M.E. DAUBE-WITHERSPOON, G. MUEHLLEHNER, "An iterative image space reconstruction algorithm suitable for volume ECT", *IEEE Trans. Med. Imag.*, **MI-5** p.61(1986)

[dep]   A.R. DE PIERRO, "A modified expectation maximization algorithm for penalized likelihood estimation in emission tomography", *IEEE Trans. Med. Imag.,* **14**(1) p.132 (1995)

[dsp]   "DSPECTM. Digital Gamma-Ray Spectrometer", EG&G ORTEC Catalog, Oak Ridge.

[erd]   H. ERDOGAN, J.A FESSLER, "Ordered subset algorithms for transmission tomography", *Phys. Med. Biol.*, **44** p.2835 (1999)

[erd2]   H. ERDOGAN, J.A. FESSLER, "Monotonic algorithms for transmission tomography", *IEEE Tr. Med. Im.*, **18**(9) p.801 (1999)

[fes]   J.A. FESSLER, A. O. HERO, "Space-Alternating Generalized Expectation-Maximization Algorithm", *IEEE Sig. Proc.*, **42**(10) p.2664 (1994)

[fes1]   J.A. FESSLER, A. O. HERO, "Penalized Maximum-Likelihood Image Reconstruction Using Space-Alternating Generalized EM Algorithms", *IEEE Trans. Image Processing*, **4**(10) p.1417 (1995)

[fes2]   J.A. FESSLER, "Penalized Weighted Least-Squares Image Reconstruction for Positron Emission Tomography", *IEEE Trans. Med. Imag.*, **13**(2) p.290 (1994)

[fes3]   J.A. FESSLER, "Aspire 3.0 User's Guide: A Sparse Iterative Reconstruction Library", Technical Report No. 293 Communications & Signal Processing Laboratory, University of Michigan (2001)

[fes4]   J.A. FESSLER, "Grouped coordinate descent algorithms for robust edge-preserving image restoration" Proc. SPIE 97, *Im. Recon. and Restor. II*, **3170** p.184 (1997)

[fes5]   J.A. FESSLER, "Spatial resolution properties of penalized likelihood image reconstruction: space invariant tomographs", *IEEE Trans. Image Processing*, **5**(9) p.1346 (1996)

[gam]   "GammaVisionTM-32. Gamma-Ray Spectrum Analysis and MCA Emulation for Microsoft®Windows® 95 and Microsoft Windows NT. A66-B32 Software User's Manual", EG&G ORTEC Part No. 774780 Manual Revision A, Oak Ridge

[gar]   R.J. GARDNER, "Geometric Tomography", *Cambridge University Press*, Cambridge (1995)

[gil]   G. GILMORE, J.D. HEMINGWAY, "Practical Gamma-ray Spectrometry", *John Wiley & Son Ltd*, New York (1995)

[gor]   R. GORDON, R. BENDER, GT. HERMAN, "Algebraic reconstruction techniques (ART) for three-dimensional electron microscopy and X-ray photography", *J. Theor. Bio.,* **29**(3) p.471 (1970)

[gue]   I. GÜNTER -LEOPOLD, Private Communication (2006)

[her]   G.T. HERMAN, "Image reconstruction from projections: The fundamentals of computerized tomography", *Academic Press,* New York (1980)

[hor]   M. I. HORVATH, Private Communication (2006)

[hou]   G.N. HOUNSFIELD, "A method of an apparatus for examination of a body by radiation such as x-ray or gamma radiation," Patent specification 1283915, The Patent Office, 1972

[hub]   P.J. HUBER, *Robust Statistics*. John Wiley & Sons, New York (1981)

[hud]   H.M. HUDSON, R.S. LARKIN, "Accelerated image reconstruction using ordered subsets of projection data", *IEEE Trans. Med. Imag.*, **13** p.601 (1994)

[lan]   K. LANGE R. CARSON. "EM reconstruction algorithms for emission and transmission tomography", *Jour. Comp Assisted Tomogr.*, **8** (2) p.306 (1984).

[lan2]   K. LANGE, M. BAHN, R. LITTLE, "A theoretical study of some maximum likelihood algorithms for emission and transmission tomography", *IEEE Trans. Med. Imag.,* **6** p.106 (1987)

[kau]   L. KAUFMAN, "Maximum likelihood, least squares, and penalized least squares for PET". *IEEE Trans. Med. Imag.*, **12** p.200 (1993)

[kno]   G.F. KNOLL, "Radiation Detection and Measurement. Second Edition", *John Wiley& Sons,* New York (1989)

[lev]   E. LEVITAN, G.T. HERMAN, "A maximum a posteriori probability expectation maximization algorithm for reconstruction in emission tomography", *IEEE Transactions on Medical Imaging*, **MI-5** p.16 (1986)

[lew]   R.M LEWITT, G.MUEHLLEHNER, „Accelerated iterative reconstruction for positron emission tomography based on the EM algorithm for maximum likelihood estimation", *IEEE Trans. Med. Imag. Mar.,* **6** p.185 (1987)

[mat]   "Matlab 7.0.4", The MathWorks, Inc.

[mum]   E. MUMCUOGLU, R. LEAHY, S. CHERRY, "A statistical approach to transmission image reconstruction from ring source calibration measurements in PET", Proceedings of the 1992 Nuclear Science Symposium and Medical Imaging Conference, 1992, p.910

[oga]   K. OGAWA, "A Pratical Method for Position-Dependent Compton-Scatter Correction in Single Photon Emission CT*", IEEE Tran. Med. Imag.*, **10**(3) p.408 (1991)

[rad]   J. RADON, "Ueber die Bestimmung von Funktionen durch ihre Intergralwerte langs gewisser Mannigfaltigkeiten (On the determination of functions from their integrals along certain manifolds)," Berichte Saechsische Akademie der Wissenschaften, **29** p.262 (1917)

[raj]   N. RAJEEVAN, K RAJGOPAL, G.KRISHNA, "Vector-extrapolated fast maximum likelihood estimation algorithms for emission tomography", *IEEE Trans. Med. Imag.,* **11** p.9 (1992)

[ram]   G.N. RAMANCHANDRAM and A.V. LAKSHMINARAYANAN, "Three dimensional reconstructions from radiographs and electron micrographs: Application of convolution instead of fourier transforms" Proceedings of the National Academy of Sciences, **68** p.2236 (1971)

[roc]   A.J. ROCKMORE, A. MACOVSKI, "A maximum likelihood approach to emission image reconstruction from projections", *IEEE Trans Nucl Sci,* **NS-23** p.1428 (1976)

[sau]   K. SAUER, C. BOUMAN, "Bayesian estimation of transmission tomograms using segmentation based optimization", *IEEE Trans. Nucl. Sci.*, **39** p.1144 (1992)

[sau2]   K. SAUER, C. BOUMAN, "A local update strategy for iterative reconstruction from projections", *IEEE Trans. Signal Process,* **41** p.534 (1993)

[shen]   J. SHENG, L. YING, "A fast image reconstruction algorithm based on penalized-likelihood estimate", *Med. Eng. Phys.,* **27**(8) p.679 (2005)

[shep]   L.A. SHEPP, Y. VARDI "Maximum likelihood reconstruction for emission tomography", *IEEE Trans. Med. Imaging* **MI-1** p.113 (1982)

[tan]   R.H. TANKE, J.E. JASPER, P.A.M. GAALMAN, D. KILLIAN, "Applications of tomography in nuclear research", *Kerntechnik,* **56**(5) p.283 (1991)

5.   Gamma-Emission Measurements and Results

While a general introduction to computerised tomography was provided in Chapter 4, the present chapter is devoted exclusively to emission tomography aspects, i.e. the solution of two-dimensional single photon emission computerised tomography (SPECT) problems in the context of obtaining within-pin nuclide distributions for the irradiated fuel rod samples. This topic has been addressed in previous work for lightly irradiated UO_2 rods [pra], as well as in irradiated fuel rods [ale-bar-buu-mue], but never, to the author's knowledge, in such highly irradiated rods as are investigated here. In this chapter, the main results obtained from Chapter 4, i.e. the attenuation coefficient maps, have been employed to increase the accuracy of the derivation of the within-pin distributions. Section 5.1 gives a brief introduction to the basic principles of SPECT and the steps required to perform a reconstruction. The gamma-scanning and data processing procedures for emission tomography are presented in Section 5.2, while Section 5.3 is devoted to describing the development of the so-called efficiency system matrix. The statistical aspects of reconstruction are touched on in Section 5.4, and the principal reconstruction results obtained from simulation tests and the burnt fuel samples are presented in Section 5.5. Finally, a summary of the chapter is given in Section 5.6.

5.1. Basic Problem Formulation

As mentioned in Section 2.3.3, single photon computerised tomography (SPECT) is a non-destructive technique that generates cross-sectional images of an object on the basis of measurements of γ-rays emitted by separate "portions" of this object [her-tar]. The γ-rays collected from a single portion constitute a "projection element". A set of projection elements obtained for a particular direction of propagation of the γ-rays, as defined by a certain direction of a collimator slit, is called a "projection". Sets of projections, collected from different angular views, are needed to be able to reconstruct an object. The quality of the final image is strongly determined by the total number of projections collected.

Let p_k ($p(s,\theta)$ in Fig. 5.1) denote the kth projection element, K the total number of projection elements and $\vec{p}$ the corresponding vector. Let $f(\vec{x})$ be the unknown distribution of the γ-source within the object ($f(x,y)$ in Fig. 5.1). The mathematical relationship between p_k and $f(\vec{x})$ can be described using a projection operator $\mathcal{W}_k$, which essentially models the transport of the photons of interest through the different materials of the system in a geometry corresponding to the kth measurement configuration:

$$\mathcal{W}_k f_i \cong p_k \tag{5.1}$$

Reconstructing $f(\vec{x})$ from the measured projection elements reverts to inverting this operator. This is usually achieved by discretising the problem and expanding the sought distribution over a finite set of i linearly independent basis functions $b_i(\vec{x})$ such that $f(\vec{x})$ is:

$$f(\vec{x}) \cong \sum_{i=1}^{I} f_i b_i(\vec{x}) \tag{5.2}$$

The problem to be inverted may be posed in a matrix form:

$$\mathcal{W}_k f \cong \sum_{i=1}^{I} \underbrace{\left(\mathcal{W}_k b_i\right)}_{w_{ki}} f_i \cong p_k \tag{5.3}$$

$$W\vec{f} \cong \vec{p} \tag{5.4}$$

$\vec{f}$ is the vector of parameters f_i and W is the "system matrix", whose element w_{ki} of the kth row and i^{th} column is the projection of the basis function b_i in the system geometry k. The basis functions can be pixels, analytical functions, etc. Here, pixels have been chosen as basis functions for their flexibility and other specific motivations described in the following sections.
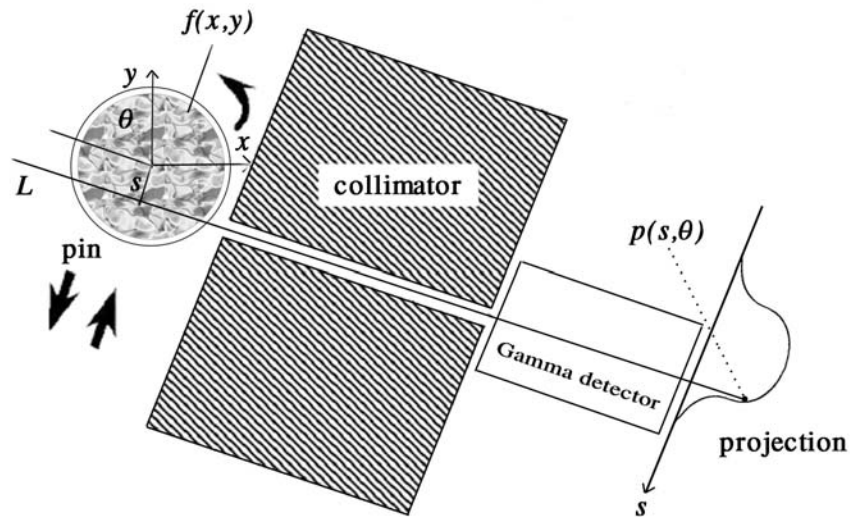
Fig. 5.1: Schematic illustration of the basic principles of using the gamma-scanning station for emission tomography.

To approximate the sought distribution and find the set of parameters f_i, it is necessary to have:

- a set of measured projection elements p_k in a suitable form, i.e. sinogram.

- a system matrix W properly modelling the involved physics processes, according to the type of discretisation chosen, i.e. according to the type of basis functions chosen.

- detailed information about sample morphology, i.e. linear attenuation coefficient map

- a reconstruction technique, i.e. a way of performing the inversion of the direct problem described above, as explained in the previous chapter.

Each of these steps requires developing techniques or models that are specific to the problem under study. In the following sections, each aspect is reviewed in detail in the context of SPECT investigations of burnt fuel pin segments.

5.2. Projection Elements Acquisition Procedure

In this section, the procedure for the acquisition of projection elements and the consequent development of input sinograms necessary for tomographic processing is detailed. This includes the gamma-scanning procedure, the photo-peak treatment, and the main operations necessary to convert the data into a suitable format.

5.2.1. High resolution gamma-scanning

Basically, the spectra were acquired as described in Chapter 4, but with some differences that will be explained in this section. In fact, the gamma-scanning data for both transmission and emission tomography on each sample were derived from the same sets of spectra (see Table 4.1 for the measurement plan), i.e. the cobalt source was present during the measurements. This approach has both positive and negative consequences. A positive consequence is the opportunity to apply appropriate and accurate attenuation corrections in the emission reconstruction by using the linear attenuation coefficient maps (see Chapter 4) derived from exactly the same set of measurements. A negative aspect is the presence of the Compton continuum from the high-intensity external gamma source. However, for the samples under consideration, the latter impact is relatively insignificant because of the high self-generated background continuum. It should be mentioned that some separate measurement sessions were also carried out for each sample, viz. without the ^{60}Co source and with a modified detector setup. The tomographic results shown and discussed here, however, are those obtained from the combined transmission and emission sessions.

The detectable radio-nuclides are ^{137}Cs with its 0.662 MeV γ-ray, ^{134}Cs with 0.569, 0.605, 0.796, 1.039, 1.168 and 1.365 MeV γ-rays, ^{154}Eu with 0.723, 0.873, 0.996, 1.005, 1.275 and 1.597 MeV γ-rays, and, of course, the ^{60}Co with 1.173 and 1.333 MeV γ-rays. The emission tomography reconstruction was implemented using the most intense γ-peaks that have least interference from others peaks: 0.662 MeV for ^{137}Cs, 0.796 MeV for ^{134}Cs, and 1.275 MeV for ^{154}Eu. In the upper part of Fig. 5.2, a spectrum acquired from sample S#2 is shown. The γ-peaks employed are highlighted with an ellipse and zoomed. The counts are shown on a logarithmic scale.

In the lower part of Fig. 5.2, a spectrum of sample S#4 is shown, again with the γ-peaks used highlighted and zoomed. In the main spectrum, the counts are again on a logarithmic scale, but the peaks in the zoom area are shown here, for clarity, on a linear scale. In Chapter 6, a more detailed description of all the peaks in the spectrum will be given.
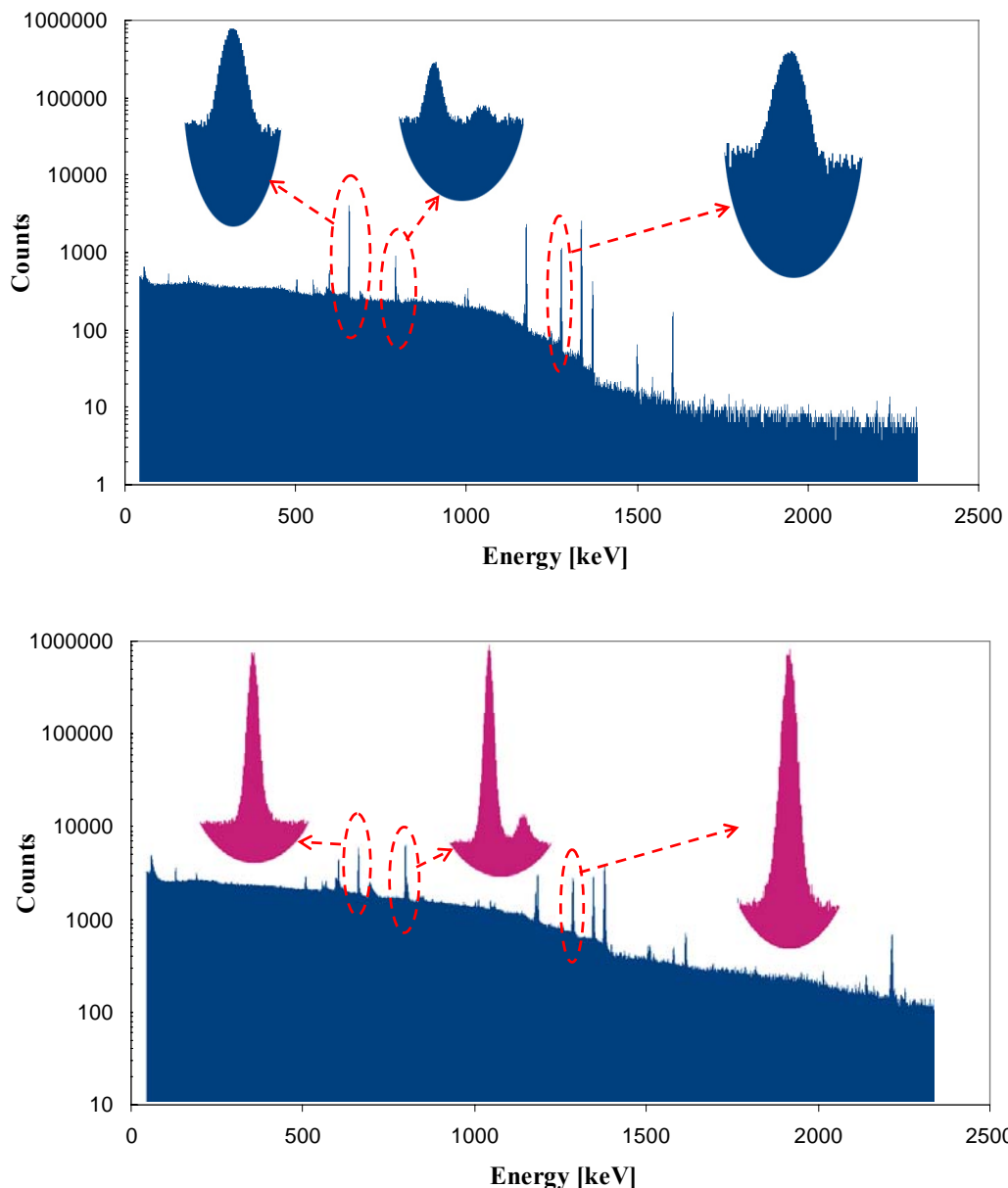
Fig. 5.2: Spectra of sample S#2 (above) and S#4 (below). The peaks of interest are highlighted and zoomed (in logarithmic scale for S#2, linear scale for sample S#4).

5.2.2. <u>Peak area determination methodology</u>

An important requirement for a tomographic setup is to employ a collimator in a manner as close as possible to the ideal situation, in which photons not passing directly through the slit never reach the detector. In practice, this cannot be achieved and a compromise between the thickness of the collimator, the dimensions of the slit and the intensity of the source to be measured must be found. The optimal compromise is to ensure high enough count rates for useful peak count statistics, keeping the dead time during acquisition reasonably low. Of course, this depends strongly on the energies of the photons that are analysed, and also on the activity of the sample. In this work, the collimator works quite well for photon energies below 1 MeV. However, for higher energies (e.g. the ^{154}Eu 1.275 MeV γ-ray), it becomes more transparent and the spatial resolution deteriorates significantly. In addition, the dead time increases more rapidly than one would wish with increasing burnup of the sample. To compensate for the non-ideal effectiveness of the collimator, i.e. the leakage of photons through the body of the collimator, each projection element was corrected with a background projection, as described in Section 5.2.4.

Each main spectrum acquired, there being a total of k main spectra, i.e. projection elements, for each one of the total m angular projections measured, was analysed as follows. A region of interest (ROI) was chosen for each relevant peak such that the effect of neighbouring peaks was minimised. To maintain a high consistency in the global tomographic procedure and in the treatment of all the samples, the ROI limits selected for a specific peak were employed for that peak in the analysis of all of the spectra, for all the collected projections, and for all samples. The ROI gross area for each peak for each lateral position (projection element) was derived and divided by the live time. An identical procedure was used in the background spectra analysis.

In addition to the ROI for the peak of interest, two regions of the continuum were defined, one higher and one lower in energy than the main peak (See Fig. 5.3). The same continuum region limits were employed in the analysis of all of the spectra.

The final net count rate, for a particular peak, is determined as follows. The mean difference between the main and background continuum regions is added to the background peak ROI area and the resultant is then subtracted from the main peak ROI. In this way, the increased level of the continuum during a main measurement is allowed for during the subtraction of the background in the ROI.

5.2.3. Baseline subtraction

In most of the measurements, non-contiguous background continua were chosen because of the presence of numerous interference peaks that affect the spectra. In fact, besides the direct gamma-ray background, the presence of a strong neutron source arising from the spent fuel rods (the segment under investigation, as well as all the others stored in the transport flask/sample changer on top of the measurement cell) contaminates the basic acquisition of the spectra by introducing additional peaks produced by neutron capture in the surrounding materials, e.g. lead, cadmium and the germanium itself. In Fig. 5.3, the criteria of selection of ROI regions (ROI^{cen} and ROI^{bkg} in the picture) and related continua regions are illustrated in a detail of the main and background spectra, measured for the 71 GWd/t sample (S#2). Cl^{cen} and Cr^{cen} illustrate the two continua regions in the main measurement, at the low energy and high energy side of the peak respectively, whilst Cl^{bkg} and Cr^{bkg} are the two continua regions in the background measurement. The 604 keV peak of ^{134}Cs and the interference peak from neutron capture in ^{73}Ge (595 keV) are illustrated in the same Fig. 5.3.

The net count-rate in the photo peak is given by the following expression:

$$ROI^{cen} - \left[ROI^{bkg} + \left(\frac{(Cl^{cen} + Cr^{cen})}{2(n+m)}k - \frac{(Cl^{bkg} + Cr^{bkg})}{2(n+m)}k \right) \right] \qquad (5.5)$$

where *n*, *m* and *k* are the channel numbers of *Cl*, *Cr* and *ROI* respectively. *Cl*, *Cr* and *ROI* are gross areas.
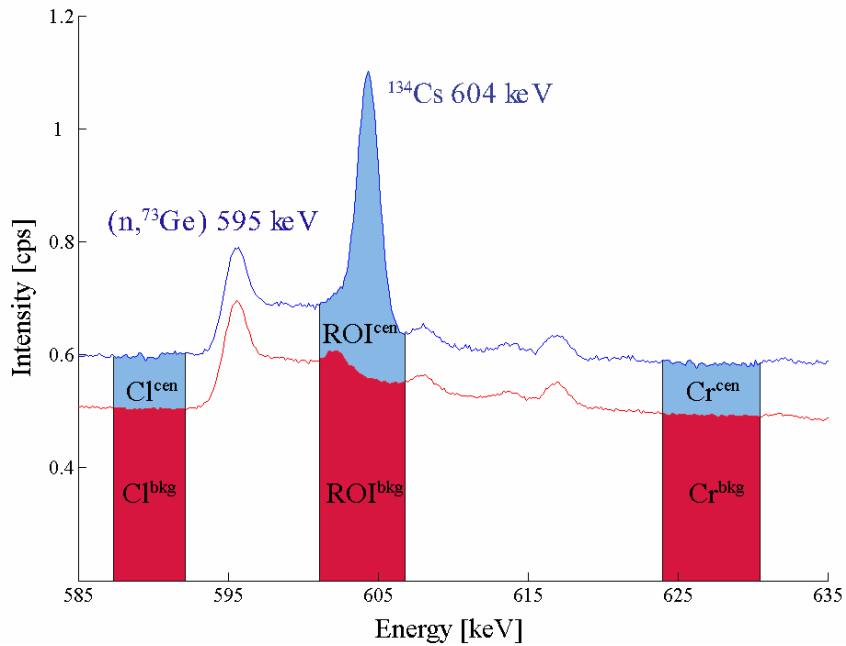
Fig. 5.3: ROI area for the main (blue) and for the background (red) measurements, and related continua regions (Cl^{cen} and Cr^{cen} for the previous, Cl^{bkg} and Cr^{bkg} for the latter). The spectra detail refers to the 71 GWd/t sample (S#2).

A C++ program was written to automate all this analysis, as for the transmission case, because of the large number of spectra to be processed.

This peak analysis methodology has been found to be very robust, in comparison to standard peak fitting treatments (see Appendix A), as most of the peaks were not really Gaussian and some of them were close to interference peaks (typically neutron-capture gammas), which may have led to inaccuracy in the derivation of the final results. Further, the same principle was applied not only to emission tomography, but also to the derivation of the isotopic burnup monitors described in Chapter 6.

5.2.4. Sinogram development

For each angular projection collected, there being a total of k main spectra, i.e. projection elements, a "background projection" contribution is produced. This "background projection" is actually derived as the average of the net count-rate of two pairs of projection elements acquired in lateral positions with respect to the collimator slit, on both sides of the pin, so as to be not directly visible by the detector, but close to the pin edge. The background thus includes gamma-rays which penetrate the collimator block rather than passing through the slit. Then the net count-rate of each projection element is corrected by subtraction of the background net count rate, for each isotope. Treating the data in this way allowed the possibility to subtract the non-collimated background from each of the main k x m net count-rates collected (k lateral projection elements acquired for each angular projection m).

Optimising the acquired data is an important issue if accurate and reliable images are to be produced. The treatment used for the numerical re-alignment because of precession anomalies, described in detail in Chapter 4, was employed for the emission case too. Exactly the same correction offsets were used for the mis-alignment between the angular projections as those derived in the transmission tomography analysis. The major benefit in the use of correction offsets derived from the transmission measurements is the ability to detect accurately the edges of the UO_2 pellets. This helps to prevent the degradation of spatial information at the pin periphery, which may happen if the numerical re-alignment is attempted directly on emission data sets.
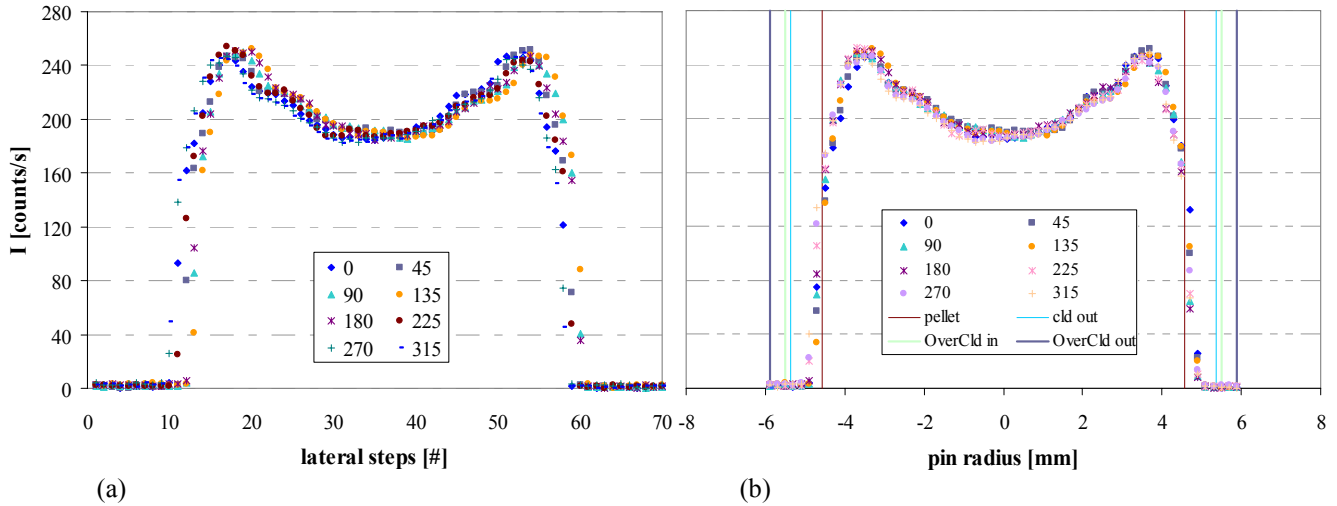
Fig. 5.4: Measured counts/s of ^{137}Cs for sample S#4, acquired at different lateral and angular positions (a) before, and (b) after application of the precession correction.

In Fig. 5.4, the measured counts per second for ^{137}Cs are plotted in function of the lateral and angular steps, (a) before application of the correction, and (b) after. In this example, where each point is a single projection element, 70 projection elements (k) for each of the 8 main projections (m), have been acquired. The measurement data shown correspond to sample S#4.

5.2.5. Final sinograms and attenuation coefficient maps

The sinograms have been generated using the same procedure as that used for transmission tomography. Eight sets of angular projections (m) have been used, each projection consisting of 60 elemental projections (only the elements bringing information are kept for the final sinogram) representing the counts per second acquired from gamma-rays produced by a single radio-nuclide (k). An eight-step angular interpolation was made, between the original adjacent angular projections, to obtain a total number of 64 angular projections, as was done for the transmission case. An example of a sinogram is shown in Fig. 5.5a, for the sample S#1. On the left axis, r, are the 60 lateral positions, and on the horizontal axis, θ, the 64 angular projections. Each step of lateral displacement corresponds to the collimator slit width, 0.2 mm, which allows images of 64x64 pixels by adding four blank pixels.

As mentioned earlier, detailed information about the sample morphology is necessary to increase the accuracy of reconstructed images [tun]. For this reason, transmission tomography has been used to produce the linear attenuation coefficient maps. However, the coefficient maps, as obtained from transmission measurements, are not directly employable in the reconstruction algorithm, and must first be scaled to the energy of the emitted photon to be reconstructed. In Fig. 5.5b, the linear attenuation

coefficient map corresponding to 662 keV for sample S#1 is shown. This image has been obtained by rescaling (to 662 keV) the map for 1332 keV photon energy as obtained from the transmission measurements. The expression used is

$$\mu'(l) = \mu'(m) \; [\mu^o(l) \, / \mu^o(m)] \tag{5.6}$$

where $\mu'(l)$ and $\mu^o(l)$ are the linear attenuation values at the desired (662 keV) and measured (1332 keV) energies, respectively, and $\mu'(m)$ and $\mu^o(m)$ are the corresponding mass attenuation values (derived from the XCOM database [xco]).
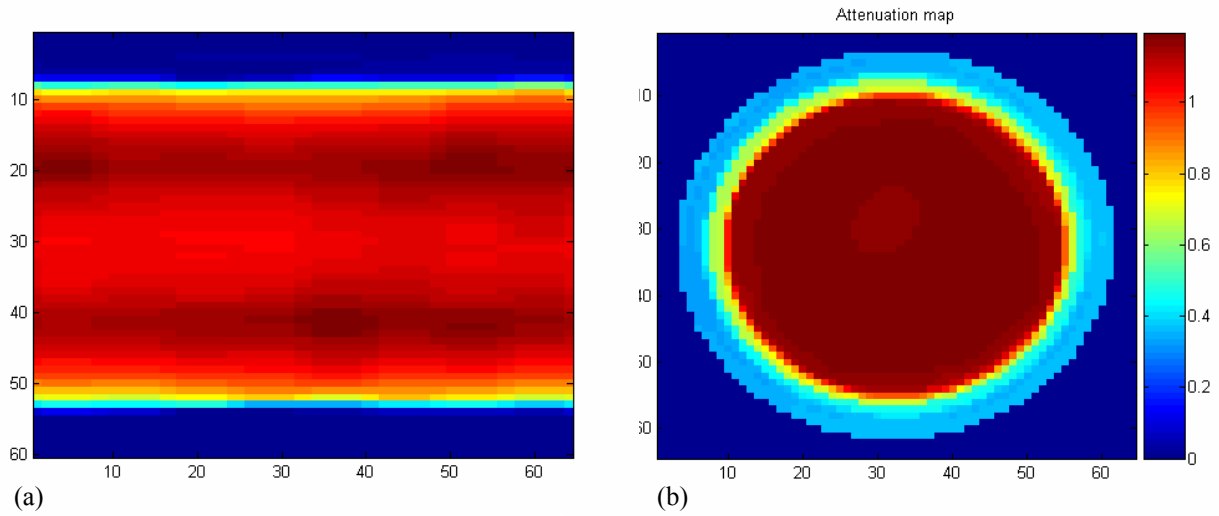
Fig. 5.5: (a) ^{137}Cs input sinogram for sample S#1 ($<r,\theta>$ domain), and (b) the derived linear attenuation coefficient map of sample S#1 scaled to 662 keV.

5.3. System Matrix Development

To calculate the elements w_{ki} (with k^{th} row and i^{th} column) of the system matrix W, i.e. the projections of the basis functions chosen to expand the distribution to be reconstructed, it is necessary to develop a model of the system, simulating the transport of the photons in the materials and geometrical configurations corresponding to those used in the experiments. Clearly, the system model has to be as representative as possible of the material compositions and the geometry of the system. In particular, the dimensions of the sample, the collimator, and the detector (crystal) should be well represented, and the relative position of the slit/collimator/detector with respect to that of the sample should be simulated as accurately as possible. The role of the system matrix is to relate the geometry of the tomographic system to an image grid defined within its field of view by way of a realistic interpolation model. Thus, each element defines the probability of an emission being registered in the detector after having originated from a known image location. In principle, two main approaches are possible for simulating the transport of the photons, viz. via use of either a stochastic code such as

MCNP [bri] or a deterministic tool such as QAD-CG [qad]. However, application of a stochastic approach is not realistic in the present situation because of the computational time that would be required, as explained below.

QAD-CG is not very flexible as regards the source distributions that can be implemented. The only variations that can be defined as functions are cosine distributions. For this reason, the source was defined by subdividing the source area into square pixels (Cartesian coordinates), by sequentially calculating the desired detector response to a uniform source located in each pixel, and by combining these responses using weights that are determined by the average value of the source intensity (analytical function) in the corresponding pixel. This approach requires a large number of pixels in order not to distort the distribution. In the present case, a flat distribution was chosen to achieve a uniform system model, not dependent on the source distribution. Using equal area pixels as basis functions, weighting factors must be attributed to account for the pixels intersected by the pin periphery, when calculating the system matrix elements.

To obtain a sufficient resolution, the number of square pixels I must be large (typically "50x50"). Currently, the image grid of "64x64" pixels, each of 200 μm width, was considered a good option. Each pixel is discretised during the computation using an internal mesh of "60x60x5" (number of source points in the x, y and z-direction). The total number of projection elements K is equal to k x m, where k is the total number of pin lateral displacements (60) and m is the total number of pin rotations (8). Theoretically, a calculation must be performed for each angular position and each step of the lateral scan with a uniform photon source in each pixel. Thus, the total number of calculations required to obtain the system matrix elements is equal to $T = I$ x $K= 1966080$. However, accounting for symmetries in the system and omitting the calculations corresponding to zero source-emission elements, this number can be reduced considerably. Considering a radial symmetry in the pin source distribution, the number of lateral steps k can be halved (30), and m can be reduced to 2 (simulating with the code only the angular positions at 0° and 45°). Using symmetry to evaluate all the other angular positions, the 64 angular projections can be obtained by interpolation. The total number of calculations T is finally reduced to 101520, which is much less than before, but not small enough to allow a stochastic approach in a "reasonable" time. The deterministic approach seems to be the only one appropriate, with Cartesian pixels chosen as basis functions. Further, once the pixel responses are available, this method is very flexible for implementing any type of basis functions one wishes to use, since responses to nearly any type of function can be derived by scaling without any additional simulation.

The system matrix elements, once calculated for one sample, do not need to be re-calculated for the other samples, first because the measurement geometry was kept exactly the same for all the samples, and second because the fuel density distribution is not used at this stage of the process. The simulation was performed for 14 energy groups (all the detectable gamma-rays coming from ^{137}Cs, [134]Cs and [154]Eu) to obtain a system model allowing different photon energy options. As regards fuel density related information, the linear attenuation coefficient maps, derived with transmission tomography, were used not in the matrix development, but rather later, directly by the reconstruction process routines.

The deterministic photon transport code which has been employed for the system matrix calculation, as mentioned earlier, is QAD-CG. This is a point-kernel ray-tracing code. The point kernel, representing the transfer of energy by the uncollided flux along a line-of-sight path, is optionally combined with an appropriate buildup factor to account for photon scattering contributions. However, only first flight photons are of interest here. Thus, for an isotropic source emitting S(r) photons of energy E per second per unit volume, the basic expression for the uncollided flux is:

$$I(\vec{r}) = \int_V \frac{S(\vec{r}\,')\exp(-\mu\langle\vec{r}-\vec{r}\,'\rangle)}{4\pi\langle\vec{r}-\vec{r}\,'\rangle^2}dV \tag{5.7}$$

where $\vec{r}$ is the point at which the gamma flux is calculated, while $\vec{r}\,'$ is the location of the source in volume V, and μ the total attenuation factor.

The global system matrix W is a multidimensional matrix $[i,j,k,m,en]$ ($i = j$ = the number of pixels, k = the number of steps, m = the number of angles, and en = the number of energy groups) of dimensions [64,64,60,64,14]. From this basic matrix, it is possible to extract a sub-matrix appropriate to a desired photon energy. This sub-matrix is then converted into a format suitable for the tomographic reconstruction routines (.wtf), using Aspire 3.0 [fes] software commands. All the routines for the development of the system matrix have been coded in FORTRAN. However, Aspire gives the possibility to develop a simplified system matrix which just implements basic information on the geometry of the system. This option is interesting for studying the impact on the sinograms of different system models, but it is less effective than implementing a global system matrix as described above.

5.4. Reconstruction Techniques

5.4.1. <u>Statistical model for emission</u>

As mentioned in Section 4.2.2, the Poisson nature of the measured data cannot be guaranteed if one applies corrections (such as those for radioactive decay, branching ratios, cladding and filter attenuation compensation), because these affect the frequency distribution of the raw data [erd]. Theoretically, this is the case for SPECT when an absolute activity needs to be calculated. Nevertheless, the Poisson nature of the data can be assumed to be preserved if only relative estimates of activity or concentration are required, since only rather small corrections are necessary to the raw data. In this way, a statistical approach similar to that for the transmission tomography case can be employed, using the transform method (i.e. FBP) [bra-ram-her] for the evaluation of the first-guess image, and appropriate statistical methods for the optimisation of the results.

Let the emission distribution be characterised by N pixels with non-negative emission rates x_j, and let the measured counts y_i denote the emission density (for γ-ray i) of the jth pixel. We may now assume independent Poisson distributions [fes2]:

$$y_i \sim Poisson\left\{\sum_j a_{ij}x_j + r_i\right\}, i = 1,....,k \qquad (5.8)$$

where r_i is the mean value of background events (Compton scattering), $a_{ij} = c_i g_{ij}$ where c_i are the ray-dependent calibration factors (such as detector efficiency), g_{ij} represents the geometric portion of the system matrix, k is the number of measured γ-rays, and $j = 1,....,N$ with N the total number of pixels.

In the implementation of iterative methods, the background events contribution r_i is usually provided to the algorithm input. In this study, instead, the collected measured γ-ray projections are implicitly cleaned from Compton scattering by using the previously described peak area treatment (Section 5.2), such that no additional correction is required in the reconstruction phase. This approach may lead to more precise results [oga].

The cost function for the implementation of iterative methods has been developed and used in the same way as described in Section 4.2.2. The several tomographic algorithms used for the reconstruction of within-pin distributions are described in the following sub-section.

5.4.2. Methods employed

The reconstruction techniques employed to obtain the results presented in this section are listed below, together with the corresponding acronym used:

- Filtered Back-Projection (FBP)

- Maximum-Likelihood Expectation-Maximisation (ML-EM) [lan]

- Ordered Subset Expectation Maximisation (OSEM) [hud]

- Penalised Maximum-Likelihood with Space-Alternating Generalised EM (PL-SAGE) [fes2-fes3]

- Penalised Maximum-Likelihood with Ordered Subset De Pierro (PL-DP) [dep]

- Penalised Maximum-Likelihood with Paraboloidal Surrogates Coordinate Ascent (PSCA) [erd]

- Penalised Weighted Least Square (PWLS) [fes4]

Some words need to be addressed to explaining how the above methods have been implemented. Basically, the FBP method works without the global system matrix. It uses the input sinogram, a system file for geometrical description, and a calibration sinogram C_i built with the Aspire [fes] routines from the linear attenuation coefficient map derived by transmission tomography. All the other methods also use the system model W' and the FBP result as an initial image to start the iterations. ML-EM and OSEM are unregularised methods (no penalty functions are used), and their results may be less accurate than the other regularised techniques.

Before the final implementation of such image reconstruction methods to investigate radio-nuclides within-pin distribution in spent fuel rods, a preliminary study has been carried out to test their response on known and simple simulated shapes, as described in the following sub-section.

5.4.3. Simulation tests

Some simple source shape distributions have been defined and used to test the reconstruction techniques and to set the main parameters. Especially the filter to be used in the FBP algorithm, the trade-off parameter β [fes5], the iterations number, and the penalty function parameters [hub-fes4] (when used) were chosen by trial and error, until a valid reconstruction was obtained. Subsequently,

having been tested for known artificial distributions, the same settings of these parameters were used for the real measurements.

The projections for the simulation were developed from the system model, using the FORTRAN procedures written for the development of the system matrix, with slight modifications. Two main cases are shown here, because they are quite representative of the problem at hand:

1. A cylinder of the same circumference as the fuel pins, with a flat distribution.

2. A narrow ring, with a flat distribution.

The second case, the flat ring distribution, was considered to be a test of particular relevance to the centrally depressed distributions that are expected in these studies. In fact, it can be considered as an extreme case (not so easy to deal with), where the source is distributed annularly and diminishes to zero in a steep step. The other flat case is, nevertheless, an interesting test of the quality of the reconstructed image.

The results are shown here for the two cases. Fig. 5.6 shows a comparison of the results obtained with the most promising methods for the reconstruction of Case 1. Pictured is a view of the vertical section taken at the image centre. The y-values in the plots are normalised to unity for the highest value in each case. At first glance, one can say that the PSCA and the FBP images are the ones that provide the most realistic answer. The FBP, even if it is used just as a first guess for further iterations, despite being quite an old method (not even provided with the system efficiency model), gives very reasonable results, conserving the physical properties of the object investigated. Clearly, the best answer comes from the PSCA method, where the edge-preserving penalty function ensures a realistic image with good resolution, respecting the physical properties of the body. The presence of small undulations at the top of this image is a consequence of the filter function used in the FBP algorithm (a sinusoidal filter "sinc(x)"). This is, actually, not a big problem to deal with, because such undulations are relatively easy to recognise during the elaboration of real images, as compared to other artefacts (e.g. rounded edges produced by PL techniques) where more complicated post-processing methods need to be used. The implementation of this filter was chosen because of its relatively good performance at the edge of the images, although it does not completely preserve the integrity of the fuel pin periphery. On the other hand, other tested filters showed unsatisfactory treatments of the edge and were also not completely free from undulations.

A selected 3D image is shown in Fig. 5.7 for (a) FBP, and (b) PSCA.

In the present analysed case, one can assert that other methods do not compete with PSCA. The main problem of the PL-SAGE, PL-DP and PWLS techniques, in this specific case, is their implementation

of quadratic penalty functions that tend to "over-smooth" the edge of the image, as is clearly seen in Fig. 5.6. This limitation is basically related to the ASPIRE toolbox, which is able to implement several methods with several penalty functions, but is not able to cover all the quite large number of combinations.
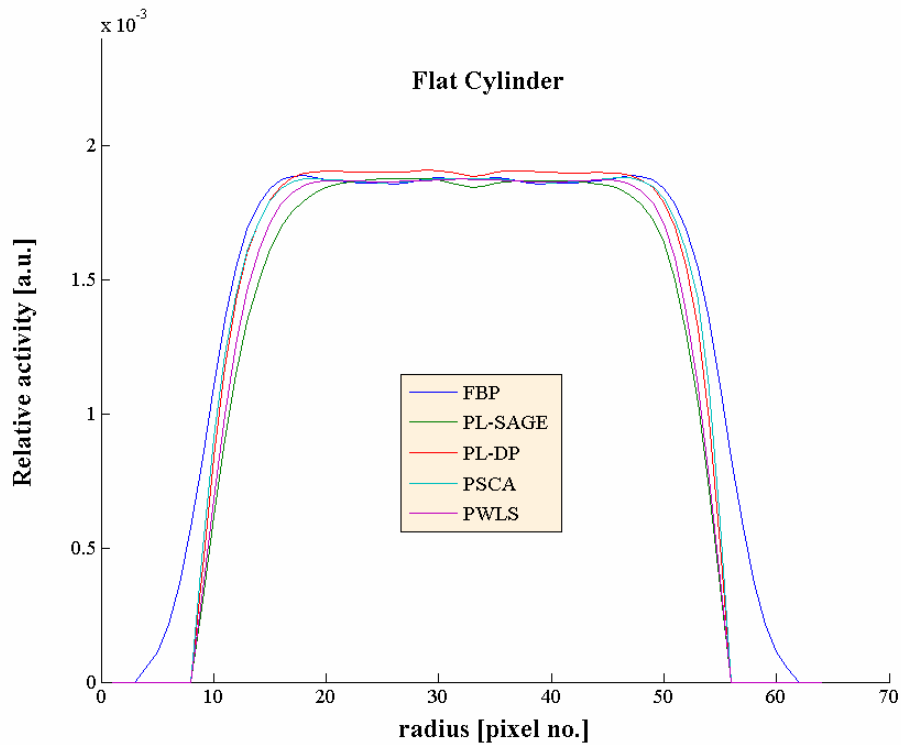

Fig. 5.6: Flat cylindrical distribution reconstructed by FBP, PL-SAGE, PL-DP, PSCA and PWLS methods. The values in each plot are normalised to the highest value.
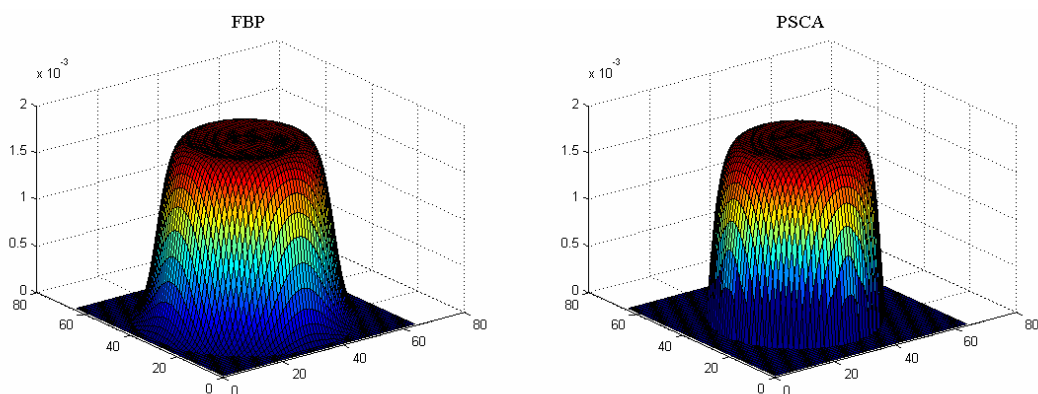

Fig. 5.7: 3D image of a flat cylindrical distribution reconstructed by (a) FBP, and (b) PSCA.

It should be noted that these pictures are discrete images, constructed of pixels. This means that lines that are neither exactly vertical nor exactly horizontal will have a ragged appearance, a point which needs to be borne in mind during the evaluation of all the reconstructed images.

The second case considered for this simulation, the small ring, will be treated in greater detail. In Fig. 5.8a, a sinogram of the projection is shown for illustration purposes. In Fig. 5.8 (b) to (h), the results of the reconstructions (horizontal view) made with FBP, ML-EM, OSEM, PL-SAGE, PL-DP, PWLS and PSCA, respectively, are shown**.**

(a)

(b)

(c)

(d)

(e)

(f)

(g)   (h)
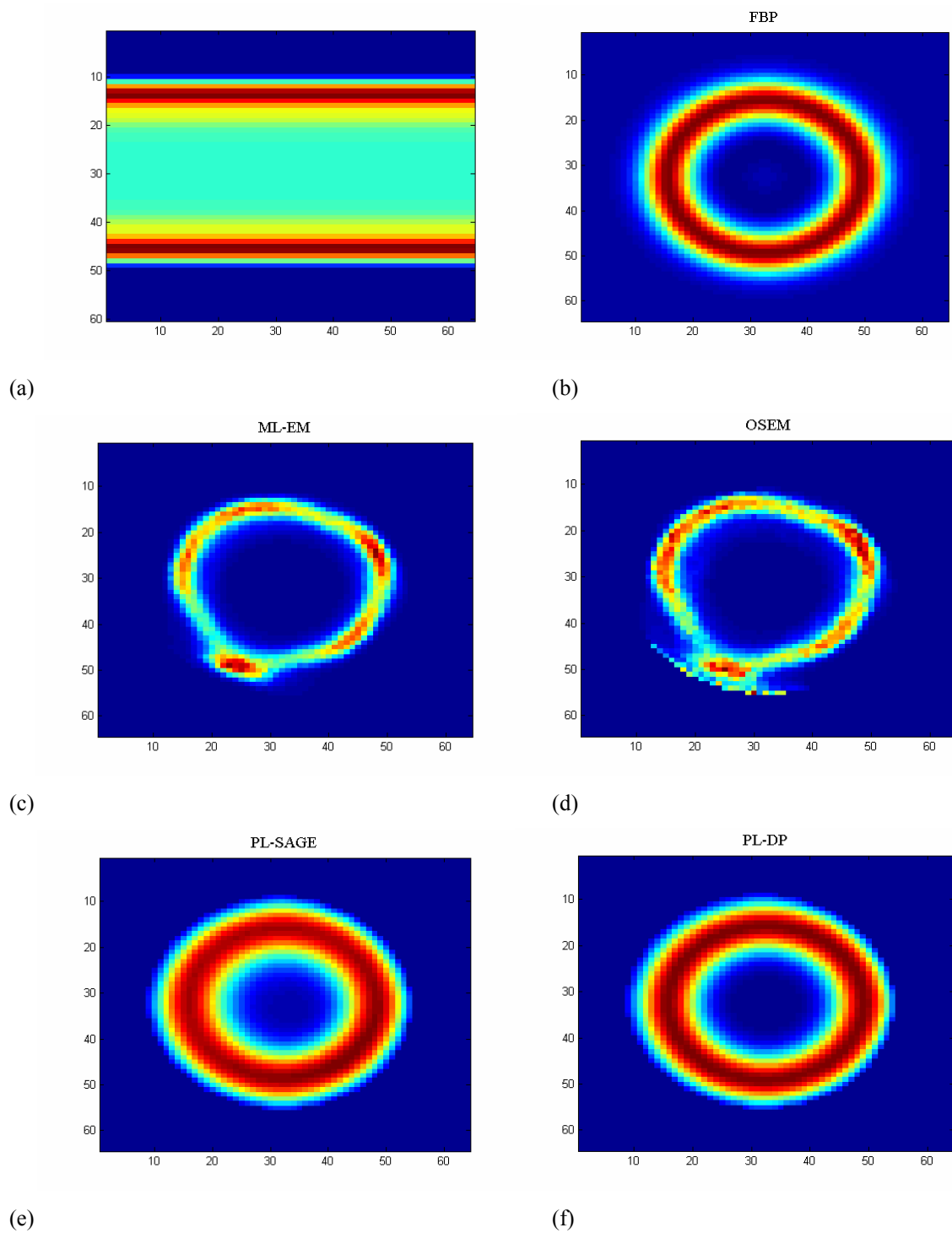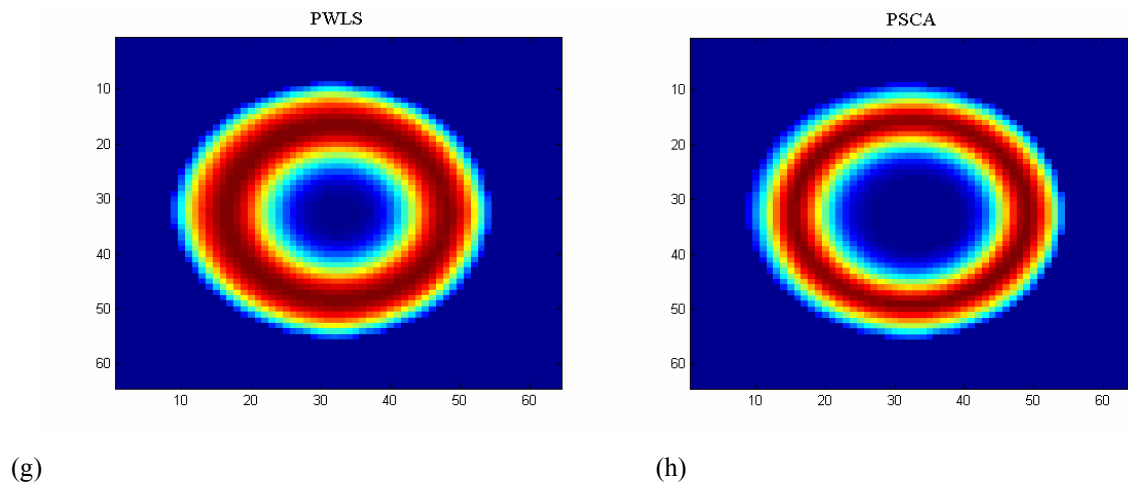
Fig. 5.8: (a) Sinogram of a ring distribution, and (b) to (h) results using, respectively, the following reconstruction techniques: FBP, ML-EM, OSEM, PL-SAGE, PL-DP, PWLS and PSCA.

The ML and OSEM results are not satisfactory, as expected for unregularised methods. In this case, additional post-processing work needs to be done to achieve better performances. The FBP gives a good performance. The others are fairly faithful to the real geometry, but the image is too blurred (especially for PWLS). PSCA gives quite a sharp distribution, much closer to reality, as shown in Fig 5.9a. In Fig. 5.9b, the results of FBP and the other regularised methods are compared for a vertical cut view, normalised in each case to the greatest PSCA value.

(a)   (b)
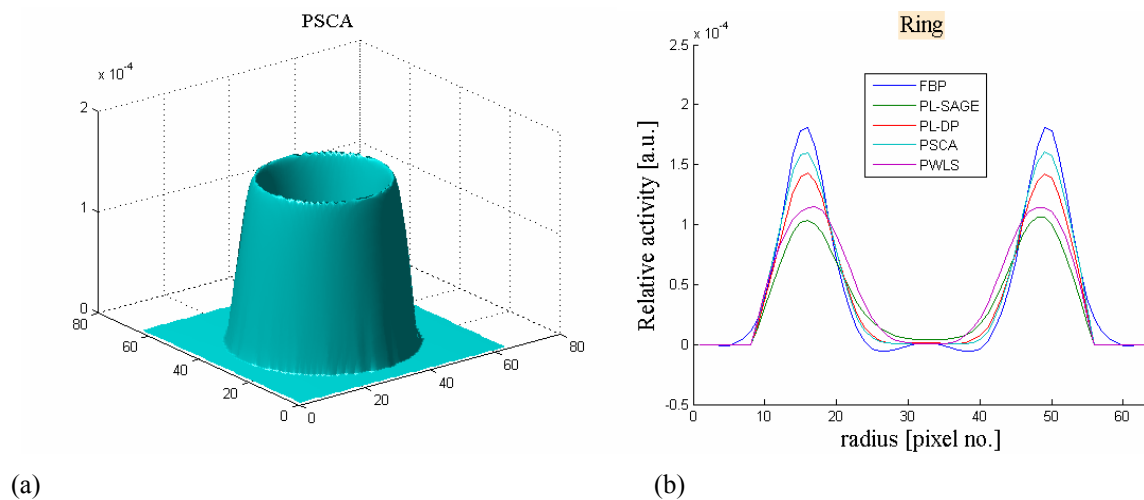
Fig. 5.9: (a) 3D image of the ring distribution obtained with PSCA, and (b) vertical cut views of images reconstructed with the best performing methods (normalised to the highest PSCA value in each case).

Of all the methods employed, PSCA is seen to show the best performance, modelling much better the depressed region than the others, and has, in the following, been adopted as the standard algorithm for emission tomography on the spent fuel rod samples. One may argue about the capability of such a technique to model exactly the peripheral region, which ideally should not suffer from smoothed edges. Nevertheless, the difficulties stemming from the relatively small number of projections

119

employed here and the limitation in the use of edge-preserving filter functions must be borne in mind, before any attempt is made to compare the quality of standard medical image reconstructions with these results [kak].

5.5. Image Reconstruction Results

5.5.1. Within-pin radionuclide distributions

Once the measured data were processed and converted to the correct format, the system matrix built, and the tomographic reconstruction techniques tested and customised for the investigation of within-pin radionuclide distributions, progress could be made towards the final reconstructions.

The relative within-pin distributions of ^{137}Cs (662 keV γ-line), ^{134}Cs (795 keV γ-line) and ^{154}Eu (1275 keV γ-line), reconstructed using the Aspire 3.0 program are shown in the following figures, with horizontal view (left) and 3D image (right) for sample S#1 (Fig. 5.10), sample S#2 (Fig. 5.11), sample S#3 (Fig. 5.12) and sample S#4 (Fig. 5.13). The algorithm used is the PSCA, with a trade-off β=5. The first guess is produced with FBP, using a sinusoidal filter function which best matched the penalised methods used in the final reconstruction.

The best performance has been obtained using the Huber penalty function (see Equation (4.15)), with a resolution setting of δ=0.02 and with a 2nd-order neighbourhood. Two iterations ensured a satisfactory image with low noise propagation. The relative activity is plotted in arbitrary units (a.u.). From the observation of the ^{137}Cs and ^{134}Cs distributions shown in Fig. 5.10 - 5.13, one may notice that the caesium is concentrated in the peripheral region. At the centre of the pin, there is a large depression in the distribution, in the nature of a hole. This hole in the caesium is very large in the case of sample S#1, and extremely large in S#4 (a factor of ~2.5 for ^{137}Cs, a factor of ~3 for ^{134}Cs), the ultra-high burnup sample. Further, ^{137}Cs and ^{134}Cs distributions seem to be slightly different to each other in most pins, with ^{134}Cs having a more prominent central depression. The relative activity distribution of ^{154}Eu seems to be quite flat in comparison to caesium. However, the ^{154}Eu interpretation is more problematic because of the presence of undulations on the image, which originate and propagate from the initial noise present in the input sinograms and from the sinusoidal filter employed by the FBP algorithm.
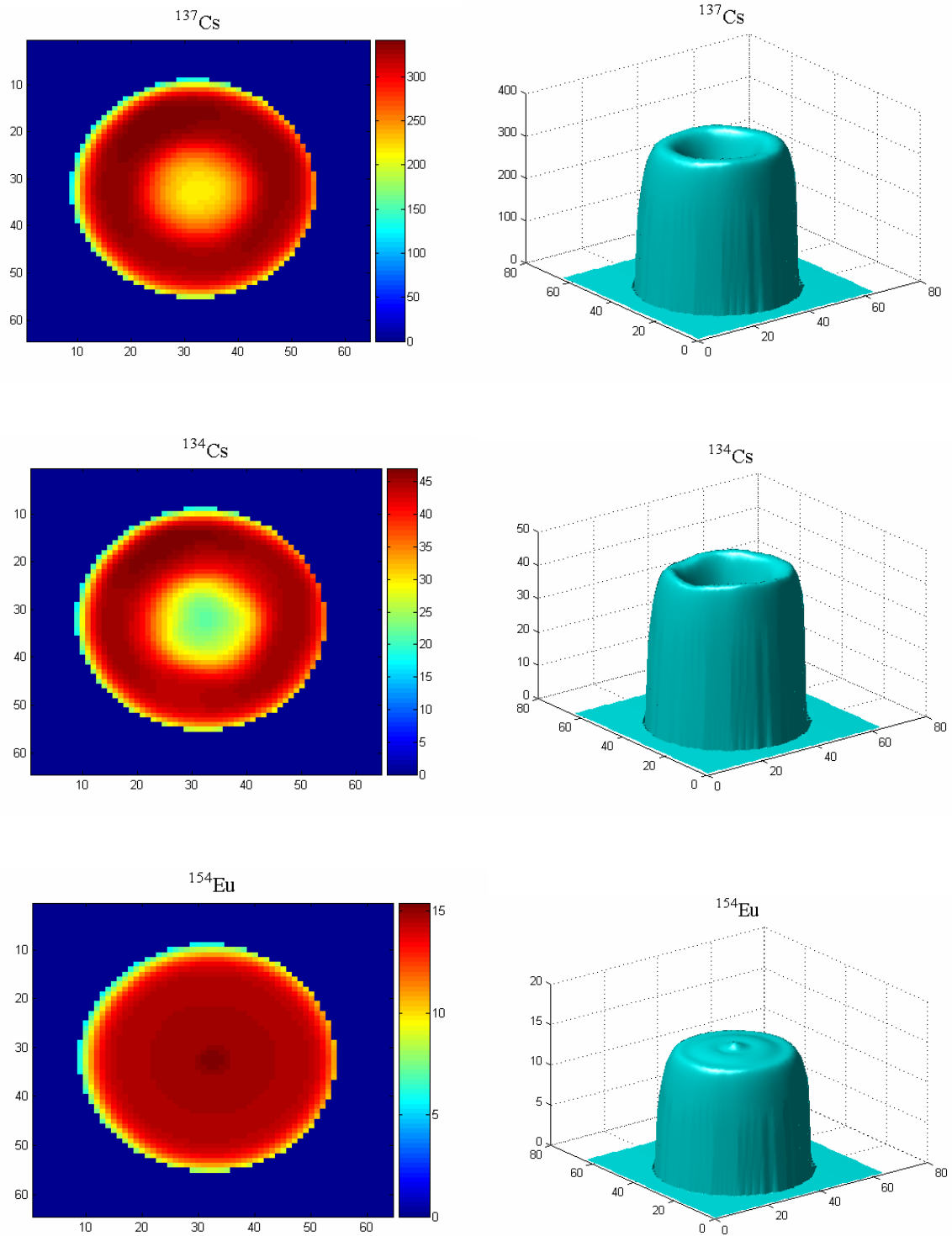
Fig. 5.10: Relative within-pin activity (a.u.) distributions of ^{137}Cs (upper), ^{134}Cs (middle) and ^{154}Eu (lower) for sample S#1, reconstructed with PSCA. Plan view on the left, and 3D image on the right.
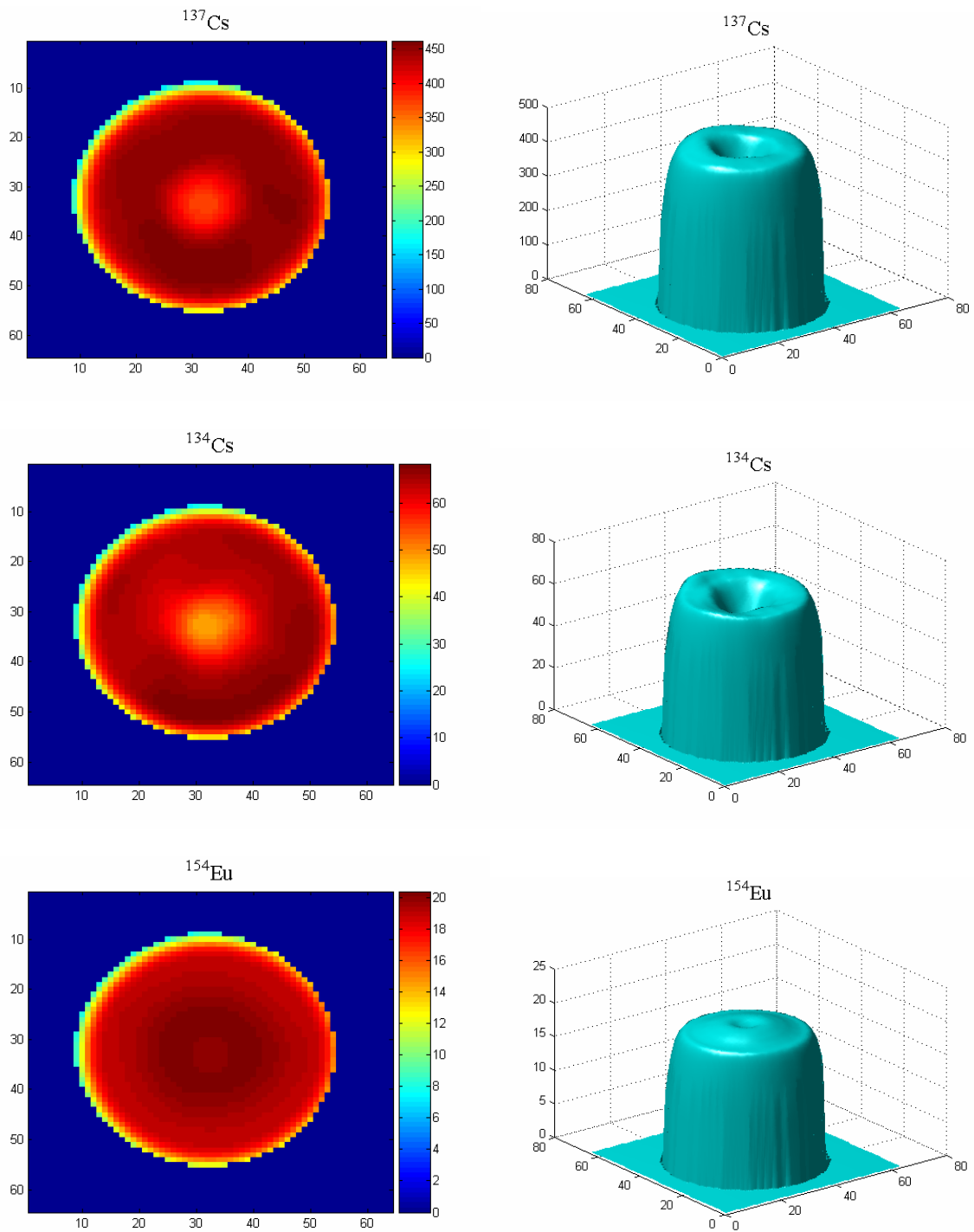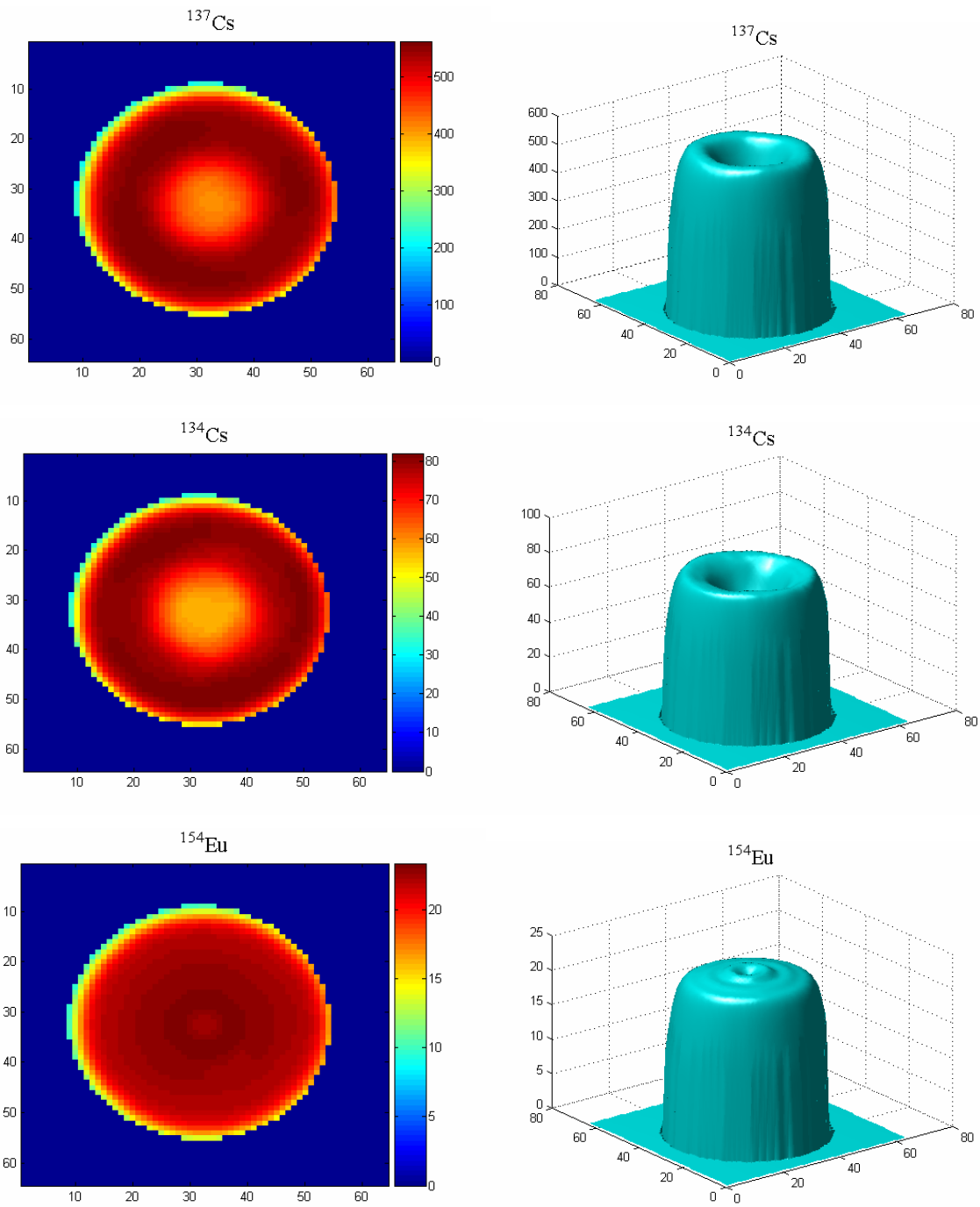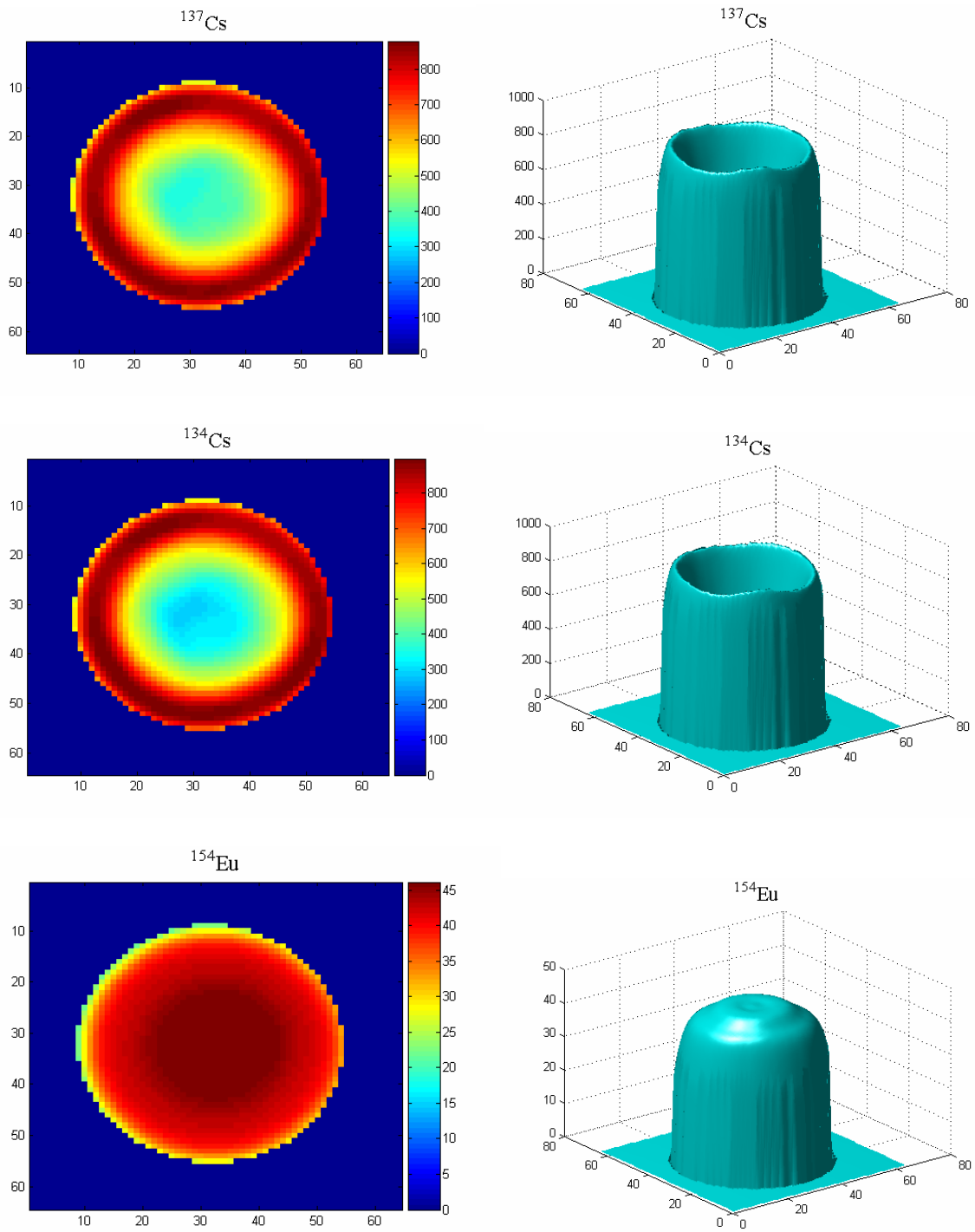
Fig. 5.11: Relative within-pin activity (a.u.) distributions of ^{137}Cs (upper), ^{134}Cs (middle) and ^{154}Eu (lower) for sample S#2, reconstructed with PSCA. Plan view on the left, and 3D image on the right.

Fig. 5.12: Relative within-pin activity (a.u.) distributions of [137]Cs (upper), [134]Cs (middle) and [154]Eu (lower) for sample S#3, reconstructed with PSCA. Plan view on the left, and 3D image on the right.

Fig. 5.13: Relative within-pin activity (a.u.) distributions of ^{137}Cs (upper), ^{134}Cs (middle) and ^{154}Eu (lower) for sample S#4, reconstructed with PSCA. Plan view on the left, and 3D image on the right.

The caesium input sinograms were much cleaner than those for the europium, the latter having worse counting statistics[16]. For this reason, the europium sinograms were characterised by more scattered projections, consequently affecting the final sinogram. In order to avoid such noise propagation from the initial sinogram, and because the azimuthal variation was estimated to be quite negligible (evident from the observation of the different measured angular projections), the final sinogram was developed by averaging the angular projections.

The central undulations originating from the "first guess" may be corrected by the iterative methods at the cost of smoothing the images. However, this is not acceptable for our kind of analysis based on PSCA, which is less effective in the suppression of this kind of disturbance compared to other methods, especially PL-DP (see Fig.5.16). However, the PSCA method has the ability to preserve, at least partially, the edge of the image if compared to the other methods. Nevertheless, even if the produced europium images suffer from smoothed edges and undulation effects at the pin centre, one may exclude the presence of a deep central hole in the ^{154}Eu distribution, but the possibility of a light depression can not be excluded.

In Fig. 5.14, the relative activity distributions (in arbitrary units) of ^{137}Cs, ^{134}Cs and ^{154}Eu are plotted in a vertical cut view at the centre of the image, for samples S#1, S#2, S#3 and S#4. The values in the plots are corrected for decay to discharge time. The reconstruction method is the same as before (PSCA). The error bars correspond to 1σ, derived with a sensitivity study (see Section 4.4.4).

---

[16] Actually the statistics of europium, from the 1275 keV photo-peak used for tomography, are initially not so bad, but the subsequent background correction (as described in Section 5.2) is the relevant factor responsible for the worsening of the final uncertainties.
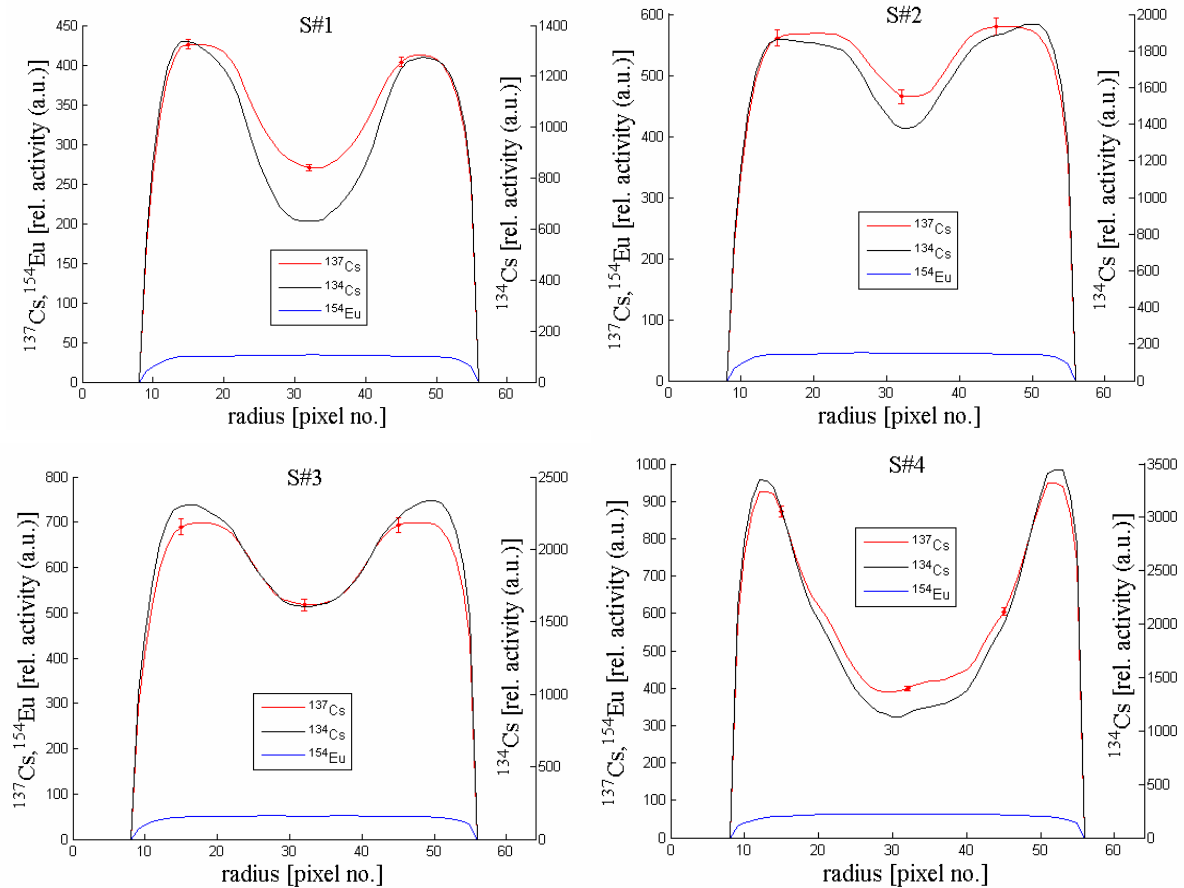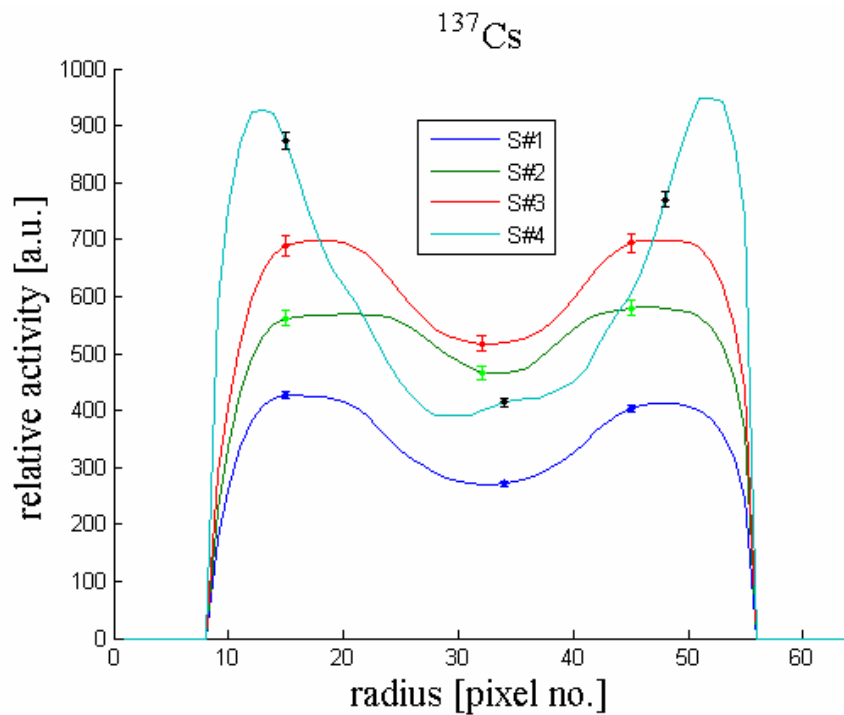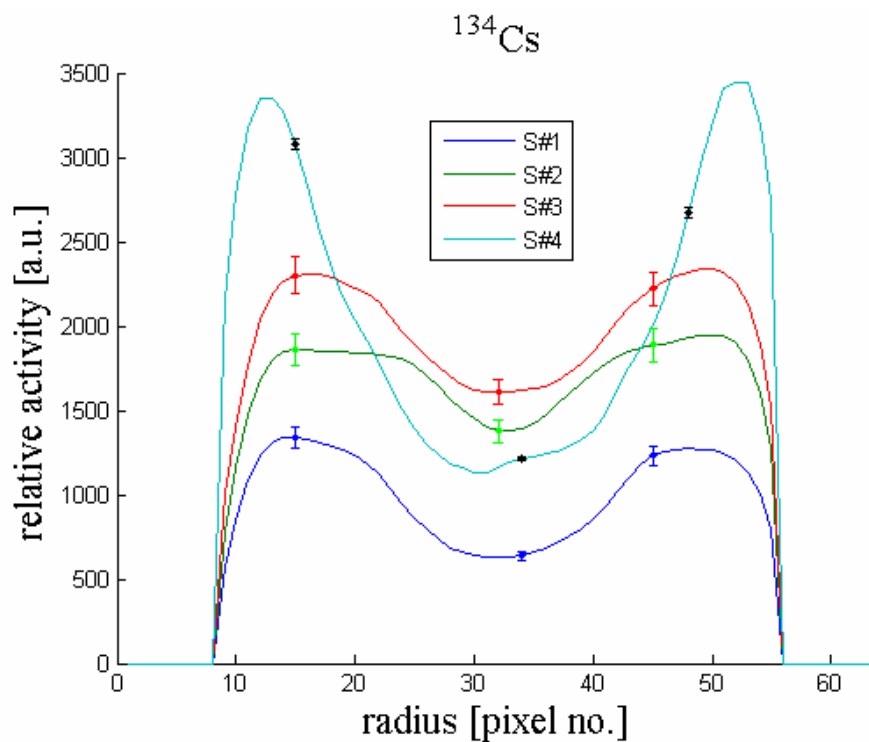
Fig. 5.14: Relative activity distributions, decay corrected at discharge time and in arbitrary units (a.u.), of ^{137}Cs, ^{134}Cs and ^{154}Eu in samples S#1, S#2, S#3 and S#4, reconstructed with PSCA, in a vertical cut view at the centre of the image. The error bars correspond to 1σ, derived from a sensitivity study.

From Fig. 5.14, it is clearly evident that there are differences, to a greater or lesser extent, between the relative activity distributions of ^{137}Cs and ^{134}Cs for each sample. In fact, the depression of ^{134}Cs seems to be more marked than that for ^{137}Cs. This may be due to the different origins of the two isotopes. The ^{137}Cs is created effectively directly by fission, as it is at the end of a short-lived fission product decay chain, and its migration then starts from its point of birth. The ^{134}Cs, however, is the result of neutron capture in the ^{133}Cs fission product, which could have already started to migrate towards the rod periphery. It follows that these two isotopes could have different within-pin distributions, especially after long residence in the reactor. Other studies confirm such differences in the two distributions [phi-hsu], and assert that these distributions are also a function of the axial position. The amount of migration depends on the temperature (no caesium migrations at a fuel centreline temperature <1200°C), the oxygen-to-metal ratio (the higher the ratio is, the less migration tends to occur), the fuel density, and the burnup.

In Fig. 5.15, a comparison between the four samples has been made for the ^{137}Cs, [134]Cs, and [154]Eu relative activity distributions. Here again, the values are corrected for decay at discharge time. The error bars on the plots are the 1σ uncertainty, derived with the sensitivity study, the numerical results being summarised in Table 5.1.

(a)

(b)
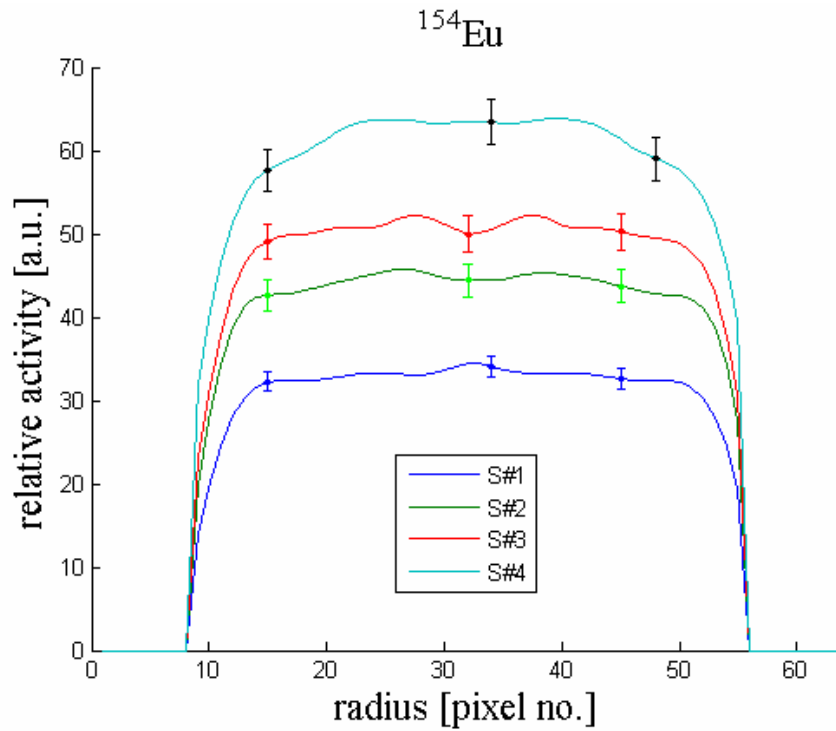
(c)

Fig. 5.15: Relative activity distribution of (a) ^{137}Cs, ^{134}Cs (b) and ^{154}Eu (c) for all the spent fuel rod samples. The reconstruction is with PSCA, each plot corresponding to a vertical cut at the centre of the image. The error bars correspond to 1σ, derived from the sensitivity study.

Noting the standard deviations reported in Table 5.1 (and in Fig. 5.15c), the decrease of precision for the europium reconstructions, as explained previously, appears after subtraction of the background activity leaking through the collimator block at the relatively high energy of 1275 keV. The differences in the standard deviations between samples are due to the different counting statistics (due to different "live times" during spectra acquisition and the different activity and cooling time of each sample).

Table 5.1: Uncertainty (1σ) values calculated for the ^{137}Cs (662 keV γ-line), ^{134}Cs (795 keV γ-line) and ^{154}Eu (1275 keV γ-line) distributions in the four spent fuel rod samples.

	1 σ [%]			
	S#1	S#2	S#3	S#4
^{137}Cs	1.4	2.4	2.5	1.7
^{134}Cs	4.6	5.2	4.6	1.1
^{154}Eu	3.6	4.4	4.4	4.3

In Fig. 5.16, the results of using different algorithms (FBP, PL-SAGE, PL-DP, PSCA, and PWLS) are compared for the within-pin activity reconstruction of (a) ^{137}Cs for sample S#4, and (b) ^{154}Eu for sample S#3. Actually, all the proposed techniques produce a central depression of the caesium, although to different extents. The main differences arise at the periphery of the pin, where, in the case of PL-SAGE, PL-DP, and PWLS, the distributions are over-smoothed. The regularised PSCA method, implementing Huber penalty functions, ensures edge preservation. The unregularised FBP also gives surprisingly good results. Concerning the europium, as explained above, PSCA does not correct the undulations as well as the others, but preserves the edge much better.

(a)

(b)
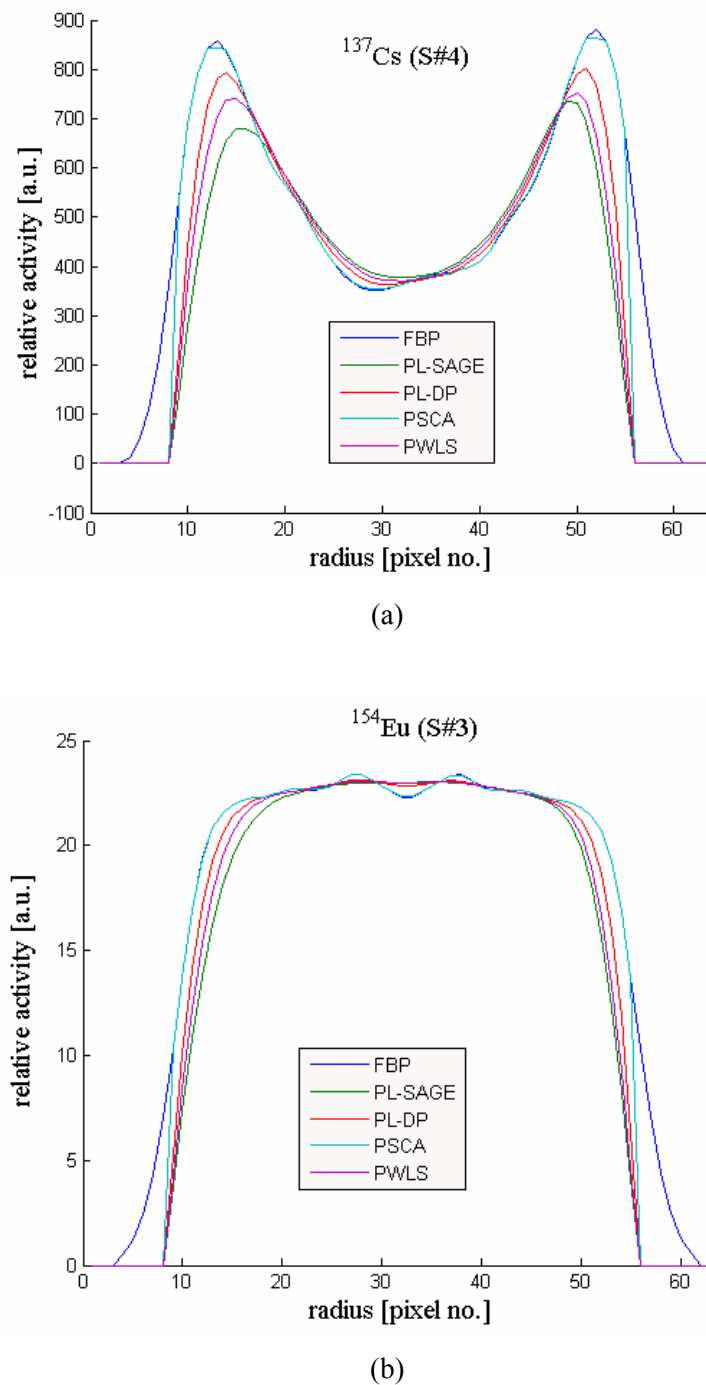
Fig. 5.16: Comparison of different-algorithm results (FBP, PL-SAGE, PL-DP, PSCA and PWLS) for the within-pin activity reconstruction for (a) ^{137}Cs, sample S#4, and (b) ^{154}Eu, sample S#3.

129

In Fig. 5.17, a 3-D reproduction of the ^{134}Cs within-pin distribution (PSCA) for sample S#4 is presented to provide more visual details. In fact, in this figure (image produced using AVS/Express program [avs]), a vertical section is shown together with iso-lines and multidimensional graphics. The details of the central region are better visible because of the advanced graphic tracings of AVS/Express. From Fig. 5.17, the within-pin azimuthal variations are also recognisable, even if this variation is purely indicative (eight angular projections are clearly not enough to describe the azimuthal variations of an object in detail).
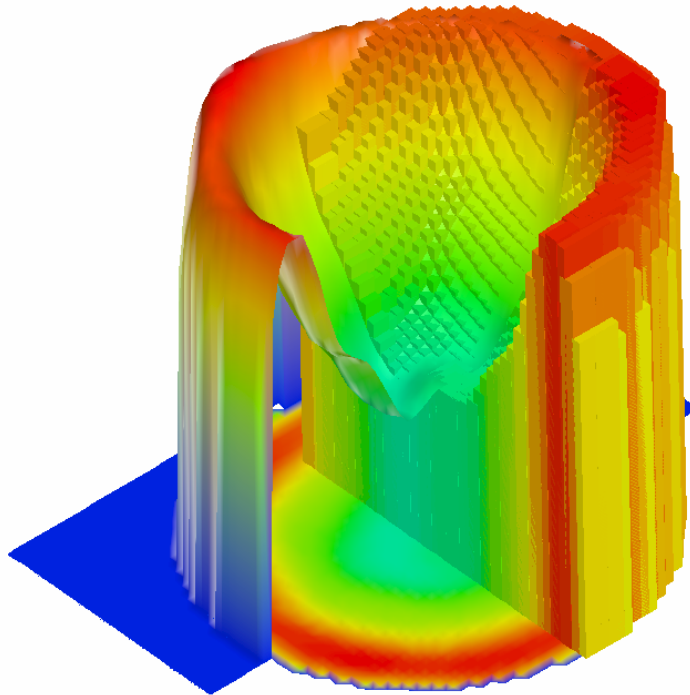
Fig. 5.17: 3-D image of ^{134}Cs within-pin activity reconstruction for sample S#4. Also shown in the same figure (image produced using AVS/Express) is a vertical section together with iso-lines and multi-dimensional graphics.

5.5.2. Distributions of fission-product concentrations

The within-pin activity distributions, derived with emission tomography, have been combined with the transmission-tomography density measurements to obtain concentration distributions (#/g cm^{-3}) for the three fission product nuclides investigated. The results, in arbitrary units, are shown in Fig 5.18 for sample S#4: ^{137}Cs (upper), ^{134}Cs (middle) and ^{154}Eu (lower), with horizontal views on the left and 3D images on the right.
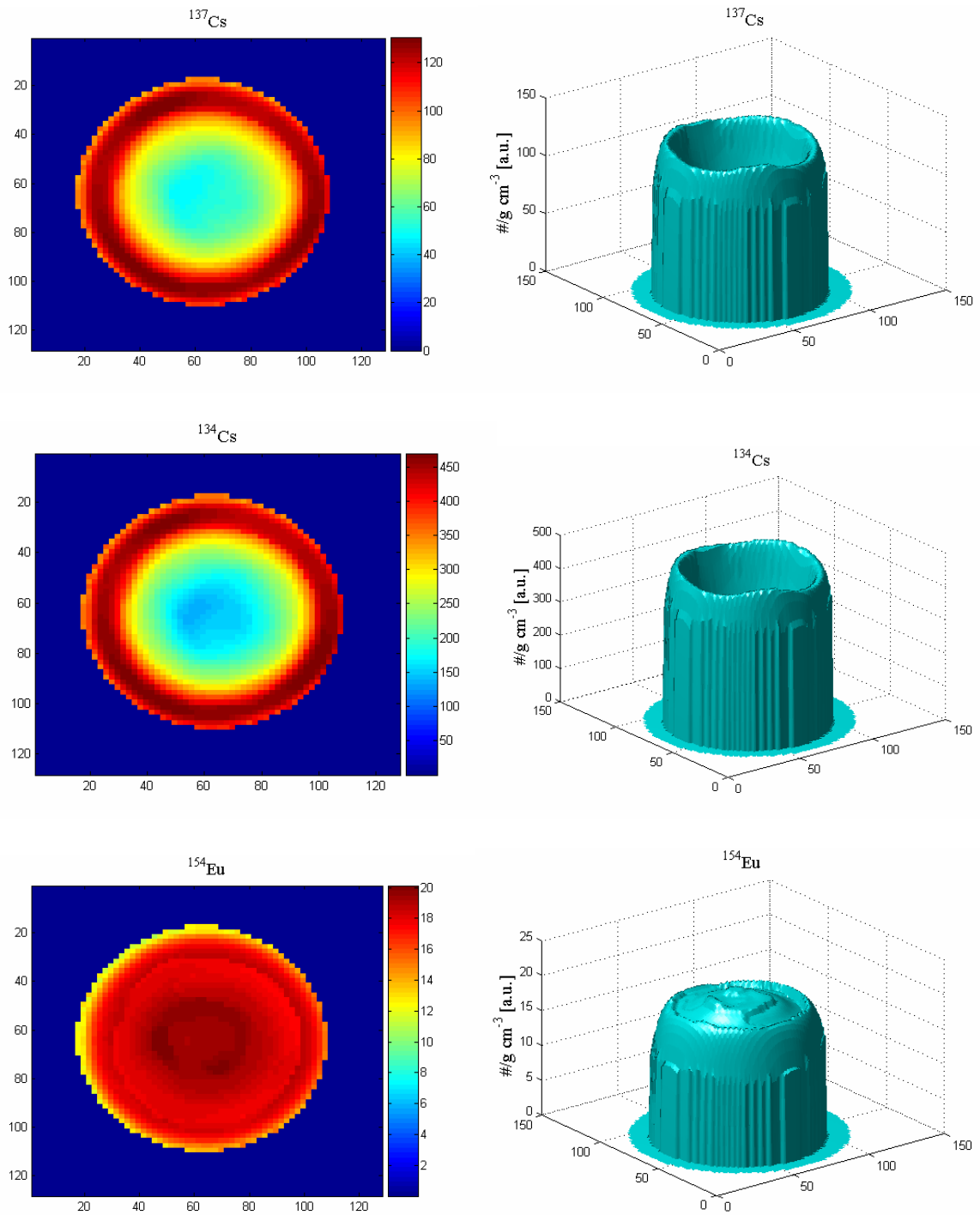
Fig. 5.18: Concentration distributions (#/g cm^{-3}), in arbitrary units, of ^{137}Cs (upper), ^{134}Cs (middle), and ^{154}Eu (lower) in sample S#4. Plan view on the left, and 3D image on the right.

5.5.3. Tomography versus chemical assays

As shown in the previous section, the results of the non-destructive technique of computerised tomography (CT), applied to high burnup fuel rods for the determination of the within-pin distribution of fission products, indicates a large central depression in the caesium distributions. The extents of the depressions vary from sample to sample and are not, apparently, related to burnup. In order to support these findings, the results have been examined with respect to destructive chemical measurements made on other samples from the same fuel rod.

Thus, some EPMA (Electron Probe Microanalysis) measurements were performed by the PSI Hotlab team [izm] on a segment of the same NPP fuel rod from which sample S#4 originated. Different within-pin elemental distributions were obtained for several fission products and actinides. Amongst these elements, caesium was investigated as well. Further, in order to obtain information about the isotopic composition, the combination of a laser ablation system with an inductively coupled plasma mass spectrometer (LA-ICP-MS), also performed by the PSI Hotlab team [izm], was used as a complementary analytical method. Amongst the various isotopes investigated, two which were free of isobaric interferences are ^{133}Cs and ^{135}Cs. These are relevant because the first is the parent of ^{134}Cs and the second is a directly produced fission product, analogous to ^{137}Cs.

In Fig. 5.19, the caesium elemental distribution, measured with EPMA, and the distribution of the ratios of ^{133}Cs/^{138}Ba and ^{135}Cs/^{138}Ba measured with LA-ICP-MS, and normalised to the average value, are compared with the within-pin distributions of ^{137}Cs and ^{134}Cs derived with emission tomography (also normalised to average values). All the techniques seem to confirm, to different extents, the peculiarity of caesium to be depressed at the centre of the pin.

The EPMA shows a large central depression, where the caesium concentration almost reaches zero. These very low values of concentration may be a side effect of the phase of sample polishing. Further, the EPMA, being applied to a generic diametrical profile along the sample, is highly sensitive to caesium spot (fuel pores/cracks filled by caesium precipitates) measurements, as is evident from the observation of Fig. 5.19 (see the spikes in the plot). This is different from the tomographic approach, which is not able to resolve caesium spots.

The LA-ICP-MS results are closer to the CT results, even if the concentrations plotted are ^{133}Cs/^{138}Ba and ^{135}Cs/^{138}Ba ratios. However, the fact that the samples analysed here are not exactly the same (belonging to the same rod but at different axial positions[17]) must be borne in mind before attempting

---

to compare the quality of the different experimental techniques. In fact, there is some evidence that the caesium distributions depend significantly on the axial position [phi].
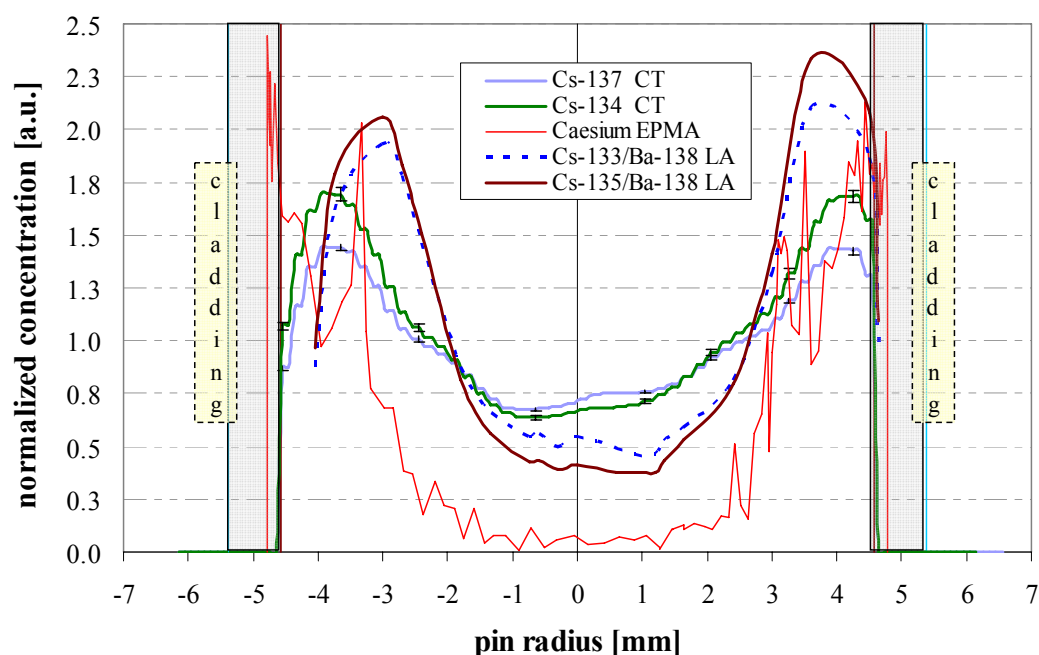

Fig. 5.19: Comparison of emission tomography (CT) results with EPMA and LA-ICP-MS (LA) results for within-pin distributions of caesium in sample S#4.

5.6. Chapter Summary

The determination of the migration of volatile fission products, such as caesium, is important from the viewpoint of characterising the behaviour and integrity of irradiated fuel rods from nuclear power plants. Thereby, destructive chemical analysis methods are usually employed.

The non-destructive technique of computerised tomography (CT) has currently been applied to high burnup fuel rods for determining the within-pin distributions of the fission products caesium and europium. The specially constructed, high resolution gamma-ray spectrometry measurement station, allowing transmission and emission tomography, has been employed for the purpose. Results provided by transmission tomography measurements have been employed in the emission tomography reconstruction phase, together with a calculated global efficiency matrix and input sinograms derived from the processing of measured projections. Different tomographic algorithms have been tested and tuned using known test distributions, and then applied to the real measurements. Amongst the various

---

[17] In the framework of the LWR-PROTEUS Phase II programme, the full-length rods were inspected first, and then punctured and cut into a number of segments. Two of these segments were subsequently used, one for the PROTEUS measurements and the other for chemical assays.

methods, described in detail in the chapter, PSCA was chosen for the presentation of the final results, because it ensures good precision, especially in resolving the most difficult peripheral regions of the pins.

The obtained results have indicated large central depressions in the caesium distributions, but of varying extent from sample to sample. Particularly interesting, is the case of the 126 GWd/t sample (S#4), showing a very deep central depression (a factor of ~2.5 for ^{137}Cs, a factor of ~3 for ^{134}Cs). In addition, a difference in the relative activity distributions of ^{137}Cs and ^{134}Cs has been observed for all the samples. In fact, the depression of ^{134}Cs seems to be more marked than that of ^{137}Cs, probably due to the different origins of the two isotopes. Other studies confirm such differences in the two distributions [phi]. In contrast, the europium shows an almost flat distribution. However, in this case, there are relatively high uncertainties in the experimental data and, because of over-smoothing of the image edge, one can not exclude the presence of a light depression.

In order to support the CT measured caesium distributions, the results of chemical analysis techniques applied to other samples from the same fuel rod (S#4) were examined. EPMA and LA-ICP-MS analyses have been performed by the PSI Hotlab team. Both these different analytical techniques compare reasonably well with the CT, showing depressed distributions at the centre of the pin. Because the samples analysed by the different techniques are not exactly the same (coming from the same rod but taken from different axial positions), and because the caesium distributions vary with the axial position, a detailed quantitative comparison of the techniques is not appropriate.

Finally, it must be emphasised that destructive chemical methods require a much greater effort than computerised tomography. For this reason, the latter, once "tuned" and tested, can indeed be considered a very valid approach, especially if "on-line" measurements need to be carried out.

References

[avs] AVS/Express Visualization Edition, Version 7.0

[ale] A. ALEXA, T. CRACIUNESCU, G. MATEESCU, R. DOBRIN, "The Tomographic Maximum Entropy Method in the 3-D Analysis of Nuclear Fuel Pins", *J. Nucl. Mat.*, **218**, p.139 (1995)

[bar] B.K. BARNES, J.R. PHILLIPS, M.L. BARNES, "Reconstruction of radial fission product distributions in reactor fuels from a small number of projections", *J. Nucl. Mat.*, **106** p.147 (1982)

[bou] L. BOUWENS & al., "Image-correction techniques in SPECT", *Computerized Medical Imaging and Graphics,* **25** p.117 (2001)

[bra] R.H. BRACEWELL & A.C. RIDDLE, "Inversion of fan beam scans in radio astronomy," *Astrophysics Journal*, **150** p.427 (1967)

[bri] J.F. BRIESMEISTER, "MCNP – A General Purpose Monte Carlo N-Particles Transport Code", Version 4C LA-12625-M

[buu] H. A. BUURVELD, G. DASSEL, "Emission Computer Tomography on a Dodewaard Mixed Oxide Fuel Pin", *Report ECN-C—93065*, Petten (1993)

[dep] A.R. DE PIERRO, "A modified expectation maximization algorithm for penalized likelihood estimation in emission tomography", *IEEE Trans. Med. Imag.,* **14**(1) p.132 (1995)

[erd] H. ERDOGAN, J.A. FESSLER "Ordered subset algorithms for transmission tomography", *Phys. Med. Biol.,* **44** p.2835 (1999)

[fes] J.A. FESSLER "Aspire 3.0 User's Guide: A Sparse Iterative Reconstruction Library", Technical Report No. 293 Communications & Signal Processing Laboratory, University of Michigan (2001)

[fes2] J.A. FESSLER, A.O. HERO, "Penalized Maximum-Likelihood Image Reconstruction Using Space-Alternating Generalized EM Algorithms", *IEEE Trans. Image Processing*, **4**(10) p.1417 (1995)

[fes3] J.A. FESSLER, A.O. HERO, "Space-Alternating Generalized Expectation-Maximization Algorithm", *IEEE Sig. Proc.*, **42**(10) p.2664 (1994)

[fes4] J.A. FESSLER, "Penalized Weighted Least-Squares Image Reconstruction for Positron Emission Tomography", *IEEE Trans. Med. Imag.*, **13**(2) p.290 (1994)

[fes5] J. A. FESSLER "Spatial resolution properties of penalized likelihood image reconstruction: space invariant tomographs", *IEEE Trans. Image Processing*, **5**(9) p.1346 (1996)

[her]   G.T. HERMAN, "Image reconstruction from projections: The fundamentals of computerized tomography", *Academic Press*, New York (1980)

[hsu]   S.T. HSUE, T.W. CRANE, W. L.TALBERT, J.C. LEE, "Nondestructive Assay Methods for Irradiated Nuclear Fuels", Los Alamos National Laboratory report LA-6923 (1978)

[hub]   P.J. HUBER, "Robust Statistics". *John Wiley & Sons*, New York, (1981)

[hud]   H.M. HUDSON, RS. LARKIN, "Accelerated image reconstruction using ordered subsets of projection data", *IEEE Trans. Med. Imag.*, **13** p.601 (1994)

[izm]   A. IZMER, S. CARUSO, M. HORVATH, N. KIVEL, R. RESTANI, I-GÜNTER-LEOPOLD, "Determination of the caesium distribution in high Burnup fuel samples with different analytical techniques", 2007 European Winter Conference on Plasma Spectrochemistry, Poster ThPo39, Taormina, Italy (2007)

[kak]   A.C. KAK, M. SLANEY, "Principles of Computerized Tomographic Imaging", *IEEE PRESS*, New York, (1999)

[lan]   K. LANGE R. CARSON. "EM reconstruction algorithms for emission and transmission tomography", *Jour. Comp Assisted Tomogr.,* **8**(2) p.306 (1984)

[mue]   J. MUELLHAUER, "Kernbrennstoffanalyse mittels Gamma-Emissions-Computer-Tomografie", Seminar Computertomografie, *Deutsche Gesellschaft für Zerstörungsfreie Prüfung e.V*.

[nat]   F. NATTERER, "The Mathematics of Computerized Tomography", *Proc. IEEE,* **71**(3) p.320 (1983)

[oga]   K. OGAWA & al. "A Practical Method for Position-Dependent Compton-Scatter Correction in Single Photon Emission CT", *IEEE Transactions on Medical Imaging*, **10**(3) p.408 (1991)

[phi]   J.R. PHILLIPS, "New Techniques in Precision Gamma Scanning, Application to Fast-Breeder Reactor Fuel Pins" Los Alamos Scientific Laboratory report LA-5260-T (July 1973)

[pra]   C. PRALONG, "Investigation of Within-Pin Reaction Rate Distributions in a Highly Heterogeneous BWR Fuel Assembly", *Thèse EPFL No 2663* (2002)

[qad]   "QAD-CGGP. A Combinatorial Geometry Version of QAD-P5A, a Point Kernel Code System for Neutron and Gamma-Ray Shielding Calculations Using the GP Building Factor", *RSIC Computer Code Collection, Radiation Shielding Information Center,* Oak Ridge National Laboratory (1977)

[ram]   G.N. RAMANCHANDRAM and A.V. LAKSHMINARAYANAN, "Three dimensional reconstructions from radiographs and electron micrographs: Application of convolution instead of fourier transforms" *Proceedings of the National Academy of Sciences*, **68** p.2236 (1971)

[tar]   A. TARANTOLA, "Inverse Problem Theory. Methods for Data Fitting and Model Parameter Estimation", *Elsevier*, Amsterdam (1987)

[tun]   C-H TUNG & al., "Non-uniform attenuation correction using simultaneous transmission and emission converging tomography", *IEEE Transactions on nuclear science,* **39**(4) p.1134 (1992)

[xco]   http://physics.nist.gov/PhysRefData/Xcom/Text/XCOM.html

6. <u>High Burnup Indicators and Comparison with Calculation and Others Experiments</u>

As mentioned earlier, there are various gamma spectrometric techniques for determining the burnup of nuclear fuel, based on the non-destructive measurement of the long-lived fission products ^{134}Cs, ^{137}Cs, and ^{154}Eu. These methods - whether relying on the measurement of individual isotopic concentrations [iae-wil], of single ratios [leb-phi-kri], or of multiple ratios such as $(^{134}$Cs$/^{137}$Cs$)^2/(^{106}$Ru$/^{137}$Cs$)$ [nak] (see Section 2.3) - require further validation at burnup values higher than 50 GWd/t. This is so for a number of physical reasons. First, caesium is volatile and migrates from the centre of the pellet to its periphery as the burnup increases, the effective migration being slightly different for the two Cs-isotopes. The latter aspect may require corresponding within-pin activity distribution measurements to be made, so that appropriate corrections can be applied for gamma self-attenuation inside the pin, as also for the collimator detector geometric efficiency. Second, the radioactivity of highly burnt fuels increases to levels at which it becomes necessary to have adequate shielding and filters to maintain an appropriate signal-to-background ratio. Third, the neutron source intensity in high burnup pins, originating in the spontaneous fission and ^{18}O$(\alpha,$n$)$ reactions from the decay of minor actinides such as ^{244}Cm and ^{252}Cf, produces, through captures, an additional gamma background which perturbs the measurements. There can also be a rapid degradation in the resolution of the Ge-detectors used through neutron damage.

This chapter is divided into four main sections. The first concerns the assessment, on a relative scale, of individual isotopic concentrations as high-burnup monitors, measured by non-destructive high-resolution gamma-spectrometry. Thereby, three different approaches have been taken for obtaining integral values for the relative concentrations, viz. (a) integration of the tomography projection scans, (b) individual slit measurements (made by taking longer counts while keeping the collimator slit fixed at the centre of the pin), and (c) integration of the final tomography reconstructions. While (a) and (b) are described in paragraphs 6.1.1.1 and 6.1.1.2, respectively, (c) simply corresponds to a direct utilisation of the emission tomography results reported in Chapter 5. Paragraph 6.1.1.3 discusses the important corrections which need to be applied in deriving the individual relative concentrations. The three sets of results obtained are presented in Section 6.1.2, together with comparisons with destructive chemical analysis (viz. multicollector inductively coupled plasma mass spectrometry).

Section 6.2 is devoted to validating the experimental results obtained for the isotopic concentration ratios ^{134}Cs$/^{137}$Cs, ^{154}Eu$/^{137}$Cs and ^{134}Cs$/^{154}$Eu. The basis for the reported results is provided by two separate sets of relative measurements of the individual concentrations, viz. those corresponding to

approaches (a) and (b) above. In Section 6.3, a numerical study of the variation of ^{134}Cs, ^{137}Cs, and ^{154}Eu single ratios with burnup is presented. Here, pin-cell depletion calculations performed for each segment using the deterministic code CASMO-4 [ede] are discussed in detail, a comparison being made between calculational and experimental results for the ratios.

In Section 6.4, consideration is given to the possibility of using, as burnup indicators, spatial ratios for individual isotopic concentrations. This has been done on the basis of the experimental results reported in Chapter 5 for the within-pin isotopic distribution maps derived from gamma-ray emission tomography. Finally, Section 6.5 summarises the current findings on burnup indices and monitors for high burnup fuel.

6.1. Validation of Individual ^{134}Cs, ^{137}Cs and ^{154}Eu Activities as Burnup Monitors

The basic idea here is to study the measurability of individual isotope buildup and to establish a direct correlation between burnup and isotopic concentration. As indicated, three different experimental approaches, based on high resolution gamma-ray spectrometry, have been used to derive the relative activities of ^{134}Cs, ^{137}Cs, and ^{154}Eu of the samples using the germanium detector in the tomography system. The first method (integral scan, see paragraph 6.1.1.1) is based on integrating the appropriate gamma-ray peak areas from every step of each emission tomography traverse. Secondly, longer measurements were made with the collimator slit in a fixed position aligned with the axis of the pins, i.e. detecting the activity through the central diameter of each pin (see paragraph 6.1.1.2). Most of the analysis follows similar paths for these two methods. Thirdly, the within-pin distributions of ^{134}Cs, ^{137}Cs and ^{154}Eu, as reconstructed by emission tomography using the FBP method (Chapter 5), have been integrated. The results derived from each of the three methods have been compared with chemical measurements in Section 6.1.2.

6.1.1. High resolution gamma-ray measurements

6.1.1.1. Integral scan method (SCAN)

The emission tomography procedure, as well as the collection and initial analysis of the data, have been described in Chapter 5. Briefly, using the remote handling system of the tomographic station, the spent fuel segments were traversed past the collimator slit and a spectrum collected at each

0.2 mm step. A background measurement region was defined, and the segment was moved beyond the collimator slit so as not to be directly visible by the detector. The background thus included gamma-rays which penetrated the collimator block, rather than passing through the slit. Acquiring the spectra in this way allowed the possibility to subtract the non-collimated background contribution from the main measurement. Integration of these experimental results is, in effect, equivalent to measuring the samples with a 20 mm high collimator extending over the full width of the sample in eight azimuthal positions.

The experimental setup, described in detail in Chapter 3, was optimised for these measurements. The distance from detector to fuel segment and the type of filter in front of the detector were modified to obtain an optimum count rate. The preferred configuration consisted of a 30 mm thick lead filter in front of the detector, to attenuate effectively low energy gammas and consequently to reduce the detector dead time. Furthermore, the pulse shape (rise time, flattop width and tilt) of the digital-spectrometer virtual amplifier were optimised.

Once again, it should be pointed out that standard peak treatments were not found adequate for these measured spectra, as most of the peaks were not really Gaussian and some of them were close to interference peaks, typically neutron-capture gammas, which may have led to inaccuracy in the final activity derivation. A few examples concerning the standard Gamma-Vision [gam] peak analysis are shown in Appendix A. A different approach to peak evaluation, found to be more robust, has been used. This peak area treatment is described fully in Sections 5.2.2 and 5.2.3.

6.1.1.2. *Central slit method (SLIT)*

Also in this case, the distance between detector and fuel segment, as also the type of filter in front of the detector, were modified to obtain an optimal count rate. The preferred configuration again consisted of a 30 mm thick lead filter in front of the detector, together with a paraffin wax neutron filter (40 mm thick) to reduce neutron damage to the detector. The latter aspect was particularly important for sample S#4. In fact, at the beginning of the measurement campaign, surprisingly strong neutron damage was noticed, degrading slowly the resolution of the two crystals used and necessitating repair by annealing. In addition, a customised pulse shape had to be used for this sample, in order to keep the dead time reasonably low.

Using the remote handling system of the tomographic station, the spent fuel segments were measured in front of the collimator slit ("central measurement"), followed by a background measurement as in the case of emission tomography and the SCAN method. The use of a long measuring time (1-2 days) was necessary to gain enough statistics for the low intensity gamma-peaks. A typical central measurement spectrum "cen" measured for the sample S#2 (71 GWd/t) is shown in Fig. 6.1, together with its background measurement "bkg"(scaled by a factor of 100). In the same picture, the difference of the two spectra ("dif") is illustrated (scaled by a factor of 1000). The intensity in the plot is in counts per second and the main peaks are marked with arrows. The leakage of the collimator for photons with energies above 1 MeV is evident in the background spectrum ("bkg") of Fig. 6.1, whilst the "dif" spectrum illustrates the benefit of such a background subtraction, showing the peaks of interest much more prominently throughout the energy range.
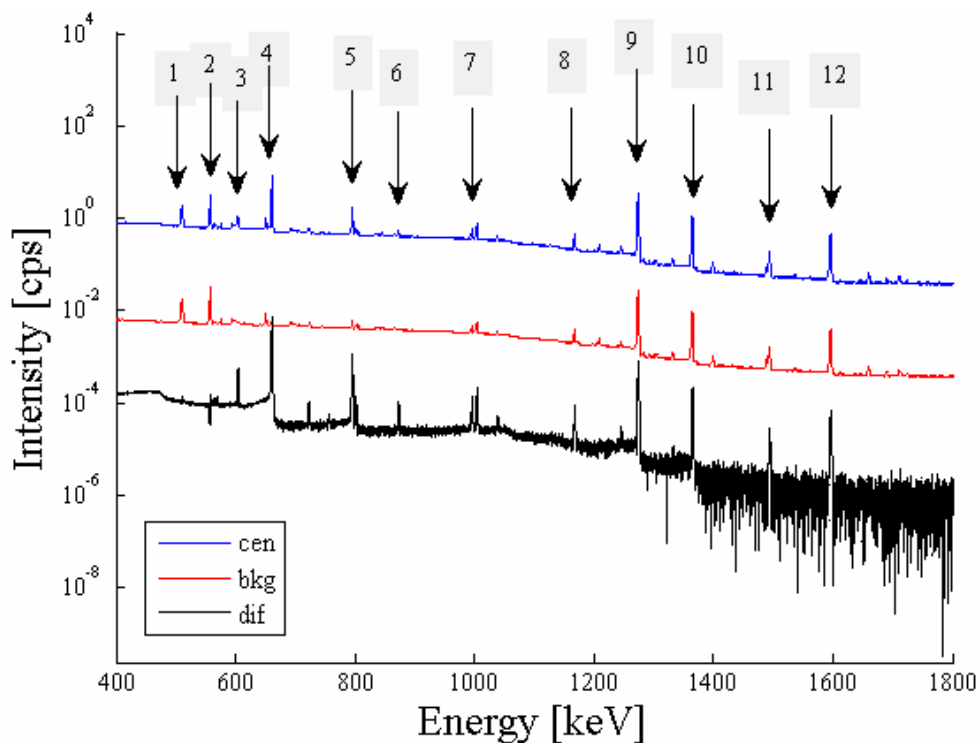
Fig. 6.1: HPGe gamma-ray spectra: central measurement "cen", vs. background measurement "bkg", for the 71 GWd/t sample (S#2). The background spectrum is reduced by a factor 1/100 for illustration purposes. The difference "dif" of the two spectra is shown as well. The main peaks illustrated by means of arrows are: 1) annihilation peak 511 keV; 2) (n,^{113}Cd) 558 keV; 3) 605 keV ^{134}Cs; 4) 662 keV ^{137}Cs; 5) 796 keV ^{134}Cs; 6) 873 keV ^{154}Eu; 7) 996,1005 keV ^{154}Eu; 8) 1168 keV ^{134}Cs; 9) 1275 keV ^{154}Eu; 10) 1365 keV ^{134}Cs; 11) 1494 keV ^{154}Eu; 12) 1597 keV ^{154}Eu.

The detectable radio-nuclides employed for this study are ^{137}Cs with its 662 keV γ-ray, ^{134}Cs with 569, 605, 796, 1039, 1168 and 1365 keV γ-rays, and ^{154}Eu with 723, 873, 996, 1005, 1275, 1494 and 1597 keV γ-rays. Besides these, other interfering peaks are present in the spectrum; 558, 651 keV from n-capture in ^{113}Cd, and 2223 keV n-capture in H.

6.1.1.3. Necessary corrections

To obtain the relative activity results, the net count rate derived for each gamma peak was divided by its branching ratio and corrected for decay to discharge time. However, the particular measurement conditions corresponding to a collimator with a narrow vertical slit call for two further important corrections, both of which are associated with the specific within-pin activity distribution for the isotope under consideration.

The first of these, viz. that for gamma self-attenuation, is common to all three approaches, (a) - (c), and has been discussed in the context of emission tomography in Chapter 5. Thus, the effect of the different within-pin gamma source distributions on the gamma self-shielding coefficient was quantified using the point kernel code QAD-CG [qad], a correction being introduced as a function of energy and applied to the estimation of individual count rates. The maximum derived impact on the concentration ratios was 1.3% (for sample S#4 at 569 keV). Concerning the other samples, the correction was <1%, and almost zero for samples S#2 and S#3. These values seem to be surprisingly low at first glance, in view of the depressed caesium distribution. However, a compensating effect is present, in as much as both the notionally flat distribution considered as reference and the actual caesium distribution are weighted by the same attenuation correction at any given point. As the integrals of the activities of the flat and the depressed distributions are defined as equal, the attenuation has only a second-order effect. MCNP [bri] simulations and simple ray tracing calculations have confirmed the QAD calculations (see Fig. 6.2 for a simple illustration of the two distributions in the fuel pin, in horizontal view, as generated in the MCNP simulation). In addition, the attenuation corrections obtained here are in line with previous work, which would indicate a correction to the Cs-134/137 ratio of about 1-2% for sample S#4 at 569 keV [hsu].
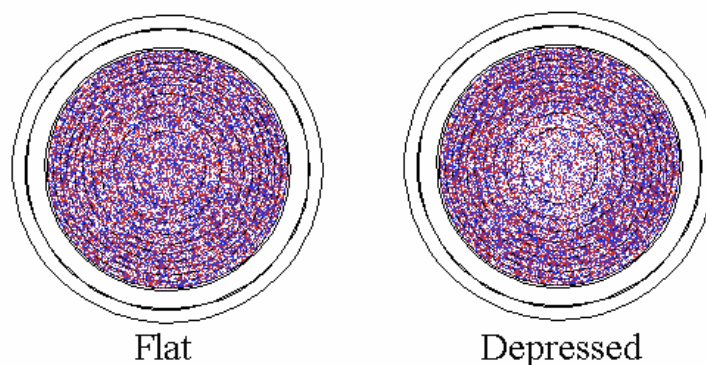
Flat   Depressed

Fig. 6.2: Simple illustration of a flat and depressed distribution in the fuel pin, as generated in the MCNP simulation. Plan view.

To illustrate the compensating effect, a graphical description, based on simple ray tracing calculations for a photon energy of 569 keV, is shown in Fig. 6.3. In this figure, the measured within-pin distribution of [134]Cs in sample S#1 is plotted using the primary vertical axis and the detector responses (activities weighted by attenuation and solid angle corrections) for both the [134]Cs distribution and a flat distribution are plotted against the secondary vertical axis. The detector responses are plotted as if the detector were located to the right of the figure. One can see that the detector responses are, in fact, just the original distributions distorted by the attenuation and solid angle corrections. As, by definition, the [134]Cs distribution has an equal area above and below unity, this situation is, to a large extent, preserved in the detector response. Only with severe attenuation, for a gamma-ray say below 400 keV, does the effect of the depressed distribution become really significant.
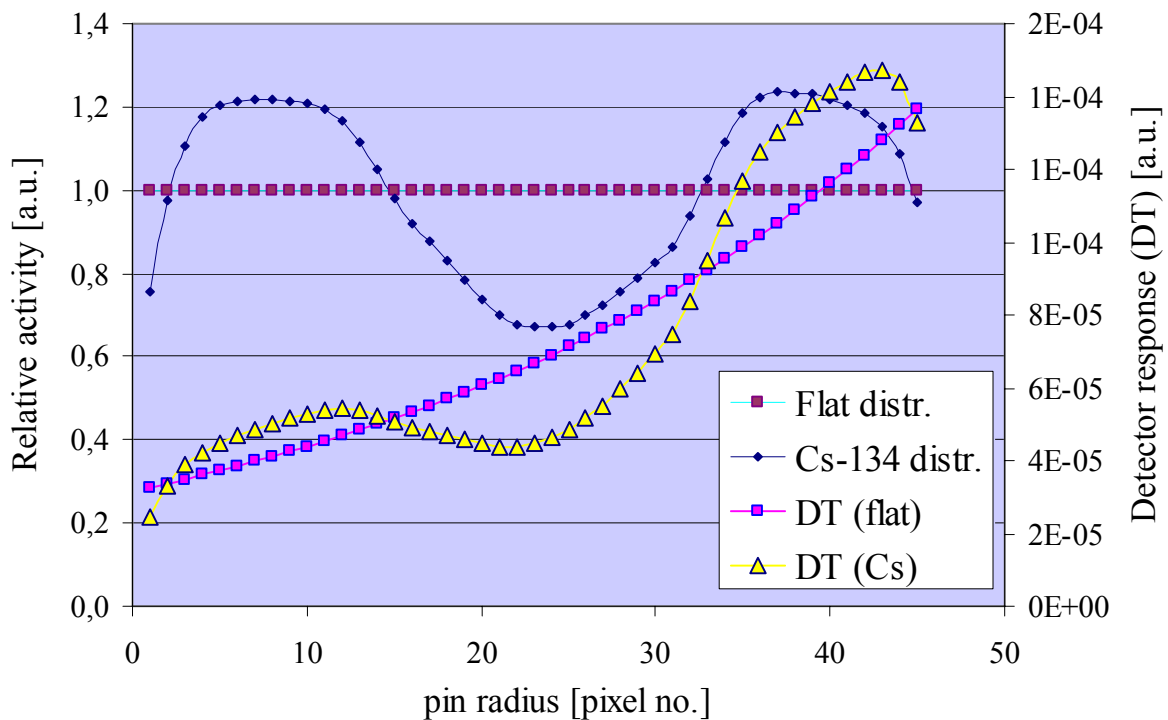
Fig. 6.3: Example of the compensating effect between within-pin distribution of [134]Cs in sample S#1 and a flat distribution, based on simple ray tracing calculations. The [134]Cs and the flat distributions are plotted using the primary vertical axis, and the detector responses (activities weighted by attenuation correction), relative to the [134]Cs and flat distributions, are shown on a secondary axis. The two detector responses (DT), for a photon energy of 569 keV, are plotted such that the detector is considered to be located on the secondary axis, i.e. at the right side of the figure.

Besides the effect of the different distributions on the gamma-ray attenuation, it is necessary, in the case of the central slit method, to allow for the fact that only a narrow vertical slice of the sample is observed through the collimator slit. Thus, the activity distributions, obtained as a slice through the

144

tomographic reconstructions, are weighted by the inverse of the radius from the sample axis to allow for the fraction of each notional ring of activity seen through the collimator. The tomographically derived within-pin distributions (see Chapter 5) have been employed to derive a factor to be applied to correct the final isotopic activity. In comparison with a flat distribution, the correction was about 16% in the case of the caesium (on the basis of calculations for both isotopes) in the highest burnup sample.

The case of ^{154}Eu required much smaller corrections but was somewhat more problematic. Simple reactor physics reasoning suggests that the within-pin distributions may be expected to be peaked at the pin edge, as shown by calculations described in the following Section 6.5. Unfortunately, the tomographic reconstructions were characterised by a less precise image for ^{154}Eu, with the edge too over-smoothed to be correctly representative. For this reason, the ^{154}Eu reconstructions were not accurate enough to generate a geometric correction factor and consequently it was postulated to be unity. This choice assumes that the europium depression is not greater than about 20%. (Since the geometrical correction is weighted by the inverse of the radius from the sample axis, the central region of the pin plays a more important role.)

It should be emphasised that the geometrical correction is not needed for the methods involving integration of the scans and/or tomographic reconstructions, the entire width of the pin being measured in these cases.

6.1.2. Results and comparisons with HPLC-MC-ICP-MS measurements

As a check on systematic errors, the relative isotopic concentrations for the irradiated fuel rod samples, as measured by the gamma spectrometry method, have been compared to the relative concentrations measured by means of a sophisticated HPLC-MC-ICP-MS method (high-performance liquid chromatographic multi-collector inductively coupled plasma mass spectrometry) used in the PSI Hotlab [gue-gue2].

In principle, different inorganic mass spectrometric techniques such as glow discharge, spark source, laser ionisation, thermal ionisation or inductively coupled plasma mass spectrometry [bec-pla] can be used for the determination of the isotopic composition of different elements. Among these techniques, ICP-MS is by far the most frequently applied method and is used routinely. In a multi-collector (MC)-ICP-MS system, the ions produced in an argon plasma are separated in a magnetic sector field and the detection is carried out by a set of 9 to 12 Faraday cups that allow the simultaneous detection of

different isotopes over a restricted mass range of about 15 %. Isotopic ratio measurements with MC-ICP-MS can provide a precision as good as 0.002 % RSD for some elements.

Compared to radioanalytical techniques, MC-ICP-MS offers very low detection limits also for long-lived radionuclides, provides information on the isotope composition and elemental concentrations, and is capable of measuring stable as well as radioactive nuclides with similar sensitivity. In recent years, increasing attention has been given to the technique of MC-ICP-MS because it permits the precise measurement of isotope compositions for a wide range of elements, combined with excellent limits of detection due to high ionisation efficiencies.

The main results for ^{134}Cs, ^{137}Cs, and ^{154}Eu, derived with the integral scan (SCAN) method, are displayed in Figs. 6.4 - 6.6, where HPLC-MC-ICP-MS and SCAN are shown in arbitrary units on the X and Y axes, respectively. The SCAN results are relative activity (counts per second divided by branching ratio), as measured with the tomographic station. The activity of ^{134}Cs is obtained from the analysis of the 796 keV peak, whilst for ^{154}Eu the 1275 keV peak is used. The values of HPLC-MC-ICP-MS are in atoms/fuel g. All the values were decay corrected to the time of fuel discharge. The error bars for both types of measurements are smaller than the symbols in almost all cases. The total statistical uncertainties are <0.3% for ^{137}Cs (662 keV), <0.1% for ^{134}Cs (796 keV) and <0.1% for ^{154}Eu (1275 keV). Because the same gamma-ray energies are being measured from similar samples, it is not necessary to attempt an absolute efficiency calibration for the purpose of this relative activity determination.
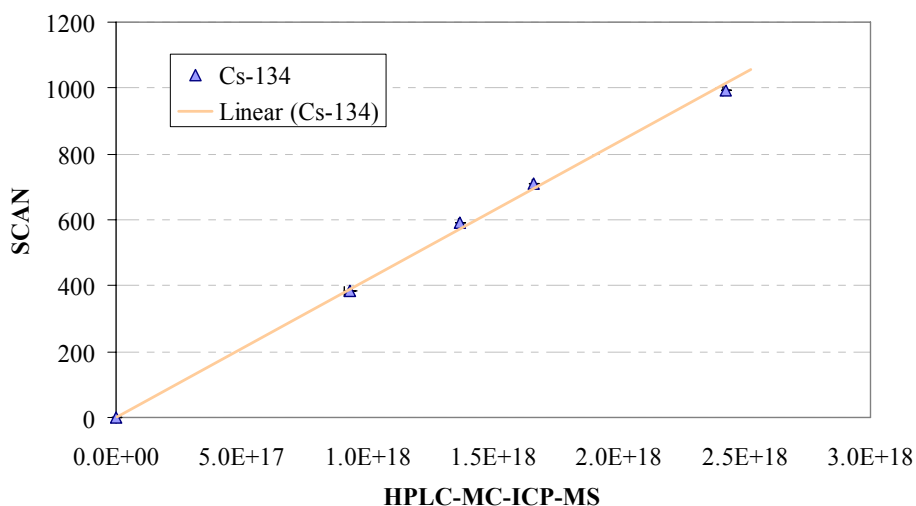
Fig. 6.4: SCAN vs. HPLC-MC-ICP-MS in arbitrary units, for ^{134}Cs.
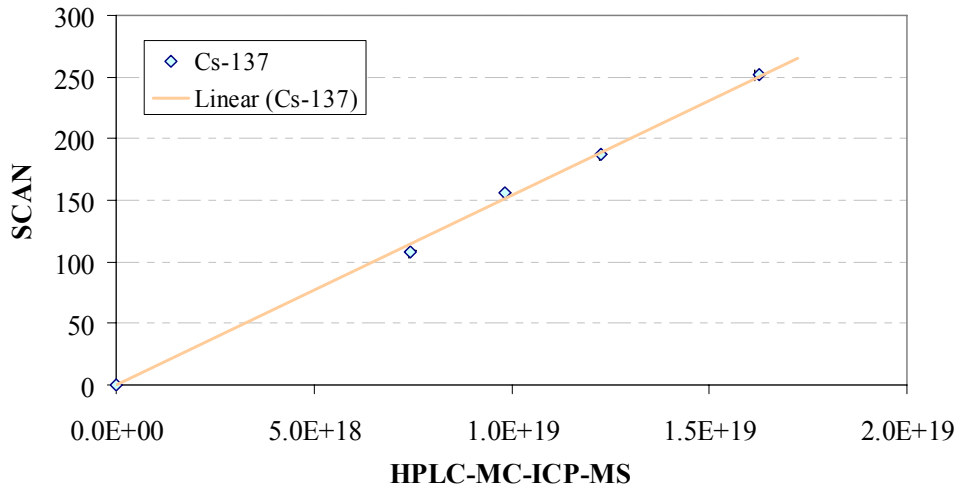
Fig. 6.5: SCAN vs. HPLC-MC-ICP-MS in arbitrary units, for ^{137}Cs.
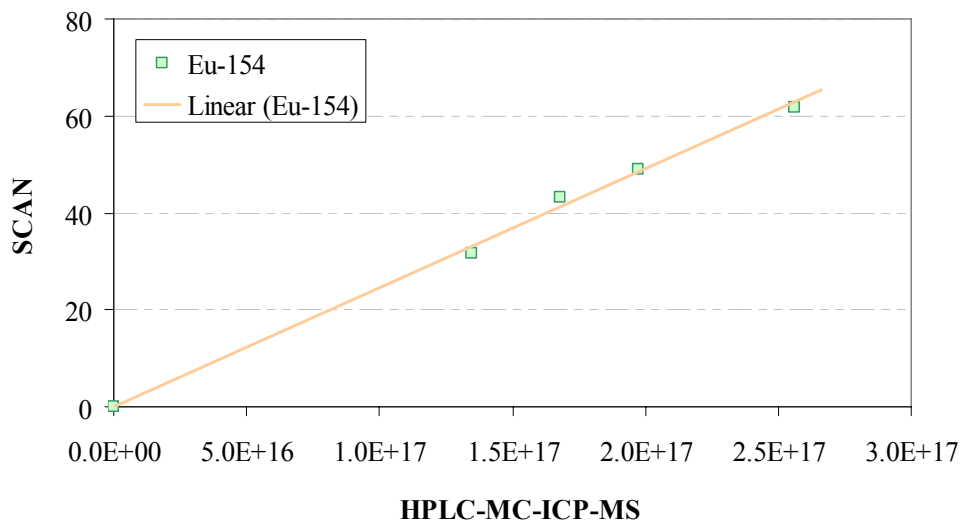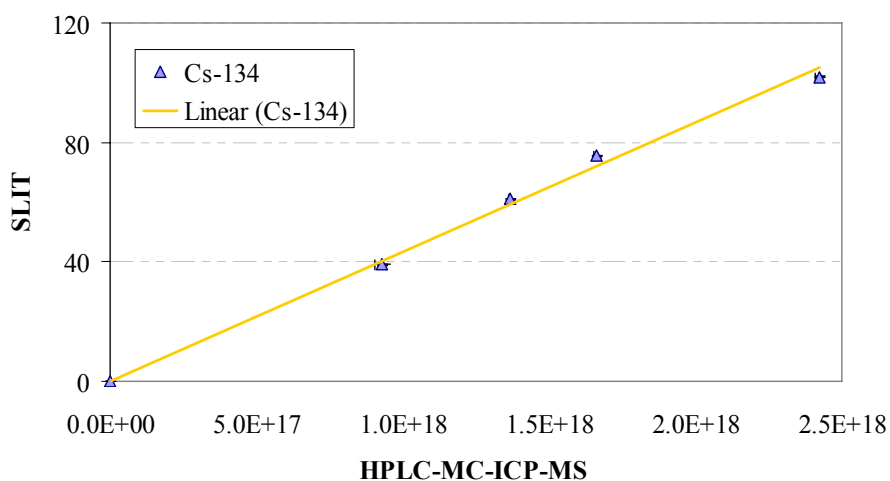

Fig. 6.6: SCAN vs. HPLC-MC-ICP-MS in arbitrary units, for ^{154}Eu.

Each isotopic data set was fitted with a linear function passing through zero, trying to identify a linear relationship between HPLC-MC-ICP-MS and SCAN. The results are seen to be in good agreement, with the fitting line touching almost all the points.

The main results for ^{134}Cs, ^{137}Cs, and ^{154}Eu, derived by the integration of the 3D tomographic reconstructions (TOMO), using images produced by the FBP algorithm, for each isotope and each sample, are displayed in Figs. 6.7 - 6.9, where HPLC-MC-ICP-MS and TOMO are in arbitrary units on the X and Y axes, respectively. Here, the agreement is less satisfactory, in comparison to the previous case. Especially the experimental point of sample S#4 in the caesium cases seems to depart

from the linear relation. Concerning the europium, the relatively large uncertainty reduces the utility of the method somewhat.
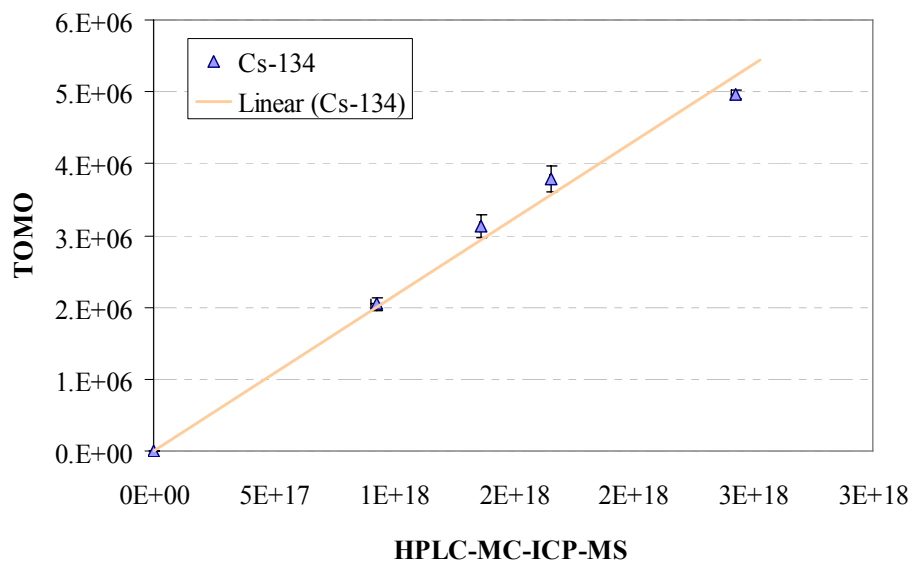
Fig. 6.7: TOMO vs. HPLC-MC-ICP-MS in arbitrary units, for ^{134}Cs.
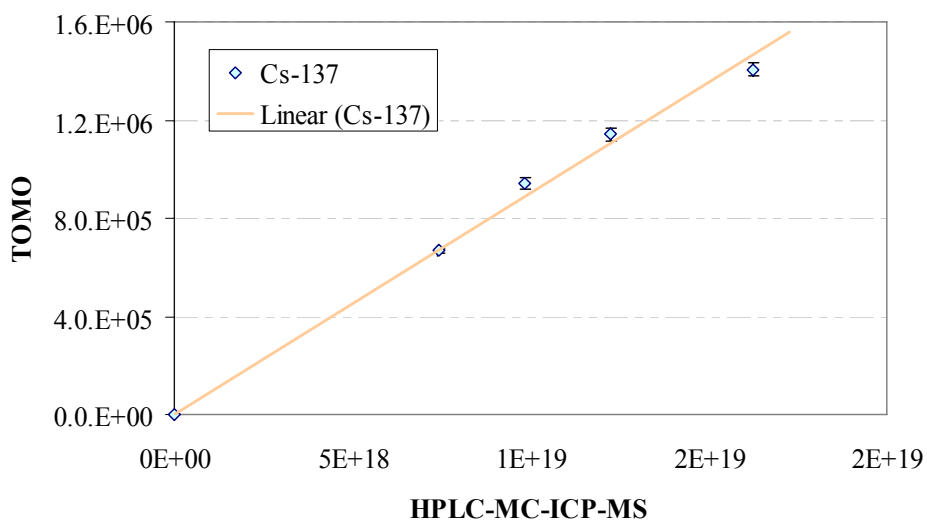
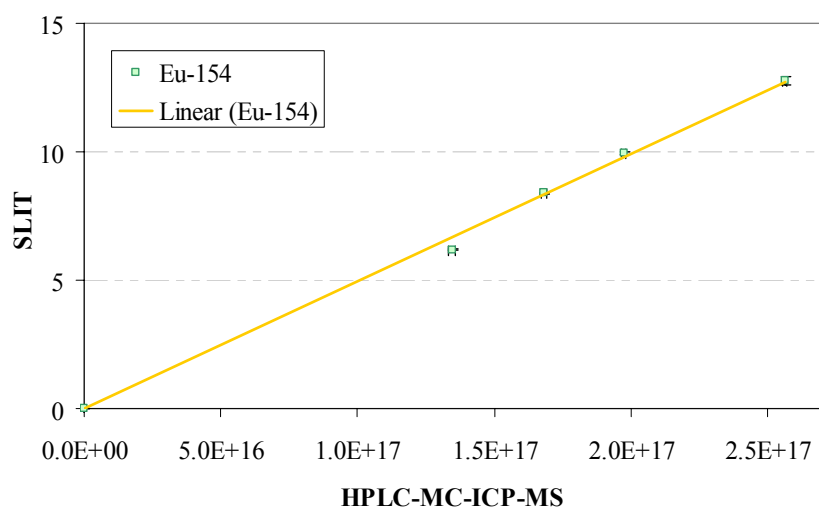Fig. 6.8: TOMO vs. HPLC-MC-ICP-MS in arbitrary units, for ^{137}Cs.
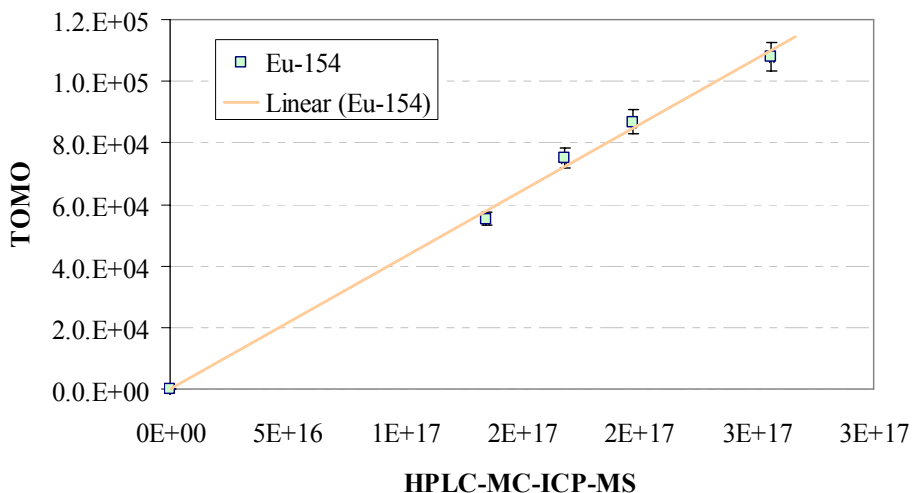
Fig. 6.9: TOMO vs. HPLC-MC-ICP-MS in arbitrary units, for ^{154}Eu.

The main results for ^{134}Cs, ^{137}Cs, and ^{154}Eu derived with the central slit (SLIT) method are displayed in Figs. 6.10-6.12, where HPLC-MC-ICP-MS and SLIT are, in arbitrary units, on the X and Y axes, respectively. The SLIT results are relative activity divided by the corresponding sample average density as measured with the tomographic station by means of transmission tomography. In this case, the agreement is very good, with only sample S#1 indicating a systematic departure from the fitting line.

Fig. 6.10: SLIT vs. HPLC-MC-ICP-MS in arbitrary units, for ^{134}Cs.
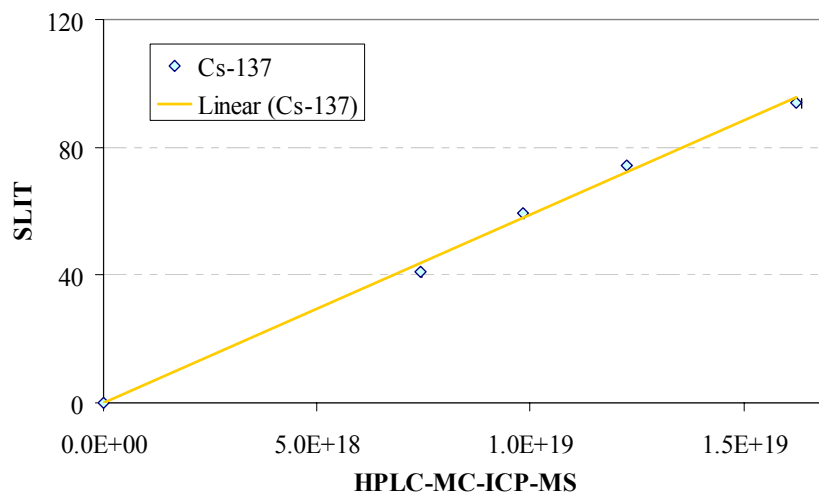
Fig. 6.11: SLIT vs. HPLC-MC-ICP-MS in arbitrary units, for ^{137}Cs.

Fig. 6.12: SLIT vs. HPLC-MC-ICP-MS in arbitrary units, for ^{154}Eu

Direct comparisons between TOMO and SLIT results for ^{134}Cs, ^{137}Cs, and ^{154}Eu are shown in Figs. 6.13 - 6.15, where SLIT and TOMO are on the X and Y axes, respectively. The agreement between these two different approaches is very satisfactory, in as much as it is consistent with the uncertainties.
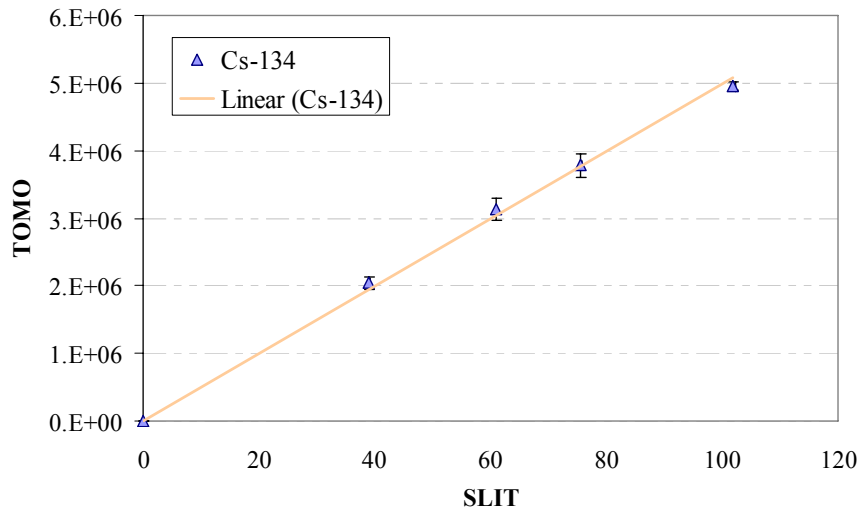
Fig. 6.13: TOMO vs. SLIT in arbitrary units, for ^{134}Cs.
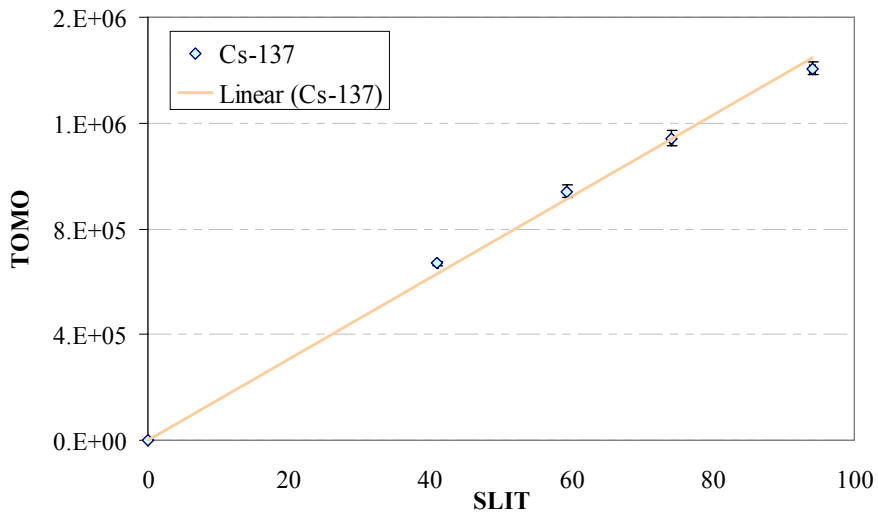
Fig. 6.14: TOMO vs. SLIT in arbitrary units, for ^{137}Cs.
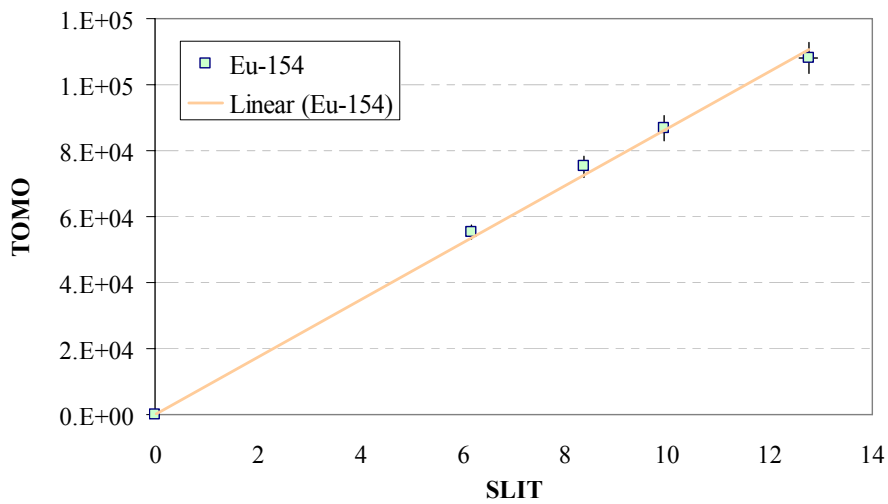
Fig. 6.15: TOMO vs. SLIT in arbitrary units, for ^{154}Eu.

151

The derived relative activities of all four samples, measured by the central slit method, have been plotted as a function of burnup to study the isotopic build-up and to examine, for each isotope, the potential for its utilisation as burnup monitor up to ultra-high burnup values (see Fig. 6.16).

[137]Cs is expected to be linear with burnup, whilst [134]Cs and [154]Eu are expected to be quadratic (see Section 6.4.1 for more details about fission product build-up). The calculations of Section 6.4 show the tendency of all these isotopes to saturate at high burnup and these experimental data seem to confirm such behaviour. However, the slope of each plot still indicates the clear possibility of being able to identify the burnup from the sample activity, so that all three isotopes seem to have the potential of being employable as burnup indicator. Considering that caesium is a volatile metal, which migrates from centre to periphery, it is clear that the non-volatile [154]Eu may be expected to be better. Further, [154]Eu is rather insensitive to irradiation history, in contrast to [134]Cs, and this is a further advantage.
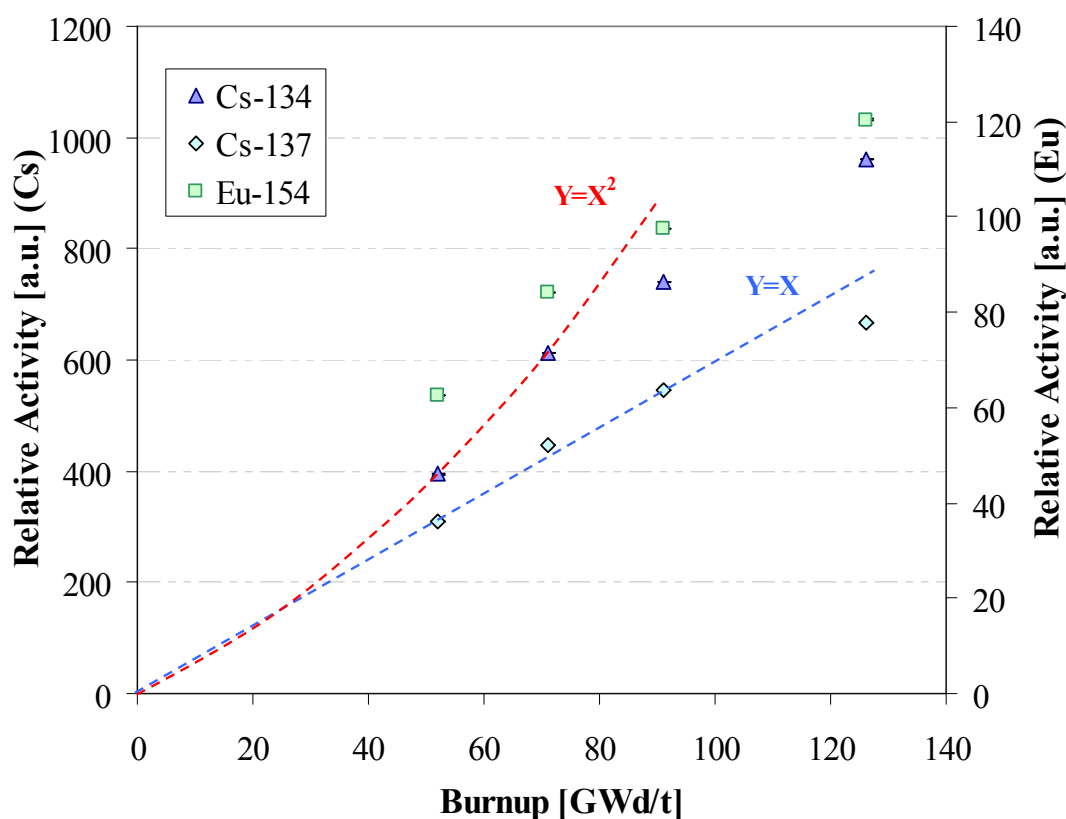

Fig. 6.16: Measured activity (SLIT method) in arbitrary units, as function of burnup. [137]Cs was increased by a factor of 3 for illustration purposes. Error bars are smaller than symbols in most of the cases.

Thus, the [154]Eu gamma-activity, which can be measured with very good accuracy by choosing the most prominent photo-peak at 1275 keV, can serve as a relative indicator up to ultra-high burnup values. Once a calibrated sample is available, the burnup of many fuel pins could be determined rather quickly and precisely, on the basis of an appropriate, empirically established correlation.

6.2. Validation of ^{134}Cs, ^{137}Cs, and ^{154}Eu Single Ratios as Burnup Monitors for Ultra-High Burnup UO$_2$ Fuel

This section is devoted to validating the accuracies and precisions in the measurement of ^{134}Cs/^{137}Cs, ^{154}Eu/^{137}Cs, and ^{134}Cs/^{154}Eu isotopic concentration ratios by the use of non-destructive high-resolution gamma spectrometry with a high-purity germanium detector (HPGe) and the tomographic measurement station. The two different approaches considered in this context are: the integral scan method (SCAN), based on integrating the appropriate gamma-ray peak areas from every step of each emission tomography traverse, and the single collimator slit method, consisting of measurements with the slit in a fixed position aligned with the axis of the pins, i.e. detecting the activity through the diameters of the pins. The experimental basis of the two approaches has been described above in Section 6.1 and will not be repeated here. However, a description of the technique used to derive the ratios will be provided, pointing out the differences between the cited methods.

6.2.1. Relative efficiency function and isotopic ratios

In the derivation of the isotopic ratios, use is made of a relative efficiency curve derived from the ^{134}Cs gamma-ray peaks of different energies. To produce this curve, the net count rate derived for each gamma peak is divided by its branching ratio. The resultant values give the effective relative efficiency at each energy. In the central slit method, the measurements from all four samples were normalised to form a common data set, and then a global function was generated with a weighted least-squares fit, whilst in the integral scan method a separate relative efficiency function was used for each pin (see Fig. 6.17 for the central slit method and Fig. 6.18 for the integrated scan method). A cubic and a parabola, respectively, have been found empirically to be the most suitable and statistically appropriate functions in the two cases. Using these functions, the effective relative efficiency could then be deduced at any energy within the bounds of the original data.
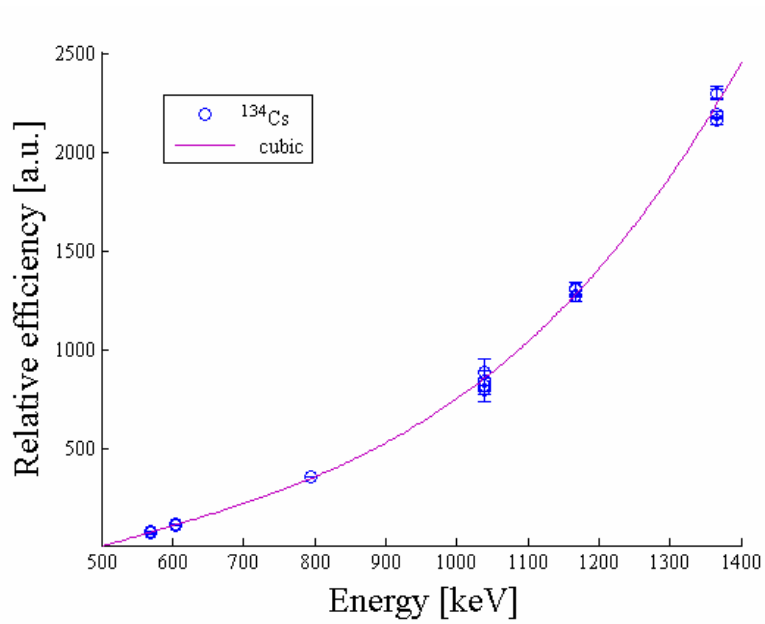
Fig. 6.17: Relative efficiency function (polynomial of third degree) for central slit, produced from ^{134}Cs data points, used for scaling the measured activities, for all the samples.
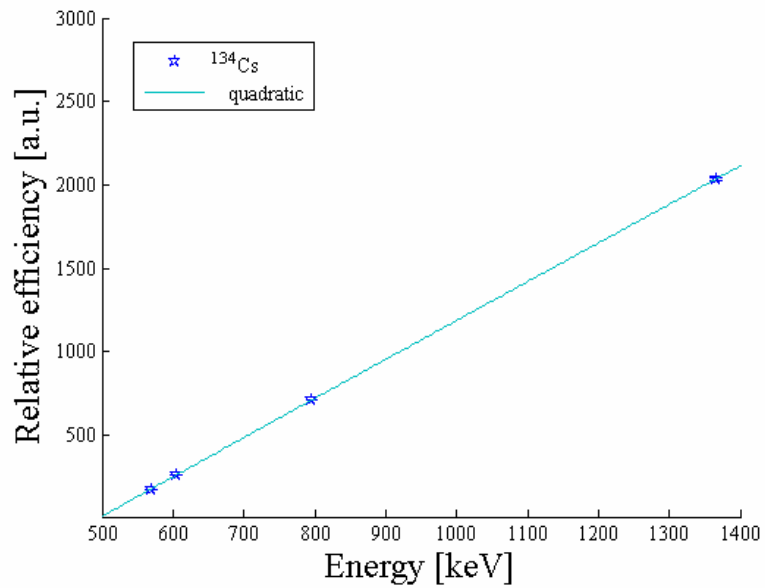

Fig. 6.18: Relative efficiency function (polynomial of second degree) for integral scan, produced from ^{134}Cs data points, used for scaling the measured activities, for sample S#3. Error bars are smaller than the symbols.

The ^{134}Cs/^{137}Cs ratio was derived by using the relative efficiency function to predict the detection efficiency at the photo-peak energy of the ^{137}Cs (662 keV) and thus to relate the ^{137}Cs activity to that of ^{134}Cs. The ^{134}Cs/^{154}Eu ratio was derived analogously by using the function to predict the efficiency at each ^{154}Eu peak energy (in the range 723-1275 keV). Finally, the ^{154}Eu/^{137}Cs ratio was obtained as the quotient of the previous two ratios.

154

It must be emphasised that the 796 keV photo-peak of ^{134}Cs is dominant in the development of the relative efficiency curve because of its very good statistics (relative standard deviation <0.3% for the central slit method, <0.1% for the integral scan method), whilst the 1275 keV photo-peak of ^{154}Eu (<0.4% for the first three samples; for sample S#4, ~1.4% for the central slit method and <0.1% for the integral scan method) is dominant in the derivation of the ^{134}Cs/^{154}Eu ratio.

The experimental ratios obtained with the above procedure are more accurate than they would be by using an absolute calibration of the HPGe detector system, the dependence on intrinsic and geometrical efficiency factors and gamma-ray absorption in the samples being eliminated in building the ratios [phi]. The deduced concentration ratios depend essentially on the efficiency corrected count rates, the branching ratios and the half-lives:

$$\frac{A_1}{A_2} = \frac{\lambda_1 N_1}{\lambda_2 N_2} \Rightarrow \frac{N_1}{N_2} = \frac{A_1}{A_2} \cdot \frac{T_{1/2}^1}{T_{1/2}^2} = \frac{C_1}{C_2} \cdot \frac{BR_2}{BR_1} \cdot \frac{T_{1/2}^1}{T_{1/2}^2} \tag{6.1}$$

where N_i is the concentration of isotope i, λ_i the decay constant ($\lambda_i = \ln 2/T_{1/2}^i$ with $T_{1/2}^i$ the isotope half-life), A_i the activity at measurement time of isotope i already corrected for the within-pin activity distribution, C_i the corresponding count rate in counts/s (corrected using the generated relative efficiency function), and BR_i the branching ratio.

The ^{137}Cs 661.66 keV peak FWHM resolutions were: 1.8, 2.0, 1.8, and 2.1 keV for S#1 to S#4, respectively, in the case of central slit method. The dead time varied from 7% to 12% for the first three segments and was ~27% for S#4, for the central slit method.

The total uncertainties on the ratios were derived by considering the statistical uncertainties of the photo-peaks and a confidence analysis on the relative efficiency function prediction. The total uncertainties are, indeed, dominated by the uncertainty of the relative efficiency function, and this explains the larger uncertainty in the final ratios although the single gamma peaks are very precise. The systematic errors, given by branching ratios and decay corrections, although negligible, have been considered too.

6.2.2. Comparison with chemical analysis

In Table 6.1, the measured isotopic concentration ratios are reported for the four samples using the two different experimental techniques, integral scan (SCAN) and HPLC-MC-ICP-MS [car].

For the integral scan measurement, the 1σ experimental errors for each isotopic ratio vary from 0.3% to 4.5%, mainly depending on the goodness of the fitting function used in the relative efficiency derivation (for sample S#3, this is $\leq0.4\%$, because the function fitted the experimental points very precisely). For the HPLC-MC-ICP-MS analyses, the 1σ errors are always below 1.0%, except for S#1 for ratios containing ^{134}Cs, where it is 2.6 - 2.8%.

The ratio between HPLC-MC-ICP-MS and SCAN gamma spectrometry results is also shown in Table 6.1. The agreement between the two techniques is well within statistics in many cases, but significantly worse for samples S#1 and S#3. The largest disagreement is observed for sample S#1 for the $^{134}Cs/^{137}Cs$ ratio (>7%), but it should be noted that the ICPMS uncertainties are particularly high for this sample. The results agree particularly well (within a combined 1σ) for the $^{154}Eu/^{137}Cs$ ratios, and for all the ratios in the case of sample S#4.

Table 6.1: Segment-averaged isotopic concentration ratios of the four spent UO_2 fuel rods: comparison between experimental results obtained from SCAN gamma-ray spectrometry and HPLC-MC-ICP-MS

Ratio	Technique	S#1	S#2	S#3	S#4
$^{134}Cs/^{137}Cs$	SCAN	$0.135 \pm 1.2\%^*$	$0.145 \pm 2.9\%$	$0.145 \pm 0.3\%$	$0.151 \pm 1.6\%$
	HPLC-MC-ICP-MS	$0.125 \pm 2.7\%$	$0.139 \pm 0.5\%$	$0.135 \pm 0.4\%$	$0.149 \pm 0.8\%$
	(HPLC-MC-ICP-MS)/ SCAN - 1	*-7.4%±2.9%***	*-4.1%±3.0%*	*-6.6%±0.5%*	*-1.2%±1.8%*
$^{154}Eu/^{137}Cs$	SCAN	$0.0185 \pm 1.7\%$	$0.0174 \pm 4.5\%$	$0.0162 \pm 0.4\%$	$0.0159 \pm 2.5\%$
	HPLC-MC-ICP-MS	$0.0181 \pm 1.0\%$	$0.0171 \pm 0.6\%$	$0.0161 \pm 0.4\%$	$0.0158 \pm 0.7\%$
	(HPLC-MC-ICP-MS)/ SCAN - 1	*-2.2%±2.0%*	*-1.8%±4.5%*	*-0.4%±0.6%*	*-0.5%±2.6%*
$^{134}Cs/^{154}Eu$	SCAN	$7.30 \pm 1.3\%$	$8.33 \pm 3.4\%$	$8.96 \pm 0.3\%$	$9.52 \pm 1.9\%$
	HPLC-MC-ICP-MS	$6.91 \pm 2.8\%$	$8.13 \pm 0.8\%$	$8.40 \pm 0.5\%$	$9.46 \pm 0.7\%$
	(HPLC-MC-ICP-MS)/ SCAN - 1	*-5.3%±3.1%*	*-2.3%±3.5%*	*-6.2%±0.6%*	*-0.6%±2.0%*

(*) In the expression x $\pm y\%$, the parameter *x* represents the best estimate and *y%* the 1σ relative error expressed in percent.

(**) SCAN and HPLC-MC-ICP-MS combined relative 1σ.

In Table 6.2, the measured isotopic concentration ratios are reported for the four samples using the central slit method (SLIT) and HPLC-MC-ICP-MS. For the central slit spectrometric measurements, the 1σ experimental errors for each isotopic ratio are less than 2.4% for all samples (1.4 - 1.5% for the ^{134}Cs/^{137}Cs ratio). The SCAN method clearly offers a larger precision because it is based on the integration of more than 300 different measurements. The SLIT measurements, even if characterised by very long measurement time, do not gain the same statistical precision.

The ratio between HPLC-MC-ICP-MS and SLIT gamma spectrometry results is also shown in Table 6.2. The agreement between the two techniques is good in general for all the samples (within about two standard deviations). The largest disagreement is observed for sample S#1, for the ^{134}Cs/^{154}Eu ratio (~6%), where the chemical precision is worst. Again, the results agree particularly well (within a combined 1σ) for the ^{154}Eu/^{137}Cs ratios, and for sample S#4. The ratios measured by SCAN and SLIT methods agree within the uncertainties.

Table 6.2: Segment-averaged isotopic concentration ratios of four UO$_2$ spent fuel rods: comparison between experimental results obtained from SLIT gamma-ray spectrometry and HPLC-MC-ICP-MS

Ratio	Technique	S#1	S#2	S#3	S#4
^{134}Cs/^{137}Cs	SLIT	$0.132 \pm 1.4\%*$	$0.142 \pm 1.4\%$	$0.140 \pm 1.4\%$	$0.150 \pm 1.5\%$
	HPLC-MC-ICP-MS	$0.125 \pm 2.7\%$	$0.139 \pm 0.5\%$	$0.135 \pm 0.4\%$	$0.149 \pm 0.8\%$
	(HPLC-MC-ICP-MS)/SLIT - 1	*-4.9%±3.0%***	*-1.8%±1.5%*	*-3.5%±1.5%*	*-0.6%±1.7%*
^{154}Eu/^{137}Cs	SLIT	$0.0189 \pm 2.1\%$	$0.0169 \pm 2.0\%$	$0.0160 \pm 2.0\%$	$0.0160 \pm 2.4\%$
	HPLC-MC-ICP-MS	$0.0181 \pm 1.0\%$	$0.0171 \pm 0.6\%$	$0.0161 \pm 0.4\%$	$0.0158 \pm 0.7\%$
	(HPLC-MC-ICP-MS)/SLIT - 1	*0.8%±2.3%*	*1.4%±2.1%*	*0.9%±2.1%*	*-1.4%±2.5%*
^{134}Cs/^{154}Eu	SLIT	$7.73 \pm 1.5\%$	$8.40 \pm 1.5\%$	$8.78 \pm 1.5\%$	$9.39 \pm 1.9\%$
	HPLC-MC-ICP-MS	$6.91 \pm 2.8\%$	$8.13 \pm 0.8\%$	$8.40 \pm 0.5\%$	$9.46 \pm 0.7\%$
	(HPLC-MC-ICP-MS)/SLIT - 1	*-5.7%±3.2%*	*-3.2%±1.6%*	*-4.3%±1.6%*	*0.8%±2.0%*

(*) In the expression x $\pm y\%$, the parameter *x* represents the best estimate and *y%* the 1σ relative error expressed in percent.

(**) SLIT and HPLC-MC-ICP-MS combined relative 1σ.

6.3. Calculations and Comparisons with Measurements

6.3.1.   Fission-product build-up

In further investigating the feasibility of the ^{134}Cs/^{137}Cs, ^{154}Eu/^{137}Cs and ^{134}Cs/^{154}Eu gamma-intensity ratios as burnup monitors for highly burnt fuel, a closer look at the process of build-up and destruction of the fission products can provide useful insight into the correct application of this methodology. The general expression for isotopic balance is the following:

$$\frac{dN}{dt} = YN_f \sigma_f \phi + \sum_i \lambda_i N_i + \sum_j \sigma_j \phi N_j - (\lambda + \sigma \phi) N \qquad (6.2)$$

where the production of a species by fission, decay of a radionuclide, neutron capture in other nuclides (first three terms), and the removal of the same species by its decay and transmutation by neutron capture (last term) are represented. In the formula, N is the concentration of a specific nuclide, Y is the fission yield, λ is the decay constant, ϕ is the neutron flux, and σ is the neutron cross section. The subscripts f, i and j denote, respectively, fission/fissile, nuclide parent for production by decay and nuclide parent for production by neutron capture. As is evident in Equation (6.2), the build-up of a species with burnup is a function of several parameters. Some are intrinsic, such as the decay constants, others depend on the irradiation conditions, such as the effective neutron cross sections (with dependencies on the fuel composition, initial enrichment, and burnup) and the neutron flux (strongly dependent on the fuel location in the core). Consequently, a good knowledge of the irradiation history is essential to characterise highly burnt fuels accurately. Nevertheless, certain radio-isotopes, which are relatively less sensitive to irradiation history, can be identified among the few detectable species in long-cooled fuel, for building activity ratios that are more effective for burnup monitoring.

The predictability of long-lived fission-product build-up at various burnup levels was first examined using the CASMO-4 code to model a single fuel pin (UO$_2$ of 3.5% original enrichment and typical PWR geometry), assuming a simple depletion history. Two libraries were employed for this computational study: JEF2.2 "update b" [nea] and ENDF/B-IV [bnl]. The build-up of the fission products of interest for this simplified case and their dependence on the mentioned cross section libraries are shown in Fig. 6.19. The burnup axis has been divided into four regions: low (<30 GWd/t), medium (30-60 GWd/t), high (60-90 GWd/t) and ultra-high (>90 GWd/t). The isotopic fraction of ^{137}Cs is on the right axis, whilst the others are on the left axis, all in weight percentage. As explained in Chapter 2, ^{137}Cs is a direct fission product, which can be assumed to be proportional to the neutron

fluence, and consequently to burnup. From the plot, there is evidence of a linear behaviour of ^{137}Cs only for burnups lower than 50 GWd/t. With the increase of the burnup, the departure from linearity increases, and the discrepancies between the predictions of the two libraries increases too. Concerning ^{134}Cs and ^{154}Eu, these are not direct fission products, being formed by neutron capture in fission products, and may be assumed to be proportional to the square of the burnup. However, in the case of ^{134}Cs, a quadratic behaviour is preserved only up to about 40-50 GWd/t. Further, at high burnup, a large discrepancy (up to 40%) between JEF2.2 and ENDF/B-IV is observed in the ^{154}Eu prediction. Here, the predictability of ^{154}Eu needs to be improved, i.e. the large differences due to the cross section libraries employed need to be resolved. (One reason that has been suggested for the observed discrepancies is the over-prediction of ^{153}Eu [rou]). For the caesium isotopes, the discrepancies due to the different libraries are <10%.
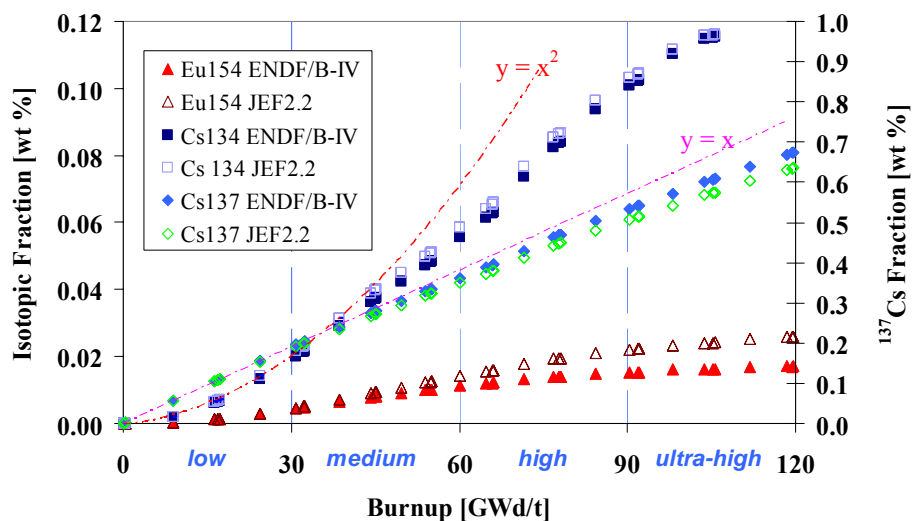
Fig. 6.19: Build-up of fission products (^{134}Cs, ^{137}Cs and ^{154}Eu) calculated with CASMO-4 using the JEF2.2 "update b" and ENDF/B-IV-based cross section libraries.

6.3.2. Depletion calculations for spent fuel segments

Originally, all the four considered irradiated fuel segments corresponded to identical fuel rods with an initial ^{235}U-enrichment of 3.5%. Recalling the main characteristics of the four segments *S#1* to *S#4* (Section 3.1), these were irradiated for ever-increasing periods, i.e. 3, 5, 7 and 10 cycles (corresponding to power-plant-estimated burnups of >40, >60, >80 and >100 GWd/t), respectively. The cooling time, i.e. the time between discharge and measurement, was ~10 years for *S#1* to *S#3* and ~4 years for *S#4*.

The evaluation of the burnup range of applicability of the ^{134}Cs/^{137}Cs, ^{154}Eu/^{137}Cs, and ^{134}Cs/^{154}Eu concentration ratios as burnup monitors for highly burnt UO$_2$ fuel requires detailed computations of the individual isotopic build-up processes. CASMO-4E [rho] pin cell depletion calculations, employing the code's ENDF/B-VI and JEF2.2 "update d" based cross section libraries (C$_{ENDF/B-VI}$ and C$_{JEF2.2}$, respectively), and CASMO-4 employing the code's ENDF/B-IV-based cross section library (C$_{ENDF/B-IV}$), were carried out for these fuel rod segments using, in each case, four different descriptions of their irradiation histories, with varying degree of detail. The following are the four descriptions applied:

o *"Life-average"*: the various parameters (power density, fuel and coolant temperature, and boron concentration) were simplified to correspond to values averaged over the entire irradiation period.

o *"Cycle-average"*: cycle-specific averaging of the parameters was considered for the different reactor cycles.

o *"Core-follow"*: the most detailed fuel rod irradiation history, as provided by the utility, was employed. Several time steps were used within each cycle for a more explicit accounting of changes in reactor conditions.

o *"Core-follow wdc"*: a water density correction (*wdc*) factor was used together with the detailed fuel rod irradiation history, increasing the accuracy of the pin cell to correspond to a fuel assembly depletion model.

The water density correction factor consists of modifying the water density of the pin cell to take into account the fuel rod environment in the fuel assembly during its irradiation, e.g. for rods in a fuel assembly corner position or with one or more guide tube neighbours. The *wdc* factor is effectively obtained by requiring the preservation in the pin cell calculation of individual isotopic variations with burnup (e.g. ^{235}U and ^{239}Pu) obtained explicitly in a detailed 2D fuel assembly depletion calculation [att]. The depletion calculations were performed using a temporal grid defined by steps of irradiation during the cycle (*DEP card*) and outage periods (*SDC card*), with the same time mesh provided for the four modelled irradiation histories. This dense time mesh corresponds to rather small burnup steps (<2.5 GWd/t). The burnup variations of the concentration ratios ^{134}Cs/^{137}Cs, ^{154}Eu/^{137}Cs, and ^{134}Cs/^{154}Eu obtained with CASMO-4E, using the code's ENDF/B-VI based cross section libraries, are given in Figs. 6.20 - 6.21. The following observations are derived from this depletion study:

o The corrections introduced using the *wdc* factors are not very significant for the build-up of ^{137}Cs (negligible), and ^{134}Cs (<2%). For ^{154}Eu the discrepancies reach ~4-5%.

o Results for the most detailed irradiation histories ("core-follow" and "core-follow wdc") compare well with those for the other cases only for burnups lower that 50 GWd/t. Differences with respect

to the "life-average" case are effectively significant only for the ratios involving ^{134}Cs. This can be attributed to the ^{134}Cs sensitivity to power density, i.e. sensitivity to the stretching of the last reactor cycles. For segment *S#4*, differences occur mainly at medium burnups, viz. immediately after the long intermediate cooling (~3 years) between the fourth and fifth cycles.

o The standard burnup monitors depart from linearity markedly at very high burnups. The variation of ^{134}Cs/^{137}Cs is highly linear only up to medium burnup values (~40 GWd/t), and the same is true for ^{154}Eu/^{137}Cs where linearity is lost even at lower burnup. At high and ultra-high burnup levels, both ratios indicate saturation, hence decreasing their usefulness as burnup indicators. The situation is worse in the case of ^{154}Eu/^{137}Cs which, in fact, shows a decreasing trend with burnup above ~70 GWd/t.

o For the ^{134}Cs/^{154}Eu ratio, the lower graphs in Figs. 6.20 and 6.21 show a trend opposite to that of ^{154}Eu/^{137}Cs. Thus, while decreasing with burnup up to ~40 GWd/t, this ratio displays a very smooth positive variation at high and ultra-high burnups.
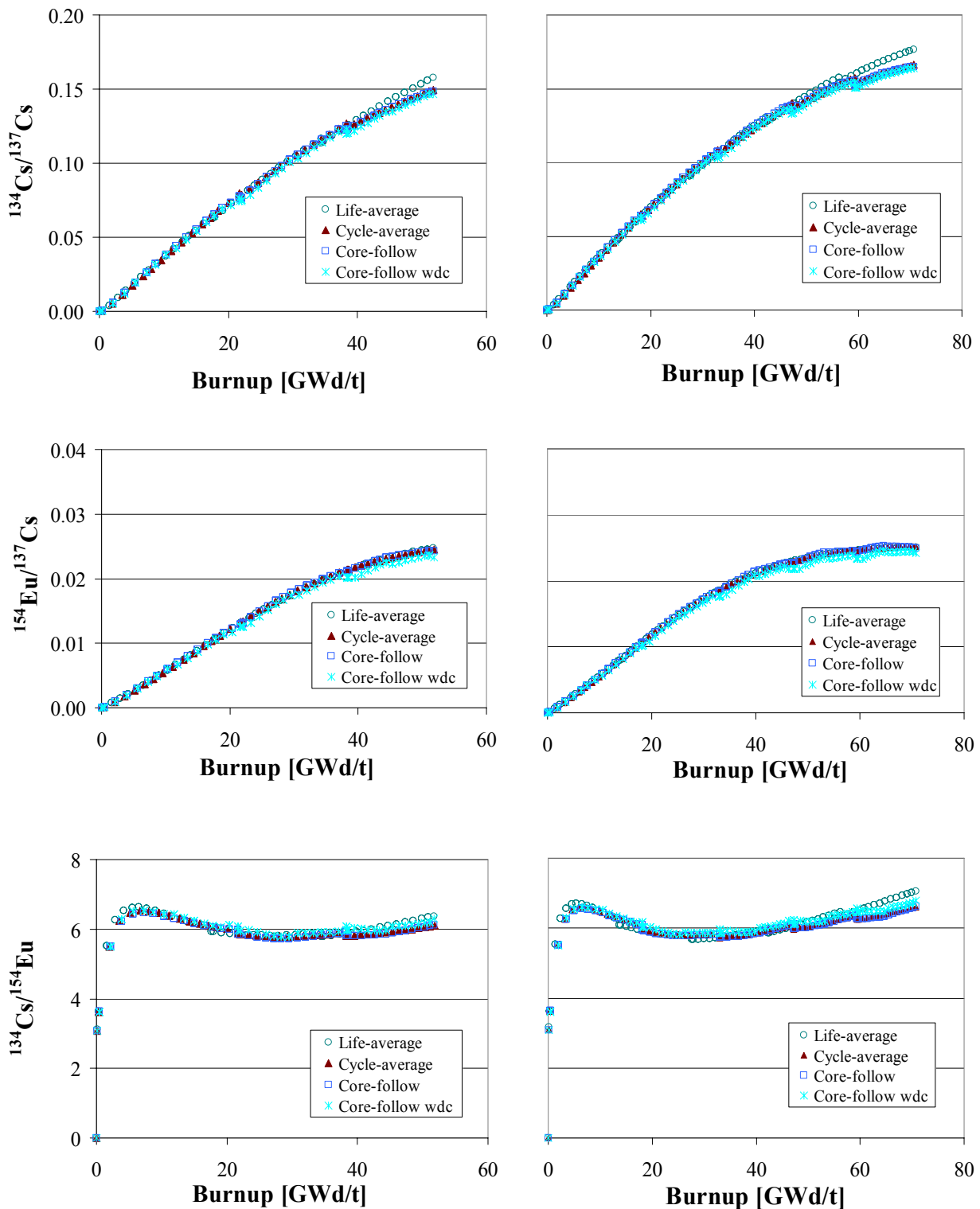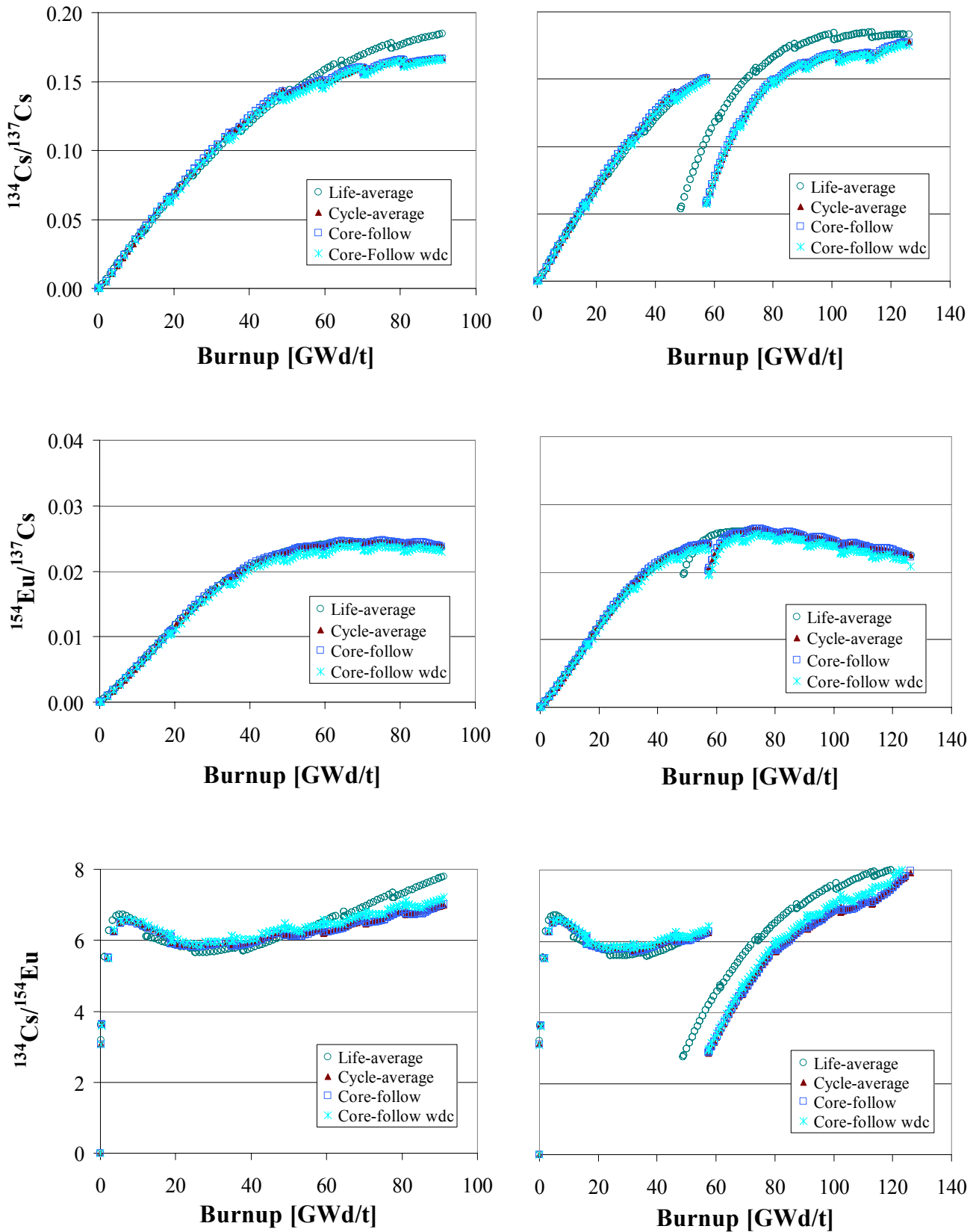
Fig. 6.20. Concentration ratios from CASMO-4E depletion calculations performed for the UO$_2$ fuel rod segments *S#1* (left) and *S#2* (right), with four different irradiation history descriptions using ENDF/B-VI-based libraries. Top: ^{134}Cs/^{137}Cs. Middle: ^{154}Eu/^{137}Cs. Bottom: ^{134}Cs/^{154}Eu.

Fig. 6.21. Concentration ratios from CASMO-4E depletion calculations performed for the UO$_2$ fuel rod segments *S#3* (left) and *S#4* (right), with four different irradiation history descriptions using ENDF/B-VI-based libraries. Top: ^{134}Cs/^{137}Cs. Middle: ^{154}Eu/^{137}Cs. Bottom: ^{134}Cs/^{154}Eu.

163

6.3.3. Comparison with measurements

A first comparison with experiment of calculational results for the isotopic ratios was reported for samples S#3 and S#4, on the basis of the preliminary experiments described in Section 3.1 [car2]. The present section describes comparisons with the final measurements for all four fuel rod segments.

The measured isotopic concentration ratios, belonging to the central slit experimental approach (SLIT), and their comparison with CASMO-4E calculated results using ENDF/B-VI ($C_{ENDF/B-VI}$) and JEF2.2 "update d" ($C_{JEF2.2}$) as well as with CASMO-4 using ENDF/B-IV ($C_{ENDF/B-IV}$) are given in Table 6.3. The most accurate "core-follow wdc" irradiation history cases have been considered for these comparisons. The agreement between experimental and calculated values is seen to be significantly better for the $^{134}Cs/^{137}Cs$ ratio than for the ratios including the ^{154}Eu concentration, and for the ENDF libraries. The former ratio, nevertheless, shows C/E discrepancies between 10-25% (11-18% for ENDF/B-VI), clearly indicating that further studies are needed if agreements within 2-3% are to be attained, as is commonly achieved for the low and medium burnup ranges. However, the relatively good agreement between these experimental values and the chemical analyses presented in Section 6.2.2 needs to be borne in mind.

For the $^{154}Eu/^{137}Cs$ ratios, significantly poorer C/E results have been obtained (between 30-44% for ENDF/B-VI). Nevertheless, for these ratios the prediction seems to be improved by ~30% compared to the ENDF/B-IV results. The use of ^{154}Eu for the determination of burnup clearly still needs a far better predictability of the ^{154}Eu concentration. However, the $^{134}Cs/^{154}Eu$ ratios are rather better predicted, except using ENDF/B-IV. For the caesium ratio, the discrepancies between the calculations using different libraries (ENDF/B-IV, ENDF/B-VI and revised JEF2.2) are <10%, although the values were not in very good agreement with experiment.

For the CASMO-4E calculations based on the revised JEF2.2 cross section library, the results are quite similar, in general, to the ENDF/B-VI results. However, very large differences (up to 60% for the highest burnup segment) have been found for the ^{154}Eu concentrations between the old JEF2.2 "update b", implemented for CASMO-4, compared to ENDF/B-IV. This has been observed and reported in previous work [roq-car-car2]. The differences from ENDF/B-VI results are up to 80%. As the calculations using the old JEF2.2 "update b" were very discrepant with respect to all the other calculations, these have not been included in Table 6.3 (for a better readability of the results).

Table 6.3: Isotopic concentration ratios for the fuel rod segments *S#1* (52 GWd/t), *S#2* (70 GWd/t), *S#3* (91 GWd/t) and *S#4* (126 GWd/t): experimental results from high-resolution gamma-ray spectrometry (SLIT), compared to CASMO-4E calculations using ENDF/B-VI and the JEF2.2 "update d" library, and to CASMO-4 calculations using ENDF/B-IV. All calculational results relate to the case "core-follow wdc".

Ratio	Result	*S#1*	*S#2*	*S#3*	*S#4*
$^{134}Cs/^{137}Cs$	Experiment (SLIT)	$0.132 \pm 1.4\%$*	$0.142 \pm 1.4\%$	$0.140 \pm 1.4\%$	$0.150 \pm 1.5\%$
	$C_{ENDF/B-VI}$ / SLIT	1.11	1.16	1.18	1.16
	$C_{ENDF/B-IV}$/ SLIT	1.10	1.15	1.18	1.18
	$C_{JEF2.2}$/ SLIT	1.20	1.24	1.25	1.22
$^{154}Eu/^{137}Cs$	Experiment (SLIT)	$0.0189 \pm 2.1\%$	$0.0169 \pm 2.0\%$	$0.0160 \pm 2.0\%$	$0.0160 \pm 2.4\%$
	$C_{ENDF/B-VI}$/ SLIT	1.30	1.43	1.44	1. 30
	$C_{ENDF/B-IV}$/ SLIT	1.66	1.77	1.71	1.57
	$C_{JEF2.2}$/ SLIT	1.30	1.47	1.49	1.37
$^{134}Cs/^{154}Eu$	Experiment (SLIT)	$7.73 \pm 1.5\%$	$8.40 \pm 1.5\%$	$8.78 \pm 1.5\%$	$9.39 \pm 1.9\%$
	$C_{ENDF/B-VI}$/ SLIT	0.86	0.81	0.82	0.89
	$C_{ENDF/B-IV}$/ SLIT	0.66	0.65	0.69	0.75
	$C_{JEF2.2}$/ SLIT	0.92	0.84	0.84	0.90

(*) SLIT: experimental result from the central slit gamma spectrometry measurements; R: relative error (1σ); $C_{ENDF/B-VI}$: CASMO-4E predictions using the ENDF/B-VI-based library; $C_{ENDF/B-IV}$: CASMO-4 predictions using the ENDF/B-IV-based library; $C_{JEF2.2}$: CASMO-4E predictions using the revised JEF2.2-based library.

In Figs. 6.22 - 6.24, the experimental values of $^{134}Cs/^{137}Cs$, $^{154}Eu/^{137}Cs$ and $^{134}Cs/^{154}Eu$ derived with SLIT and SCAN methods are compared with the ENDF/B-VI calculated values related to the case "core-follow wdc" of sample S#4. Error bars for the experimental values are visible. As mentioned in Section 6.3.2, for segment S#4, there was an intermediate cooling of ~3 years after its fourth cycle, and this is visible in the calculated ratios. In spite of this disturbance, it can be seen that the trends of the measured ratios approximate to those of the calculated ratios. In particular, the $^{134}Cs/^{154}Eu$ ratio continues to increase monotonically even at ultra-high burnups, thus highlighting its usefulness as a burnup indicator. The measured $^{134}Cs/^{137}Cs$ ratio, on the other hand, shows a much greater saturation effect.

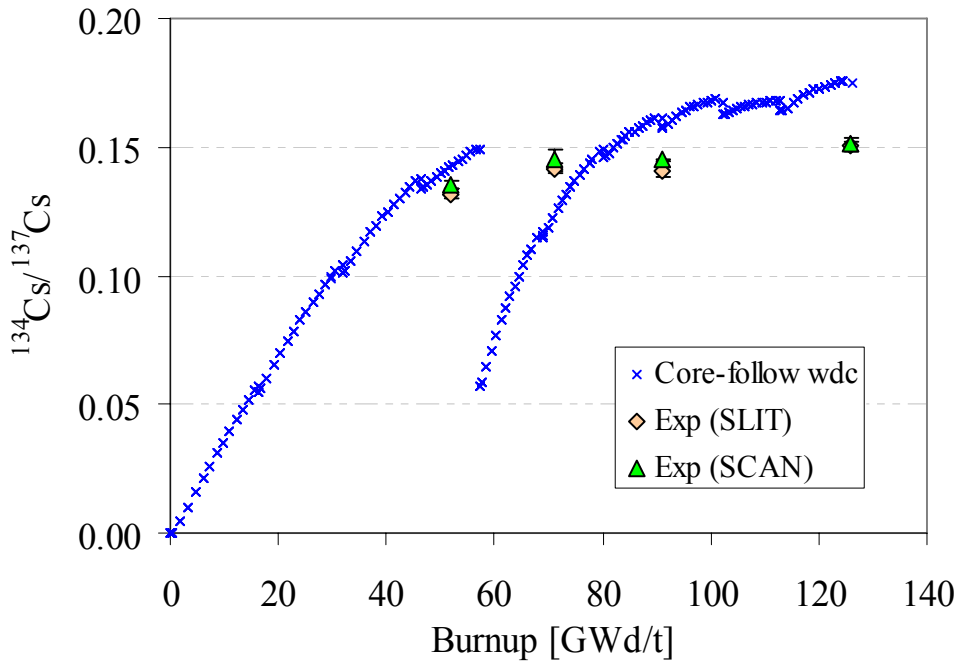Fig. 6.22: ^{134}Cs/^{137}Cs concentration ratio from CASMO-4E depletion calculations ("core-follow wdc" case) performed for the sample *S#4*, together with the measured ratios (SLIT and SCAN methods).
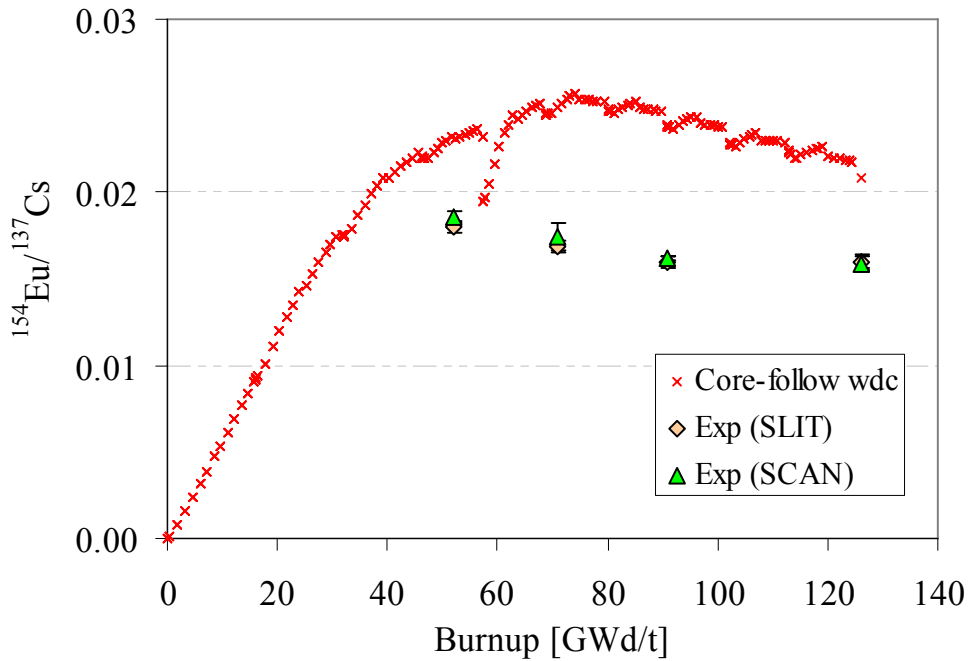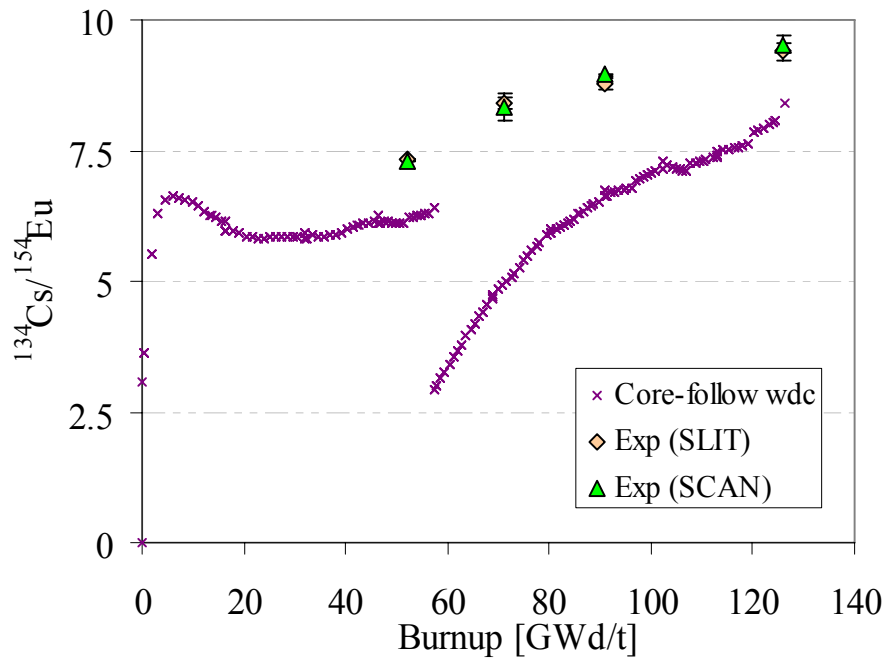

Fig. 6.23: ^{154}Eu/^{137}Cs concentration ratio from CASMO-4E depletion calculations ("core-follow wdc" case) performed for the sample *S#4*, together with the measured ratios (SLIT and SCAN methods).

Fig. 6.24: $^{134}Cs/^{154}Eu$ concentration ratio from CASMO-4E depletion calculations ("core-follow wdc" case) performed for the sample *S#4*, together with the measured ratios (SLIT and SCAN methods).

Concluding this section, one may say that the use of the $^{134}Cs/^{137}Cs$ ratio as a burnup monitor is not straight-forward in the high and ultra-high burnup ranges. Whereas errors of a few percent are expected in the range of low and medium burnups, much higher discrepancies between calculations and measurements (10-25% typically) have been identified for the currently investigated record burnup values. Several factors need to be evaluated to reduce the $^{134}Cs/^{137}Cs$ discrepancies at high burnups. These include the saturation of ^{137}Cs, the sensitivity of ^{134}Cs buildup to irradiation history, and the differential migration of the caesium isotopes in the rod.

The comparisons of measured and calculated isotopic ratios including ^{154}Eu show even larger discrepancies (30-44% for ENDF/B-VI). Here, the predictability of ^{154}Eu needs to be improved i.e. the high sensitivity to the cross section libraries employed needs to be resolved. One reason that has been suggested for the observed discrepancies is the over-prediction of ^{153}Eu [cor]. However, improvements have been found in the ENDF/B-VI-based cross section library with respect to the ENDF/B-IV and in particular to the two releases of JEF2.2.

Whereas $^{134}Cs/^{137}Cs$ and $^{154}Eu/^{137}Cs$ ratios are valid monitors at low and medium burnups, their use for values >50 GWd/t is less accurate for physical reasons (saturation). In contrast, the $^{134}Cs/^{154}Eu$ ratio builds up smoothly at high and ultra-high burnups and can be measured accurately, thus having the

potential to become a useful burnup monitor as soon as significant improvements are made in basic cross-section data and overall predictability.

6.4. Radial Spatial Indexes

The isotopic within-pin distributions derived through tomographic reconstruction (details in Chapter 5) have been used to derive spatial isotopic ratios. Two zones of the pin were identified: an inner zone, comprising the central part of the pin (1.6 mm radius), and an outer zone, a 2.8 mm thick ring, contiguous with the inner zone but not extending quite to the periphery of the pin. These zones are shown in Fig. 6.25. The picture shows the ^{137}Cs distribution of S#4 in plan view at the centre, and two vertical cut views of the radial ^{137}Cs distribution for all the samples, with two different perspectives. The 0-deg position is shown below and on the right is the 90-deg position. In these vertical cut views, the spatial zones are marked using two different colours (inner zone in green and outer zone in pink).
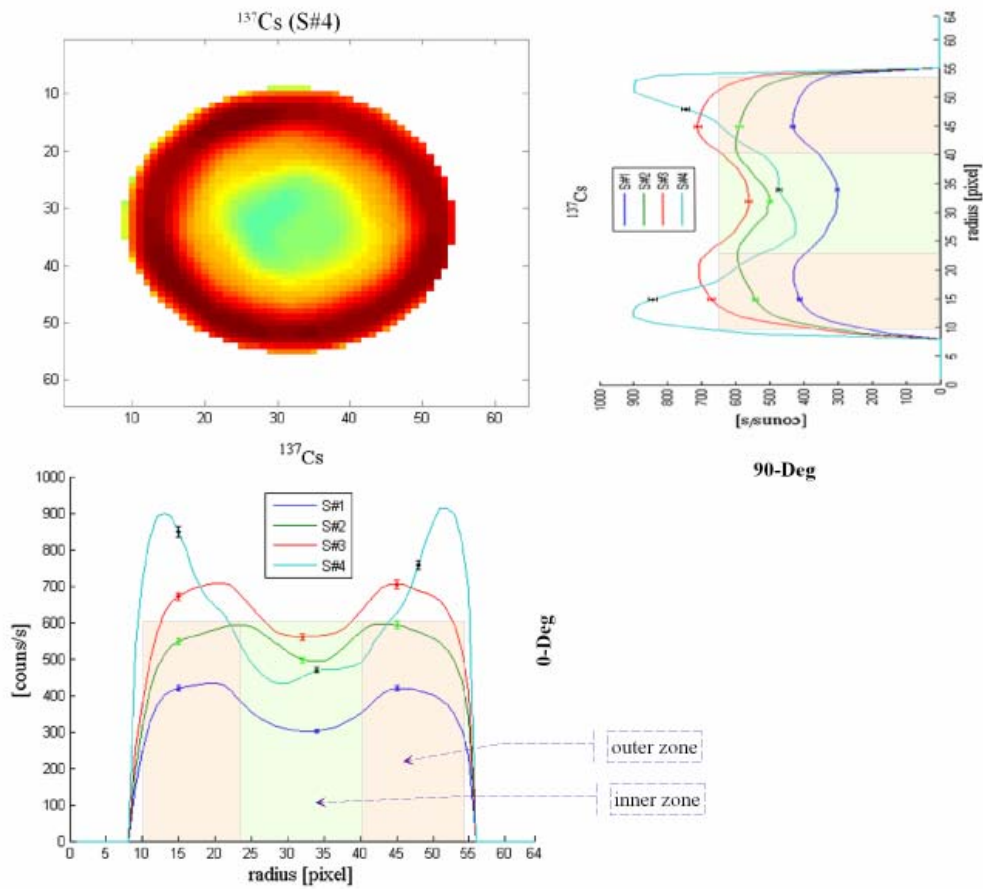

Fig. 6.25: The 0-deg and 90-deg radial ^{137}Cs distribution for all the samples. The spatial zones are marked using two different colours (inner zone in green and outer zone in pink).

The spatial ratios have been derived, in each case, as the quotient of the value for the outer region over that for the inner region. The results used for this exercise come from the reconstructions based on the PSCA algorithm. The spatial ratios so obtained were plotted versus burnup, as shown in Fig. 6.26 (a), for ^{137}Cs, ^{134}Cs, and ^{154}Eu, whilst spatial ratios of the isotopic ratios (^{134}Cs/^{137}Cs, ^{154}Eu/^{137}Cs, and ^{134}Cs/^{154}Eu) are plotted in Fig 6.26 (b).

(a)   (b)
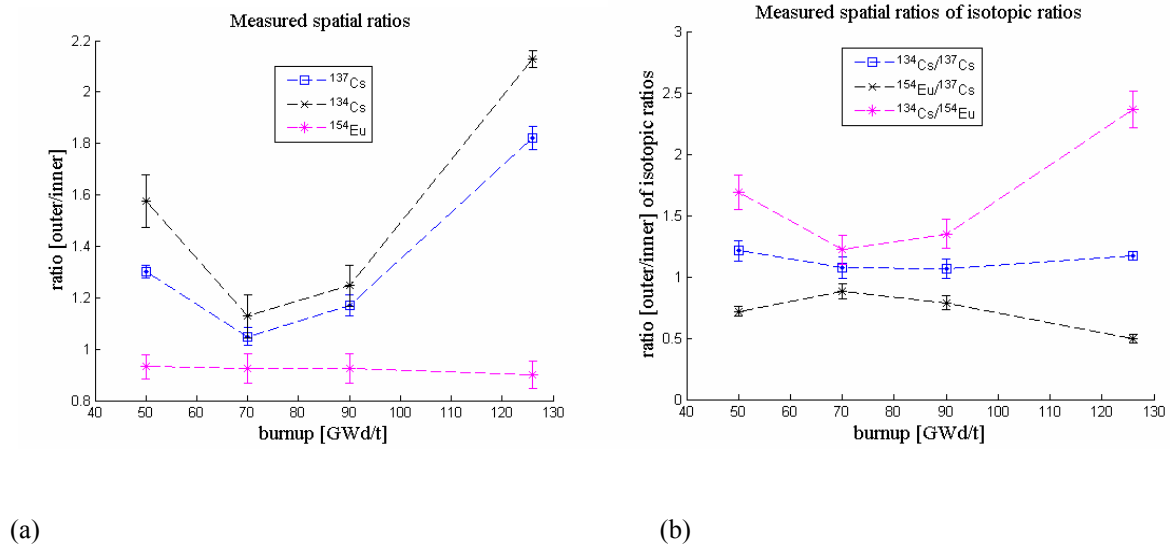
Fig. 6.26: (a) Spatial ratios derived from tomographic reconstruction, as function of burnup, for ^{137}Cs, ^{134}Cs and ^{154}Eu. (b) Spatial ratios of isotopic ratios.

Considering ^{137}Cs and ^{134}Cs, one can observe that the dependence of their spatial ratios on burnup is not straightforward, especially considering the behaviour of the lower burnup sample. This behaviour, where the low burnup ratio has an opposite trend to that for the high burnup samples, may be explained by the fact that the migration process appears to be a function of a variety of physical and chemical characteristics of the fuel material, such as thermal gradient, fuel density and oxygen-to-metal ratio. At low burnup, the higher fuel temperature (and power density in the rod) may be the main cause for the migration (and consequently of the depression). The power density plot of Fig. 6.27, as a function of the irradiation history of the samples, may support this analysis. When the burnup value is very high, other physical phenomena start to be predominant.

Other observations can be made while regarding the differences in the spatial ratios between ^{137}Cs and ^{134}Cs. The spatial ratio of ^{134}Cs is greater than that of ^{137}Cs. This may be explained by the fact that ^{134}Cs appears to migrate more readily than ^{137}Cs (because of the longer half-lives of its precursors, the volatile ^{133}I (half life of 20.8 hours) and the gaseous ^{133}Xe (half life of ~5.2 days), compared to those of ^{137}Cs [gui]). However, as already mentioned, the ^{134}Cs is formed by neutron

169

capture in the fission product ^{133}Cs, which will have already started to migrate, and this may be the dominant mechanism. Lastly, ^{154}Eu, having a spatial ratio which changes only very little with burnup, is seen not to be useful for this kind of analysis.
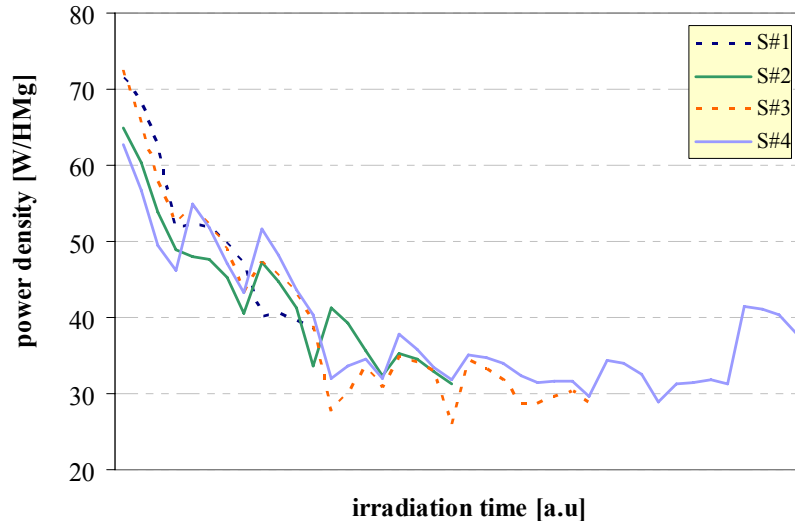

Fig. 6.27: Power density history of the four samples.

As a complementary study, CASMO-4E depletion calculations have been performed to study the within-pin distributions of ^{137}Cs, ^{134}Cs, and ^{154}Eu and to derive the same spatial ratios as obtained from the measured tomographic data. CASMO-4E pin cell depletion calculations, employing the code's ENDF/B-VI-based cross section libraries, were carried out for these fuel rod segments using the most accurate and detailed irradiation history description ("core-follow wdc", as described in Section 6.3.1). With the use of the *RAD* card of CASMO, it was possible to obtain the concentration as a function of the pin radius as shown in Fig. 6.28. The distributions of the three isotopes are quite similar and, as the code is unable to model the caesium migration processes, no relevant differences can be observed between the volatile metal isotopes of caesium and those of the more stable metallic europium.

The spatial indices have been built in function of burnup using the calculated data, employing the same spatial regions as described in Fig. 6.25 for the measurements. As shown in Fig. 6.29 (a), the predicted spatial indices do not agree with the ones derived from measurements. In the calculation, the spatial ratio of ^{134}Cs and ^{137}Cs are monotonically increasing with burnup. The europium has a tendency to decrease, but not really significantly. The calculated caesium spatial ratios reflect, indeed, the absence of a migration process model in the depletion calculations. Fig. 6.29 (b) shows the calculational results for the spatial ratios of the isotopic ratios.
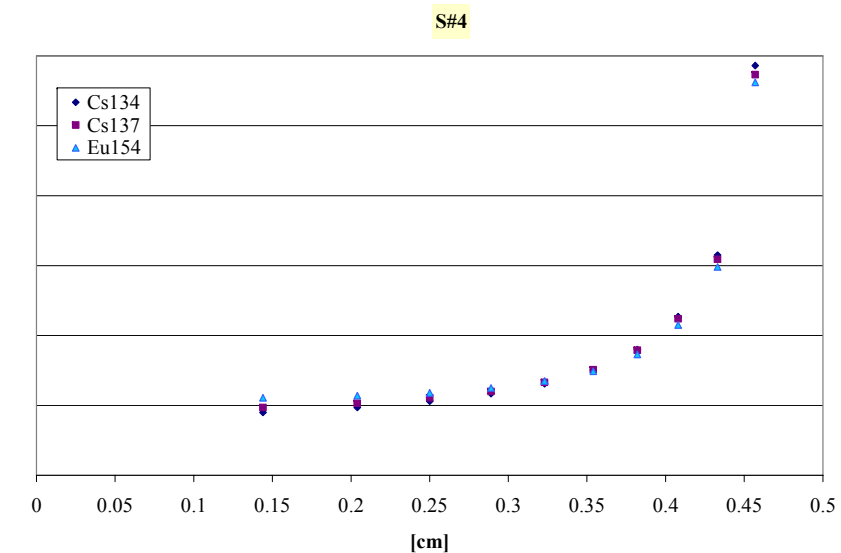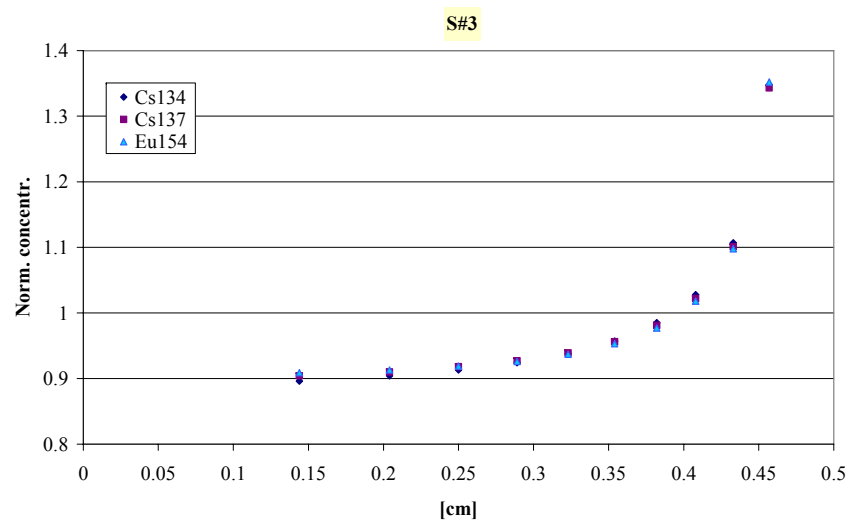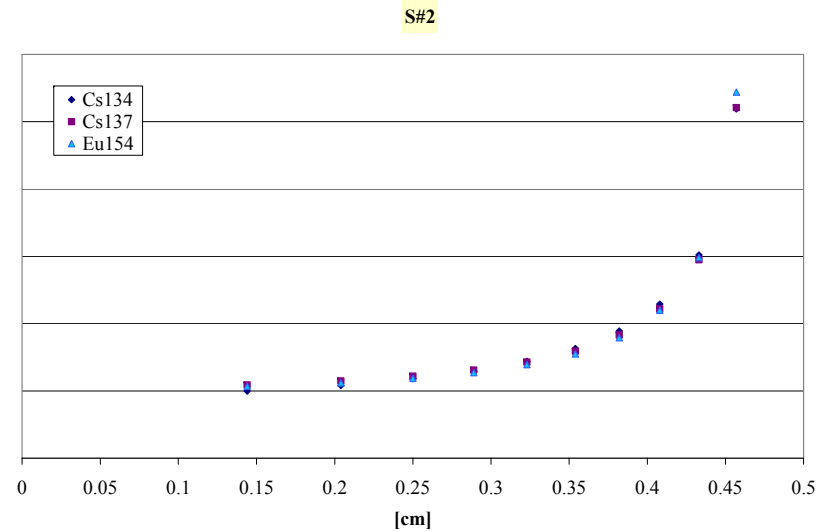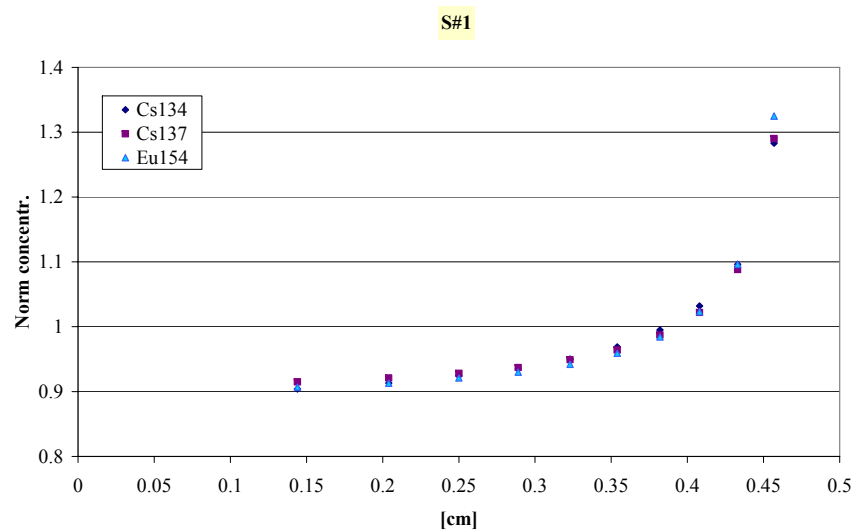
Fig. 6.28: CASMO-4E pin cell depletion calculations, employing the code's ENDF/B-VI-based cross section libraries, in function of radius pin for the four fuel rod segments and using the most accurate and detailed irradiation history description ("core-follow wdc"). The values in the plots are normalised to an average value of unity.
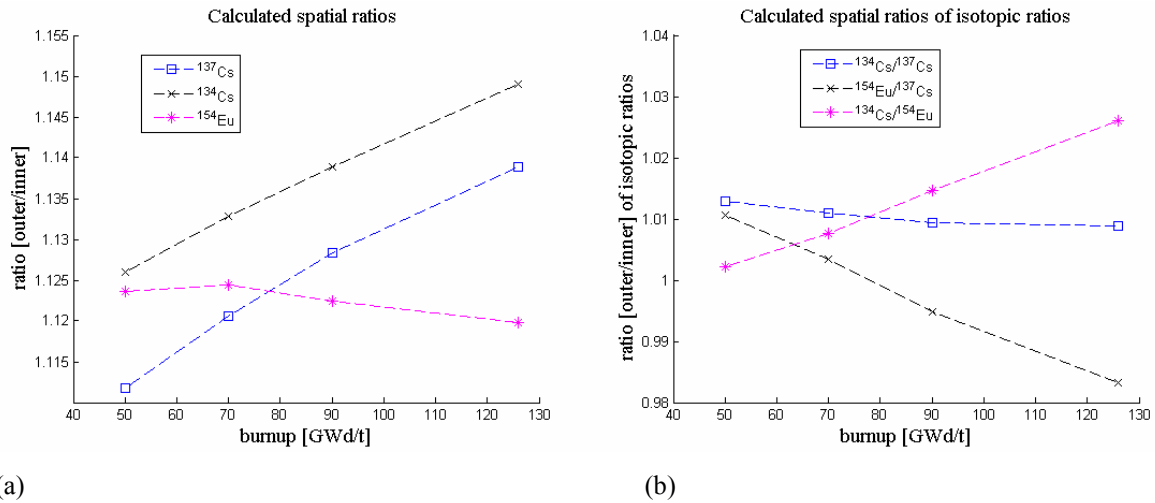
Fig. 6.29: (a) Spatial ratios, predicted with CASMO-4E, as a function of burnup for ^{137}Cs, ^{134}Cs, and ^{154}Eu.
(b) Spatial ratios of isotopic ratios.

The main conclusion one can draw from the consideration of spatial ratios is that a correlation between within-pin isotopic distributions and burnup is not easily possible, because of the complexity of the phenomena involved.

6.5. Summarised Findings on High Burnup Indices and Monitors

A study has been carried out for the implementation of ^{134}Cs, ^{137}Cs, and ^{154}Eu gamma-activities as burnup monitors at very high burnups. Measurements on the four spent fuel rod samples were made using three different approaches: integral values obtained by integrating the tomography projection scans (SCAN), individual measurements obtained with longer measurement times, with the collimator slit in a fixed position aligned with the axis of the pins (SLIT), and integral values obtained by integrating the final tomography reconstructions (TOMO). The thereby deduced relative concentrations have been compared with destructive chemical analysis (Section 6.1.2). All three isotopes show the potentiality to be employed as burnup indicators, even though, in each case, a certain tendency to saturate at high burnup is confirmed by the measurements. Considering that caesium is a volatile metal, which migrates from centre to periphery, the best candidate as burnup indicator is clearly the physically stable ^{154}Eu. Once an empirical correlation is established and a calibrated sample is available, the ^{154}Eu activity could serve as a very easy-to-employ index of absolute burnup.

172

Gamma-spectroscopic measurements of ^{134}Cs/^{137}Cs, ^{154}Eu/^{137}Cs, and ^{134}Cs/^{154}Eu isotopic concentration ratios, based on the SCAN and SLIT methods, have been validated up to ultra-high burnup values, through comparisons with destructive chemical analysis (Section 6.2.2). The results have also been compared with CASMO depletion calculations (Section 6.3.3). It has been shown that the ^{134}Cs/^{137}Cs ratio, frequently used as a burnup monitor, is considerably less precise for burnup values exceeding 50 GWd/t. Whereas the chemical results confirm the gamma-spectroscopic measurements, the agreement between experiment and calculation is not satisfactory. The ^{154}Eu/^{137}Cs ratio shows saturation at high burnup, and the code predictions are considerably less accurate due to the difficulties of predicting the ^{154}Eu content. The agreement with the chemical measurements is even better for this ratio (differences of <1.4% in the SLIT method and <2.2% in the SCAN method). A third ratio, ^{134}Cs/^{154}Eu, has been proposed as a burnup index because of its smooth build-up at high and ultra-high burnups. Encouragingly, it shows reasonable agreement with the chemical analysis (within a few percent for samples S#1 to S#3 and less than 1.5% for sample S#4).

In the derivation of the isotopic ratios, the impact of corrections necessary to account for the different within-pin isotopic distributions (affecting the gamma-ray self-attenuation) has been found to be relatively minor (<1.3%). In the case of the SLIT method, however, the effect of the different distributions on the system geometric efficiency has to be taken into account as well. This correction has been found to be more significant, particularly in the case of sample S#4, where the effect of the highly depressed caesium distribution is as high as ~16%.

All in all, HPLC-MC-ICP-MS is clearly a more precise method for determining the ratios discussed here than gamma spectroscopy, with statistical errors generally a fraction of a percent (compared to the currently achieved 1.4 - 2.4% for SLIT and 0.3 - 4.5% for SCAN). However, the analytical effort required for the destructive analysis of fuel samples, including the fuel dissolution and the HPLC-MC-ICP-MS measurements themselves, is much higher. Concerning the calculated values, better agreement can be achieved as soon as significant improvements are made in basic cross-section data and overall predictability, especially for ratios containing ^{154}Eu.

Finally, another study was carried out using the emission tomographic measurements to develop radial spatial indices, mainly for ^{137}Cs and ^{134}Cs, as a function of burnup (Section 6.4). These spatial indices are ratios of the activity in the outer zone of the pin over that in the inner zone, reflecting the level of central depression in the isotopic distribution. Because of the complex phenomena related to species migration and high burnup physics, a linear or smooth correlation between spatial ratios and burnup could not be identified.

References

[att]   F. ATTALE, Private Communication 2006

[bec]   J.S. BECKER, "State-of-the-art and progress in precise and accurate isotope ratio measurements by ICP-MS and LA-ICP-MS: plenary lecture", *J. Anal. Atom. Spectrom*., **17** p.1172 (2002)

[bnl]   BNL, 1990. "ENDF-102 data formats and procedures for the evaluated nuclear data file ENDF-6", BNL-NCS-44945-01/04 (last revised 2001)

[bri]   J.F. BRIESMEISTER, "MCNP – A General Purpose Monte Carlo N-Particles Transport Code, Version 4C", LA-12625-M

[car]   S. CARUSO, I. GÜNTER-LEOPOLD, M. MURPHY, F. JATUFF, R. CHAWLA, "Validation of optimised germanium gamma spectrometry vs. multicollector inductively coupled plasma mass spectrometry for the determination of ^{134}Cs,^{137}Cs and ^{154}Eu single ratios in highly-burnt UO$_2$", to be submitted to *Nucl. Instr. and Meth. A* (2007)

[car2]   S. CARUSO, M. MURPHY, F. JATUFF, R. CHAWLA, "Validation of ^{134}Cs,^{137}Cs and ^{154}Eu single ratios as burnup monitors for ultra-high burnup UO$_2$ fuel", *Annals of Nuclear Energy,* **34** p.28 (2007)

[cou]   A. COURCELLE, C. CHALBERT, O. LITAIZE, B. ROQUE, A. SANTAMARINA, O. SEROT, "Experimental Validation of Main Fission Products and Actinide Nuclear Data: Improvements for JEFF-3", PHYSOR 2002, Seoul Korea, Oct. 7-10 2002.

[dsp]   DSPECTM. Digital Gamma-Ray Spectrometer, EG&G ORTEC Catalog, Oak Ridge

[ede]   M. EDENIUS, K. EKBERG, B.H. FORSSEN, D. KNOTT, "CASMO-4. A Fuel Assembly Burnup Program. User's Manual", Studsvik Report SOA-95/1, Studsvik of America, 1995

[gam]   "GammaVisionTM-32. Gamma-Ray Spectrum Analysis and MCA Emulation for Microsoft®Windows® 95 and Microsoft Windows NT. A66-B32 Software User's Manual", EG&G ORTEC Part No. 774780 Manual Revision A, Oak Ridge

[gue]   I. GÜNTER-LEOPOLD, B. WERNLI, Z. KOPAJTIC, D. GÜNTER. "Measurement of isotope ratios on transient signals by MC-ICP-MS", *Anal. Bioanal. Chem.*, **378** p. 241 (2004)

[gue2]   I. GÜNTER-LEOPOLD, J. KOBLER WALDIS, B. WERNLI, Z. KOPAJTIC, "Measurement of plutonium isotope ratios in nuclear fuel samples by HPLC-MC-ICP-MS". *International Journal of Mass Spectrometry,* **242** p.197 (2005)

[hsu]   S.T. HSUE, T.W. CRANE, W.L. TALBERT, J.C. LEE, "Nondestructive Assay Methods for Irradiated Nuclear Fuels", Los Alamos internal report LA-6923, (1978)

[iae]   "Guidebook on Non-Destructive Examination of Water Reactor Fuel", 1991, IAEA-TECDOC-322.

[kri]   E. KRISTOFF et al., "Gamma Spectrometric Assessment of Nuclear Fuel", *Nuc. Instr. and Meth. In Phys. Res. A*, **297** p.507 (1990)

[leb]   A. LEBRUN, G. BIGMAN, "Non-destructive Assay of Nuclear Low-enriched Uranium Spent Fuels for Burnup Credit Application", *Nucl. Technol.,* **135** p.216 (2001)

[nak]   Y. NAKAHARA et al., "Experimental Verification of Availability of (^{134}Cs/^{137}Cs)^2/(^{106}Ru/^{137}Cs) Gamma-ray Intensity Ratio as a Burn-up Monitor for LWR Fuels", *Sixth International Conference on Nuclear Criticality Safety*, ICNP'99, Versailles, France, Sep 20-24 1999

[nea]   NUCLEAR ENERGY AGENCY, "*The JEF-2.2 nuclear data library*", NEA-JEFF Report 17 (2000)

[phi]   J.R. PHILLIPS et al., "Quantitative Determination of Fission Products in Irradiated Fuel Pins Using Non-Destructive Gamma Scanning", *Anal. Chem.,* **47** p.71 (1975)

[pla]   I.T. PLATZNER (Ed.), *Modern Isotope Ratio Mass Spectrometry,* Wiley, Chichester, (1997)

[pra]   C. PRALONG FAUCHERE, "Irradiation Histories of LWR-PROTEUS Phase II Samples", PSI internal report (2004)

[qad]   "QAD-CGGP. A Combinatorial Geometry Version of QAD-P54, a Point Kernel Code System for Neutron and Gamma-Ray Shielding Calculations Using the GP Buildup Factor", RSIC Computer Code Collection, Radiation Shielding Information Center, Oak Ridge National Laboratory (1977)

[rho]   J. RHODES, K. SMITH and M. EDENIUS, "CASMO-4E Extended Capability CASMO-4 User's Manual, SSP-01/401 Rev 2", Studsvik Scandpower (2004)

[rou]   B. ROUCHE et al., "Experimental Validation of the Code System "DARWIN" for Spent Fuel Isotopic Predictions in Fuel Cycle Applications", PHYSOR 2002, Seoul Korea, October 7-10

[sas]   A. SASAHARA, T. MATSUMURA, G. NICOLAOU, D. PAPAIOANNOU, "Neutron and Gamma-ray Source Evaluation of LWR High Burn-up UO2 and MOX Spent Fuels", *J. Nucl. Sci. Technol.,* **41** p.448 (2004)

[wil]   CH. WILLMAN, A. HÅKANSSON, O. OSIFO, A. BÄCKLIN, S. JACOBSSON SWÄRD, "Nondestructive Assay of Spent Nuclear Fuel with Gamma-Ray Spectroscopy", *Ann. Nucl. Energy,* **33** p.427 (2006)

7. <u>General Conclusions</u>

The present research has focused on the investigation of high burnup fuel rods by using a dedicated measurement station, built for high resolution gamma-ray spectrometry and gamma-ray emission and transmission tomography. Four burnt fuel rod samples, with different burnups in the range 52 GWd/t to 126 GWd/t, have been studied. The average density of each sample, as also the spatial density distribution has been derived using transmission tomography. The within-pin distributions of ^{134}Cs, ^{137}Cs, and ^{154}Eu have been reconstructed by emission tomography that embody the transmission tomography results (as density maps), in order to ensure optimal image quality. Finally, burnup monitors have been characterised for high and ultra-high burnups, through the use of caesium and europium concentration ratios and/or by single isotope activities.

The following sections summarise the work carried out and the main achievements. Recommendations for further work are given in the penultimate section.

7.1. Summary

The first chapter of the thesis serves to introduce the reader to the present doctoral research, by describing the general framework for its conception and realisation. The main aim of the second chapter is to provide certain basic information, which may help the non-specialist reader to achieve a more complete comprehension of the topic at hand, in particular the experimental aspects. Thus, the first part of the chapter concentrates on the main parameters and relevant aspects (e.g. burnup, fuel properties, etc.), whilst the second part is focused on the investigation methods. The third chapter concerns the experimental setup currently developed and employed. First, the experiments performed as a preliminary study are described, followed by the exploratory design calculations. Details are then provided of the developed gamma tomography station, in terms of its basic components, as also of the irradiated fuel rod samples investigated.

Chapter 4 is devoted to transmission tomography measurements, including a large section describing the principles of tomography and the main tomographic reconstruction methodologies (for both emission and transmission). Experimental procedures, currently developed as state-of-the-art for transmission tomography, as also the corresponding results obtained, are given in the last part. These are effectively for the linear attenuation coefficient distributions, the density maps, and average densities for the four burnt fuel segments, as also for a fresh pin.

Chapter 5 is devoted exclusively to emission tomography aspects, i.e. the solution of two-dimensional single photon emission computerized tomography (SPECT) problems in the context of obtaining within-pin nuclide distributions for the irradiated fuel rod samples. First, a brief introduction to the basic principles of SPECT and the required steps needed to address the problem are given. Then the gamma-scanning and data processing procedures for emission tomography are presented, followed by the description of the system efficiency matrix development. The principal results obtained from simulation tests and for the actual burnt fuel samples are given in the last part, where different algorithms have been compared. The measured within-pin distributions of ^{137}Cs, ^{134}Cs, and ^{154}Eu are illustrated and commented on, for each sample. Further, caesium distributions for sample S#4 have been compared with different destructive chemical analyses.

Chapter 6 is divided into four main sections. The first concerns the development of single isotope high-burnup monitors, on a relative scale, using integrated values from the tomography projection scans, the tomography reconstructions, and subsidiary measurements with the collimator slit at the centre of the pin. The non-destructive results obtained with the germanium detector system, using two different experimental approaches, have been compared with destructive chemical analysis (viz. multicollector inductively coupled plasma mass spectrometry). The second part is devoted to validating the accuracies and precisions of the experimental results for ^{134}Cs/^{137}Cs, ^{154}Eu/^{137}Cs, and ^{134}Cs/^{154}Eu isotopic concentration ratios obtained using the gamma tomography station. In the third part, a theoretical study of the build up of ^{134}Cs, ^{137}Cs, and ^{154}Eu single ratios with burnup is presented, where pin cell depletion calculations performed for each segment using the deterministic code CASMO-4 are discussed in detail. The last part is based on the results of Chapter 5, viz. use of the isotopic within-pin distribution maps derived with gamma-ray emission tomography to obtain radial spatial indices as a function of burnup.

7.2. Main Achievements

A novel tomographic measurement station has been developed for the investigation of irradiated fuel rod segments of 400 mm length. A unique feature of the station is that it allows both transmission and emission tomography to be performed on single fuel pins. Preliminary measurement campaigns, followed by Monte Carlo analysis, were necessary to design the most critical parts of the station, such as collimator and shielding. Thereby, special attention was paid to ensure adequate flexibility for the investigation of samples having a very wide range of burnups, and consequently a wide range of activities. The large differences in the activity of the samples under investigation represented a major challenge, leading to the decision to implement a collimator with a capability to modify the slit width

as required. After the data processing, and especially after a first tomographic analysis, one could benefit from the flexibility of the apparatus, adding or removing lead and paraffin filters. Although particular pulse shaping treatment was necessary for the most active sample, the main design of the station was very satisfactory, and the collimator slit, although it was variable, was ultimately employed with its initially planned width.

The application of transmission tomography to fresh and spent fuel rods has been a major task, because of difficulties of implementation and the uniqueness of the experiments. In fact, to the author's knowledge, transmission tomography has never been applied directly to spent fuel rods before. Different tomographic algorithms have been tested currently, as described in Chapter 4 and, amongst these, PSCA was chosen for presentation of the final results. The main achievements of the transmission measurements have been successful determination of:

i) Fuel rod average material density

ii) Fuel rod linear attenuation coefficient distribution (for use in emission tomography)

iii) Fuel rod material density distribution

Concerning the first point, a linear relationship between density and burnup was established, whilst the second point has given important information about the photon linear attenuation in the fuel rods so that more precise emission tomography reconstructions can be achieved. Regarding the third point, the variation of density in function of pin radius provides interesting information about the change of the morphology of nuclear fuel with burnup. Especially for the highest burnup sample, the periphery is characterised by a lower density (a steep decrease of almost 10% from the adjacent region) characteristic of the ultra-high burnup structure. It is relevant to note that once the linear relationship between density and burnup has been validated, one may eventually be able to evaluate burnup directly from density variation through gamma-transmission techniques.

The non-destructive technique of emission computerised tomography (CT) has been applied to high and ultra-high burnup fuel rods for the determination of the within-pin distributions of caesium and europium fission-product isotopes. The gamma spectrometric analysis of the irradiated fuel rod samples has been challenging because of the need to properly derive non-Gaussian gamma-peak areas and subtract the background from perturbing capture gammas produced by the high intensity of the neutron source in the spent fuel. As mentioned, results provided by transmission tomography measurements have been employed in the emission tomography reconstruction phase, together with a calculated global efficiency matrix and input sinograms derived from the processing of measured projections. Different tomographic algorithms have been tested and tuned, using known test

distributions, and then applied to the real measurements. Amongst all the methods, PSCA penalised likelihood was chosen for the presentation of the final results, because it ensures high precision, especially in resolving the most difficult peripheral regions of the pins. To the author's knowledge, emission tomography has never been applied to such high burnup samples before, nor have so many different and advanced reconstruction methods been tested at the same time.

The results of the emission tomography have indicated large central depressions in the caesium distributions, but of varying extent from sample to sample. Particularly interesting is the case of the 126 GWd/t sample, showing a very deep central depression (a factor of ~2.5 for ^{137}Cs, a factor of ~3 for ^{134}Cs). In addition, a difference in the relative activity distributions of ^{137}Cs and ^{134}Cs has been observed for all the samples. In fact, the depression of ^{134}Cs seems to be more marked than that of ^{137}Cs, probably due to the different origins of the two isotopes. In contrast, the europium shows an almost flat distribution. In this case, however, larger uncertainties present in the experimental data, as also over-smoothed image edges and artificial undulations, do not allow one to exclude the presence of a finite central depression. In order to support the tomographically measured caesium distributions, the results of other analytical techniques on samples from the same fuel rod (S#4) were examined. Both EPMA and LA-ICP-MS results, generated by the PSI Hotlab, compare well with the tomography, confirming depressed distributions at the centre of the pin. Because the samples analysed by the different techniques were not exactly the same (coming from the same rod, but from different axial positions), a detailed quantitative comparison is not appropriate. It must of course be emphasised that the destructive chemical approaches require a much greater effort, as compared to non-destructive computerised tomography.

In addition to the tomographic reconstructions, advantage has been taken of the data accumulated during these investigations to try to characterise the burnup of the fuel. First, a study was carried out for the implementation of ^{134}Cs, ^{137}Cs, and ^{154}Eu as absolute burnup monitors at very high burnups. A measurement of the individual isotopic concentration variations was performed using three different approaches: integral values obtained by integrating the tomography projection scans (SCAN), individual measurements obtained with longer measurements using the collimator slit in a fixed position aligned with the axis of the pins (SLIT), and integral values obtained by integrating the final tomography reconstruction (TOMO). Isotopic concentrations, obtained on a relative scale with the above techniques, have been compared satisfactorily with destructive chemical analysis. All three isotopes show the potentiality to be employed as burnup indicators, even though, in each case, a certain tendency to saturate at high burnup is confirmed by the measurements. Considering that caesium is a volatile metal, which migrates from centre to periphery, the physically stable ^{154}Eu, with

its low sensitivity to irradiation history, is clearly the best candidate. Once a calibrated sample is available, ^{154}Eu gamma-activity measurements could indeed serve as a very convenient burnup monitor,

Validation has been carried out for the accuracies and precisions achievable in the measurement of ^{134}Cs/^{137}Cs, ^{154}Eu/^{137}Cs, and ^{134}Cs/^{154}Eu isotopic concentration ratios by the use of non-destructive high-resolution gamma spectrometry. These concentration ratios have been compared with destructive chemical analysis and with depletion calculations. It has been shown that the ^{134}Cs/^{137}Cs ratio, frequently used as a burnup monitor, is considerably less accurate when burnup values exceed 50 GWd/t. Whereas the chemical results confirm the current gamma-spectroscopic measurements (within ~5% for the SLIT method and within ~7% for the SCAN method), the agreement between measurements and calculations is not satisfactory. The ^{154}Eu/^{137}Cs ratio shows saturation at high burnup, and the code predictions are rather inadequate (due largely, in this case, to difficulties in predicting the ^{154}Eu content accurately). The agreement with the chemical measurements is significantly better for this ratio. Finally, one has been able to propose a third ratio, viz. ^{134}Cs/^{154}Eu, as a more appropriate burnup index for high and ultra-high burnups. This ratio, which also shows adequate agreement with the chemical analysis, has been found to continue building up smoothly at high burnup values.

Considering that the overall effort required for the destructive chemical analysis of fuel samples is much higher, the current investigations have clearly demonstrated that non-destructive gamma spectroscopic measurements (incorporating computerised tomography results), can indeed be considered a very valid approach for assessing fuel burnup in the high/ultra-high range. This is especially the case if "on-line" measurements need to be carried out.

7.3. Recommendations for Further Work

Even though detailed preliminary studies were carried out while designing the measurement setup, certain problems only became evident during actual use of the apparatus. In some cases, the problems could be overcome by ad hoc solutions. On the other hand, not all the problems could be solved, compromise solutions needing to be employed at times. In the following paragraphs, suggestions and recommendations, garnered from the current experience, are proposed for further work in this field.

- Experimental Setup

Special care is needed in the design of the collimator, especially with respect to possible interfaces between the collimator and shielding enclosure. One must avoid these interfaces, which produce leakage paths for gamma-rays, as much as possible. The best solution is to employ a solid collimator block that completely shields the entire length of the pin from the detector.

During the measurement campaign, the highly active samples, being stored in the sample flask/changer above the measurement station, produced a high Compton gamma background, which contributes to degrade the accuracy of the measurements. Further, the neutron source intensity in high burnup pins, originating from the spontaneous fission and $^{18}O(\alpha,n)$ reactions from the decay of minor actinides such as ^{244}Cm or ^{252}Cf, produces an additional capture gamma background perturbing the measurements and degrading the resolution of HPGe detectors rather rapidly through neutron damage. A valid shielding solution must be taken to prevent this in advance (using paraffin wax or some other hydrogen bearing material, or storing the samples far from the measurement position, if feasible). In our case, paraffin wax was employed to limit the damage. Concerning the gamma background, a better solution is to use a collimator thicker than 15 cm, and consequently to increase the spectrum acquisition time. Lower background can mean better final statistics for the photo-peak. However, this solution must take due account of increased measurement times necessary to accumulate sufficient counts.

Another recommendation is to employ a completely symmetric clamping system, to avoid, as much as possible, precession during the rotation of the samples and to have uniform photon attenuation, not dependant on the angular position.

- Tomography

Amongst the large number of tomographic algorithms available, only a few were used here. However, the techniques employed were the ones which appeared the most promising, being those most widely applied in medical imaging currently. Nevertheless, better solutions can be envisaged for the future. In any case, the application of a given tomographic algorithm depends on several parameters and functions that need to be tested on known shapes, in order to ensure being able to obtain the best reconstruction. Such a test phase was indeed carried out currently, but the author's recommendation is to pay extreme care to this aspect. The development of one's own reconstruction technique, customised to a specific problem, is a challenging task, and this can only be achieved if sufficient time

is devoted uniquely to this purpose. Otherwise, and this was the case here, one may implement available algorithms and/or test existing software packages.

A large effort must be invested in the development of the system efficiency matrix, to be as faithful to the measurement setup as possible. A strong recommendation is to increase the measurement time for each scan to achieve better statistics in the photo-peaks and consequently better image resolution. If possible, setting a narrow collimator slit width may be a very good improvement for the resolution, but this involves a significant increment of the acquisition time and makes leakage through the collimator block more of a problem. Concerning the number of angular projections, eight is a very small number compared with typical medical application, but the increment of this number is not really feasible. However, for fuel rod investigations, where the azimuthal variation may not be very severe, a good solution is to average the angular projections (as done for the case of europium). To make use of typical software that expects a large number of azimuthal positions, a graded interpolation between the discrete positions should be used.

- Burnup Monitors

The measurement of isotopic ratios as burnup monitors using a collimator with a narrow vertical slit is not a convenient solution, because correction factors based on accurately measured isotopic within-pin distributions must be invoked. (Otherwise, the uncertainty on the final measurement may be very large for caesium isotopes, especially for highly burnt fuels.) For this reason, one suggestion is to use only a horizontal slit. Further, if a vertical slit is necessary for other purposes (e.g. tomography, etc.), a valid solution may be to install a collimator having a vertical slit, but provided with the capability to be extracted and rotated by 90° so that the slit becomes horizontal. This is a feasible option which does not imply large costs.

- Measurement Strategies and Further Investigations

Important improvements in nuclear fuel rod tomography could be achieved by means of a dedicated strategy focused on privileging the acquisition of projections at the periphery of the pin. For instance, reducing the slit width, or increasing the acquisition time of the spectrum when measuring the pin periphery, may improve the resolution of the reconstructed image at pin edge level.

The tomographic measurement of MOX fuel rods represents an interesting extension of the present work. Effort in the realisation of transmission and emission tomography in this context would be of particular significance from the viewpoint of validating standard LWR assembly codes for MOX

applications. The possibility of correlating measured MOX-fuel density directly to burnup is an additional advantageous aspect.

The assessment of neutron emitters in burnt fuels is another interesting and complex topic, with the potential for providing an alternative to gamma spectroscopy for non-destructive quantification of high burnups. During the current research, attempts were made to use the tomography station also for neutron measurements on the four irradiated fuel rod samples. A calculational study of the main neutron emitters at high and ultra-high burnups was carried out. However, achieving a sufficiently clear breakdown of the main components of the neutron count rates registered proved to be too difficult a task in the time available.

7.4. Concluding Remarks

In conclusion, the present research has clearly demonstrated that transmission and emission gamma tomography is applicable to highly burnt nuclear fuel rods. To the author's knowledge, transmission tomography has never been applied directly to spent fuel before. This technique provides a powerful analytical tool in its own right, in providing detailed information on the fuel density variation with burnup. The latter, when used in conjunction with emission tomography, is most effective in improving the corresponding image quality.

An interesting linear relationship has been found between density and burnup, for the UO_2 fuel rod samples investigated. Concerning the emission tomography carried out, very interesting ^{137}Cs and [134]Cs within-pin distributions were derived, even if suffering from over-smoothed edges during the image processing. In particular, the 126 GWd/t sample showed a very deep central depression (factors of ~2.5 and ~3 for ^{137}Cs and [134]Cs, respectively). Again, to the knowledge of the author, emission tomography has never been applied to such high burnup samples, and with so many different and advanced reconstruction methods tried out at the same time.

The present research has also investigated the possibility to use both single isotope activities and isotopic concentration ratios as burnup indicators for very high and ultra-high burnups. The corresponding non-destructive measurements have been compared with chemicals assays, as well as with reactor physics calculations. It has been shown that certain indicators, well established for application at low and medium burnups, suffer a serious loss of accuracy at high burnup. Nevertheless, the possibility of successfully employing other burnup monitors has been clearly brought out.

Appendix A: Non-Gaussian Peak Behaviour

Standard peak treatments were found to be inadequate for the measured gamma spectra of high and ultra-high burnup samples, as most of the peaks were not really Gaussian and some of them were close to interference peaks, typically neutron-capture gammas, which may have led to inaccuracy in the derivation of ^{134}Cs/^{137}Cs, ^{154}Eu/^{137}Cs, and ^{134}Cs/^{154}Eu isotopic concentration ratios and in the tomographic reconstruction procedure.

For illustration, a typical gamma spectrum, from sample S#2, acquired during the measurement campaign devoted to validating isotopic ratios as burnup indicators, is shown in Fig. A.1. The main peaks belonging to ^{134}Cs (605, 796, 1168, 1365 keV), ^{137}Cs (662 keV), ^{154}Eu (873, 996, 1005, 1275, 1494 keV, 1597 keV), are indicated in the picture, together with potential interferences peaks such as the annihilation peak at 511 keV, and the (n,^{113}Cd) gammas at 558 and 651 keV .
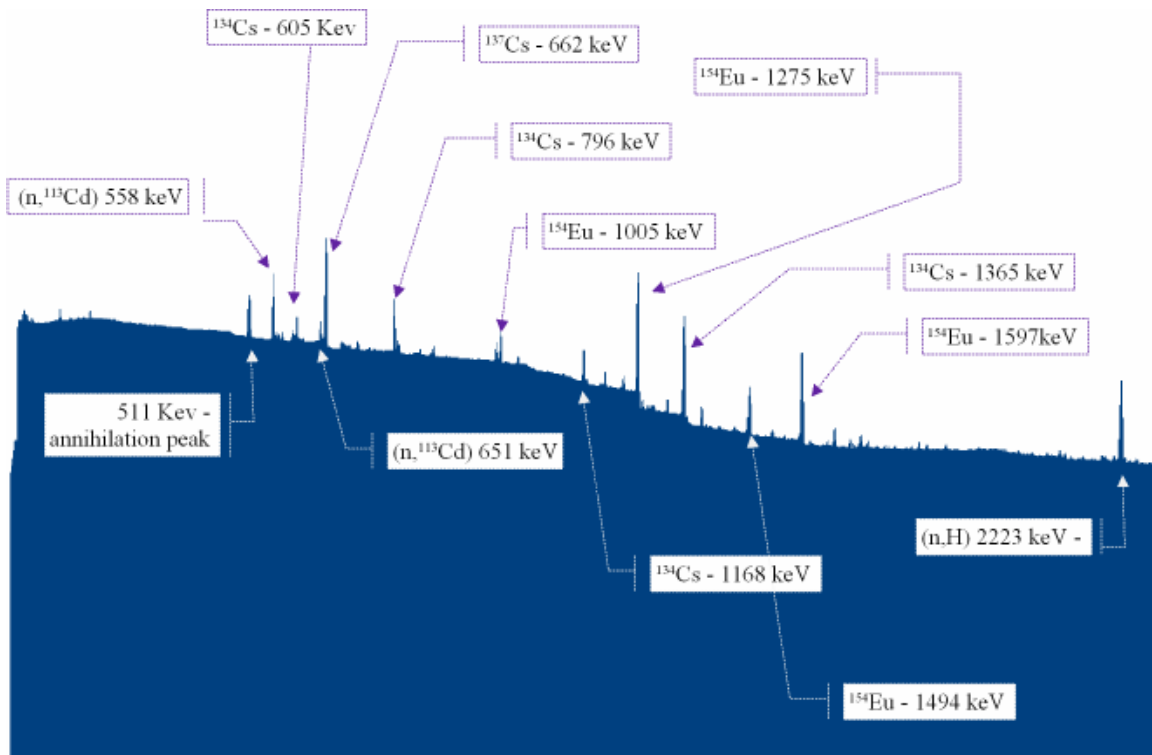
Fig. A.1: Gamma-ray spectrum from sample S#2.

A detail of the Gamma-Vision peak analysis (WAN32, widely used for standard gamma spectrum analysis) for a spectrum measured for the sample S#3 (91 GWd/t), is illustrated in Fig A.2-3. (In this work, the use of Gamma-Vision was limited to the acquisition of the spectra.) This spectrum was acquired with the collimator slit positioned at the centre of the pin. In this specific case, the 1275 keV

[154]Eu peak of Fig. A.2 is treated with a Gaussian fit (red line). The difficulty to fit the peak properly is clearly seen. By use of the approach described in Section 5.2.1, most of the problems associated with peak fitting have been avoided.

On the left, in Fig. A.3, another example of non-Gaussian peaks is shown, viz. in relation to the [134]Cs γ-lines at 795 keV and 802 keV. On the right, in the same figure, an example is given of strong interference, viz. that for the 873 keV [154]Eu peak, due to the high rate of neutron capture in the HPGe crystal ((n,[73]Ge) 867 keV) resulting from the high neutron source intensity of the fuel at this burnup level.
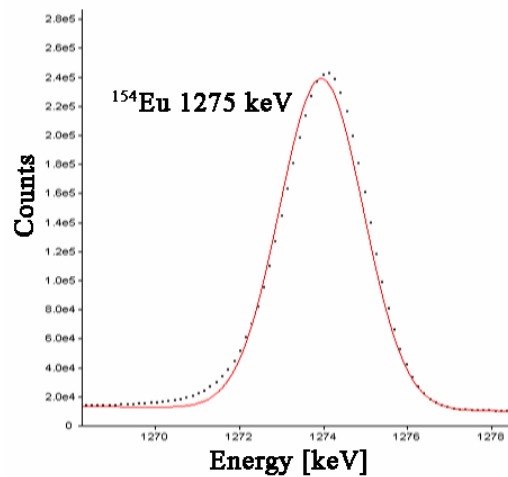
Fig. A.2: Details of typical Gamma-Vision peak analysis from the spectrum measured for the 91 GWd/t sample (S#3). The 1275 keV [154]Eu peak is treated with a Gaussian fit.
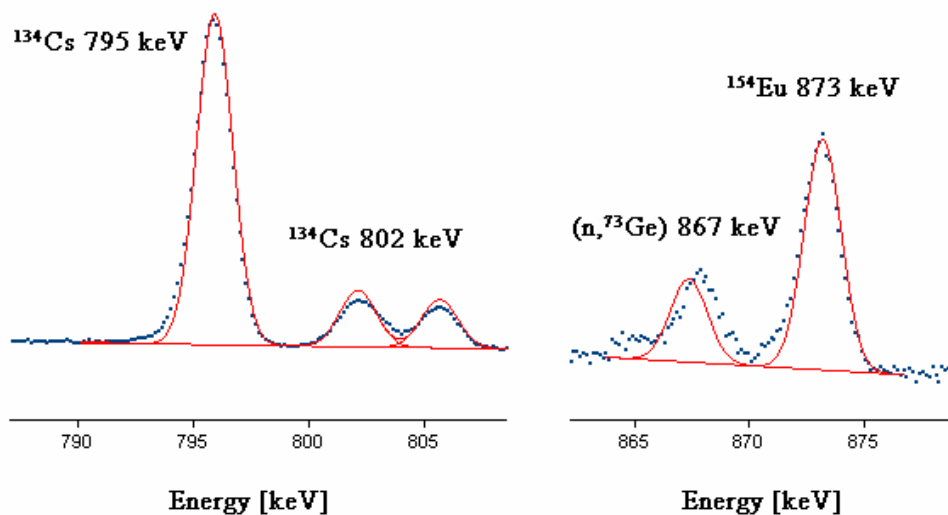
Fig. A.3: Details of typical Gamma-Vision peak analysis from the spectrum measured for the 91 GWd/t sample (S#3). Left: example of non-Gaussian peaks; right: strong interference in the [154]Eu peak due to neutron capture in the HPGe crystal because of the high neutron source intensity of the fuel at this burnup level.

Appendix B: Dose Rate Map

Dose rates measurements for both gamma and neutron emissions were curried out at the beginning of the experimental campaign, as part of the for standard radioprotection procedure. These measurements were performed by the operators while the samples where inside the PROTEUS transport flask/sample changer. The main results (µSv/h), corresponding to five different positions around the flask (see Fig B.1), at contact surface and at one meter distance from the surface, are provided in Table B.1.
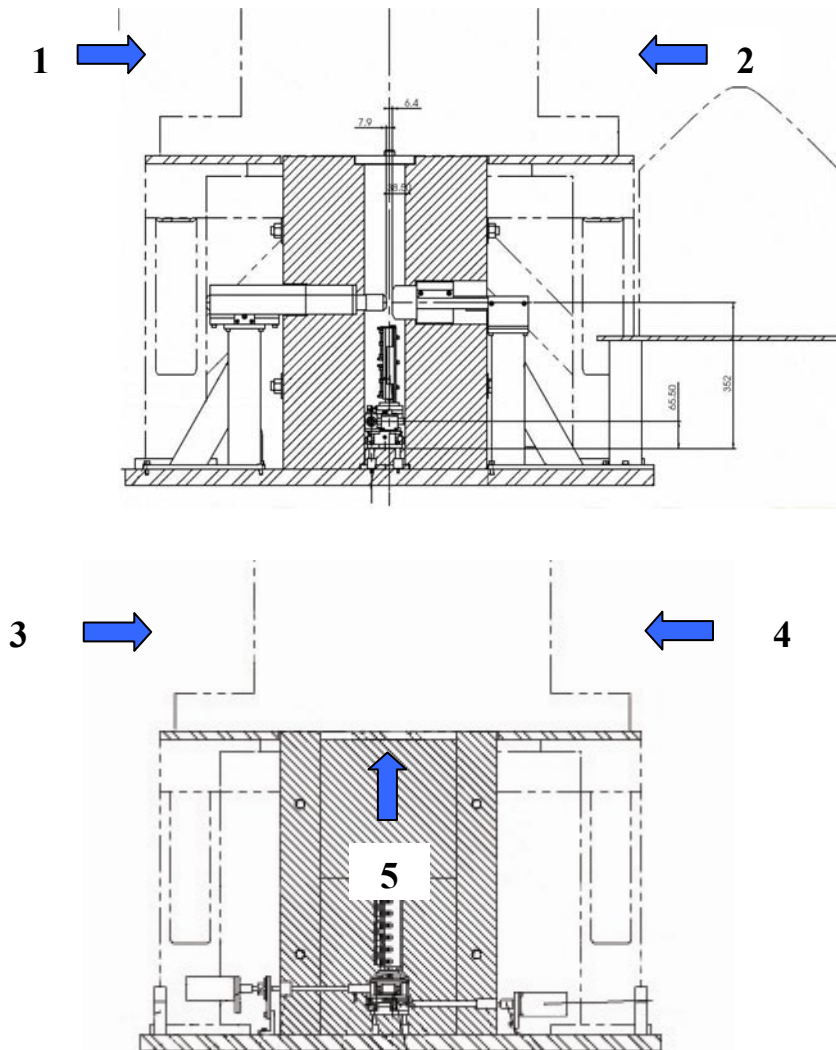
Fig B.1: Dose rate measurement positions around the PROTEUS transport flask/sample changer.

Table B.1: Dose rate values (µSv/h) for gammas and neutrons, at contact surface and at a distance of one meter from the surface.

| Measurement positions | Dose Rate in µSv/h | | | |
| | At contact | | At 1 meter | |
	gamma	n	gamma	n
1	8	360	0.9	37
2	6	300	1	45
3	4	250	0.8	36
4	5	290	1	48
5	2	90	0.5	15

List of Abbreviations

ANN	Artificial Neural Network
ART	Algebraic Reconstruction Technique
BU	Fuel Burnup
CT	Computerised Tomography
EM	Expectation Maximisation
EPMA	Electron Probe Microanalysis
FBP	Filtered Back Projection
GP	Gamma Projector
HPGe	High-Purity Germanium
HPLC-MC-ICP-MS	High-Performance Liquid Chromatographic Multi-Collector Inductively Coupled Mass Spectrometry
ICP	Inductively-Coupled-Plasma
LA	Laser Ablation
LWR	Light Water Reactors
MAP	Maximum *a posteriori*
ML	Maximum Likelihood
ML-EM	Maximum-Likelihood Expectation-Maximisation
MR	Magnetic Resonance Tomography
MS	Mass Spectrometry
NDA	Non-Destructive Assay
NPP	Nuclear Power Plant
OS	Ordered Subset
OSEM	Ordered Subset Expectation Maximisation
OSTR	Ordered Subset Transmission
PET	Positron Emission Tomography
PIE	Post-Irradiation Examination
PL-DP or OSDP	Penalised Likelihood De Pierro or Ordered Subset De Pierro
PML-EM	Penalised Maximum Likelihood Expectation Maximisation
PSCA	Paraboloidal Surrogate Coordinate Ascent
PWLS	Penalised Weighted Least Square
RCU	Remote Control Unit
RHS	Remote Handling System
ROI	Region of Interest
SAGE	Space-Alternating Generalised EM

SCAN	Integral scan gamma-spectrometry method
SEM	Scanning Electron Microscopy
SIMS	Secondary Ion Mass Spectrometry
SLIT	Central Slit gamma-spectrometry method
SPECT	Single Photon Emission Computerised Tomography
TC	Tomographic Control unit
TF	Transport Flask/sample changer
TFCU	Transport Flask/sample changer Control Unit
TMS	Tomographic Measurement Station
TOMO	Tomographic reconstruction integrated
TSCU	Tomographic Station Control Unit

CURRICULUM VITÆ ET STUDIORUM

STEFANO CARUSO

CONTACTS

WORK CONTACTS		HOME CONTACTS
NOK – Kernkraftwerk Beznau, Döttingen	Address	Dorfstrasse 227, 5426 Siglistorf (CH)
+41 (0) 56 266 7408	Telephone	+41 (0) 56 281 30 39
stefano.caruso@nok.ch	Email	stefanocaruso@hotmail.com

PROFESSIONAL EXPERIENCES END EDUCATION

Nuclear Engineer employed by Nordostschweizerische Kraftwerke (NOK) at the Beznau Kernkraftwerk, Döttingen, Switzerland.	Jan 2007 -
Doctoral Candidate in Reactor Physics: EPFL, Lausanne, & PSI, Villigen, Switzerland. PHD THESIS: "*Characterisation of high-burnup LWR fuel rods through gamma tomography*"	Jul 2002 – Dec 2006
Programmer analyst employed by Datamat S.p.A. in Rome. Main task: design and development of on-board "Command and Control System" for intermarine minehunters ("Lerici" Class).	Sep 2000 – Jul 2002
Auxiliary agent within the IUCLID team of the European Commission (Euratom) at the European Chemicals Bureau - IHCP of the Joint Research Centre at Ispra, Italy.	Sep 1999 – Aug 2000
Programmer analyst employed at Sosinel s.r.l. and consultant for Siemens working at the TIM (Telecom Italia Mobile) in Marghera (Venice).	May 1999 – Aug 1999
Programmer analyst for Telespazio S.p.A. in Rome.	Sep 1998 – Apr 1998
Laurea (B.Sc, M.Sc.) Nuclear Engineering degree obtained at the University of Rome "La Sapienza". THESIS: "*A Study of Avalanche Photodiodes for the Calorimeter of CMS at LHC of CERN*" on line at http://www.roma1.infn.it/exp/cms/tesi	Oct 1989 – Dec 1997
Trainee at the INN-TEC Department of ENEA "LA CASACCIA" (under the supervision of Dr. S. Baccaro) and at the Rome section of INFN (under the supervision of Prof. E. Longo), in the context of a study of radiation damage on avalanche photodiodes.	Jun 1996 - Nov 1997

ADVANCED COURSES

- 2005 Frédéric Joliot / Otto Hahn Summer School on Nuclear Reactors (08/2005)
- ENEN's Eugene Wigner Training Course for Reactor Physics Experiments (05/2003)
- MCNP-5 Intermediate Level Training Course (03/2003)

PUBLICATIONS

1. S. Caruso, I. Günther-Leopold, M. Murphy, F. Jatuff, R. Chawla, "Validation of optimised germanium gamma spectrometry vs. multicollector inductively coupled plasma mass spectrometry for the determination of ^{134}Cs, ^{137}Cs and ^{154}Eu single ratios in highly-burnt UO$_2$", submitted to *Nucl. Instr. and Meth. A* (2007).
2. A. Izmer, S. Caruso, M. Horvath, N. Kivel, R. Restani, I. Günther-Leopold, "Determination of the caesium distribution in high Burnup fuel samples with different analytical techniques", 2007 European Winter Conference on Plasma Spectrochemistry, Poster ThPo39, Taormina, Italy 2007.
3. S. Caruso, M. Murphy, F. Jatuff, R. Chawla, "Validation of ^{134}Cs, ^{137}Cs and ^{154}Eu single ratios as burnup monitors for ultra-high burnup UO$_2$ fuel", *Annals of Nuclear Energy* Vol. 34 p.28-35 (2007).
4. S. Caruso, M. Murphy, F. Jatuff, R. Chawla, "Non-invasive characterization of burnup for PWR spent fuel rods with burnups > 80 GWd/t", Proceeding of ICAPP '06, Reno, NV USA, June 4-8, 2006.
5. S. Caruso, C.J.A. Heidorn. Public data on high volume chemicals: The IUCLID CD-ROM 'Year 2000 edition'. EUR Report No. 19559 EN Office for Official Publications of the European Communities, L-2985 Luxembourg, ISBN 92-828-8647-7 (2000).
6. S. Baccaro, B. Borgia, S. Caruso, F. Cavallari, I. Dafinei, M. Diemoz, I. Emeliantchik, A. Festinesi, E. Longo, M. Montecchi, G. Organtini, G. Rosi, APD properties and recovery from radiation damage, CERN report: CMS NOTE - 1997/030 ECAL Electronics (1997).

PERSONAL

Date of birth:	8 - 11 - 1969
Place of birth:	Rome
Nationality:	Italian
Civil status:	Married/one child